Quantum Well Intersubband Transitions: Nonlinear Optics, Refractive Index and Infrared Modulation

Thesis by

Gilad Almogy

In Partial Fulfillment of the Requirements
for the Degree of
Doctor of Philosophy

California Institute of Technology
Pasadena, California
1995
(submitted May 15, 1995)

to my parents Yuta and Yoram Almogy

and to the memory of my grandfather Joseph Almogy

Acknowledgments

I would like to thank my advisor, Professor Amnon Yariv, for giving me the opportunity to conduct research in such a stimulating environment. I have been greatly inspired by his scientific vision and privileged to work with the talented group of students and research fellows he assembled at Caltech. In particular I enjoyed the collaboration with John O'Brien on vertical cavity surface emitting lasers and beyond. His deep understanding and scientific approach were a constant source of inspiration. Much credit is due to Yuanjian Xu who did an endless amount of work on the monolithically integrated modulators, as well as Ali Shakouri who grew the MBE samples for my experiments and with whom I could always consult. I greatly benefited from, and also enjoyed working with, Andrew Tong in the course of his undergraduate research.

Special credit is due to Dr. Mordechai Segev who has taught me so much about the academic world, Dr. Ilan Gravé who helped me with my first processing steps, Dr. Amir Levinson with whom I enjoyed stimulating discussions and collaboration, and Prof. Bruno Crosignani with whom it was a true privilege to interact.

I have greatly enjoyed the collaboration with Dr. Axel Scherer on vertical cavity surface emitting lasers. Although that work is not included in this thesis, it was an invaluable experience. I would also like to thank Chuan-cheng Cheng, Weihua Xu and Charles Sharman, for their collaboration on the same subject. The help of Prof. George Rossman in infrared characterization is greatly appreciated. In working with him I got to see the epitome of a true, curiosity-driven, scientific approach. I am grateful to Steve J. Sanders for having the patience to hear out my uncooked ideas and proofread my first publications.

I would also like to thank current group members: Randy Salvatore, Bill Marshall, Matthew McAdams, and Sergei Orlov, and the recent graduates Drs. Lars Eng, Bin Zhao, John Kitching, Anthony Kewitch, Rudi Hofmeister, Thomas Schrans, and John Iannelli for their help and/or advice.

I owe a great debt to the people who made the experimental work possible. In particular I am grateful to Reynold Johnson, an endless source of knowledge and willingness to help, Larry Begay who always did the impossible so experiments wouldn't have to wait, Kevin Cooper who was always ready to help and Ali Ghaffari who supported our lab work. The help of Jana Mercado, Paula Samazan, and Illiana Salazar is appreciated.

Beyond the boundaries of Caltech I would like to thank Dr. Moshe Oron, Prof. Roni Agranat, and Prof. Aaron Lewis of the Hebrew Univeristy at Jerusalem for their encouragement and for making it possible for me to study at Caltech. Special thanks is due to Prof. Nisim Ben Joseph who through his teaching instilled in me the appreciation of electrooptics. During my thesis I greatly enjoyed the summer of working in the Weizmann Institute with Prof. Israel bar-Joseph, Dr. Udi Meirav, Dr. Konstantin Gartzman, and Prof. Mordechai Heiblum.

I am indebted to the funders, contributors and all others who have made the academic research possible. I hope we have lived up to their expectations and used the resources made available to us wisely. Most of all I would like to acknowledge the support of my parents, brothers and my soon to be wife Nechi, who have stood by me all along.

Abstract

The nonperturbative theory for the nonlinear optical interaction of quantum well intersubband transitions is developed. The nonlinear optical response of intersubband transitions in quantum wells is rigorously derived and the implications of their resonantly-enhanced nature are examined. Limitations on the use of the standard expansion of the induced polarization in terms of perturbative nonlinear coefficients are presented and it is shown that an alternative nonperturbative formalism is necessary for analyzing intersubband device applications. Upper limits are derived on the magnitudes of several key intersubband transition-induced nonlinear processes. It is shown that for both electrooptic and all-optic modulation, resonantly-enhanced absorption modulation is inherently preferable to phase modulation. A limit on the second-harmonic intensity that may be generated in a given propagation length and modified design criteria for optimizing second-harmonic generation in quantum wells are also obtained from the nonperturbative formalism.

The large and highly dispersive refractive index contribution of intersubband transitions was observed for the first time through the birefringence induced in a GaAs/AlGaAs multi-quantum well stack. It is shown that this index, rather than the absorption induced by intersubband transitions, may become the dominant limitation on frequency conversion efficiencies. Potential applications of this controllable refractive index for a

novel phase-matching technique of second-harmonic generation and for improved waveguiding in semiconductors is suggested and analyzed.

Removal of charge integration limitations upon the performance of thermal imagers through the 'ac'-coupling of infrared focal-plane arrays is suggested. This is achieved by the monolithic integration of an intersubband infrared absorption modulator and detector leading to a modulation depth of 45% at a wavelength of 10.6μm. The uniquely accurate design of the coupled quantum well infrared modulator was based on a self-consistent computer model of the Schrödinger and Poisson equations in quantum wells, taking into account many body effects, band nonparabolicity and flat band boundary conditions. Monolithic integration of the modulator and detector also turns out to be a simple and accurate method of studying the optical properties of quantum wells under bias. This technique led to the first observation of the exchange-interaction's contribution to the charge transfer between coupled quantum wells.

Contents

Part I

Part II

Part IV

Monolithic Integration of Quantum Well Infrared Photodetector and Modulator..210

Part I

Intersubband Transitions in Quantum Wells

Chapter 1

Introduction and Review

1 .1 Heterostructures

Low-dimensional structures exhibit what is perhaps the most straightforward manifestation of quantum mechanical principles in a man-made device: restriction of a particle's motion in one or more dimensions leads to quantization of its allowed states. Being a manifestation of the particle's wave nature, quantum size phenomena are observable only when the particle maintains coherence over the quantization dimension, i.e., when the influence of the quantization dominates that of random and temporal fluctuations. Semiconductor layers therefore have to be less than several hundred Angströms thick, a size regime beyond the tolerances of standard mechanical processing techniques, for these quantum size phenomena to become observable. Due to this difficulty, nearly half a century passed between the development of quantum mechanics [1] and the realization of controllable quantum size phenomena in semiconductor heterostructures.

The first suggestion of using alternating semiconductor compositions which would lead to the quantization of electronic motion in semiconductors was made by Esaki and Tsu in the early seventies [2,3]. A periodic variation of semiconductor layers, where the composition of each layer itself constitutes a periodic lattice, would impose a superlattice upon the material properties. As the lattice periodicity splits the atomic states into energy bands, the imposed super-period would split each energy band into subbands. The ability to grow epitaxial semiconductor layers with alternating material composition and near-atomic layer thickness control [4], or heterostructures, led to the demonstration of negative differential resistance in the current-voltage characteristics [5,6] of semiconductor superlattices. This was the first artificial quantum size effect to be measured. Research into the effects of heterostructure quantization on the optical properties of bulk semiconductors soon followed [7]. Confinement of excitons in one dimension led to observations of increased binding energy, modified selection rules, and enhanced optical nonlinearities [8] which are currently being used to develop ultrafast electrooptic modulators [9]. By far the dominant application of heterostructures, however, are quantum well lasers [10], in which one or several quantum wells are grown in the intrinsic region of a p-i-n laser diode. These wells serve on the one hand for “classical” purposes: confinement of the charge carriers and reduction of the volume that requires population inversion, but also for the reduction in the density of states which is quantum-mechanical in nature.

1 .2 Subbands

When layers of wide and narrow bandgap materials are sequentially deposited, carriers with an energy which is between that of the low and high bands will be trapped in potential wells. These are termed quantum wells (QWs) when they are narrow enough to significantly quantitize the energy of the confined charge. As a convention, the term multiquantum wells (MQWs) is used to distinguish structures in which the trapped carriers are essentially isolated within each period, from the term superlattice used when the wave states extend over several periods of the structure. Whereas quantization only modifies the optical response associated with the interband transitions, it leads to optical intersubband transitions which have no analog in bulk media. These transitions, termed quantum well intersubband transitions (QW-ISBTs), were first observed by West and Eglash [11] in 1985 and have been the focus of a growing research effort ever since.

A feature that is unique to intersubband transitions in quantum wells is the almost total control available over their optical characteristics by bandgap engineering, i.e., by the control of material thickness and composition. Essentially any required optical property can be designed within the limitations of the materials which can be epitaxially grown on each other. This has led to the suggestion [12], demonstration [13] and development [14] of quantum well infrared photodetectors (QWIPs) which are currently nearing commercialization [15]. It has also led to the demonstration of greatly enhanced nonlinear optical properties [16], and more recently to the development of the extremely promising quantum cascade (QC) unipolar semiconductor laser operating at infrared wavelengths [17,18].

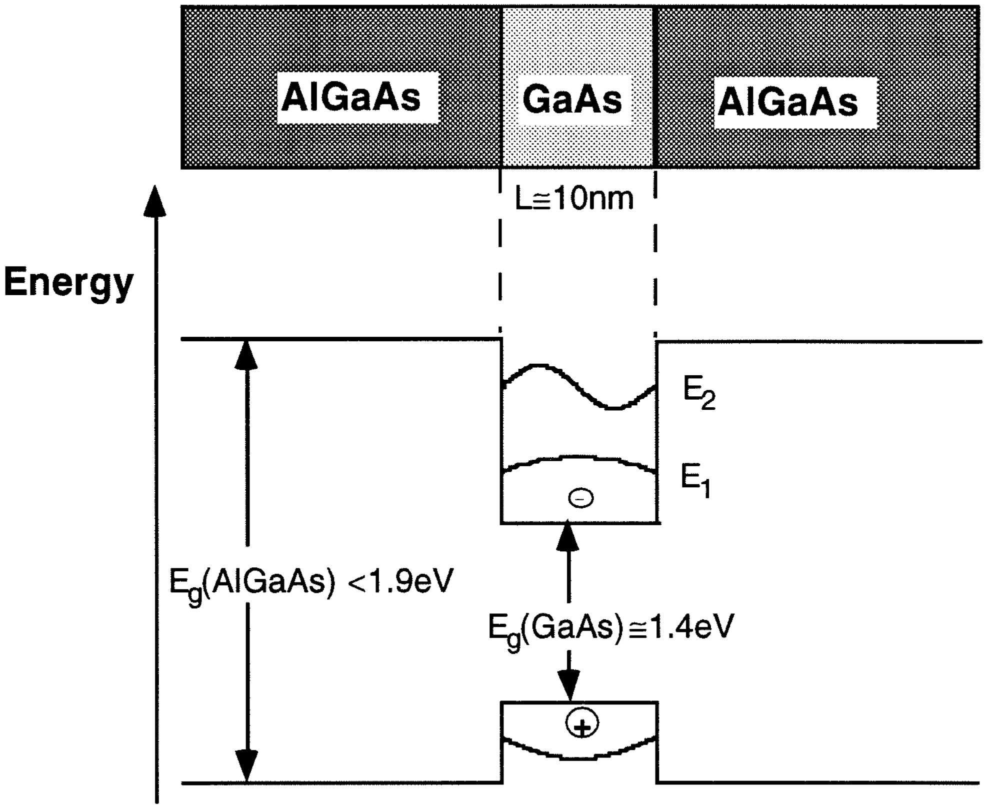

Figure 1.1 A schematic of a quantum well. The material composition is shown on top. The wells in the conduction and valence band and the resultant envelope states are also shown.

For completeness it should be noted that intersubband transitions where first observed in the inversion layers created at Silicon/Silicon-Oxide interfaces [19] more than a decade before their observation in heterostructures. These layers, however, led to relatively small subband separations ($\Delta E \cong 20$meV), and the resultant intersubband transitions were difficult to observe at room temperature. The inability to grow multiple periods and the generally limited design capability made inversion layers impractical for the applications for which heterostructure quantum wells are currently being developed. Although interest in these layers had faded, they served as a testing ground for many of the concepts that later played a major role in intersubband transitions [8].

1 .3 Quantum Well Models

In the simplest model, quantum well subbands are the solutions of the basic "particle in a box" problem. Assuming that all subbands involved in the optical processes are composed of the same bulk Bloch states, the envelope function formalism [20] leads to an effective mass Hamiltonian given as:

$$[-\frac{\hbar^2}{2}\frac{\partial}{\partial z}\frac{1}{m^*(z)}\frac{\partial}{\partial z}-\frac{\hbar^2}{2m^*(z)}\frac{\partial^2}{\partial r_\perp{}^2}+V_b(z)]\psi(r_\perp)\psi(z)=\varepsilon\cdot\psi(r_\perp)\psi(z) \tag{1.1}$$

where m* is the effective mass of electrons in the relevant band, $V_b(z)$ is the band's potential profile, $\psi(z)$ and $\psi(r_\perp)$ are the envelope functions along the axis of quantization and perpendicular to it respectively, and we have used the single band approximation and multiplied by the conjugate Bloch state on both sides. In order to derive an explicit analytical solution that may be used for an intuitive understanding of intersubband process we assume that the particle is confined between infinite potential barriers. The boundary conditions at the potential barriers (at ±L/2) are thus:

$$\psi(\frac{-L}{2}) = \psi(\frac{L}{2}) = 0 \tag{1.2}$$

and using separation of variables, the components of the eigenstates along the z (growth) direction are found as:

$$\psi_n(z) = \sqrt{\frac{2}{L}}\cos[\frac{n\pi z}{L}]; \ |z| \le \frac{L}{2}; \ n = 1,3,5,... \tag{1.3a}$$

and:

$$\psi_n(z) = \sqrt{\frac{2}{L}}\sin[\frac{n\pi z}{L}]; \ |z| \le \frac{L}{2}; \ n = 2,4,6,... \tag{1.3b}$$

for the odd and even states, respectively. The in-plane components of these states are merely the plane waves of the unperturbed bulk crystal given as:

$$\psi(r_\perp) = e^{ik_\perp r_\perp} \tag{1.4}$$

and the allowed energies are thus given as:

$$E_n(k_\perp) = \frac{\hbar^2\pi^2 n^2}{2m^* L^2} + \frac{\hbar^2 k_\perp{}^2}{2m^*}; \ n = 1,2,3... \tag{1.5}$$

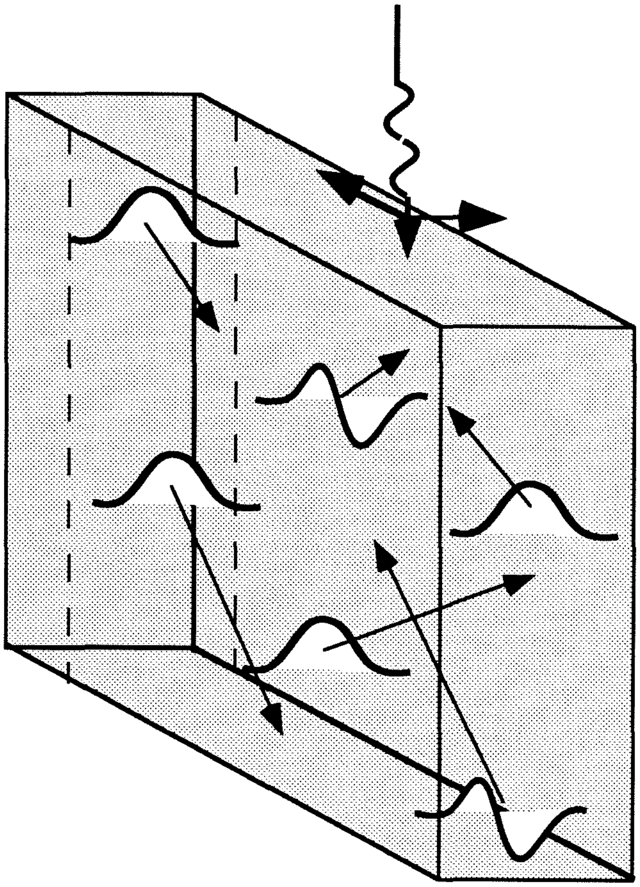

Figure 1.2: A schematic of the one-dimensional quantization induced by a thin layer with infinite potential barriers. The electrons motion is confined in the direction perpendicular to the plane, but they remain free to move within it.

It can be seen from Equation 1.5 that in quantum wells the subbands do not represent discrete energy levels as the momentum is only quantitized in one dimension. Only zero-dimensional structures, i.e., quantum dots, will have a true energy gap between subbands. The lattice itself is of course a 0-dimensional array whose discrete states are split by the strong coupling into wide bands. It is only the fact that the dispersion relations for subbands of the conduction band are nearly parallel that makes them behave as optically discrete transitions due to the negligible photon momentum. This is schematically shown in Figure 1.3 where the vertical arrows represent the direct optical interband and intersubband transitions.

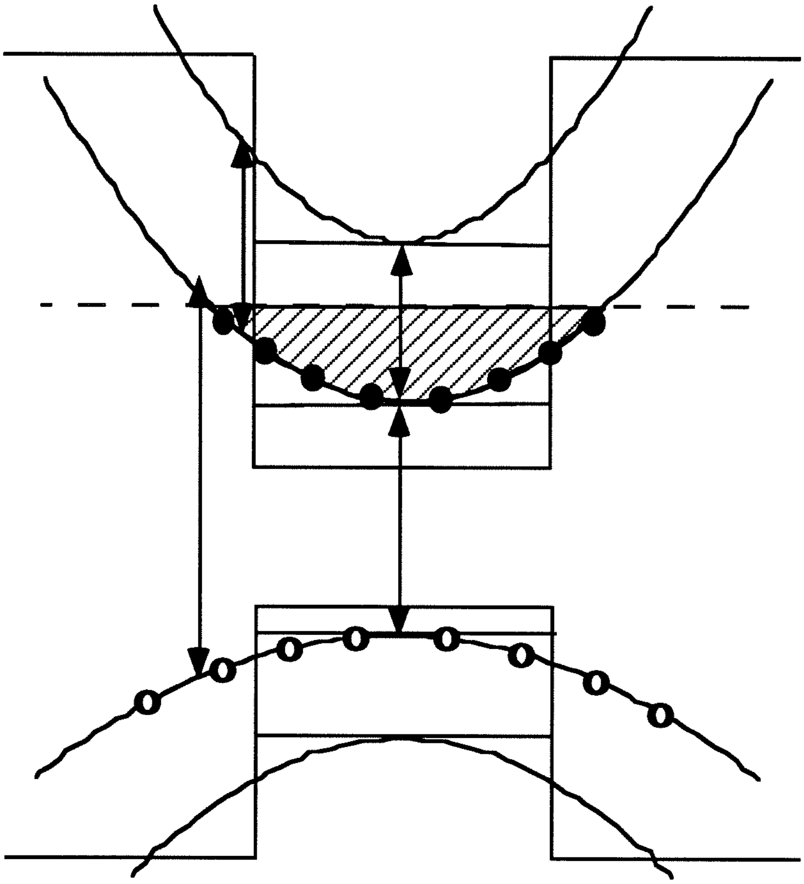

Figure 1.3 Schematic conduction and valence band dispersion relations of a quantum well. Both the pseudo-discrete intersubband states (drawn with a perfectly parabolic effective mass) and the broadened interband transitions are shown. The hashed area shows the extent of the occupied conduction band states.

The infinite barrier approximation used in the above derivation (Equations 1.1-1.5) leads to a picture of intersubband transitions which is qualitatively correct but overestimates the subband energies by neglecting the leakage of the wavefunctions into the barriers. Although transcendental solutions taking the finite barrier height into account may be obtained for simple structures [20], they will not be presented here as they too are incapable of predicting intersubband transition energies with sufficient accuracy. Extension to arbitrary structures and arbitrary electric fields, and inclusion of band-mixing and many-body effects, require a more extensive numerical solution which is presented in chapter 2.

1 .4 Optical Transitions

To understand the difference between interband and intersubband transitions we examine the optical dipole matrix element between two subbands which is given as:

$$\langle f_i(r)u_i(r)|p|f_f^*(r)u_f^*(r)\rangle \cong \frac{1}{V}\left\{\int d^3r u_i(r) p u_f^*(r)\cdot\int d^3r f_i(r) f_f^*(r) + \int d^3r u_i(r) u_f^*(r)\cdot\int d^3r f_i(r) p f_f^*(r)\right\} \tag{1.6}$$

where $u_i(r)$ and $f_i(r)$ denote the initial Bloch and envelope functions, and $u_f(r)$ and $f_f(r)$ the final Bloch and envelope functions, respectively. In writing Equation 1.6 the single band approximation was made, i.e., it was assumed that each subband is composed of one bulk Bloch state, and its rapid oscillation was used to separate the integral. Using orthogonality this expression is re-written as:

$$\langle f_i(r)u_i(r)|p|f_f^*(r)u_f^*(r)\rangle \cong \frac{1}{V}\left\{\langle u_i(r)|p|u_f^*(r)\rangle\int d^3r f_i(r) f_f^*(r) + \langle f_i(r)|p|f_f^*(r)\rangle\delta_{if}\right\} \tag{1.7}$$

The first term on the right-hand-side (RHS) of equation 1.7 corresponds to transitions between subbands with different Bloch functions - or interband transitions. These transitions are only allowed between envelope states of the same parity, and, for infinite barrier heights, only between envelope states with the same quantum number. Since the initial and final Bloch states belong to bands with opposite signs for their effective masses (the conduction and valence bands), inclusion of in-plane momentum (Equation 1.5) will lead to broadened transitions as can be seen in Figure 1.3.

The second term on the right-hand-side of Equation 1.7 is responsible for the intersubband transitions. Replacement of the envelope functions with those derived in Equation 1.3 leads to:

$$\left\langle \psi_n(z) e^{ik_\perp r_\perp} \left| p_z \hat{e}_z + p_{r_\perp} \hat{e}_{r_\perp} \right| \psi_m^*(z) e^{-ik'_\perp r_\perp}) \right\rangle = \hbar k_\perp \hat{e}_{r_\perp} \delta_{nm} \delta_{k_\perp k'_\perp} + \delta_{k_\perp k'_\perp} \hat{e}_z \cdot \int d^3 r \psi_n(z) p_z \psi_m^*(z) \tag{1.8}$$

where we have split the momentum operator into its in-plane ($p_{r_\perp}$) and perpendicular (p_z) components. The first term on the right-hand side, the optical intraband term, may not simultaneously satisfy both energy and momentum conditions and is therefore forbidden. The second term corresponds to transitions between subbands with the same Bloch functions - or intersubband transitions. These transitions are only allowed between states of opposite parity, and, as can be shown from Equation 1.5, are strongest between a subband and the following one (from quantum number m to m+1). Unlike the interband transitions, the intersubband ones will remain optically discrete, despite the in-plane dispersion (Equation 1.5), as they are composed of the same Bloch state and hence have the same effective mass and parallel dispersion curves within the single band model. Equation 1.8 also shows the geometrical selection rule: intersubband transitions may only be induced by radiation polarized perpendicular to the planes of the quantum wells.

1 .5 Design and Applications of Intersubband Transitions

The ability to design conduction bands with almost arbitrarily band profiles through bandgap engineering leads to a much higher level of control than just the obvious determination of subband separation. The intersubband transition energies, optical dipole matrix elements, population distribution between coupled wells, and even the relaxation times to some extent are directly controlled by growth parameters. The quantum wells can thus be optimized for almost any electrooptical application: intersubband detectors, nonlinear optics, intersubband lasers, and infrared modulators.

The first of these applications to be suggested [12] and demonstrated [13] was the quantum well infrared photodetector (QWIP). Transitions from a bound to quasi-bound or continuum states may be used for detection of arbitrary wavelength radiation. Next to be studied were the nonlinear characteristics of intersubband transitions [21], where the resonant enhancement and controllable symmetry lead to nonlinearities of unprecedented magnitude [16,22]. Much of this thesis deals with the difficulty of converting the extremely large nonlinear coefficients typical of intersubband transitions into practical devices. An application which I believe is closer to maturity is the use of intersubband transitions for infrared modulation which will be discussed in chapter 10. Perhaps the most promising application of intersubband transitions is the recently demonstrated intersubband laser [17,18]. This has the potential to become a semiconductor laser source for the whole infrared through sub-millimeter wavelength range. If that turns out to be the case, many of the issues discussed in this thesis: intersubband modulators, the influence of many-body effects on intersubband transitions, the refractive index contribution of intersubband transitions, and the nonperturbative formalism for the nonlinear optical interaction with intersubband transitions may have a larger technological impact than at the present.

1 .6 Practical Limitations of Intersubband Transitions.

Despite their great promise, intersubband transitions have found a mere fraction of the applications interband transitions have. The cause of this lies in fundamental differences between these two types of transitions. The available conduction band offset between lattice matched semiconductors is, in most cases, much smaller than the bandgaps themselves (Figure 1.1) - limiting intersubband transitions to longer wavelengths. Other limits are the short intersubband relaxation time and the polarization selection rule, both of which are due to the one-dimensional quantization. When comparing interband to intersubband transitions at a given wavelength all these limitations may be viewed as the consequence of using a wide gap instead of a narrow gap material. On the other hand this also leads to some of the advantages of intersubband transitions: the mature technology, high uniformity, and radiation hardness of wide- versus narrow-gap materials.

The wavelength of intersubband transitions is limited by the conduction band offsets between lattice matched materials. For the GaAs/$Al_xGa_{1-x}As$ material system used in our experiments the maximum offset of roughly 320 millivolt (mV) is reached at the crossover point of the direct and indirect conduction band valleys in $Al_xGa_{1-x}As$ ($x \cong 0.4$). This limits intersubband transitions to the mid-infrared region ($\lambda \geq 6\mu m$). For lattice matched AlInAs/GaInAs compositions the offset is somewhat larger - roughly 500mV, but this is still too small to obtain intersubband transitions in the near infrared region ($\lambda \cong 1.55\mu m$). One method of extending intersubband transitions to this wavelength range relies on strain relaxing layers introduced between the substrate and the quantum wells to allow growth of non-lattice-matched material compositions [23]. Attempts are currently being pursued to develop the growth of InGaAs/AlAs quantum wells on a GaAs substrate thus obtaining conduction band offsets of over a Volt [24]. However, even if growth quality limitations are overcome, the subbands will no longer be envelope functions constructed of the same Bloch function because the intersubband separation is on the order of the interband one. Therefore the subbands will no longer have parallel dispersion curves and the optical dipole matrix elements between subband will not remain as large. A more promising alternative for near infrared intersubband transitions may emerge in the near future from the Nitride based materials (GaN/AlN) which are currently being developed mainly for blue-green interband light emission [25]. Due to the very large interband separation, the large conduction band offset may lead to highly energetic transitions between subbands retaining their single-band nature. It should be noted, however, that the larger bandgaps are accompanied by larger effective masses necessitating narrower quantum wells and correspondingly smaller optical dipole matrix elements for a given transition energy. Still, the potential of utilizing the design flexibility and resonant-enhancement of intersubband transitions at near-infrared and visible wavelengths may be significant.

Another limitation on intersubband transitions is due to the geometrical selection rule allowing interaction only with optical fields polarized along the growth direction. This, combined with the relatively narrow layers (<10μm) available from epitaxial growth, dictates the use of limiting experimental schemes and hinders the development of device applications. Relaxation of the selection rules requires coupling of the quantitized growth direction to the in-plane direction, i.e., electrons with an effective mass tensor which is not diagonal in the growth direction coordinates. For electrons in the Γ-valley of the GaAs conduction band, which have a scalar effective mass, the selection rules may be relaxed by band-mixing. This, however, only becomes significant for extremely narrow wells. Alternatively, the selection rules are relaxed for subbands of states that have an effective mass which is a non-diagonal tensor to begin with. This is the case either for valence band states, or for states in the X-valley of the conduction band for certain crystal growth orientations [26]. The electrons may be confined to the X-valley for aluminum concentrations of over 40%, where the $Al_xGa_{1-x}As$ alloy becomes indirect.

A third fundamental limitation of intersubband transitions is the extremely short excited-state life time, on the order of one picosecond, which is 3 to 6 orders of magnitude shorter than the interband lifetime. Although the exact value of the life time may vary somewhat, the fast relaxation is a direct consequence of the lack of an energy gap. Optical phonons are the main cause of intersubband relaxation, which is then followed by an extremely fast intrasubband thermalization. The short life times impose limitations on the performance of quantum well infrared photodetectors, influence the nonlinear optical properties of intersubband transitions, and have been the cause of the difficulty in obtaining population inversion and hence an intersubband laser.

1 .7 Outline of the Thesis

This thesis is based on the work of the author in the field of optical intersubband transitions in quantum wells carried out at the California Institute of Technology from July 1992 through April 1995. It does not include the work on vertical cavity surface emitting lasers carried out in a collaboration between the groups of Dr. Amnon Yariv and Dr. Axel Scherer at Caltech [27,28], nor the results of work on infrared focal-plane arrays carried out in the Submicron Center at the Weizmann Institute of Science.

The thesis follows the path of our research into the optical properties and applications of intersubband transitions, with some rearrangements made for clarity. After measuring the refractive index induced by the intersubband transitions we intended to pursue the electrooptic modulation of infrared radiation in asymmetric quantum wells. However, while realizing that there may be other important applications for this controllable refractive index, we came to the conclusion that phase-modulation is inherently inferior to absorption modulation when using resonantly-enhanced transitions. This conclusion resulted from our derivation of a nonperturbative formalism for the nonlinear interaction of intersubband transitions, replacing the standard one that fails at the intensities required for practical device applications. This formalism also led to radically different conclusions concerning the optimization of second-harmonic generation in quantum wells and the feasibility of obtaining a high frequency conversion efficiency. The thesis ends with a presentation of the monolithic integration of a quantum well infrared photodetector and modulator, and of some of the phenomena observed in this experiment.

Chapter 2 will present a self-consistent solution for the electronic states in quantum wells. The computer program used solves the Schrödinger and Poisson equations iteratively, while taking into account: many body corrections, band nonparabolicity, temperature dependence of the semiconductor parameters and flat band boundary conditions. This program turned out to be a powerful tool for the design of quantum wells and for the analysis of observed intersubband phenomena. It led to the uniquely accurate design capability used in the growth of the monolithicly integrated quantum well intersubband detector and modulator presented in Chapter 10.

In Chapter 3 we report the first observation of the large, highly dispersive, and temperature dependent refractive index contribution of intersubband transitions through the birefringence induced in a GaAs/AlGaAs multi-quantum well stack [29]. The refractive index change we observed in an unoptimized structure: $\Delta n \cong \pm 0.07$ at a 45 degree incidence, suggests that an intersubband transition-induced refractive index change as high as $\Delta n \cong \pm 0.4$ can be obtained in an optimized structure for an optical polarization perpendicular to the plane of the quantum wells.

In chapter 4, we suggest and analyze a potential application of the controllable intersubband transition-induced refractive index for the phase-matching of second-harmonic generation in semiconductors [30]. We specifically analyze the feasibility of phase-matching GaAs by the growth of quantum wells with an intersubband transition-induced refractive index contribution which will offset the bulk's dispersion. The analysis, however, is general to any bulk media which may be embedded with a material with a controllable optical transition. It will hopefully find applications in other material systems in the future. On the other hand, it is also shown in this chapter, that the intersubband transition induced refractive index may shorten the coherence length to the point where it, rather than the absorption induced by the intersubband transitions, will limit the conversion efficiency in resonantly-enhanced second-harmonic generation processes.

In part II of the thesis (Chapters 5-9) we rigorously derive the optical response of intersubband transitions in quantum wells [31] which are unique in being a completely designable system of resonantly-enhanced discrete level transitions. Limitations of the Rotating-Wave Approximation (RWA), the Slowly-Varying Envelope Approximation (SVA), and the dipole approximation are discussed. The phenomena expected once these assumptions break down are examined in Chapters 5 and 6 [32]. Particular emphasis is placed on the divergence of the standard perturbative expansion of the susceptibility in terms of a power series of nonlinear coefficients. We show that the perturbative approach is incapable of describing the nonlinear response of intersubband transitions at the intensities required for practical applications, and present an alternative formalism. We explicitly solve for the 'ac' Kerr coefficient ($\chi^{(3)}_{(\omega,\omega,-\omega,\omega)}$) (Chapter 7), the electrooptic coefficient ($\chi^{(2)}_{(\omega,\omega,0)}$) (Chapter 8), and the second-harmonic generation coefficient ($\chi^{(2)}_{(2\omega,\omega,\omega)}$) (Chapter 9), which are the standard tools for analyzing electrooptic modulation (EOM), all-optical modulation (AOM), and second-harmonic generation (SHG), respectively. It is shown that, despite the extremely large electrooptic and all-optic coefficients measured, resonantly-enhanced absorption modulation is inherently preferable over phase-modulation [33] (Chapters 7 and 8). A limit on the second-harmonic intensity that may be generated in a given propagation length and modified quantum well design criteria for optimizing intersubband transition-induced second-harmonic generation are also presented in Chapter 9 [34,35].

In the final part of the thesis (Chapter 10) the monolithic integration of an intersubband infrared absorption modulator and detector, designed for the 'ac'-coupling of infrared focal-plane arrays, is presented [36]. Charge transfer between 50 periods of asymmetric coupled quantum wells led to a 45% modulation depth at a wavelength of 10.6μm. The monolithic integration of the modulator and detector also turned out to be a simple and accurate method of studying the optical properties of quantum wells under bias, leading to the first observation of the exchange-interaction's contribution to the charge transfer between coupled quantum wells.

References:

[1] P. A. M. Dirac, *The Principles of Quantum Mechanics*, Oxford, England: Oxford University Press, 1930.

[2] L. Esaki and R. Tsu, "Superlattice and negative differential conductivity in semiconductors," *IBM J. Res. Dev.*, **14**, 61, 1970.

[3] R. Tsu and L. Esaki, "Tunneling in a finite superlattice," *Appl. Phys. Lett.*, **22**, 562, 1973.

[4] A. Y. Cho, "Growth of periodic structures by molecular beam method," *Appl. Phys. Lett.*, **19**, 467, 1971.

[5] L. L. Chang, L. Esaki, and R. Tsu, "Resonant tunneling in semiconductor double barriers," *Appl. Phys. Lett.*, **24**, 593, 1974.

[6] L. Esaki and L. L. Chang, "New transport phenomenon in a semiconductor superlattice," *Phys. Rev. Lett.*, **33**, 495, 1974.

[7] R. Dingle, W. Wiegmann, and C. H. Henry, "Quantum states in confined carriers in very thin $Al_xGa_{1-x}As/GaAs/Al_xGa_{1-x}As$ heterostructures," *Phys. Rev. Lett.*, **33**, 827, 1974.

[8] T. Ando, A. B. Fowler, and F. Stern, "Electronic properties of two-dimensional systems," *Rev. Mod. Phys.*, **54,** 437, 1982.

---

[9] T. H. Wood, “Multiple quantum well (mqw) wave-guide modulators,” *J. Lightwave Technol.*, **6**, 743, 1988.

[10] Y. Arakawa and A. Yariv, “Theory of gain, modulation response, and spectral linewidth in AlGaAs quantum well lasers,” *J. Quantum. Electron.*, **21**, 1666, 1985.

[11] L. C. West and S. J. Eglash, “1st observation of an extremely large-dipole transition within the conduction band of a GaAs quantum well,” *Appl. Phys. Lett.*, **46**, 1156, 1985.

[12] L. C. Chiu, J. S. Smith, S. Margalit, A. Yariv, and A. Y. Cho, “Application of internal photoemission from quantum-well and heterojunction super-lattices to infrared photodetectors,” *Infrared Physics*, **23**, 93, 1983.

[13] B. F. Levine, C. G. Bethea, G. Hasanain, J. Walker, and R. J. Malik, “High-detectivity $D^*= 1.0\times10^{10}[\mathrm{cm}\sqrt{\mathrm{hz}}/\mathrm{w}]$ GaAs/AlGaAs multiquantum well $\lambda= 8.3\mu\mathrm{m}$ infrared detector,” *Appl. Phys. Lett.*, **53**, 296, 1988.

[14] B. F. Levine, “Quantum-well infrared photodetectors,” *J. Appl. Phys.*, **74**, R1-R80, 1993.

[15] T. S Fiasco, W. A. Beck, J. W. Little, A. C. Goldberg, B. Rosner, and M. Stegall, “Staring LWIR MBT quantum-well sensor performance using the commercial infrared ImagIR camera system,” *Proc. of SPIE Infrared Imaging Systems: Design, Analysis, Modeling and Testing IV*, vol.1969-25, 1993.

---

[16] See references in “Resonantly-enhanced nonlinear optics of intersubband transitions” by G. Almogy and A. Yariv, to be published in *J. of Nonlinear Opt. Phys. Mat.*, or in Chapter 5.

[17] J. Faist, F. Capasso, D. L. Sivco, C. Sirtori, A. L. Hutchinson, and A. Y. Cho, “Quantum cascade laser - An intersubband semiconductor-laser operating above liquid-nitrogen temperature,” *Electron. Lett.*, **30**, 1360, 1994.

[18] C. Sirtori, J. Faist, F. Capasso, D. L. Sivco, A. L. Hutchinson, and A. Y. Cho, “Quantum cascade laser operating at 8.4μm wavelength,” submitted to *Appl. Phys. Lett.*.

[19] F. Stern and W. E. Howard, “Properties of semiconductor surface inversion layers in electric quantum limit,” *Phys. Rev.*, **163**, 816, 1967.

[20] G. Bastard, *Wave Mechanics Applied to Semiconductor Heterostructures*, ch. III, Paris, France: Les Editions de Physique, Les Ulis Cedex, 1988.

[21] M. M. Fejer, S. J. B. Yoo, R. L. Byer, A. Harwit, and J. S. Harris, Jr., "Observation of extremely large quadratic susceptibility at 9.6-10.8 mm in electric-field -biased AlGaAs quantum wells," *Phys. Rev. Lett.*, **62**, 1041, 1989.

[22] C. Sirtori, F. Capasso, D. L. Sivco, and A. Y. Cho, "Giant, triply resonant, third-order nonlinear susceptibility $\chi^{(3)}_{3\omega}$ in coupled quantum wells," *Phys. Rev. Lett.*, **68**, 1010, 1992.

---

[23] H. C. Chui, S. M. Lord, E. Martinet, M. M. Fejer, and J. S. Harris, Jr., ”Intersubband transitions in high indium content InGaAs/AlGaAs quantum wells,” *Appl. Phys. Lett.*, **63**, 364, 1993.

[24] S. M. Lord, B. Pezeshki, J. S. Harris, Jr., "Investigation of high In content InGaAs quantum wells grown on GaAs by molecular beam epitaxy," *Electron. Lett.*, **28**, 1193, 1992.

[25] H. Moroç, S. Strite ,G. B. Gao, M. E. Lin, B. Sverdlov, and M. Burns, “Large-band-gap SiC, III-V Nitride, and II-VI ZnSe-based semiconductor-device technologies,” *J. Appl. Phys.,* **76**, 1363, 1994.

[26] H. Xie, J. Katz, and W. I. Wang, “Orientation dependence of intersubband absorption in AlAs/$Ga_{1-x}Al_xAs$ X valley superlattices,” *J. Appl. Phys.*, **72,** 3681, 1992.

[27] A. Scherer, J. O’Brien, G. Almogy, W-H Xu, A. Yariv, J. L. Jewell, K. Uomi, B. J. Yoo, and R. J. Bhat, “Vertical cavity surface emitting lasers with dielectric mirrors,” *Int. J. of High Speed Electron Dev.*, in Press.

[28] J. O’Brien, G. Almogy, W-H Xu, A. Scherer, and A. Yariv, “Vertical cavity surface emitting lasers with SiO_2/Si_3N_4 top Mirrors, ” *Photon. Tech. Lett.*, in Press.

[29] G. Almogy, A. Shakouri, and A. Yariv, “Observation of birefringence induced by intersubband transitions in quantum wells,” *Appl. Phys. Lett.*, **63**, 2720, 1993.

[30] G. Almogy, M. Segev, and A. Yariv, “Intersubband-transition-induced phase matching,” *Optics Lett.*, **19**, 1192, 1994.

---

[31] G. Almogy and A. Yariv, "Resonantly-enhanced nonlinear optics of intersubband transitions," *J. of Nonlinear Opt. Phys. Mat.*, in Press.

[32] A. Levinson, M. Segev, G. Almogy, and A. Yariv, "Symmetry-breaking effects induced by intense laser fields," *Phys. Rev. A,* **49**, R661, 1994.

[33] G. Almogy, M. Segev, and A. Yariv, "Adiabatic nonperturbative derivation of electric-field-induced nonlinearities in quantum wells", *Phys. Rev.* ***B,*** **48**, 10950, 1993.

[34] G. Almogy and A. Yariv, "Second-harmonic generation in absorptive media," *Optics Lett.*, **19**, 1828, 1994.

[35] G. Almogy and A. Yariv, "Fundamental limits of resonantly-enhanced second-harmonic generation," *J. Opt. Soc. Am. B*, in press.

[36] G. Almogy, Y. Xu, A. Tong, A. Shakouri, and A. Yariv, "Monolithic integration of quantum well infrared photodetector and modulator", submitted to *Appl. Phys. Lett.*

Chapter 2

A Self-Consistent Solution for Quantum wells

2 .1 Introduction

An essential tool in any attempt to fully utilize the potential of intersubband transition is a computer program able to accurately find the eigenstates and eigenvalues of the electrons in the quantum well. With this in mind, Andrew Tong, a Freshman SURF student working with our group, wrote a self-consistent solution for electrons in arbitrary profile quantum wells. This program, originally solving the Schrödinger and Poisson equations iteratively, was modified and expanded over the course of the next two years. Not only did it prove to be an effective design tool saving time consuming and expansive growth iterations, it also enhanced our fundamental understanding of observed intersubband phenomena. It has directly led to the discovery of the effect of the exchange interaction on population distribution between coupled quantum wells (Chapter 10) and has helped us in obtaining a better understanding of the blue-shift of intersubband transitions.

In discussing the self-consistent solution for quantum wells it should be kept in mind, however, that the quantitative prediction of intersubband transition energies has some limits on its accuracy. The material parameters, particularly the alignment of the band offsets and the temperature dependent effective masses are only known to a finite accuracy. Furthermore, the molecular beam epitaxy (MBE) growth has a thickness variation of about one monolayer, the Aluminum concentration is known to within several percent [1], the doping concentration is often not accurately calibrated, and dopants may segregate during growth [2]. The many-body models used to consider the mutual electron interactions are also by necessity simplifications. Nevertheless, especially if one uses an interactive calibration process for the MBE and the numerical calculation, the ability to design new quantum well structures with minimal iteration and high accuracy is obtained. This capability of the self-consistent program culminated in the design used for the growth of a monolithic infrared detector and modulator (chapter 10), for which a one milli-electronvolt (meV) accuracy in the separation of the resonant energies was obtained.

2 .2 The Effective Mass Schrödinger Equation

The first stage in the calculation of quantum well subbands is the solution of the effective mass single-electron Schrödinger equation which is given as:

$$[-\frac{\hbar^2}{2}\frac{\partial}{\partial z}(\frac{1}{m^*(z)}\frac{\partial}{\partial z}) + qV_b(z) + qzE_{dc}]\psi_i(z) = \varepsilon_i\psi_i(z) \qquad (2.1)$$

where z is the growth direction, m*(z) the composition dependent (scalar) effective mass, $V_0(z)$ the composition dependent conduction band potential, and E_{dc} the applied external field. Using the shooting method [3], the second order differential equation is reduced to first order by the definitions:

$$y_1 \equiv \psi_i(z) \tag{2.2a}$$

and:

$$y_2 \equiv \frac{1}{m^*(z)}\left(\frac{\partial \psi_i(z)}{\partial z}\right) \tag{2.2b}$$

which lead to the equations:

$$y_1' = m^*(z) \cdot y_2 \tag{2.3a}$$

and:

$$y_2' = \frac{2}{\hbar^2}[V_b(z) - \varepsilon_i] \cdot y_1 \tag{2.3b}$$

To solve these coupled linear differential equations initial guesses for the eigenvalues (ε_i) are made and a fifth-order Runge-Kutta numerical routine [3] is used to propagate the variables across the defined interval $z_1 \leq z \leq z_2$. Boundary conditions are set as $y_1(z_1)=y_2(z_2)=0$, with the boundaries chosen far enough so the amplitude of the wavefunctions reaching them is negligible. This is insured by verifying a negligible dependence of the eigenvalues on changes in the boundary location. The obtained value at the far side of the propagation is compared to the boundary condition and a Newton-Raphson algorithm [3] is used to improve upon the initial eigenvalue guess until convergence is obtained. Notice that a finite value of the derivative (y_2), has to be chosen for a non-trivial solution to be obtained. The arbitrary value amounts to a normalization constant that is corrected by later imposing the normalization condition given as:

$$\int_{z_1}^{z_2} \psi_i(z)^2 dz = 1 \tag{2.4}$$

2 .3 The Hartree/Poisson Potential

Since a high doping density is required for practical device applications of intersubband transitions, the charge distribution may lead to a substantial modification of the conduction band profile and hence of the eigenvalues and states. Using the two-dimensional density of states in each subband ($\sigma = m^*/\pi\hbar^2$), and the Fermi-Dirac distribution function $f(e) = 1/(1+e^{(E-E_f)/kT})$, the total surface charge density of a given subband is given as:

$$n_i = \frac{m_i^* kT}{\pi\hbar^2} \cdot \ln[1 + \exp(\frac{E_f - E_i}{kT})] \tag{2.5}$$

where we have defined the average effective mass for a given subband by:

$$\frac{1}{m_i^*} \equiv \int_{z_1}^{z_2} \frac{1}{m^*(z)} \psi_i(z)^2 dz \tag{2.6}$$

The Fermi level (E_f) is found by imposing the neutrality condition:

$$N_D^+ = \sum_i n_i \tag{2.7}$$

where the summation is over all populated subbands and N_D^+ is the total surface doping density. The volumetric charge density is hence given by:

$$n(z) = \sum_i q n_i \psi_i(z)^2 \tag{2.8}$$

Whereas Fermi-Dirac statistics have a negligible influence on band profiles in simple quantum wells (ΔE≅100meV) at or below room temperature (kT<26meV), they may play a significant role for coupled structures. For these, the ground state energies of the coupled wells may be within a fraction of the thermal energy of each other.

Since the charge distribution is uniform in the plane of the quantum wells, the Poisson equation is reduced to the one-dimensional equation:

$$\frac{d}{dz}[\varepsilon(z)\frac{dV_H}{dz}] = \frac{q}{\varepsilon_0}[N_D^+(z) - n(z)] \tag{2.9}$$

where ε is the bulk material's static dielectric function, and $N_D^+(z)$ is the volumetric donor doping density. Solving this equation will give the Poisson potential (V_H) induced by charge distribution, also known as the Hartree potential, i.e., the lowest order term in the Hartree-Fock expansion. The differential equation is solved by making the definitions:

$$y_1 \equiv V_H \tag{2.10a}$$

and:

$$y_2 \equiv \varepsilon(z)\frac{dV_H}{dz} \tag{2.10b}$$

with which we obtain two coupled first order differential equations given as:

$$y'_1 \equiv \frac{1}{\varepsilon(z)} y_2 \tag{2.11a}$$

and:

$$y_2' \equiv \frac{q}{\varepsilon_0}[N_D^+(z) - n(z)] \tag{2.11b}$$

These are solved using the Runge-Kutta propagation method used for the solution of the Schrödinger equation in the last section.

2 .4 Self-Consistent Iterations

The Hartree potential induced by the charge distribution (V_H) is now added to the conduction band potential and the Schrödinger equation is solved again. The two steps: Schrödinger and Poisson are iterated until the solutions converge to the required accuracy. For symmetric quantum wells the process usually converges within 4 to 5 iterations to an accuracy of 10^{-2} meV as shown in Figure 2.1b.

For coupled quantum wells, however, the population may oscillate back and forth when the spread in energy space of the population is larger than the energy separation between the ground states of the individual wells (Figure 2.2). The rigorous solution of this problem involves treating the Poisson potential as a perturbation, i.e., giving the electron population a weight factor and gradually increasing it to unity. We have found that a user controlled manual population distribution leads to faster convergence if some common sense and experience are used. The closer the subbands are to degeneracy, or to the cross over point, the more sensitive the convergence process becomes.

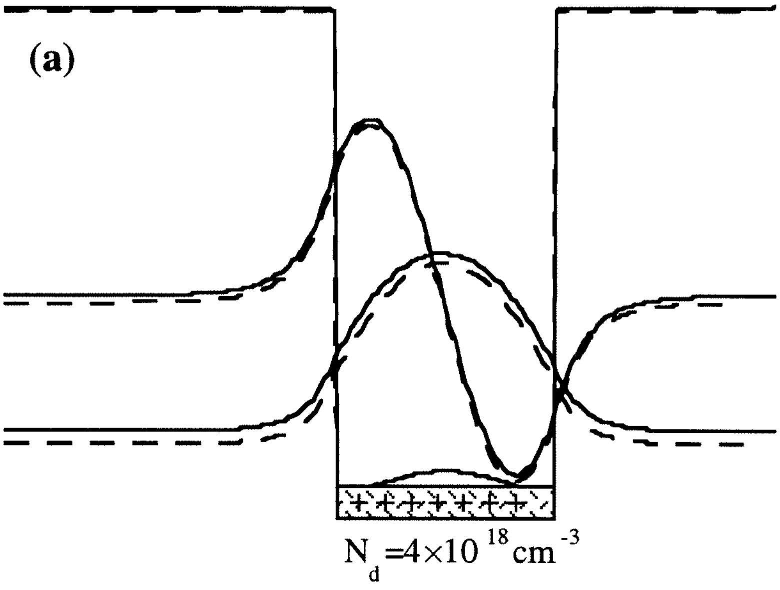

Figure 2.1 a: The single-electron (dashed curves) and self-consistent (solid curves) band profile and calculated subband envelope functions. An artificially high doping level is chosen to emphasize the many-body effects (all the population is kept in the ground subband although at this density the Fermi-level would be higher than the second subband).

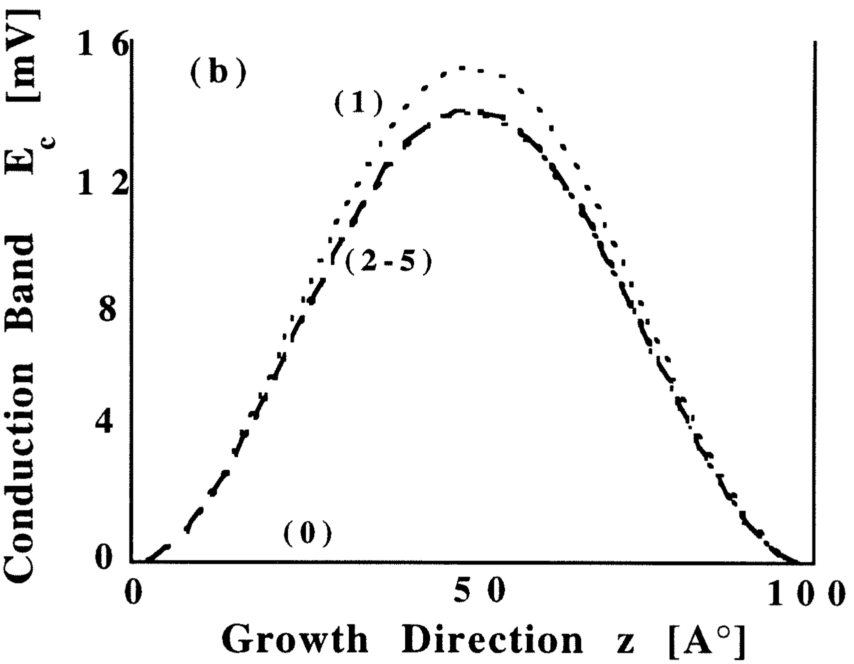

Figure 2.1b: The variation of the band profile with the iterations of the self-consistent program. The (rectangular) solid curve is the single-electron solution (0), the narrow-dashed curve includes the correction due to the Coloumbic interaction of the single electron wave-functions (1). The next iterations (2-5) are too close to tell apart.

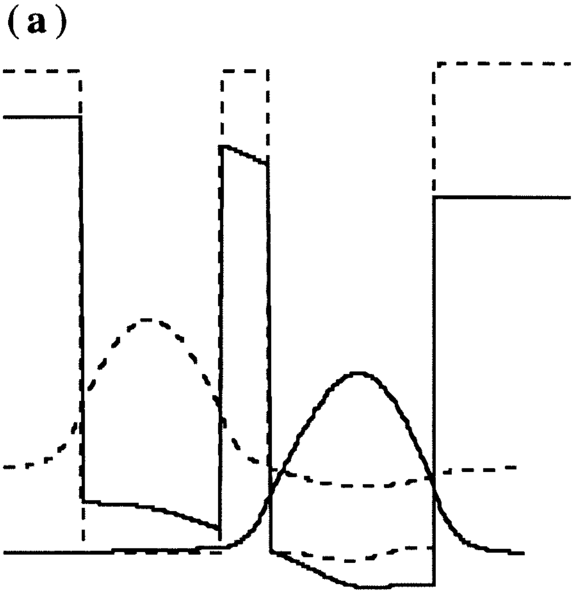

Figure 2.2a: The band profile of the coupled quantum wells at two consecutive iterations. The population oscillates back and forth and the self-consistent program does not converge unless steps are taken to dampen it. The parameters used are of the quantum well modulator described in Chapter 10.

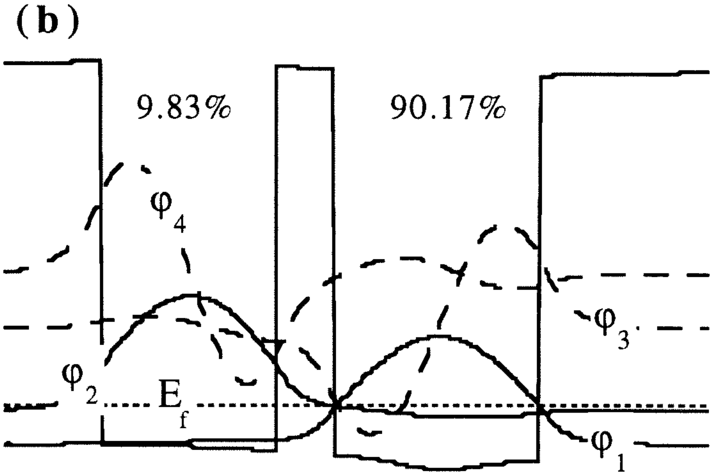

Figure 2.2b: The convergent solution of the coupled quantum well. The Fermi Level is just over the ground state of the narrow (left) quantum well containing only 9.83% of the population at 30K.

2 .5 Many-Body Effects

Accumulated experimental data has shown that the use of the Hartree approximation consistently leads to an under-estimation of the intersubband transition frequencies. Furthermore, identical quantum wells displayed a large increase of the transition frequency with doping concentration [4]. This increase was attributed by several authors to the influence of the electron-electron interactions [5,6]. Since no scheme for fully calculating the influence of the electronic many-body effects is available, we initially chose the least computationally intensive approximation available. This is an interpolation formula for the one particle exchange-correlation potential energy given by Hedin and Lundqvist [7] as:

$$V_{xc}(r_s) = -\left(\frac{9\pi}{4}\right)^{1/3}\{1+0.7734(r_s/21)\ln[1+21/r_s]\}\frac{2R_y^*}{\pi r_s} \qquad (2.12)$$

where the Rydberg energy is defined as: $R_y^* \equiv q^2/8\pi\varepsilon_s\varepsilon_0 a_0$, a_0 is the semiconductor Bohr radius, and the density parameter is given as: $r_s \equiv [3/4\pi a_0^3 n(z)]^{1/3}$. The exchange-correlation potential for a symmetric well calculated using this local density approximation is shown in Figure 2.3. While this approximation has been shown to give accurate results over a wide range of r_s in bulk, its application to heterostructures by Bloss [5] and Ando [8] stands without a rigorous justification. Its applicability to excited states is also questionable. While it brings the numerical calculation closer to the experimental results, it cannot explain some of the phenomena that we have observed and are discussed in chapter 10.

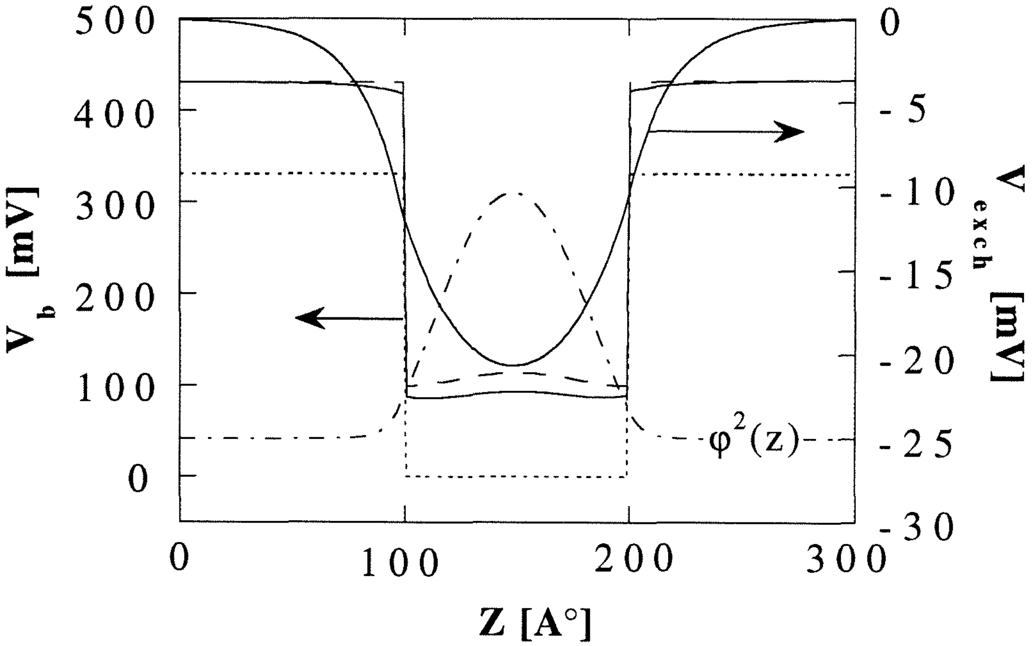

Figure 2.3: The band-profile of a 100A° $Al_{0.4}GaAs/GaAs/Al_{0.4}GaAs$ quantum well uniformly n-doped to $4\times10^{18}cm^{-3}$. The narrow-dashed line is the undoped potential profile, the dashed-line includes only the direct Coloumbic potential and the solid line includes the Lundqvist model for the exchange-correlation energy as well. The dashed-dotted line is the square of the ground state's wavefunction and the solid line shows the contribution of the exchange-energy alone (the right-hand axis).

2 .6 Nonparabolicity Corrections

Whereas the single band effective mass model leads to results which are quite accurate for the ground states in wide quantum wells (L≅10nm), it begins to break down as the separation between the bottom of the conduction band and the subband increases. To accurately treat narrower quantum wells or excited states one needs to adopt a more rigorous solution: either a **k·p** [9,10], a tight-binding [11], or a pseudo-potential [12] method. In practice, for confined and shallow continuum states in GaAs/AlGaAs systems, an energy dependent effective mass can take the band coupling effects into account [13,14] with sufficient accuracy [15]. Following the results of Ekenberg [13] for [011] orientated GaAs the perpendicular effective mass becomes:

$$m_{\perp}^{*}(E) = \frac{m^{*}(0)}{2\alpha' E}[1-(1-4\alpha' E)^{1/2}] \tag{2.13a}$$

where $m^*(0)$ is the effective mass at the bottom of the conduction band's Γ-valley. Using a 14-band **k·p** calculation, Braun and Rössler [16] determined α' to be $0.642\,\text{eV}^{-1}$ and $0.724\,\text{eV}^{-1}$ for GaAs and $Al_{0.3}Ga_{0.7}As$, respectively. This is the effective mass relevant for the confinement energy calculations. The in-plane momentum, on the other hand, has a different dispersion relation given approximately by:

$$m_{\parallel}^{*}(E) \cong m^{*}(0)[1+(2\alpha'+\beta')E] \tag{2.13b}$$

Again, using a 14-band **k·p** calculation [16] β' was determined to be $0.697\,\text{eV}^{-1}$ and $0985\,\text{eV}^{-1}$ for GaAs and $Al_{0.3}Ga_{0.7}As$, respectively. This mass is the one relevant for density of state calculations, and also for the nonparabolicity contribution to the broadening of intersubband transitions discussed in chapter 10.

The nonparabolicity was introduced into our numerical program as a secondary self-consistent loop. Once a subband's energy is found with a given effective mass, that mass is corrected using Equation 2.13a and the energy is recalculated. The iterations of the

Schrödinger and Poisson equations are continued only after the effective mass has converged. Figure 2.4 shows the effect of nonparabolicity: whereas the correction for the ground subbands is negligible, it is quite significant for typical excited state energies (>150meV). The effect of nonparabolicity is thus to red-shift the intersubband transitions - an opposite contribution from that of the many-body interactions.

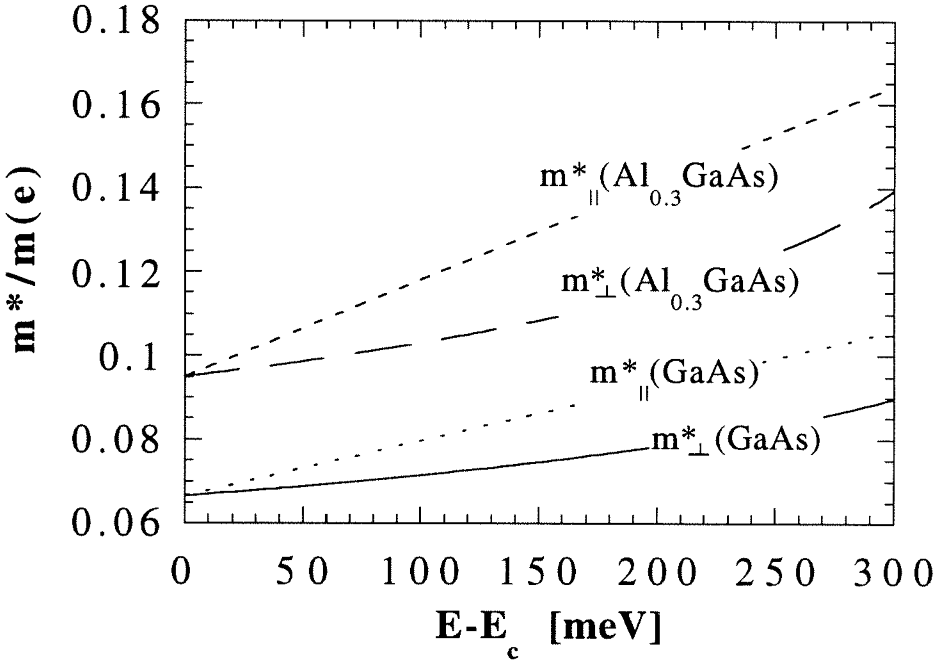

Figure 2.4: The effective mass as function of energy over the bottom of the conduction band for (011)-grown GaAs and $Al_{0.3}Ga_{0.7}As$. The perpendicular mass ($m_{\perp}$) is the one determining subband energies at $k_{\parallel}=0$. The parallel mass ($m_{\parallel}$) determines the in-plane energy dispersion relation.

2 .7 Temperature Dependence

2 .7.1 Band Offsets

The conduction band offset between two alloys depends not only on the respective bandgaps, but also on how these bands align. Whereas the former are well known and quite easy to measure, an accurate determination of the latter represents a much greater problem. The crudest approximation is Harrison's [17] common anion rule, stating that two lattice matched semiconductors with a common anion and the same crystallographic structure will have aligned valence bands. This assumption, however, is clearly inadequate for GaAs/AlGaAs quantum wells. Although more extensive studies have differed on the exact value [18,19], the ratio of the division of the energy gap between the conduction and valence bands at a GaAs/AlGaAs interface is somewhere between 60/40 and 67/33 (conduction band offset/valence band offset) and may actually change with alloy concentration. There is little information on how this ratio varies with temperature, but the fact that the blue-shift of the intersubband transitions is strongly population dependent suggests that band alignment variations are not its main cause.

2 .7.2 Bandgap

The temperature dependent bandgap parameters used in our self-consistent program were taken from a recent study by Allali et al., [20] in which they were fitted with the Varshni formula given by [21]:

$$E_g(t) = E_g(0) - \alpha(x)T^2/(T + \beta(x)) \tag{2.14}$$

where $\alpha(x)$ and $\beta(x)$ are a found experimentally for different aluminum concentrations. A summary of their data which we have used throughout our calculations is given in Table 2.1. The dependence of the bandgap on aluminum concentration may thus be given by the linear fit:

$$E_g(x) = E_g(GaAs) + a(T)x \tag{2.15}$$

with $\alpha(0)$=1.415eV and $\alpha(300)$=1.395eV. Figure 2.5 plots the bandgap for several aluminum concentrations.

Mole Fraction x	0	0.10	0.18	0.27	0.38
$E_g(0)$, [eV]	1.519	1.658	1.773	1.895	2.053
α, [meV/K]	0.895	0.644	0.806	0.90	0.782
β, [K]	538	304	451	507	383

Table 2.1: The Varshni parameters for alloys with various aluminum concentration (after ref.20).

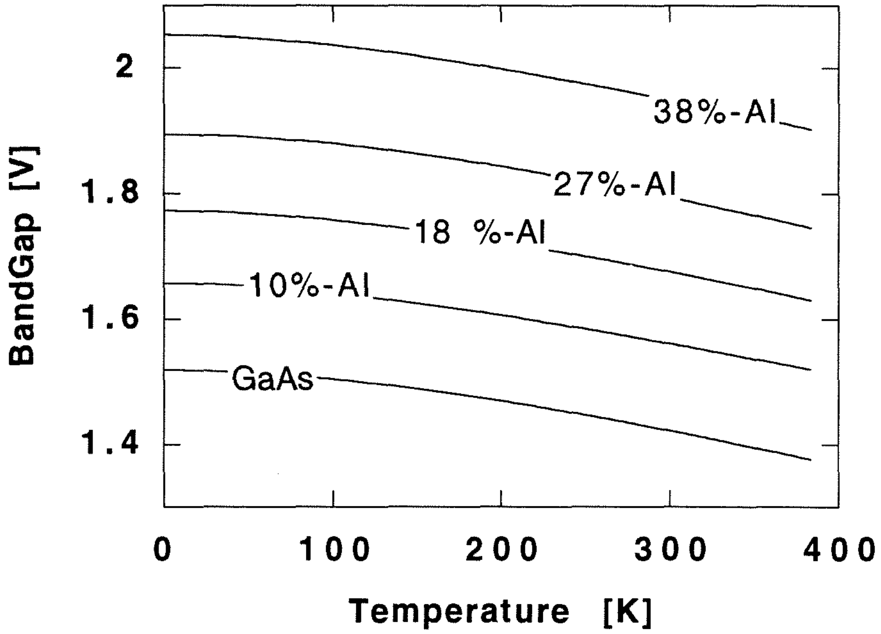

Figure 2.5: The temperature and aluminum concentration of the bandgap used in the self-consistent program (after reference 20).

An important comment at this stage is that the temperature dependence of the bandgaps as given above may not by itself explain the observed blue-shift of intersubband transitions with reduced temperatures. Although the band-shifts are substantial, they are almost identical for the various aluminum concentrations. Therefore well and barrier energies move in the same direction and the confinement energy is hardly affected by temperature. Since the temperature dependence of the barriers was wrongly neglected by early studies, the intersubband blue shift was attributed to the same bandgap variations responsible for the interband blue shift. The strong dependence of the Blue-shift's magnitude on the quantum well doping [22] suggests that it is, at least in part, due to many-body effects.

2.7.3 Effective Mass

A more significant but often neglected effect of the temperature induced bandgap variations is the resultant change of the effective mass. Accurate measurements of the effective mass across a wide temperature range are difficult to find [23], but a good estimate may be obtained from the first order **k·p** expansion [24]:

$$m^*(x,T) = \frac{1}{1 + c\left(\frac{2}{E_g(x,T)} + \frac{1}{E_g(x,T) + 0.343}\right)} \tag{2.16}$$

where $c \cong 7.51 - 3.13x$. The increase in the bandgap for lower temperatures should lead to a reduction in effective mass and hence a red-shift of the intersubband transitions as shown in Figure 2.6. The effects inducing the observed blue shift thus have to overcome this effective mass induced red shift as well.

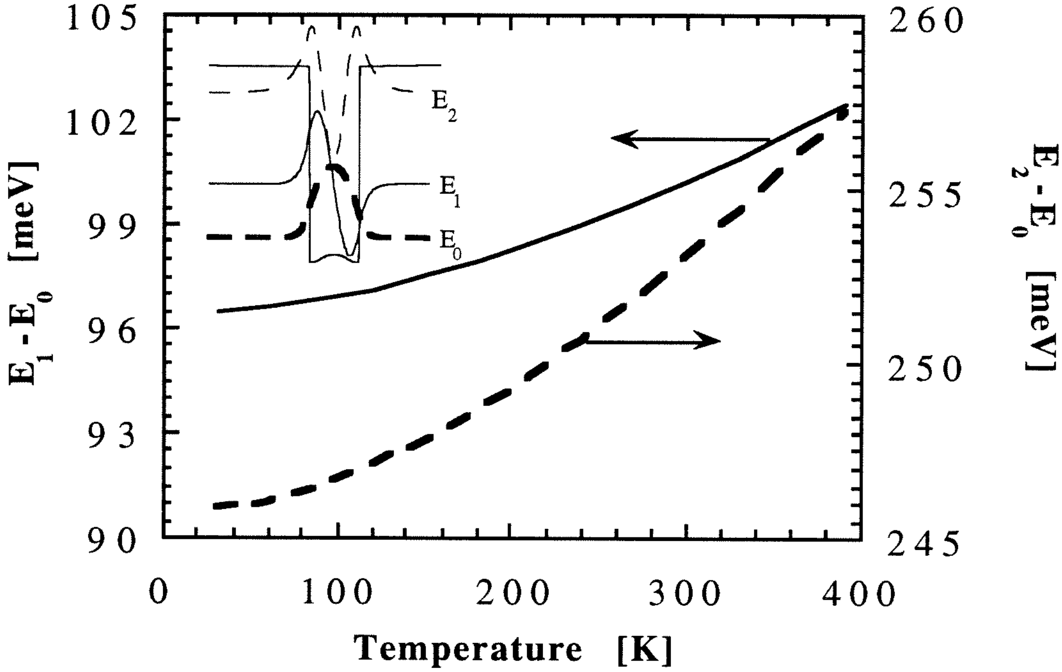

Figure 2.6: The intersubband spacing between the ground to the first and second excited subbands as a function of the temperature (taking only the variation in the bandgaps and effective mass into account).

2 .8 Voltage Boundary Conditions

2 .8.1 Unbiased Quantum Wells

As a result of charge trapping in quantum wells spatially separated from the donors, or of quantum mechanical size effects separating the donor and charge within the same well, a dipole may be induced in heterostructures. This has an effect equivalent to carrier diffusion in p-n junctions. Observing the band-profile in Figure 2.7a, we see that the electric field between the spatially separated electrons and donors leads to a voltage drop across asymmetric quantum wells which is on the order of a few tens of millivolts. It is 34mV for the step well in Figure 2.7 and may be as high as 100mV for some coupled quantum wells. The establishment of a Fermi level in equilibrium has to prevent this voltage drop, however, as it would otherwise accumulate to several volts over a typical structure with 30 to 100 periods. Rigorously, the multi-quantum well structure needs to be solved numerically with the contacts also taken into account. This computationally intractable problem may be greatly simplified by realizing that the magnitude of the charge that has to be moved between periods, or to the contacts, to offset the intra-period voltage drop is small.

Neglecting density of states limitations, and assuming charge transfer from one end of the stack to the other, we find that transfer of a surface charge density given by:

$$\sigma_p = \sigma_w \left(\frac{L_w}{L_p}\right) \tag{2.17}$$

will impose flat band conditions, where σ_w is defined as the surface doping density per period, L_p as the period length, and L_w as the spatial separation between the doping and the electronic wavefunctions. This separation is given as:

$$L_w = \int_{period} dz \cdot \{\psi_{el}(z)\psi^*_{el}(z) - N^+(z)\} \tag{2.18}$$

In practice the finite density of states will cause spreading of the excess charge amongst several periods if it is not accommodated at the contacts. For a surface density of 1×10^{12}cm^{-2}, a 3nm spatial separation (L_w) between donors and free carriers, and 30nm inter-period spacing, the charge transfer required to offset the intra-period voltage drops is roughly 1×10^{11}cm^{-2}. Imposing a condition of no voltage drop across each period (flat band) is thus a significant improvement over treating each period individually (leading to zero electric fields between periods). This condition is imposed self-consistently by adding the external field term required to offset the inter-period voltage drop. This, in turn, modifies the wavefunctions, modifying the voltage drop, and so on until the imposed external field converges. Figure 2.7 shows a step quantum well solved without (a) and with (b) imposing the flat band condition. Although the contribution of the flat band condition to the energy levels is on the order of other calculation and growth inaccuracies, its plays an important role in charge transfer between coupled quantum wells (see chapter 10).

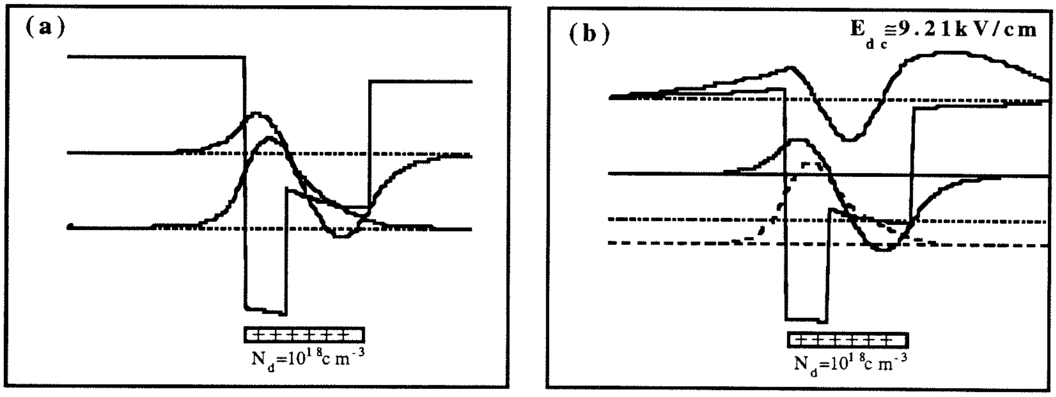

Figure 2.7: The band profile and subband states of a step quantum well without (a) and with (b) imposing flat-band boundary-conditions. The asymmetry will generate a charge transfer between periods which will induce an internal electric field of 9.21kV/cm.

2.8.2 Biased Quantum Wells

Under external bias, the problem of determining the band profile becomes significantly more complex and a rigorous treatment requires a solution of the transport and Schrödinger equations self-consistently. For strongly coupled periods the band-profile may be determined by the dominant current mechanism and even by the formation of high-field domains at low temperatures [25]. For weakly coupled periods and moderate fields, however, we can assume that the first order solution is merely a "tilting" of the unbiased solution. The total voltage drop across the structure is thus determined by the applied voltage which is the equivalent of the flat band condition in unbiased quantum wells. Since the screening in asymmetric structures cancels some of the applied bias, it must be compensated for by an increased electric field elsewhere - which in turn leads to a further increase of the screening voltage. Figure 2.8 shows a typical example of an asymmetric quantum well under negative (a) and positive (b) applied bias with the initial field boundary conditions and with the correct voltage boundary conditions respectively.

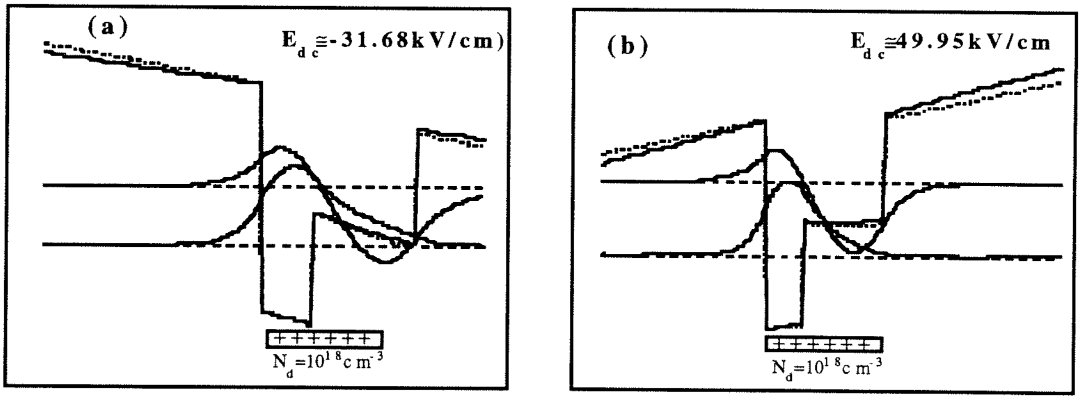

Figure 2.8: The same quantum well as in Figure 2.7 at a negative (a) and positive (b) applied field of ±40kV/cm. Using the correct boundary conditions (the solid curves) we see that the charge asymmetry will correct the applied fields to -31.68kV/cm and + 49.95kV/cm for the negative and positive applied bias, respectively.

References:

[1] P. H. Wilson, M. Lamm, H. C. Liu, Jianmeng Li, M. Buchanan, Z. R. Wasilewski, J. G. Simmons, and W. J. Schaff, "Comparison of quantum well infrared photodetectors grown on different molecular beam epitaxial systems," *Semicond. Sci. Technol.*, **8**, 2010, 1993.

[2] L. Pfeiffer, E. F. Schubert, K. W. West, and C. W. Magee, "SI dopant migration and the AlGaAs/GaAs inverted interface," *Appl. Phys. Lett.*, **58,** 2258, 1991.

[3] W. H. Press, S. A. Teukolsky, W. T. Vetterling, and B. P. Flannery, *Numerical Recepies in C*, 2nd ed., Cambridge, England: Cambridge U. Press, ch. 16-17.

[4] M. O. Manasreh, F. Smulowicz, T. Vaughan, K. R. Evans, C. E. Stutz, and D. W. Fischer, "Intersubband infrared absorption in a GaAs/$Al_{0.3}Ga_{0.7}As$ multiple quantum well," in *Intersubband Transitions in Quantum Wells*, E. Rosencher, B. Vinter, and B. F. Levine, Eds., NATO ASI Series, Series B, Physics, **287**, New York: Plenum, 1992.

[5] W. L. Bloss, "Effects of Hartree, exchange, and correlation energy on intersubband transitions," *J. Appl. Phys.*, **66**, 3639, 1989.

[6] K. M. S. V. Bandara, D. D. Coon, O. Byungsung, Y. F. Lin, and M. H. Francombe, "Exchange interactions in quantum well subbands," *Appl. Phys. Lett.*, **53**, 1931, 1988.

[7] L. Hedin, and B. I. Lundqvist, "Explicit local exchange-correlation potentials," *J. Phys. C: Solid St. Phys.*, **4**, 2064, 1971.

[8] T. Ando, "Self-consistent results for a GaAs/$Al_xGa_{1-x}As$ heterojunction I.: Subband structure and light-scattering spectra," *J. Phys. Soc. Japan.*, **51**, 3893, 1982.

[9] G. Bastard, *Wave Mechanics Applied to Semiconductor Heterostructures*, ch. III, Paris, France: Les Editions de Physique, Les Ulis Cedex, 1988.

[10] C. Mailhiot, T. C. McGill, and D. L. Smith, "New approach to the **k·p** theory of semiconductor superlattices," *J. Vac. Sci. Tech. B*, **2**, 371, 1984.

[11] J. N. Schulman and Y. C. Chang, "Reduced Hamiltonian method for solving the tight-binding model of interfaces," *Phys. Rev. B,* **27**, 6182, 1985.

[12] M. Jaros, "Microscopic phenomena in ordered superlattices," *Strained-Layer Superlattices: Physics*, T. P. Pearsall, Ed., *Semiconductors and Semimetals*, San-Diego, California: Academic Press Inc., **32,** ch. 5.

[13] U. Ekenberg, "Nonparabolicity effects in a quantum well: Sublevel shift, parallel mass and Landau levels," *Phys. Rev. B,* **40,** 7714, 1989.

[14] W. Chen and T. G. Andersson, "Effect of the nonparabolic mass on the electron confinement in arbitrarily shaped quantum wells," *Phys. rev. B*, **44**, 9068, 1991.

[15] C. Sirtori, F. Capasso, J. Faist, and S. Scandolo, "Nonparabolicity and a sum rule associated with bound-to-bound and bound-to-continuum intersubband transitions in quantum wells," *Phys. Rev. B*, **50**, 8663, 1994.

[16] M. Braun and U. Rössler, "Magneto-optic transitions and non-parabolicity parameters in the conduction-band of semiconductors," *J. Phys.* C, **18**, 3365, 1985.

[17] W. Harrison, "Elementary theory of heterojunctions," *J. Vac. Sci. Technol.*, **14**, 1016, 1977.

[18] H. Kroemer, *Molecular Beam Epitaxy and Heterostructures*, L. L. Chang, and K. Ploog, Eds., Dordrecht, Germany: Martinus Nijhoff, 1985, p.331.

[19] E. T. Yu, J. O. McCaldin, and T. C. McGill, "Band offsets in heterojunctions," *Solid State Physics*, San-Diego, California: Academic Press Inc., 1992, **46**.

[20] M. E. Allali, C. B. Sørensen, E. Veje, and P. Tidemand-Petersson, "Experimental determination of the GaAs and $Ga_{1-x}Al_xAs$ band-gap energy dependence on temperature and aluminum mole fraction in the direct band-gap region," *Phys. Rev. B*, **48**, 4398, 1993.

[21] Y. P. Varshni, "Temperature dependence of energy gap in semiconductors," *Physica,* **34**, 149, 1967.

[22] J. P. Loehr, and M. O. Manasreh, *Semiconductor Quantum Wells and Superlattices for Long-Wavelength Infrared Detectors*, M. O. Manasreh, Ed., Norwood, MA: Artech, 1993, ch. 2.

[23] *Physics of Group IV Elements and III-V Compounds*, O. Madelung, Ed., in *Landolt-Böurnstein, Numerical Data and Functional Relationships in Science and Technology, New series, Semiconductors*, Germany: Springer-Verlag Berlin-Heidelberg, 1982, **III-17a**, ch. 2.10, p.222.

[24] J. S. Blakemore, "Semiconducting and other major properties of gallium-arsenide," *J. Appl. Phys.*, **53,** R123, 1982.

[25] K. K. Choi, B. F. Levine, R. J. Malik, J. Walker, and C. G. Bethea, "Periodic negative conductance by sequential resonant tunneling through an expanding high-field superlattice domain," *Phys. Rev. B*, **35**, 4172, 1987.

Part II

Intersubband-Transition-Induced Refractive Index

Chapter 3

Contribution of Intersubband Transitions in Quantum Wells to the Refractive Index

3 .1 Introduction

The Kramers-Kronig relations [1] lead us to expect that along with the intersubband transition induced absorption, first observed by West and Eglash in 1985 [2], there should also be an intersubband transition induced refractive index correction. Due to the selection rules in quantum wells, only radiation polarized perpendicular to the plane of the wells [3] interacts with the intersubband transitions, whose refractive index correction should therefore make the material birefringent. The large and controllable absorption of intersubband transitions should hence be accompanied by a large birefringence at selected wavelengths. Since this birefringence is controllable both by bandgap engineering and by electric fields it may find applications in optical switching, phase matching, or even as electrically controlled Bragg mirrors. The index change also has a significant effect on phase-matching in parametric frequency conversion processes where it may significantly shorten or increase the coherence length depending upon the relative detuning (Chapter 4).

The refractive index contribution of intersubband transitions was predicted [4,5] soon after the first experimental observation of the absorption induced by intersubband transitions [2], but was not measured due to a host of experimental difficulties described in this chapter and to the lack of full understanding regarding its implications as described in chapters 4 and 9. In this chapter we report on the first experimental observation of the intersubband transition induced birefringence [6]. The refractive index change we observed in an unoptimized structure: $\Delta n \cong \pm 0.07$ at a 45 degree incidence, suggests that a refractive index change as high as $\Delta n \cong \pm 0.4$ can be obtained in an optimized structure and for an optical polarization perpendicular to the plane of the quantum wells. The observed refractive index was also, as expected, highly dispersive ($\Delta n \cong 0.14$ over a half micron range between $\lambda = 9.75\mu m$ and $\lambda = 10.22\mu m$) and highly temperature dependent ($dn/dT \cong 3.1 \times 10^{-4} [1/K]$).

Our initial motivation in measuring the intersubband transition induced refractive index was for it to lead up to the electrooptic modulation of infrared radiation using the control over the intersubband transition frequency in asymmetric quantum wells [7]. This effort was delayed while we were waiting for a modification in the MBE which would reduce oval defects and hence allow application of sufficient electric fields over the required stripe area. During the course of this delay we had the opportunity to re-examine the validity of applying the standard formalism of nonlinear optics to intersubband transitions and develop an alternative approach (Chapters 5 - 9). The clear conclusion from this nonperturbative approach (Chapter 8) was that phase-modulation is inherently inferior to absorption modulation when using resonantly-enhanced transitions - leading us to pursue absorption modulation instead (Chapter 10). Nevertheless, the refractive index contribution of intersubband transitions is an important phenomena by itself and may find several other applications. In the next chapter we describe the effect the intersubband transition induced refractive index will have on phase-matching in frequency conversion processes and suggest its utilization for a novel phase-matching technique. We also show that this refractive index may be used for wavelength sensitive waveguiding.

Another conclusion from the nonperturbative formalism for the nonlinear optical interaction of resonantly-enhanced transitions developed in Chapters 5 through 9 is that the nonparametric optical nonlinearities, being merely changes in the linear response, are limited by the magnitude of that linear response. The previously observed imaginary component of the linear susceptibility (absorption) [2] and the real component (refractive index change) observed by us [6], are therefore upper limits on the magnitudes of the obtainable absorption and phase nonlinearities, respectively. We will show in Chapters 7 through 9 that the magnitude of the linear optical response is the key to analyzing device applications of intersubband transitions.

3 .2 Interaction Schemes

The main difficulty in observing the refractive index induced by intersubband transitions is due to the available interaction schemes. Because of the one-dimensional quantization, subbands with scalar effective masses interact only with optical polarization perpendicular to the plane of the quantum wells. These polarization-dependent transitions, and the accompanying changes of the index of refraction, make the quantum well stack behave as a uniaxial crystal. Unfortunately, the selection rule combined with the relatively narrow layers (<10μm) available from epitaxial growth dictate the use of certain limiting experimental schemes.

The most common of these schemes are shown in Figure 3.1. To measure the birefringence, that is the index of refraction difference between the polarization interacting with the intersubband transitions (perpendicular to the plane of the quantum wells) and the polarization not interacting with the intersubband transitions (in the plane of the quantum wells), we used the scheme shown in Figure 3.1a. A beam is propagated at a 45° angle relative to the plane of the quantum wells and a polarizer is used to determine its components at an angle of 45° with the plane of the quantum wells (and normal to the propagation direction) and in the direction parallel to the plane of the quantum wells. This configuration offers a large interaction with the intersubband transitions, but leads to a structural phase shift due to the polarization dependence of the phase delay in the total internal reflections at the GaAs/Air interface.

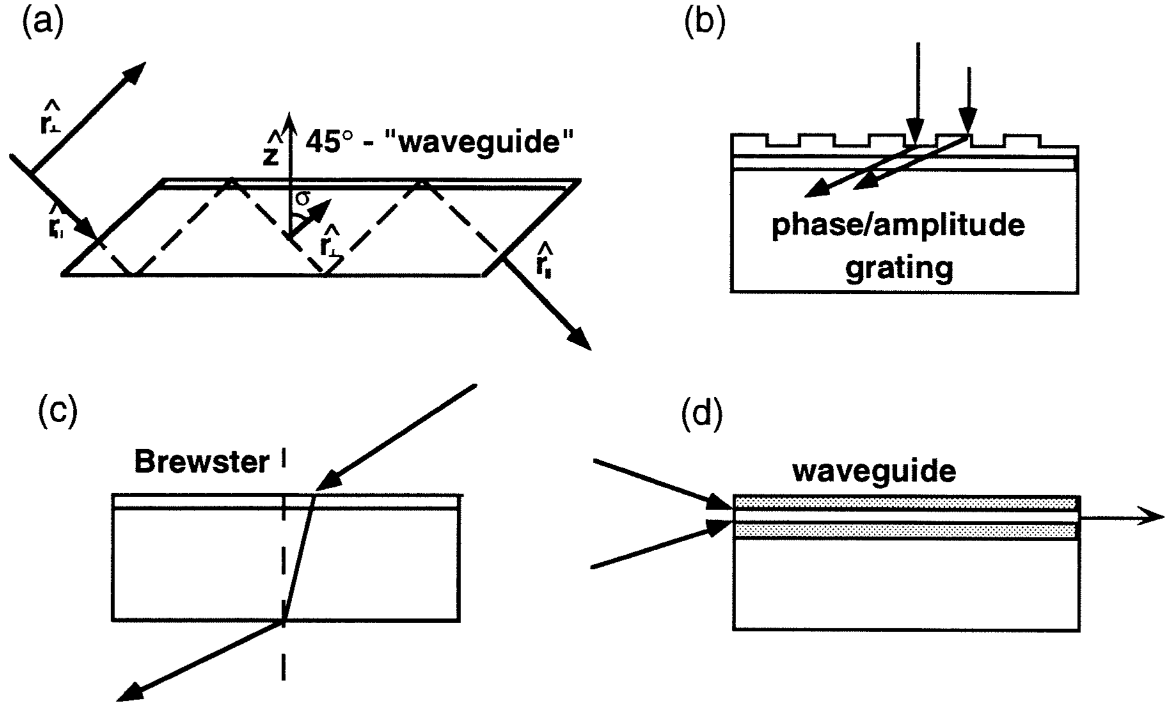

Figure 3.1: Schematic of four of the more common interaction schemes for overcoming the selection rules of intersubband transitions. Lapping of 45° crystal facets (a), a phase or intensity grating (b), interaction at the Brewster angle (c), and incorporation of waveguiding layers into the crystal growth (d). The latter may be combined with grating coupling (b).

Despite the structural phase factor, propagation at 45° still lends itself more readily to birefringence measurements than the other standard schemes for interaction with the intersubband transitions. The structural phase shift, which is a function of the nearly wavelength-independent refractive index of the bulk material, may be isolated from the strongly wavelength-dependent intersubband contribution. For the other schemes on the other hand (Figure 3.1b-d), the two polarization components are not degenerate at the incident facet. Furthermore, Brewster angle incidence (Figure 3.1c), leads to a very small interaction not only because of the single pass through the quantum wells, but also because of the quadratic dependence of the interaction strength on the projection of the optical polarization on the normal to the quantum well planes. In both waveguide and grating coupling schemes (Figure 3.1d and b respectively) the phase velocity is highly wavelength dependent. This makes it difficult to isolate the intersubband transition induced component unless it is modulated. Modulation of the population between coupled quantum wells was indeed used by Dupont et al. [8] to measure the modulation of the phase delay in a Brewster angle propagation scheme (Figure 3.1c). The interferometric technique they used, however, is only capable of measuring changes in the intersubband transition induced phase-delay and not its total magnitude.

3 .3 Linear Optical Response of the Intersubband Transitions

The linear response of the intersubband transitions, including its phase and absorption components, is calculated using the standard model for a two-level system interacting with a monochromatic electromagnetic field [1,9]. This leads to a real (χ') and an imaginary component (χ'') of the susceptibility (for an incident polarization normal to the quantum well planes) given by:

$$\chi' = \frac{Nq^2\mu_{12}^2 T_2}{\varepsilon_0 \hbar} \frac{\Delta\omega T_2}{1+(\Delta\omega T_2)^2} \tag{3.1a}$$

and:

$$\chi'' = \frac{Nq^2\mu_{12}^2 T_2}{\varepsilon_0 \hbar} \frac{1}{1+(\Delta\omega T_2)^2} \tag{3.1b}$$

respectively, where ω is the optical frequency, N is the electron density (assumed initially in the ground state), ε_0 is the vacuum permitivity, the detuning is defined by: $\Delta\omega \equiv (E_2 - E_1)/\hbar$, T_2 is the dephasing time, and μ_{12} is the intersubband dipole matrix element.

The imaginary component of the susceptibility leads to an absorption coefficient given by:

$$\alpha(\Delta\omega) \cong \frac{\pi}{n\lambda}\chi''(\Delta\omega)\cos^2(\theta) \tag{3.2a}$$

where n is the bulk's index of refraction, and θ the angle between the polarization and the normal to the plane of the quantum wells. Similarly, the real component of the susceptibility leads to a refractive index correction given by:

$$\Delta n(\Delta\omega) \cong \frac{\chi'(\Delta\omega)}{2n}\cos^2(\theta) \tag{3.2b}$$

The normal to the plane of the quantum wells thus becomes the principal axis of the crystal that is now uniaxial, i.e., the intersubband transitions have induced a birefringence. By introducing a field linearly polarized at an intermediate angle it becomes possible, using a cross-polarizer experiment and ellipsometric techniques, to deduce the phase delay and hence the refractive index difference between the polarization components. This, however, is complicated by the directional absorption coefficient of the intersubband transitions (Equation 3.2a) as well as by the structural phase delay.

For the experimental configuration shown in Figure 3.2, the field $E_{in}(0)$ will be split by the input polarizer to components along the major ($\hat{y}$) and minor axes ($\hat{x}$), $E_{in}(0)\cos\phi\hat{y}$ and

$E_{in}(0)\sin\phi\hat{x}$, respectively. The former will undergo half the maximal interaction with the intersubband transitions ($\cos^2 45°$) while the latter will not interact with the intersubband transitions at all. As they propagate through the structure, the two experience the same bulk refractive index and absorption, but a different phase shift at the total internal reflection (45°) bounces at the GaAs/Air interface. This difference, deduced from the complex values of the Bragg coefficients, is given by [10]:

$$\varphi_g = 2\tan^{-1}\left(\frac{\cos(\theta)\sqrt{\sin^2(\theta) - 1/n^2}}{\sin^2(\theta)}\right) \tag{3.3}$$

From the value of the refractive index in GaAs, which is $n \cong 3.27$ at $\lambda \cong 10\mu m$ [11], we expect a difference in the phase delay between the two polarization components of $\varphi \cong 83°$ for the total internal reflections at a 45° incidence angle. This phase delay is roughly an order of magnitude larger than that expected from the intersubband transitions, but because its variation is negligible over the wavelength range of our experiment (9.2-10.75μm), we were able to isolate and subtract its contribution. The field after propagation through the sample but before the output cross-polarizer, is thus given by:

$$E_{out}(z) = E_{in}(0)\cdot e^{-(\alpha_b + i2\pi n/\lambda)L_b}\cdot\{e^{-\frac{\pi}{n\lambda}[\chi''(\Delta\omega)+i\chi'(\Delta\omega)]\cdot\cos^2(\theta)L_p}\cdot e^{iN_b\varphi_g}\cdot\cos\phi\cdot\hat{y} + \sin\phi\cdot\hat{x}\} \tag{3.4}$$

where N_b is the number of bounces in the sample, L_b the propagation length through the bulk and L_p the propagation length in the quantum well stacks. The total phase difference between the two components hence becomes:

$$\varphi_T = \frac{\pi}{2n\lambda}\chi'(\Delta\omega)L_p + iN_b\varphi_g \tag{3.5}$$

A detector placed after the cross-polarizer at an angle of σ with respect to the normal to the plane of the quantum wells (Figure 3.2) will measure an optical power proportional to:

$$P(\sigma) \propto \cos^2\sigma + b^2\sin^2\sigma + 2b\cos\sigma\sin\sigma\cos\varphi_T \tag{3.6}$$

where b is defined as the ratio of the amplitudes of the two components and is related to the intersubband transition-induced absorption by:

$$b \equiv \frac{E_x}{E_y} = \tan\phi \cdot e^{-\frac{\pi}{2n\lambda}\chi''(\Delta\omega)L_p} \tag{3.7}$$

Knowledge of this ratio thus allows us to deduce the phase delay despite the unequal absorption of the two components. It may be simply measured by aligning the cross-polarizer along the directions of the major and minor axis. When b is known, measurement of the power for other output polarizer angles allows us to deduce the total phase delay, to within a factor of a sign and an integer multiple of 2π, by using Equation 3.6.

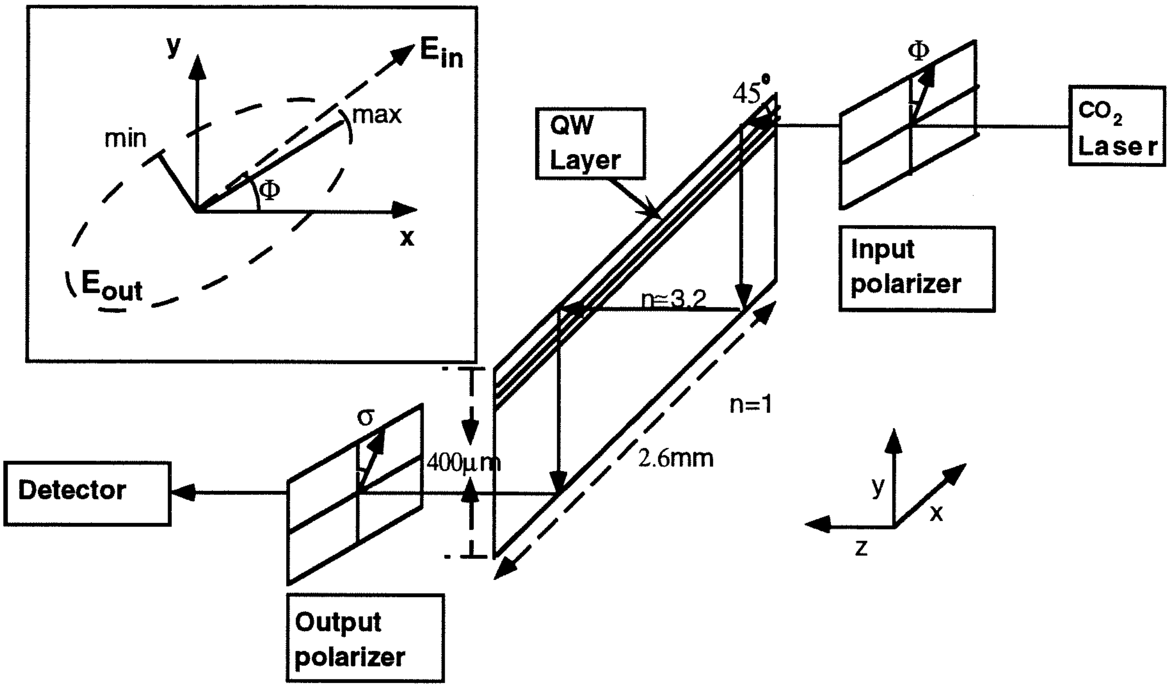

Figure 3.2: The 45° bounce cross-polarizer experimental setup. The inset displays the input (linear) and output polarization (elliptical) of the optical field. Also shown are the four output polarizer settings at which measurements are taken (x, y, min, max).

3 .4 Observation of the Intersubband Transition Induced Birefringence

To enable separation of the intersubband transition-induced phase delay from the structural one we wish to maximize the wavelength dependence of the former. This is obtained for samples whose resonance peak wavelength is near 10 microns - in the middle of the CO_2 laser's spectral range, and whose broadening is minimal. The sample used in the experiment, MBE growth 1331, was grown by Ali Shakouri a year earlier for different purposes. It contained thirty periods of 7nm GaAs quantum well, nominally silicon doped to $2\times10^{18}cm^{-3}$, with 44nm $GaAl_{0.3}As$ barriers. The quantum wells were grown by molecular beam epitaxy on a semi-insulating 400μm - thick GaAs substrate, and a 2.6mm long sample was cleaved and lapped to 45° angled facets on both ends. The sample was mounted in an MMR N_2-flow Joule-Thompson cooler equipped with ZnSe windows to allow measurements in 77-400K temperature range. Figure 3.3 shows its absorption spectrum at 77K and 300K taken in a Mattson Fourier Transform Infrared (FTIR) by subtracting the transmission of the in-plane from the interacting polarization. The excellent Lorentzian curve fits show that the broadening is mainly homogeneous, as was assumed in the derivation of equation 3.1.

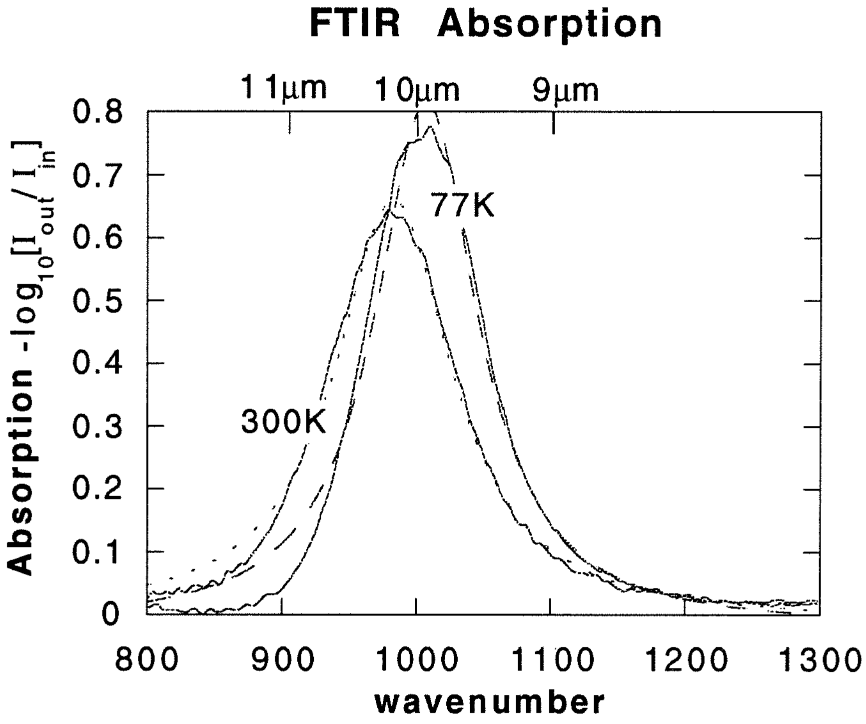

Figure 3.3: The FTIR absorption spectrum of MBE growth 1331. The sample used for the observation of intersubband transition induced birefringence is shown at room temperature and at 77K. The dashed lines are Lorentzian curve fits.

The intersubband transition induced refractive index correction was measured in a basic cross-polarizer experiment shown in Figure 3.2. The output from an air cooled, grating tunable CO_2 laser (roughly 3 Watts) is passed through the input Brewster angle polarizer.

The linearly polarized beam is focused on the sample with a 254 mm ZnSe lens. A circular input aperture with 100μm diameter is placed adjacent to the sample to insure a constant propagation length within it despite slight beam shifts as the laser wavelength is tuned. Since the beam enters the sample at normal incidence, both polarization components have equal transmission coefficients (≅30% reflection). In the sample, however, the beam propagates at a 45° angle with respect to the plane of the wells and undergoes several total internal reflections which induce different phase delays for the two polarization components. The output beam is then passed through a wire grid polarizer and focused on either a room temperature pyroelectric detector or a LN_2 cooled Mercury-Cadmium Telluride (MCT) photovoltaic detector. The detector's signal is fed to a Lock-in amplifier triggered by a mechanical chopper placed in front of the sample. The chopping frequency was around 200Hz, and a low duty cycle was used to prevent heating of the sample by the incident radiation. The optical intensity in the sample never exceeded 1/200 of the saturation intensity (roughly 500kW/cm^2 for a polarization normal to the planes of the quantum wells) to avoid heating and saturation effects.

The experiment was carried out at room temperature, and repeated at 100K. The laser is tuned in intervals across its full spectral range (it was impossible to stabilize the air cooled laser in the range of 9.75 to 10.15μm). At every wavelength the output power is measured for at least four output polarization settings: along the two principal axes: $\hat{x}$ and $\hat{y}$, and at the angles of minimal and maximal intensity. Increased accuracy was obtained by measuring the power for a scan of the output polarizer angles and fitting the results to Equation 3.6. First the intersubband absorption is found by comparing the transmission of the interacting ($\hat{y}$) and non-interacting ($\hat{x}$) polarization and shown as the empty circles in Figure 3.4 (Equation 3.7). The phase delay is now calculated using Equation 3.6 with the ratio of the principal axes output amplitude components (b) taken as a parameter. Since the measured output power is proportional to ($2\pi m \pm \varphi_T$) which includes the geometrical phase delay, an arbitrary constant leading to zero phase delay at line center is added to the results presented in Figure 3.4 as is justified below. The intersubband transition-induced phase delay reaches a maximal value of ±40° half a line width on either side of line center.

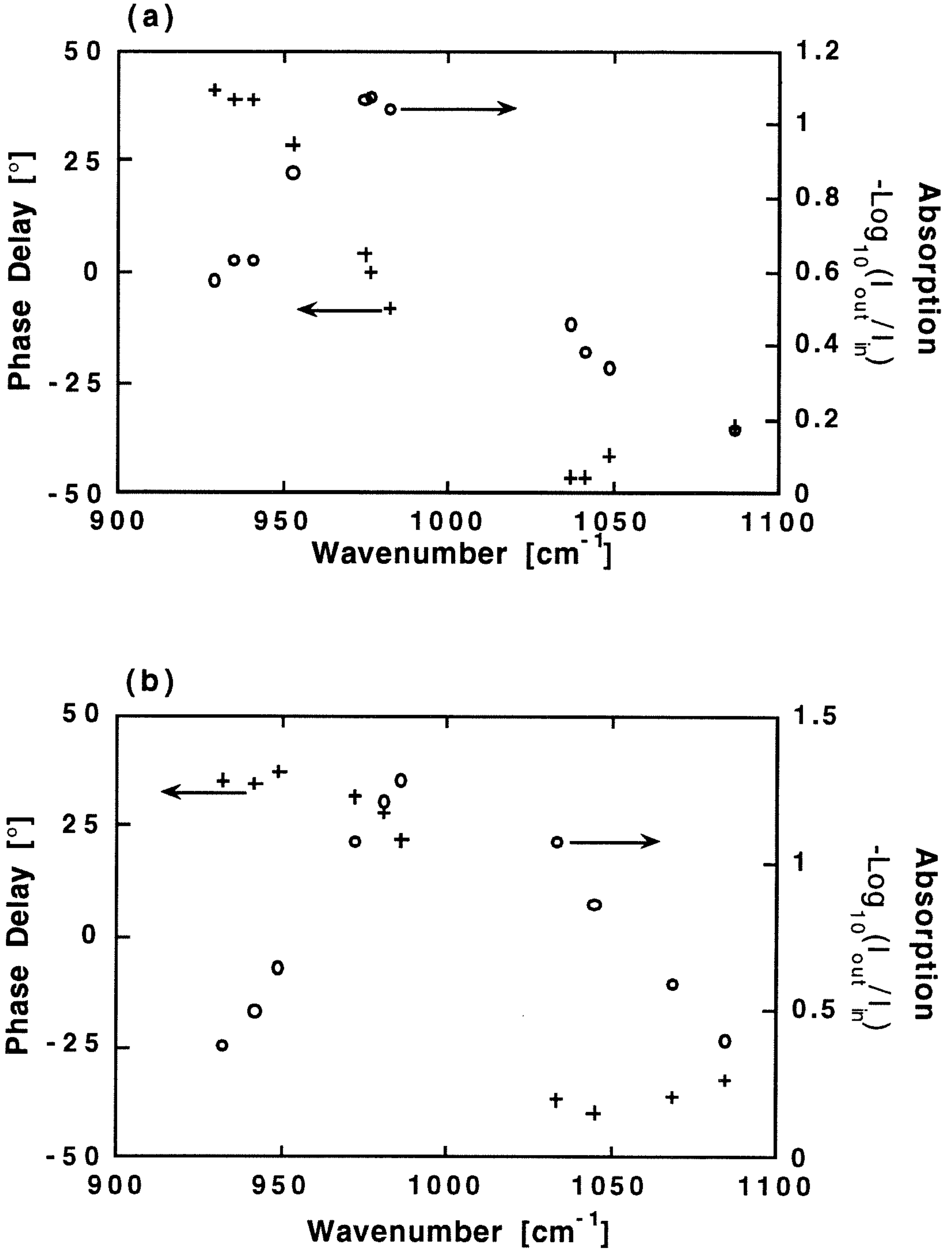

Figure 3.4: The measured absorption and phase delay as a function of wavelength at 290K (a) and 100K (b). The zero of the phase delay axis is arbitrary.

The absorption and phase delay data shown in Figure 3.4 is used to deduce the real and imaginary components of the susceptibility through equations 3.2b and 3.2a, respectively. This requires knowledge of the propagation length which can be estimated from the sample's length and hence the number of passes (or bounces - N_b). This number, however, turns out to be extremely sensitive to the location and angle at which the input beam enters the sample (hence the input aperture preventing variation when tuning the CO_2 laser) but may essentially be taken as an arbitrary factor at this stage and deduced later on.

The real (circles) and imaginary (crosses) components of the susceptibility at 290K and 100K are shown in Figure 3.5a and Figure 3.5b, respectively. Lorentzian fits to the imaginary component of the susceptibility are shown as the dashed curves. The best fits are given by a resonance at 976 cm^{-1} (10.25 microns), with 54 cm^{-1} broadening (half width at half maximum) at room temp, and resonance at 1002 cm^{-1} (9.98 microns), with 48 cm^{-1} broadening at 100K. Equation 3.2a, or the trivial case of the Kramers-Kronig relations, is now used to deduce the prediction for the real components of the susceptibility from the curve fit of the imaginary part. Notice that this result, shown as the dotted curves in Figure 3.5, **is not** a fit to the real components of the susceptibility. Only a constant offset (the arbitrary zero of Figure 3.4 in retrospect) is used as a single parameter fit for the geometrical phase delay by fitting the real susceptibility data to the Kramers-Kronig transform of the imaginary susceptibility data. An excellent fit was obtained after a subtraction of the structural phase delay of $2\pi m$-97° at room temperature, and $2\pi m$-93° at 100K. Since the number of bounces can be roughly estimated from the sample's height to length ratio, this is consistent with a total structural phase delay of $\varphi_g \cong 623°$ and $\varphi_g \cong 627°$, respectively (m=2), i.e., approximately 7.5 passes ($N_b \cong 7.5$) within the sample (Equation 3.3 - $\varphi_g \cong 83°$). This corresponds to a propagation length of 16.2μm in the region of the multiquantum stack (including barriers). The fact that the number of bounces (N_b) is not an integer shows that it is not uniform across the beam, however, it is in the range expected from the sample's height to length ratio. The excellent fit between the real susceptibility data to the transform of the imaginary susceptibility data is a demonstration of the Kramers-Kronig relations.

To validate our assumption of a nearly frequency-independent structural phase factor the experiment was repeated for a sample with a peak outside the laser's spectral range (8.6 microns), and for bulk GaAs. The clearest verification however comes from the temperature dependence of the phase delay discussed in section 3.4.

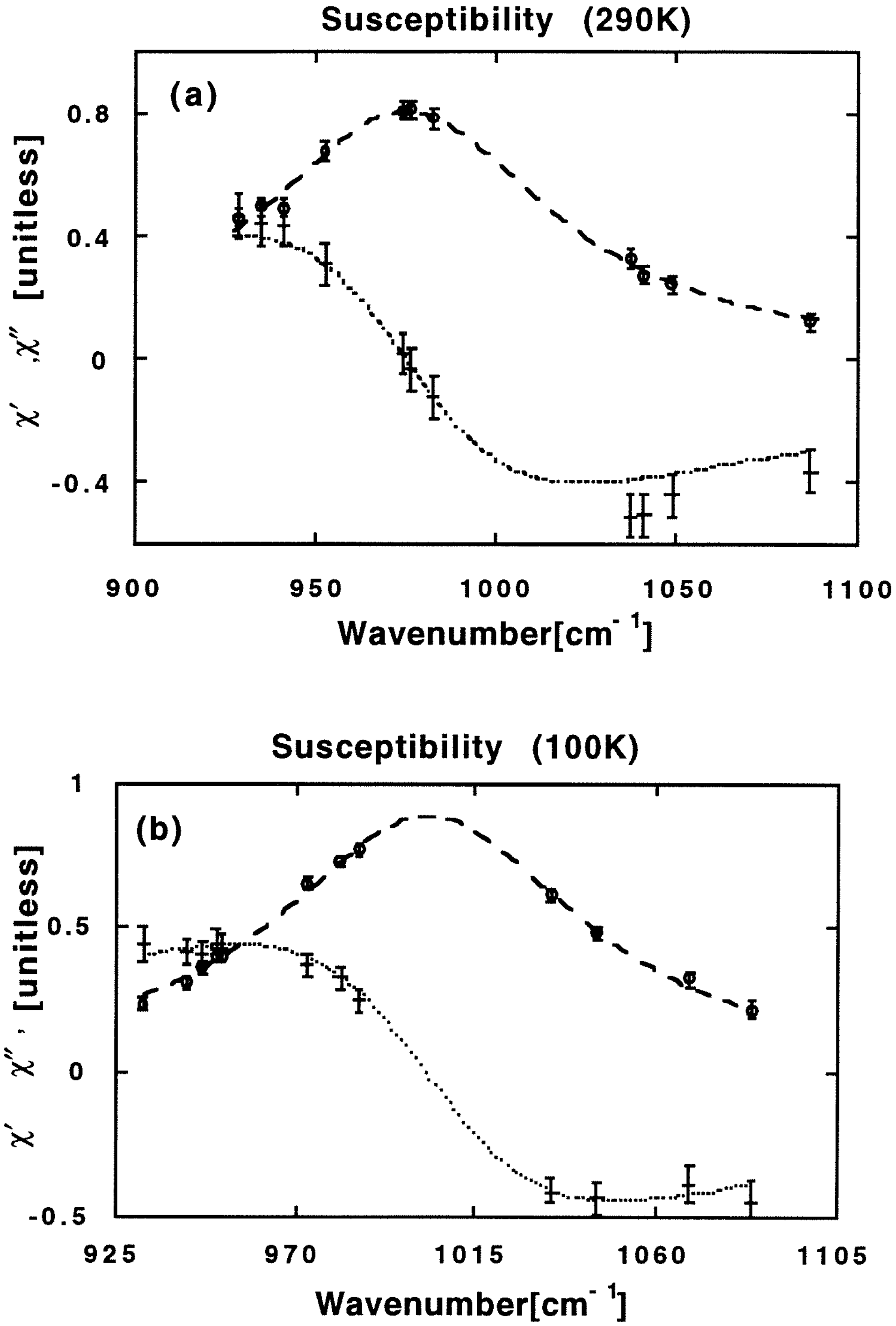

Figure 3.5: The measured real (+) and imaginary (-) polarization dependent components of the susceptibility. The dashed line is a Lorentzian fit to the imaginary part of the susceptibility corresponding to the intersubband absorption. The dotted line is a Kramers-Kronig transform of the dashed line, i.e., the expected real part of the susceptibility.

Figure 3.6 is essentially a repetition of Figure 3.5b but with the results presented in terms of the refractive index correction and the absorption coefficient, manifesting the Kramers-Kronig relations for a two-level system. Following the standard convention for the absorption coefficient of intersubband transitions we also average the refractive index contribution over both the wells and the barriers. The maximal index change is thus $\Delta n=\pm 0.07$ half a line width on either side of the resonance. The sample thus demonstrates an extremely large dispersion leading to a refractive index difference of 0.14 between the wavelengths of 9.75μm and 10.22μm.

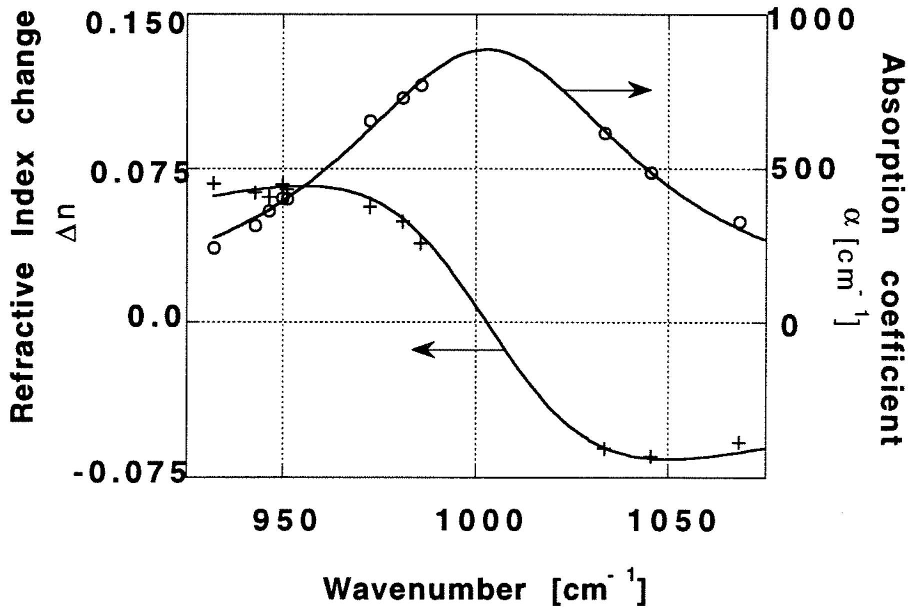

Figure 3.6: The measured absorption coefficient and refractive index correction induced by the intersubband transitions at 100K.

Interaction at a right angle, rather than at a 45° angle with the plane of the wells, will double the birefringence just as it does the absorption. Both could be further enhanced by increasing the fill factor of the quantum wells, i.e., by using narrower barriers. Assuming the 44nm barriers used in our sample may be replaced with 10nm ones without a significant increase in broadening, a refractive index correction as high as $\Delta n \cong 0.4$ should be obtainable. Thus the intersubband transitions can lead to a refractive index change of a magnitude unprecedented in semiconductors.

3 .5 Temperature Dependence of the Refractive Index

The absorption spectrum of the intersubband transitions undergoes a blue shift with reduced temperature. This phenomena, attributed to the contribution of many body effects [12], should also lead to a similar shift of the dispersion curve. Since the structural phase contribution (Figure 3.2) is nearly temperature independent (the temperature variation only caused a 4° change), the shift of the intersubband contribution should allow its isolation. At the same time the blue shift also compensates for the limited tuning range of the CO_2 laser by allowing for the acquisition of more data points along the dispersion curve.

Beyond the contribution of the blue shift to the experimental accuracy it is also interesting to observe the temperature dependence of the intersubband transition induced refractive index. The comparison of the intersubband transition induced phase delay at 100K and 290K is shown in Figure 3.7. The intersubband induced phase contribution changes by 35° at a wavelength of 983cm^{-1} (λ=10.17μm) as the temperature is varied from 100K to 290K. Linearizing this temperature induced refractive index change we obtain the derivative of the refractive index with temperature as $dn/dT \cong 3.1\times10^{-4}K^{-1}$. Although a smaller index change in Silicon ($1.86\times10^{-4}K^{-1}$ at λ=1.5μm) has actually been used to fabricate modulators operating on resistance heating [13], the significance of this large coefficient is probably limited to phase matching issues.

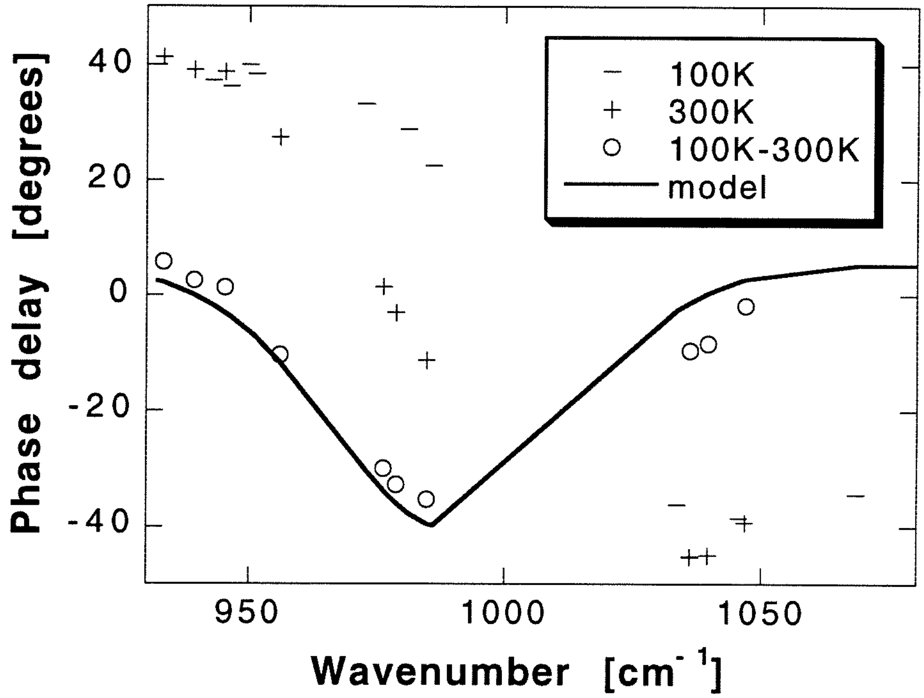

Figure 3.7: The intersubband transition-induced phase delay at 300K (+), at 100K (-) and the temperature induced shift (o). The solid line is obtained by including only the influence of the resonance frequency shift in Equation 3.9.

To estimate the temperature dependence of the refractive index we insert the empirical temperature dependence of the transition parameters into Equation 3.1a. The difference between the real component of the susceptibility at the temperatures T and T' will be given by:

$$\Delta\chi' \approx \frac{q^2\mu_{12}^2}{\varepsilon_0\hbar}\{\frac{N(\omega_r-\omega)}{1/T_2^2+(\omega_r-\omega)^2}-\frac{N'(\omega_r'-\omega)}{1/T_2'^2+(\omega_r'-\omega)^2}\} \qquad (3.8)$$

The primed terms denote the resonance frequency (ω_r'), the line width ($1/T_2'$), and the total population (N') at the temperature T'. If we consider only the contribution of the shift of the resonance. we find that the change is maximized at the half way point between the low and high temperature line centers. The solid curve in Figure 3.7, obtained by introducing only the observed blue-shift of the resonance frequency in Equation 3.8, gives an excellent fit to the experimental dispersion data.

References:

---

[1] A. Yariv, "*Quantum Electronics*," New York: John Wiley & Sons, 1989, ch. 8.

[2] L. C. West and S. J. Eglash, "1st observation of an extremely large-dipole transition within the conduction band of a GaAs quantum well," *Appl. Phys Lett.*, **46**, 1156, 1985

[3] Within the single band model analysis, applicable when the intersubband transitions are between confined conduction band states in GaAs/AlGaAs structures - ref:

A. Shik, in: *Intersubband Transitions in Quantum Wells,* E. Rosencher, Ed., New York, Plenum Press, 1992, p.319.

[4] D. Ahn and S. L. Chuang, "Calculation of the linear and nonlinear intersubband optical absorption in a quantum well model with an applied electric field," *IEEE J. Quantum Electron.*, **QE-23**, 2196, 1987.

[5] K. J. Khun, G. U. Iyengar, and S. Yee, "Free carrier induced changes in the absorption and refractive-index for intersubband optical transitions in $Al_xGa_{1-x}As/GaAs/Al_xGa_{1-x}As$ quantum wells," *J. Appl. Phys.*, **70**, 5010, 1991.

[6] G. Almogy, M. Segev, and A. Yariv, "Intersubband-transition-induced phase matching," *Optics Lett.*, **19**, 1192, 1994.

[7] W. L. Bloss, "Electric-field dependence of quantum-well eigenstates," *J. Appl. Phys.*, **65**, 4789, 1989.

[8] E. Dupont, D. Delacourt, and M. Papuchon, "Midinfrared amplitude and phase modulation by intersubband transitions in biased GaAs/GaAlAs double quantum wells," *Appl. Phys. Lett.*, **63,** 2514, 1993.

[9] See Chapter 6 for a rigorous derivation of the optical susceptibility in discrete level systems.

[10] M. Born and E. Wolf, *Principles of Optics*, 6th ed., New-York, Pergamon Press, 1989, ch. 1, p.51.

[11] E. D. Palik, Ed., *Handbook of Optical Constants of Solids*, San-Diego, California, Academic Press Inc., 1991, vol. 2, p. 524.

[12] M. O. Manasreh, F. Smulowicz, T. Vaughan, K. R. Evans, C. E. Stutz, and D. W. Fischer, "Intersubband infrared absorption in a GaAs/$Al_{0.3}Ga_{0.7}As$ multiple quantum well," in *Intersubband Transitions in Quantum Wells*, E. Rosencher, B. Vinter, and B. F. Levine, Eds., NATO ASI Series, Series B, Physics, **287**, New York: Plenum, 1992.

[13] All-silicon modulator uses resistance heating, *Laser Focus World*, p.52, May 1994.

Chapter 4

Phase-Matching Induced by Intersubband Transitions

4 .1 Introduction

The second-harmonic generation (SHG) conversion efficiency in nonlinear materials is typically limited by their coherence lengths - making phase-matching necessary for high efficiencies to be obtained [1,2]. In this chapter we suggest the use of the controllable refractive index contributions associated with the intersubband transitions in quantum wells [3], whose measurement was reported in the previous chapter, to obtain phase-matching at selected wavelengths [4]. The real component of the susceptibility generated by an intersubband transition may be tailored to offset the bulk's dispersion and lead to equal refractive indexes at the first and second-harmonic wavelengths. Unlike phase-matching by angle tuning which requires sensitive alignment, and quasi-phase-matching which requires accurate processing, the phase-matching suggested here is intrinsic. We specifically examine the increase in the conversion efficiency that may be obtained for a SHG process in bulk GaAs by growth of GaAs/AlGaAs n-doped quantum wells with a transition frequency half way between the first ($\lambda \cong 10\mu m$) and second-harmonics. It is shown that phase-matching obtained in this manner will replace the coherence length limits on conversion efficiency in a phase-mismatched bulk with absorption limits which are much less severe for typical intersubband transitions parameters. Both the ideal case of a bulk material embedded with quantum wells and the more practical case of the TM mode in a narrow dielectric wave guide [5] are considered.

We consider both index contributions originating from intersubband transitions in symmetric (2-level) quantum wells designed for phase-matching only, and in asymmetric (3-level) quantum wells designed for resonant-enhancement of the SHG as well. First we examine the former, where the source of the SHG nonlinearity is the bulk material. A transition with the real part of its optical susceptibility offsetting the bulk's dispersion will lead to phase matching. Doped quantum wells are optimal for this purpose [3] as the intersubband transitions are virtually discrete, their separation is controllable, and they have large optical dipole elements. In the following treatment we shall limit ourselves to electron intersubband transitions in quantum wells, but the treatment is valid for any two-level system that may be distributed uniformly (on a wavelength scale) in a dispersive host material. The analysis in this chapter, although focusing on quantum wells, should provide the tools to analyze the feasibility of transition-induced phase-matching in other material systems.

Just as the intersubband transition-induced refractive index may lead to an increase of the coherence length, it may if not properly designed, lead to a greatly increased dispersion. In the extreme case the refractive index contribution of the intersubband transitions may reduce the coherence length between the wavelengths of 5μm and 10μm in GaAs to a distance of under 10μm - an order of magnitude shorter than the bulk's coherence length which is about 80μm. Therefore, the intersubband transition induced refractive index must be taken into account in any intersubband transition based frequency conversion scheme. We elaborate further on the shortening of the coherence length in chapter 9 where we address the issue of resonantly-enhanced second-harmonic generation in general.

4 .2 Phase-Matching Second-Harmonic Generation

4 .2.1 Propagation Equations

The refractive index contribution of intersubband transitions designed to offset the bulk's dispersion will be unavoidably [6] accompanied by absorption which must therefore be taken into account in the solution of the propagation equations for second-harmonic generation [7]. These are now written for a field of ω and 2ω frequency components (E_ω and $E_{2\omega}$ respectively) using the slowly varying envelope approximation [8] as:

$$\frac{dE_\omega}{dz} = -\alpha_\omega E_\omega - \frac{i\omega}{2\varepsilon_0 n_\omega c} dE_{2\omega} E_\omega^* e^{-i\Delta kz} \tag{4.1a}$$

and:

$$\frac{dE_{2\omega}}{dz} = -\alpha_{2\omega} E_{2\omega} - \frac{i\omega}{\varepsilon_0 n_{2\omega} c} dE_\omega^2 e^{i\Delta kz} \tag{4.1b}$$

where n_ω and $n_{2\omega}$ are the first and second-harmonic bulk refractive indices respectively, d the bulk's SHG coefficient, and Δk is defined as the phase-mismatch vector: $\Delta k \equiv k_{2\omega} - 2k_{\omega}$. The real and imaginary components of the intersubband linear susceptibilities: χ'(ω) and χ"(ω), respectively, are given for a two level system as [8]:

$$\chi(\omega) \equiv \chi'(\omega) - i\chi''(\omega) = \frac{N\mu^2}{\varepsilon_0 \hbar} T_2 \frac{(\Delta\omega T_2 - i)}{(\Delta\omega T_2)^2 + 1} \tag{4.2}$$

where N is the average electron volume density, μ the intersubband dipole element, T_2 the dephasing time, and Δω and ω+Δω are the detuning of the first and second harmonics, respectively, from the intersubband transition. The wave-vectors are thus modified by the real components of the intersubband transition and become:

$$k_{\omega}^2 = \frac{\omega^2}{c^2}(n_{\omega}^2 + \chi'(\omega)) \tag{4.3a}$$

and:

$$k_{2\omega}^2 = \frac{(2\omega)^2}{c^2}(n_{2\omega}^2 + \chi'(2\omega)) \tag{4.3b}$$

for the first and second harmonic, respectively, while the absorption, neglecting the bulk's contribution, is given by:

$$\alpha_{\omega} = \frac{\omega}{2n_{\omega}c}\chi''(\omega) \tag{4.4a}$$

for the first harmonic, and:

$$\alpha_{2\omega} = \frac{\omega}{n_{2\omega}c}\chi''(2\omega) \tag{4.4b}$$

for the second harmonic. Normalizing the fundamental frequency and its detuning in units of half the line width ($\tilde{\omega} \equiv \omega T_2$ and $\Delta\tilde{\omega} \equiv \Delta\omega T_2$), we obtain the phase-matching condition from equations 4.1, 4.2, and 4.3 as:

$$\frac{n_\omega^2 - n_{2\omega}^2}{2n_\omega} \cong n_\omega - n_{2\omega} \equiv \Delta n = \frac{\chi_{res}}{2n_\omega}\{\frac{\Delta\tilde{\omega}}{\Delta\tilde{\omega}^2+1} - \frac{(\Delta\tilde{\omega}-\tilde{\omega})}{(\Delta\tilde{\omega}-\tilde{\omega})^2+1}\} = 0 \qquad (4.5)$$

where χ_{res} is the absolute value of the line center (imaginary) susceptibility ($\Delta\omega$=0 in Equation 4.2). When phase-matching (Δk=0) is maintained, Equations 4.1a and b are solved as:

$$E_{2\omega}(z) = -i\frac{\omega}{\varepsilon_0 n_{2\omega} c}\frac{d}{(\alpha_{2\omega} - 2\alpha_\omega)}\{e^{-2\alpha_\omega z} - e^{-\alpha_{2\omega} z}\}E_\omega(0)^2 \qquad (4.6)$$

where, as discussed in section 4.2.3, we have neglected the second term on the RHS of Equation 4.1a which accounts for the depletion of the first harmonic due to the second-harmonic generation. From Equation 4.6 we find the optimal conversion distance as:

$$z_{\max} = \frac{1}{\alpha_{2\omega} - 2\alpha_\omega}\ln(\frac{\alpha_{2\omega}}{2\alpha_\omega}) \qquad (4.7)$$

This distance represents a tradeoff between the accumulating second harmonic generation and the absorption of both harmonics. It yields a maximal (intensity) conversion efficiency of:

$$\eta(z_{\max}) \equiv \frac{I_{2\omega}(z_{\max})}{I_\omega(0)} = 2(\frac{\mu_0}{\varepsilon_0})^{3/2}\frac{\omega^2 d^2}{n_{2\omega} n_\omega^2}\{\frac{1}{\alpha_{2\omega}}(\frac{2\alpha_\omega}{\alpha_{2\omega}})^{\frac{2\alpha_\omega}{\alpha_{2\omega}-2\alpha_\omega}}\}^2 I_\omega(0) \qquad (4.8)$$

where $I_\omega(0)$ is the incident first-harmonic intensity defined as:

$$I_\omega = 2n_\omega(\varepsilon_0/\mu_0)^{1/2}|E_\omega|^2 \qquad (4.9)$$

By substituting equations 4.2, 4.4 and relation 4.5 into equation 4.8 we find a maximum of the conversion efficiency for $\Delta\omega=\omega/2$. Thus when the resonant transition is halfway between the fundamental and second harmonic the conversion efficiency is given by:

$$\eta_{\max} = \frac{1}{2e^2}(\mu_0/\varepsilon_0)^{3/2}\frac{(d/\varepsilon_0)^2}{n_\omega^2 n_{2\omega}} I_\omega (\frac{\tilde{\omega}}{\Delta n})^2 \tag{4.10}$$

while the optimal propagation length for obtaining this maximal efficiency is:

$$z_{\max} = \frac{1}{2\alpha_\omega(\Delta\tilde{\omega} = \tilde{\omega}/2)} \tag{4.11}$$

It is now limited by the absorption of the intersubband transition (which is half way between the first and second harmonics) rather than by the coherence length. Inserting the refractive index correction ($\Delta\omega=\omega/2$ in Equation 4.5) into Equation 4.11, while using Equations 4.2 and 4.4, will hence lead to:

$$z_{\max} = \frac{cT_2}{2\Delta n} = \frac{\tilde{\omega}}{\pi}\frac{\lambda}{4\Delta n} = \frac{\tilde{\omega}}{\pi} l_c \tag{4.12}$$

where ($l_C \equiv \lambda/4\Delta n$) is defined as the bulk's coherence length [8]. The propagation length may thus be increased by a factor of $\tilde{\omega}/\pi$ which is proportional to the transition frequency to half line width ratio. The phase matching condition may now be related to the transition parameters and it is given as:

$$\Delta n = \frac{2}{n_\omega}\frac{N\mu^2}{\hbar\omega\varepsilon_0}\frac{1}{1+4/\tilde{\omega}^2} \cong \frac{2}{n_\omega}\frac{N\mu^2}{\hbar\omega\varepsilon_0} \tag{4.13}$$

This expression sets the limits on the magnitude of the phase mismatch that may be corrected via intersubband transitions.

4.2.2 Conversion Efficiency

The index mismatch between the wavelengths of 10.6μm and 5.3μm in GaAs is $\Delta n_{GaAs} \cong 0.03$ [9], leading to a coherence length limit of $l_c \cong 83\mu m$ for the second-harmonic generation process. From Equation 4.12 we see that the intersubband transitions will remove this limit on the useful propagation distance and replace it by an extinction length limit of between 0.6mm to 2.6mm. From Equation 4.10 we see that the phase-matching improves the maximal conversion efficiency by a factor of $(\tilde{\omega}/2e)^2$. The transition frequency to half line width ratio ($\tilde{\omega}$) is thus the single parameter determining the increase in the conversion efficiency. Since AlGaAs/GaAs quantum wells have typical $\tilde{\omega}$'s of 25-100 [10], using their refractive index contribution for phase-matching will lead to an improvement of between one to almost three orders of magnitude in the conversion efficiency for a given pump intensity when compared to a non phase-matched bulk GaAs.

To avoid refractive index variations along the propagation path, the incident pump (first-harmonic) intensity for which this phase-matching technique may be used is limited to sub-saturation values [7] (see Chapter 9). For a large enough detuning ($\tilde{\omega}/2$), however, the limit on the pump-intensity will not be set by saturation but by GaAs surface breakdown phenomena to below 10MW/cm^2 [11]. With the second-harmonic generation coefficient of GaAs given as $d \cong 3.4*10^{-21}$m/v [12], taking I=5MW/cm^2, and $\tilde{\omega}=62$ (transition half line width of 2meV), we obtain a maximal conversion efficiency of approximately 22 percent for a propagation distance of 1.6mm. The maximal refractive index dispersion that may be compensated for using this technique is given by Equation 4.13 and is a function of the average electron density and of the intersubband transition's optical dipole matrix elements. For AlGaAs/GaAs quantum wells with optical dipole matrix elements of $\mu \cong 2$nm, a volume density of $N \cong 8.4\times10^{16}$cm^{-3} is needed to offset the phase-mismatch in bulk GaAs. A confinement factor of under 5% in quantum wells with a volumetric doping density of $N \cong 2\times10^{18}$cm^{-3} is thus sufficient to induce phase-matching in GaAs.

The refractive index correction obtained via a single intersubband transition half-way between the first and second harmonics is insensitive to the transition's frequency to the first order, making this phase matching technique tolerant of quantum well growth inaccuracies. An accuracy in the transition's interaction strength of at least $\pi / \tilde{\omega}$ is required, however, to increase the coherence length above the extinction length - leading to the full conversion efficiency improvement available with this technique. The interaction strength is correctable via electron injection mechanisms [13,14], which are thus also the way tuning may be achieved. The phase-matching is relatively broad-band, and can be tailored to cover most of the CO_2 laser's spectral range as shown in Figure 4.1.

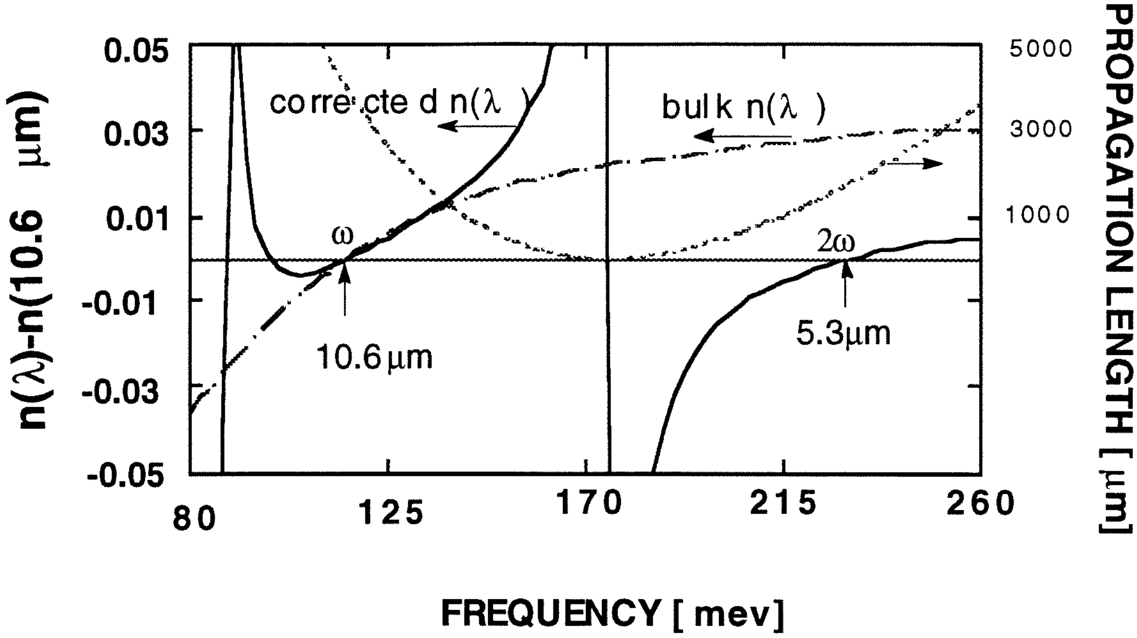

Figure 4.1: The refractive index dispersion of GaAs: n(λ)-n(10.6μm) with a single correcting intersubband transition half way between the first and second harmonics versus frequency (the solid curve). Also shown are the refractive index dispersion of bulk GaAs (the dashed-dotted curve), and the extinction length (the dotted curve - right hand axis).

4.2.3 Depletion

Since, as we have just shown, the intersubband transition-induced phase-matching may lead to significant conversion efficiencies, we must examine the neglect of the depletion term in Equation 4.1a. When phase-matching is obtained this equation may be re-written as:

$$\frac{dE_\omega}{dz} = \frac{\omega}{2n_\omega c}\{\chi''(\omega)\cdot E_\omega - i(dE_{2\omega}/\varepsilon_0)\cdot E^*_\omega\} \tag{4.14}$$

where we have used the definition of the absorption in Equation 4.4a. The contribution of the depletion will thus be smaller than that of the absorption when:

$$|E_{2\omega}| < \left|\frac{\chi''(\omega)}{d/\varepsilon_0}\right| \tag{4.15}$$

For a transition half way between the two harmonics ($\Delta\tilde{\omega} = \tilde{\omega}/2$), and assuming $\tilde{\omega} >> 1$, Equation 4.5 leads to:

$$\Delta n \cong \frac{2\chi_{res}}{\tilde{\omega} n_\omega} \tag{4.16}$$

Inserting this into the previous equation and using Equation 4.9 leads to a limit on the second-harmonic intensity for which the depletion may be neglected given by:

$$I_{2\omega} < \frac{8(\varepsilon_0/\mu_0)^{1/2} n_{2\omega} n_\omega^2 (\Delta n)^2}{\tilde{\omega}^2 \cdot (d/\varepsilon_0)^2} \tag{4.17}$$

For the above given GaAs parameters, this limit is between $I_{2\omega} \cong 45\text{MW/cm}^2$ and 700MW/cm^2 for values of $\tilde{\omega}$ between 100 and 25, respectively. Neglecting the depletion in Equation 4.1a is thus completely justifiable in this material system. Depletion does, however, set a limit on the improvement that can be gained by the use of narrower transitions (larger values of $\tilde{\omega}$).

4.2.4 Phase Matching in Waveguides

Since current technology limits the growth of high quality epitaxial layers to about 10μm, waveguiding is necessary to obtain longer interactions [5, also see Figure 3.1]. In this case one has to overcome not only the intrinsic bulk dispersion but also that induced by the waveguiding. The refractive index contribution of intersubband transitions located in the core of a dielectric waveguide must be tailored to equalize the phase velocities of the waveguide modes of the first and second harmonics. Using a numerical solution of the TM modes in arbitrary shaped dielectric wave guides [15, see Appendix A] we find that phase-matching should be achievable using intersubband transitions provided that sufficient confinement is obtained. Figure 4.2 shows a possible example of a phase-matched wave guide. The crossing of the first and second harmonic modes is due to the reversal of the dispersion relations caused by the intersubband transitions.

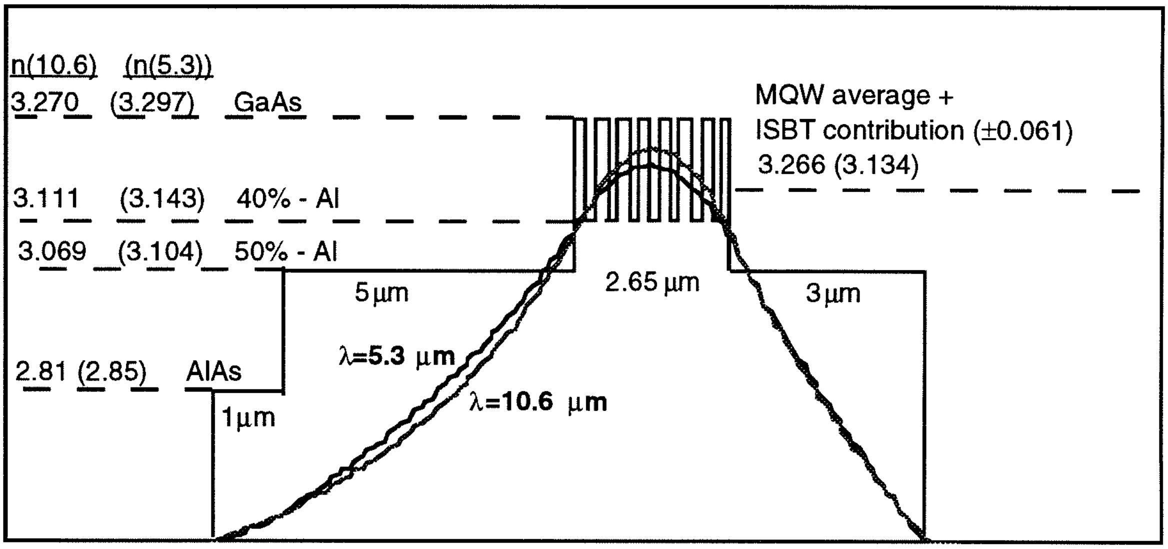

Figure 4.2: A waveguide phase-matched by the intersubband transition-induced refractive index. The structure consists of the following layers: 1μm AlAs, 5μm $Al_{0.5}GaAs$ *cladding, a multiquantum well stack of 150 periods of 62A° GaAs wells with 113A°* $Al_{0.4}GaAs$ *barriers n-doped to* $6*10^{11}$ $1/cm^2$*, and a second 3μm* $Al_{0.5}GaAs$ *cladding. The refractive index at 10.6μm (5.3μm) is given for the various material compositions.*

4 .3 Phase-Matching in Three-Level Systems

4 .3.1 Intersubband Transition-Induced Second-Harmonic Generation and Phase-Matching

Having calculated the potential improvement in conversion efficiencies that may be gained from intersubband transitions designed for phase-matching, we now consider the effect of the refractive index contributions accompanying intersubband transitions designed for resonant enhancement of second-harmonic generation. Such asymmetric three-level quantum wells have recently [16,17] led to the observation of second-harmonic generation coefficients as high as $\chi^{(2)}_{(2\omega,\omega,\omega)} \cong 9\cdot 10^{-7}\,\text{m/v}$. The assumption that was made in most of the reported studies was that since the propagation distances are much shorter than the bulk's coherence length, phase matching is unnecessary. This assumption neglects the index changes accompanying the intersubband transitions that could be tailored to offset the bulk's dispersion on one hand, but could on the other hand significantly increase the phase mismatch. In Figure 4.3 we give an example of the former case: intersubband transitions in a three-level asymmetric quantum well are used both to enhance the second-harmonic generation and to offset the bulk's dispersion. This is obtained by designing the subbands so that the detuning of the first harmonic from the ground to first state transition is opposite that of the second harmonic from the ground to second state transition. The magnitude of the detuning and the transition strength (dipole element and population) are determined to accurately offset the bulk dispersion. As can be seen in Figure 4.3 this scheme represents an inherent compromise between maximal second-harmonic generation (double resonance) and phase-matching. The applicability of this (three-level system) phase-matching technique is also limited by its high sensitivity to well parameters, and by the saturation of the near-resonant intersubband transitions [7,11].

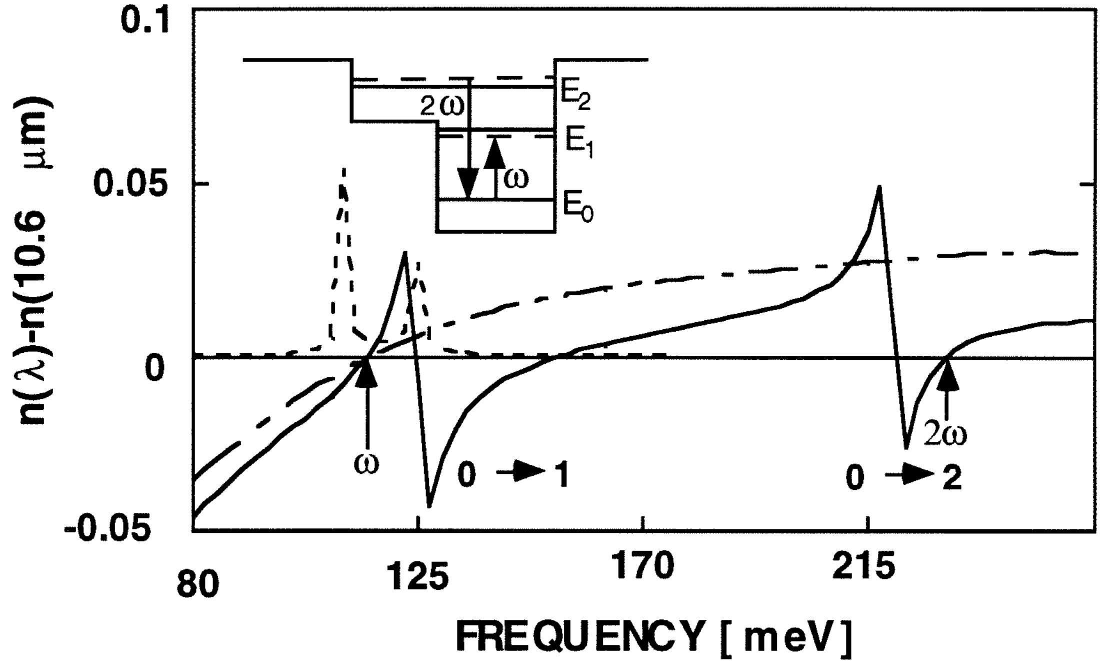

Figure 4.3: The refractive index dispersion of GaAs: $n(\lambda)$-$n(10.6\mu m)$ with intersubband transitions used for resonant enhancement of the SHG as well as phase-matching versus frequency (solid curve). Also shown are the refractive index dispersion of bulk GaAs (the dashed-dotted curve), and the resultant double-peaked SHG coefficient (short dashed curve). The transitions in the asymmetric well are depicted in the inset. A confinement factor of ~1/30 in the quantum wells is needed for phase matching in the case of $\tilde{\omega}=40$ and $\Delta\tilde{\omega}=3$.

4.3.2 Intersubband Transition-Induced Phase-Mismatch

The index contribution of the intersubband transitions, shown to lead to phase-matching in Figure 4.3, could on the other hand, greatly increase the phase-mismatch if not correctly designed. The magnitude of this intersubband transition induced dispersion is easily estimated from the simple case of equal dipole elements and opposite detuning ($\mu_{01} = \mu_{02}$, and $(\omega_{10} - \omega) = -(\omega_{20} - 2\omega)$ - see inset of Figure 4.3) for which:

$$\Delta n_{ISBT} = n(\omega) - n(2\omega) \cong \frac{1}{n}\chi_{res}\frac{\Delta\tilde{\omega}}{\Delta\tilde{\omega}^2 + 1} \qquad (4.18)$$

The accumulated phase difference at a distance of one over the absorption coefficient is therefore $2\Delta\tilde{\omega}$. Thus when the normalized detuning ($\Delta\tilde{\omega}$) is not significantly smaller than π/2, the intersubband-induced phase mismatch may limit the maximal conversion efficiency even for propagation distances shorter than the bulk's coherence length. The intersubband transition-induced dispersion, rather than absorption, may thus become the limiting factor on resonantly-enhanced second-harmonic generation [11,10]. Only on-resonant or equally detuned transitions of equal strength will not induce such a phase-mismatch. This issue is re-visited in Chapter 9 after the full derivation of resonantly-enhanced second-harmonic generation is presented.

4 .4 Summary

In summary we have considered the implications of the intersubband transitions-induced refractive index contribution on second-harmonic generation and suggested a novel phase-matching technique based upon it. This technique replaces the limit on the second-harmonic generation conversion efficiency set by the coherence length, with one set by the absorption of the intersubband transitions correcting the bulk's phase-mismatch. The potential increase in the conversion efficiency is proportional to the transition's frequency to line width ratio squared. With current technology, the use of intersubband transition-induced phase-matching may lead to an improvement of almost three orders of magnitude in the conversion efficiency of a 10μm to 5μm wavelength in GaAs. This technique may be applied to any material in which a desired wavelength transition with a sufficient refractive index correction can be introduced. Further improvement depends on the availability of transitions with narrower line widths.

Appendix A: Numerical Solution of One-Dimensional Waveguides

Maxwell's equations for a TM polarization lead to the wave equation:

$$n(z)^2 \frac{d}{dz}\left(\frac{1}{n(z)^2}\frac{\partial H_y}{\partial z}\right) + k_z^2 H_y = 0 \tag{4.A1}$$

where:

$$k_z^2 = k_0^2 n(z)^2 - \beta^2 = \left(\frac{2\pi}{\lambda}\right)^2 (n(z)^2 - n_{eff}^2) \tag{4.A2}$$

which with the normalized units $\tilde{z} \equiv \frac{2\pi}{\lambda} z$ becomes:

$$\frac{d}{d\tilde{z}}\left(\frac{1}{n(\tilde{z})^2}\frac{\partial H_y}{\partial \tilde{z}}\right) + \left[1 - \left(\frac{n_{eff}}{n(\tilde{z})}\right)^2\right] H_y = 0 \tag{4.A3}$$

As in chapter 2, we reduce this to two coupled linear differential equations by defining:

$$y_1 \equiv H_y \tag{4.A4}$$

and:

$$y_2 \equiv \frac{1}{n(\tilde{z})^2}\frac{\partial H_y}{\partial \tilde{z}} \tag{4.A5}$$

finally obtaining:

$$y_1' \equiv n(\tilde{z})^2 y_2 \tag{4.A6}$$

and:

$$y_2' \equiv [(\frac{n_{eff}}{n(\tilde{z})})^2 - 1]y_1 \tag{4.A7}$$

These equations are solved by guessing an initial value of the effective refractive index (n_{eff}) and using the same shooting method discussed in Chapter 2. For confined modes boundaries are chosen far enough so that the mode amplitude may be taken as zero (with a finite derivative which merely affects the normalization). A Runge-Kutta method is used to propagate the differential equations and a Newton-Raphson method is used to correct the eigenvalue guesses. In practice this solution was implemented by two methods: a slight modification of the C code used for the self-consistent solution of quantum well states (chapter 2), or alternatively by several lines of Mathematica® code [18] which are quite sufficient if run times are not an issue.

References:

---

[1] J. A. Armstrong, N. Bloembergen, J. Ducuing, P. S Pershan, "Interactions between light waves in a nonlinear dielectric," *Phys. Rev.*, **127,** 1918, 1962.

[2] S. Somekh, and A. Yariv, "Phase-matchable nonlinear optical interactions in periodic thin-films," *Appl. Phys. Lett.*, **21**, 140, 1972.

[3] G. Almogy, A. Shakouri, and A. Yariv, "Observation of birefringence induced by intersubband transitions in quantum wells," *Appl. Phys. Lett.*, **63**, 2720, 1993.

[4] G. Almogy, M. Segev, and A. Yariv, "Intersubband-transition-induced phase matching," *Optics Lett.*, **19**, 1192, 1994.

[5] D. D. Yang, F. H. Julien, P. Boucaud, J. M. Lourtioz, and R. Planel, "Intersubband absorption of GaAs/AlGaAs quantum wells in MBE grown mid-infrared slab waveguides," *IEEE Phot. Tech. Lett.*, **2,** 181, 1990.

[6] A possible exception is suggested by M. O. Scully, T. W. Hansch, M. Fleischhauer, C. H. Keitel, and S.-Yao Zhu, "*Physics and Probability*," W. T. Grandy, Jr., and P. W. Millonni, Eds., Cambridge, England: Cambridge U. Press, 1993, p.73.

[7] T. A. DeTemple, L. A. Bahler, and J. Osmundsen, "Semiclassical theory of resonant three-wave parametric interactions: Second-harmonic generation," *Phys. Rev. A*, **24**, 1950, 1981.

[8] A. Yariv, *Quantum Electronics* New-York: John Weily & Sons, 1988.

[9] *Handbook of Optical Constants of Solids* II, E. D. Palik, Ed., San-Diego, California: Academic Press Inc., 1991, p.534.

[10] J. Faist, C. Sirtori, F. Capasso, L. Pfeiffer, and K. W. West, "Phonon limited intersubband lifetimes and linewidths in a two-dimensional electron gas," *Appl. Phys. Lett.* **64**, 872, 1994.

[11] F. H. Julien, J-M. Lourtoiz, N. Herschkorn, D. Delacourt, J. P. Pocholle, M. Papuchon, R. Planel, and G. Le Roux, "Optical saturation of intersubband absorption in GaAs-$Al_xGa_{1-x}As$ quantum wells," *Appl. Phys. Lett.*, **53,** 116, 1988.

[12] *Handbook of Lasers*, R. J. Pressley, Ed., Cleveland, Ohio: Chemical Rubber Co., 1971, p.504. (Crystal growth direction must correspond with a bulk SHG coefficient).

[13] M. Wegener, T. Y. Chang, I. Bar-Joseph, J. M. Kuo, and D. S. Chemla, "Electroabsorption and refraction by electron-transfer in asymmetric modulation-doped multiple quantum well structures," *Appl. Phys. Lett.*, **55**, 583, 1989.

[14] G. Almogy, Y. Xu, A. Tong, A. Shakouri, and A. Yariv, "Monolithic integration of quantum well infrared photodetector and modulator", submitted to *Appl. Phys. Lett.*

[15] D. F. G. Gallagher, "Series solutions to the arbitrary profile 1-d wave-guide and quantum-well problems," *IEEE J. Quant. Electron.*, **28**, 1785, 1992.

[16] E. Rosencher, P. Bois, J. Nagle, and S. Delaitre, "Second-harmonic generation by intersubband transitions in compositionally asymmetrical MQWs," *Electron. Lett.*, **25**, 1063, 1989.

[17] Z. Chen, D. Cui, M. Li, C. Jiang, J. Zhou, and G. Yang, "High conversion efficiency of second-harmonic generation in step quantum wells," *Appl. Phys. Lett.*, **61,** 2401, 1992.

[18] R. Maeder, *Programming in Mathematica*, 2nd ed., Redwood, California: Addison-Wesley, 1991.

Part III

Theory of the Resonantly-Enhanced Nonlinear Optics of Intersubband Transitions in Quantum Wells

Chapter 5

Introduction to the Nonlinear Optical Properties of Intersubband Transitions

5.1 Introduction

In many respects intersubband transitions (ISBTs) in quantum wells [1] are the material system that nonlinear optics has been waiting for: a system where the transition energies, optical dipole matrix elements, populations, and even the relaxation times to some extent, are directly controlled by growth parameters. The resultant pseudo-discrete energy levels and the one-dimensional nature of the envelope functions allow an accurate derivation of the nonlinearities from straightforward quantum mechanical calculations, and the resonant enhancement and controllable symmetry lead to nonlinearities of unprecedented magnitude. These nonlinearities, which have attracted recent interest to the nonlinear optics of quantum well intersubband transitions, also call for caution to be exercised, as the appropriateness of some commonly used assumptions of nonlinear optics becomes questionable. We have therefore rigorously re-derived the nonlinear optical response of intersubband transitions, examining the validity of the various approximations used and the implications of their breakdown. While the accuracy of the single-band model, which has been examined in detail before [2,3], is briefly mentioned, we mainly addressed the basic nature of the nonlinear optical interaction. The limitations of the Rotating-Wave Approximation (RWA), the Slowly-Varying Envelope Approximation (SVA), and the dipole approximation are discussed. The phenomena expected once these assumptions break down are examined. Particular emphasis is placed on the divergence of the standard perturbative expansion of the susceptibility in terms of a power series of nonlinear coefficients. We show that the perturbative approach is incapable of describing the nonlinear response of intersubband transitions at the intensities required for practical applications, and present an alternative formalism. We explicitly solve for the 'ac' Kerr coefficient ($\chi^{(3)}_{(\omega,\omega,-\omega,\omega)}$) (Chapter 7), the electrooptic coefficient ($\chi^{(2)}_{(\omega,\omega,0)}$) (Chapter 8), and the second-harmonic generation coefficient ($\chi^{(2)}_{(2\omega,\omega,\omega)}$) (Chapter 9), which are the standard tools for analyzing electrooptic modulation (EOM), all-optical modulation (AOM), and second-harmonic generation (SHG), respectively. The latter is specifically addressed as a representative, and perhaps the most important, parametric nonlinearity. The tools derived for second-harmonic generation may be applied in a straightforward fashion to sum-frequency generation and any other frequency conversion process.

Before beginning with the formal nonperturbative derivation we emphasize the uniqueness of the optical response of intersubband transitions in quantum wells necessitating it (section 5.2), and review some of the more important experimental results in the field (section 5.3). We also consider the limitations of the single-band model (section 5.4), and briefly mention the influence of many-body interactions (section 5.5). We examine the validity of the dipole approximation and the slowly-varying envelope approximation (SVA) in section 5.6 and 5.7, respectively.

5.2 Uniqueness of the Intersubband Transitions

When the standard formalism of nonlinear optics [4,5,6] is applied to a substantially different material system, the validity of its underlying assumptions needs to be questioned. This is especially true when the standard treatment predicts extremely large nonlinearities, as is the case for quantum well intersubband transitions. These, due to the almost total control over intersubband transition characteristics available through bandgap engineering [7], are unique in being a completely designable system of resonantly-enhanced transitions. Within certain material limitations, both the eigenenergies and eigenstates (and hence optical dipole matrix elements) of electrons (or holes) in quantum wells may be arbitrarily designed. Furthermore the subband population may be easily controlled by doping or by interband excitation and even the intersubband lifetime is controllable to some extent [8]. This almost total control of intersubband transition parameters has led to the observation of optical nonlinearities of unprecedented magnitude (see references of section 5.3), but has yet to lead to effective nonlinear devices.

While the nonlinear optics of other resonantly-enhanced transitions has been studied since the early days of nonlinear optics [9], the level of control over transition energies, dipole elements and symmetries has been minimal. The multiple resonance required for higher-order resonantly-enhanced nonlinear phenomena are particularly difficult to obtain at optical wavelengths. Furthermore, in contrast with most materials where the derivation of the linear and nonlinear optical response from first principles is often impractical, it is quite straightforward for quantum well intersubband transitions. As the potential profiles of quantum wells are controlled, subband wavefunctions and eigenenergies may be quite accurately calculated. Although the one-dimensional quantization of epitaxial growth does not generate a true band-gap because of the in-plane momentum, the near-zero photon momentum leads, within the single-band effective mass approximation, to optically discrete transitions (Figure 1.3). Due to resonant enhancement and the dipole sum rule, no more than a few of these transitions significantly contribute to any given process. Furthermore, when the effective mass is scalar, as in the case for the Γ-valley electrons used in most of the optical experiments involving intersubband transitions, the interaction becomes one-dimensional. The cumbersome tensorial expressions of the general nonlinear formalism are thus typically reduced to a single scalar term. As we have shown [10] the same resonant enhancement which simplifies the expressions for the nonlinear coefficients also limits their applicability to moderate power regimes; fortunately, it also simplifies other alternative nonperturbative solutions. This simple model remains accurate as long as the nonparabolicity over the extent of the electronic population is negligible compared to the homogeneous broadening mechanisms. For the rest of our treatment we consider this limit which emphasizes the fundamental differences between intersubband and interband optical phenomena. A further discussion of the accuracy of this model and the influence of nonhomogeneous broadening and nonparabolicity is included in section 5.4.

Intersubband optical transitions in quantum wells are also fundamentally different from interband ones [11] despite the fact that the latter are also controllable via bandgap engineering. The interband transitions have several major limitations - the foremost being the opposite signs of the conduction and valence bands effective masses. Except for the easily saturable excitonic processes, interband transitions are nondiscrete and have no sharp resonance. Furthermore the limitations of the available bandgap and band offsets make resonantly-enhanced harmonic generation difficult [12]. Another implication of the interband energy gap is that the lifetimes, typically between 10^{-6}s and 10^{-9}s, are many orders of magnitude larger than the dephasing time which is roughly 10^{-13}s. Subbands, which are not separated by a forbidden gap, have roughly the same dephasing times but much shorter lifetimes [13] ($\cong 10^{-12}$s), making higher-order coherent phenomena more accessible before the onset of saturation.

Another characteristic of intersubband transitions which is typically cited as one of their fundamental advantages over interband transitions is their large dipole matrix elements - proportional to the spatial extent of the envelope functions rather than the extent of the

Bloch functions. In fact, as noted by Khurgin et al. [14], the ratio of the dipole matrix element to the optical transition wavelength is not inherently larger for intersubband transitions than it is for interband ones. This ratio is the fundamental quantity determining the geometrical limitations of the standard treatment, such as the validity of the dipole approximation (section 5.6), and is also a useful measure for comparing intensity regimes. Furthermore, intersubband transitions bear no advantage over interband ones in terms of the total population or of the transition's broadening. It is therefore the resonant enhancement and the control over the dipole elements and their symmetry that makes intersubband transitions so unique.

5.3 Experimental Observation of Optical Nonlinearities

The potential of quantum well intersubband transition induced nonlinear optical phenomena was discussed by Gurnick and DeTemple [15] in 1983, two years before intersubband transitions were first observed by West and Eglash [1]. The resonantly-enhanced nonlinearities were first demonstrated by Fejer et al. [16] in 1989. By breaking the symmetry of an initially symmetric stack of GaAs/AlGaAs quantum wells with a 'dc'-electric field (Figure 5.1a), second-harmonic generation (SHG) was obtained for a 10.6μm pump CO_2 laser. The second-harmonic susceptibility measured: $\chi^{(2)}_{(2\omega,\omega,\omega)} \cong 2.8 \cdot 10^{-8}$ m/v, was 73 times larger than that of bulk GaAs at the same wavelength. Soon after, Rosencher et al. [17] reported a nonlinear optical rectification coefficient of $\chi^{(2)}_{(0,-\omega,\omega)} \cong 7.2 \cdot 10^{-7}$ m/v in compositionally asymmetric quantum wells. The structure was composed of 3nm GaAs wells adjacent to 6.5nm $Al_{0.2}Ga_{0.8}As$ steps, and 50nm $Al_{0.4}Ga_{0.6}As$ barriers (Figure 5.1b). The same structure [18] was also used for second-harmonic generation and a second-order susceptibility of $\chi^{(2)}_{(2\omega,\omega,\omega)} \cong 7.6\cdot 10^{-7}\text{m/v}$ was measured, 3 orders of magnitude larger than that of bulk GaAs. The quadratic behavior of the conversion efficiency up to pump intensities of 4.5kW/cm^2 was later verified [19] in a slightly modified structure. Higher conversion efficiencies ($\eta \cong 3\cdot 10^{-4}$) were obtained by Chen et al. [20] who used a multipass 45° interaction scheme to measure $\chi^{(2)}_{(2\omega,\omega,\omega)} \cong 9\cdot 10^{-7}\text{m/v}$. Sirtori et al. [21] later demonstrated second-harmonic generation in an asymmetric coupled AlInAs/GaInAs quantum well structure (Figure 5.1c), measuring $\chi^{(2)}_{(2\omega,\omega,\omega)} \cong 4.8\cdot 10^{-8}\text{m/v}$. This structure offers several advantages: the lower effective mass of GaInAs leads to larger optical dipole matrix elements for the same transition energy, the larger band offsets offer access to shorter wavelength, the use of a single well composition is less demanding on material growth, and the coupled structure is more favorable to tuning of the resonance. Stark tuning was indeed demonstrated [22] in these structures, where a 'dc'-electric field of 38kV/cm led to an increase from $\chi^{(2)}_{(2\omega,\omega,\omega)} \cong 3\cdot 10^{-8}\text{m/v}$ to $\chi^{(2)}_{(2\omega,\omega,\omega)} \cong 7.5\cdot 10^{-8}\text{m/v}$. A similar structure was later used [23] for generation of far-infrared ($\lambda \cong 60\mu\text{m}$) radiation by doubly-resonant difference frequency mixing of two mid-infrared ($\lambda \cong 10\mu\text{m}$) sources. A second-order susceptibility of $\chi^{(2)}_{(\omega_2-\omega_1,-\omega_1,\omega_2)} \approx 10^{-6}\text{m/v}$ was measured. Recently, Martinet et al. [24], demonstrated second-harmonic generation of 2.1 μm radiation using intersubband transitions in deep

$In_{0.6}GaAs/AlAs$ coupled wells grown with a strain relaxing layer on a GaAs substrate [25,26]. While the extension of intersubband capabilities to the near-infrared wavelengths [24-27] is one of the more promising new development in the field, careful attention must be paid, as discussed in section 5.4, to just how much of the "intersubband nature" of the transitions is maintained as the energy separation is increased.

We should note that although most of the experimental work has focused on optical transitions between subbands of the conduction band, the optical nonlinearities of valence band transitions have also been thoroughly analyzed [28,29,30]. Tsang and Chuang [28] predicted large second-order susceptibilities which are almost comparable to the conduction band ones. Li and Khurgin [29] calculate the off diagonal ($\chi^{(2)}_{xzx}$) susceptibility between heavy and light hole states. They find that this term, which is not subject to the regular selection rules and thus compatible with a surface emitting configuration [31], is comparable in magnitude to the conduction band's scalar ($\chi^{(2)}_{zzz}$) susceptibility. Although these transitions may not be treated within the single band model which we use in following treatment, the limits derived within it may serve as crude upper limits for the valence band nonlinearities.

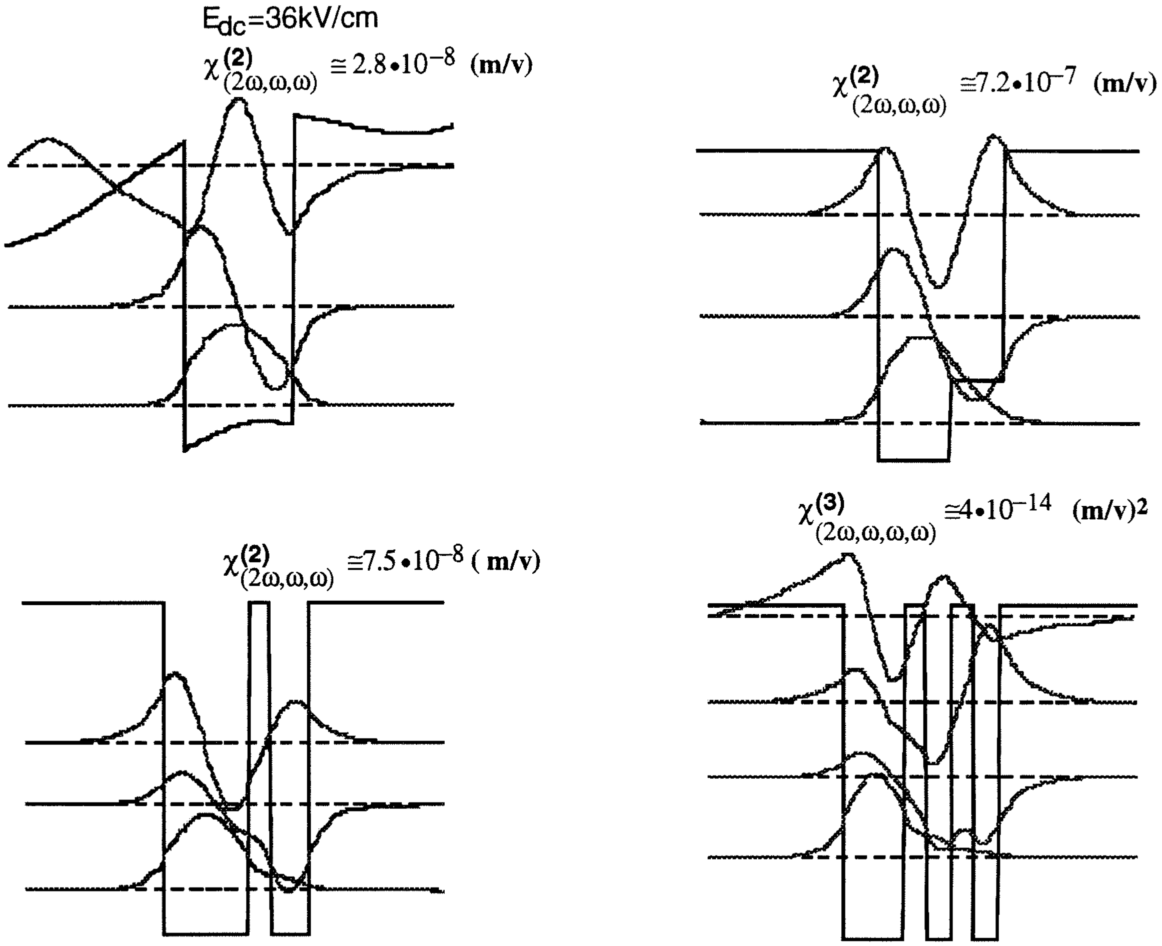

Figure 5.1 Some of the structures used for resonantly-enhanced harmonic generation via intersubband transitions in quantum wells. Figures a-c show structures used for second-harmonic generation: a GaAs quantum well with its symmetry broken by a 'dc' electric field (after reference 16), a step GaAs/AlGaAs quantum well (after reference 17), and coupled asymmetric quantum wells (after reference 21). The triple asymmetric coupled wells (d) were used for resonantly-enhanced third-harmonic generation (after reference 33).

Quantum well design was also used to lead to resonant enhancement of higher-order nonlinear phenomena. Walrod et al. [32] used nearly-degenerate four-wave mixing to observe resonant enhancement of third-order nonlinearities in AlGaAs/GaAs superlattices and measure $\chi^{(3)}_{(\omega,\omega,-\omega,\omega)} \cong 5.6\cdot 10^{-13}(\mathrm{m/v})^2$. Sirtori et al. [33] extended the coupled well concept to third harmonic generation (Figure 5.1d) and measured

$\chi^{(3)}_{(3\omega,\omega,\omega,\omega)} \cong 1\cdot 10^{-14}(\mathrm{m/v})^2$. This was later improved [34], at low temperatures (30K), to $\chi^{(3)}_{(3\omega,\omega,\omega,\omega)} \cong 4\cdot 10^{-14}(\mathrm{m/v})^2$ - the highest reported third-order susceptibility of any material to date. This result is due to the unique control over the energy levels and optical dipole matrix elements of quantum well subbands. A similar coupled-well structure was also used to demonstrate a large multi-photon ionization [35]. Overcoming growth complexity, resonantly-enhanced harmonic generation via intersubband transitions should be extendible to even higher orders. The limits on this will be the ratio of the finite barrier height to the transition's width, the breakdown of the single band model, and as we later show, saturation.

5.4 The Single Band Model

The limitations of the various semiconductor material models for the description of electronic states in semiconductors is an issue of great complexity that is beyond the scope of this chapter. We will therefore only highlight the relevance of some of the limitations of the single band model to the nonlinear optical response of intersubband transitions. As we go on to discuss the limitations of the optical treatment it will be important to remember the finite accuracy of the material's description itself.

The standard method for derivation of electronic states in quantum wells is the **k·p** approach [2] which is an expansion of the quantum well states over a finite base of the bulk material's states. Unlike the tight-binding [36,37] and the pseudo-potential methods [38], the **k·p** approach, at least in its standard form, is limited to the vicinity of the crystal's high symmetry points (Γ, X, L). Nevertheless, it gives an intuitive description of states near the bottom of the energy bands that is sufficiently accurate for most purposes. It is valid for almost all heterostructures of current interest and may need to be questioned only for high energy states in systems with very large conduction band offsets [24-27]. For low lying states in the conduction band of large bandgap materials, the analysis may be further simplified by reducing the **k·p** approach to a single band model. A single parabolic band model was indeed shown to be effective in analyzing the most common intersubband processes - those in the conduction band of $GaAs/Al_xGa_{1-x}As$ quantum wells with a maximum conduction band offset of roughly 0.3V ($x \leq 40\%$). For narrower wells with sufficiently high barriers or for materials with smaller bandgaps, band coupling begins to play a more significant role and deviations from the parabolic model are expected.

One possibility of somewhat extending the single band model without a great increase in complexity is by the use of an energy dependent effective mass [39,40] accounting for the nonparabolicity of the energy-momentum dispersion relation [41] discussed in Chapter 2.6. Sirtori et al. [42] recently showed that for energies up to 0.5V above the conduction band edge the single-band model with a nonparabolic effective mass is still a reasonable approximation. At higher energies profound modifications of the nature of the intersubband transitions are expected due to band coupling. Most markedly, there will be a breakdown of the polarization selection rules as the conduction and valence band states mix [27]. Since different subbands no longer have identical effective masses the optical transitions are no longer discrete. Furthermore, the dipole element to wavelength ratio is roughly constant [14]. Hence as the energies of intersubband transitions approach those of interband ones so does the magnitude of their dipole elements. For such transitions [24-27], not only the single-band model, but the **k·p** treatment itself may become invalid due to inter-valley coupling. In that case the high-energy intersubband transitions essentially lose most of their distinction from interband ones.

Besides the approximations involved in the **k·p** and single band models some other material issues, such as: strain [43], surface roughness [44], growth asymmetry of the interfaces [45] and donor segregation [46] need to be considered. The latter two effects induce some asymmetry which should be considered when analyzing the significance of symmetry breaking effects induced by the optical interaction itself [47,48]. For the remainder of this thesis we will use the single band model to highlight the fundamental issues of the resonantly-enhanced intersubband transitions without masking them in undue mathematical complexity. The limitations derived here are not only directly applicable to the vast majority of intersubband transitions under study, but are also easily extended to situations where a more complex band structure needs to be taken into account.

5.5 Many-Body Effects

At the high doping levels typically used ($\sigma \cong 10^{12}\mathrm{cm}^{-2}$) for optical studies of intersubband transitions, [16-24] many body effects may become significant. Several different methods have been used to estimate the contribution of these effects leading to varying conclusions [49,50,51,52,53]. It is clear, however, that many-body effects shift the subbands on the order of 10 meV to 20meV and may play a significant role in the linear and nonlinear optical interactions of intersubband devices. Khurgin and Li have shown [54] that at the typical doping levels used for intersubband transitions there is a large Coulombic enhancement of intersubband nonlinearities in asymmetric quantum wells. Zaluzny [55] later showed that even for symmetric wells the indirect many-body effects will lead to a large coulombic enhancement. A self consistent calculation of intersubband transition energies in doped quantum wells [56] shows that saturation in asymmetric quantum wells, redistributing the population between the subbands, may shift the transition energies by more than a linewidth. Thus, it should be included in detuning considerations. This large shift may also lead to bistability as was pointed out by Newson and Kurobe [57].

Whereas for nonsaturating optical interactions many-body effects may be regarded as a constant correction to the resonance frequency, they become important at high optical intensities. A nonuniform optical intensity along the optical path will lead to a varying amount of saturation, i.e. of subband populations. This will, in turn, lead to varying subband energies and hence, in a simplistic picture, to a varying detuning of the optical frequency from resonance along its propagation path. The varying detuning will, for example, make it difficult to compensate for the transition induced phase-mismatch, and hence limit harmonic generation processes (Chapter 9). Many-body effects also limit the accuracy of intersubband lifetime estimates based on pump-only saturation experiments [58,59]. Although many-body effects are only indirectly included in our treatment via the phenomenological relaxation times, they must be taken into account in any experiment involving a combination of high electron densities and optical fields that saturate the transitions.

It is also important to notice that the absorption frequencies observed in optical experiments are not directly determined by the intersubband separation energy. They may be significantly shifted by the effects of screening in accordance with the coupling scheme used. The screening correction within the Hartree approximation is termed the depolarization effect and the correction due to the exchange-correlation terms is called exciton-like or the final-state interaction. Both these shifts have been estimated for intersubband transitions by Bloss [52] using the formalism of Ando [44]. For 85A° quantum wells n-doped $1\times10^{12}cm^{-2}$, the depolarization shift was found to increase the transition energy by 8meV and the exciton correction was found to offset this by 2meV. Somewhat larger shifts were measured by Pinczuk et al. [49] using inelastic-light-scattering measurements.

5.6 The Dipole Approximation

The interaction Hamiltonian of a single electron with an electromagnetic field is given within the single band effective mass model as [2]:

$$H(z,t) = \frac{1}{2m^*(z)}[P - qA(z,t)]^2 + V(z) - \frac{q}{m^*(z)} S \cdot B(z,t) \tag{5.1}$$

where m*(z) is the effective mass, V(z) the unperturbed quantum well potential assumed to vary only along the growth direction z, and the vector potential of a plane monochromatic wave is given as:

$$A(r_{\|},t) = A_0 \hat{e}_{\perp} e^{i(kr_{\|} - \omega t)} + A_0^* \hat{e}_{\perp} e^{-i(kr_{\|} - \omega t)} \tag{5.2}$$

The electric and magnetic fields are:

$$E(r,t) = -\frac{\partial}{\partial t} A(r,t) \tag{5.3}$$

and:

$$B(r,t) = \nabla \times A(r,t) \tag{5.4}$$

respectively.

With intersubband magnetic transitions forbidden by selection rules, the Hamiltonian may be divided into the unperturbed quantum well Hamiltonian:

$$H_o(z) = \frac{P^2}{2m^*(z)} + V(z) \tag{5.5}$$

and the interaction Hamiltonian:

$$H_I(r,t) = -\frac{q}{m^*(z)} P \cdot A(r,t) + \frac{q^2}{2m^*(z)} A^2(r,t) \tag{5.6}$$

The two approximations necessary to reduce this interaction Hamiltonian to the dipole interaction: the neglect of the second-order term in A(r,t) and the dipole approximation are examined below.

5.6.1 *The A^2 Interaction*

The matrix element of the A^2 term between an initial state ψ_i and a final state ψ_f is obtained from Equation 5.2 as:

$$W_{A^2} \equiv \left\langle \psi_f \left| \frac{q^2 A_0{}^2}{m^*(z)} [1 + \cos(2k \cdot r_\parallel - 2\omega t)] \right| \psi_i \right\rangle \tag{5.7}$$

Expanding in orders of $k \cdot r_\parallel$ this becomes:

$$W_{A^2} \cong \frac{q^2 A_0{}^2}{m^*(z)} \{ \langle \psi_f | 1 + \cos(2\omega t) | \psi_i \rangle + \langle \psi_f | 2(k \cdot r_\parallel) \cdot \sin(2\omega t) | \psi_i \rangle + \ldots \} \tag{5.8}$$

The first term on the R.H.S, which is the zero'th order in $k \cdot r_\parallel$, leads to a constant energy shift of all levels and therefore induces no transitions. Only the next-order term, essentially the quadrapole term of the A^2 interaction, may lead to transitions. These will be characterized by two distinct features: they will be two-photon transitions between odd parity states, and the selection rule will be modified to optical waves propagating in the growth direction rather than polarized along it. The magnitude of these potentially novel effects is however too small to make them of any practical interest.

5.6.2 *The Linear Interaction*

The linear term in the interaction Hamiltonian (Equation 5.6) is:

$$W_A = -\left\langle \psi_f \left| \frac{q}{m^*(z)} A_0 P_\perp \cos(k \cdot r_\parallel - \omega t) \right| \psi_i \right\rangle \tag{5.9}$$

For $k \cdot r_\parallel \ll 1$ the cosine may be expended as a power series, with the zero'th order term leading to the dipole interaction:

$$W_{DE} = -\left\langle \psi_f \left| \frac{q}{m^*(z)} A_0 P_\perp \cos(\omega t) \right| \psi_i \right\rangle \tag{5.10}$$

and the first-order term leading to the quadrapole interaction:

$$W_{QE} = -\left\langle \psi_f \left| k \cdot r_\parallel \frac{q}{m^*(z)} A_0 P_\perp \sin(\omega t) \right| \psi_i \right\rangle \tag{5.11}$$

With simple manipulations, making use of the momentum-space commutation relations, the dipole term may be rewritten as:

$$W_{DE} = qE_0 \langle \psi_f | r_\perp | \psi_i \rangle (i \frac{\omega_{fi}}{\omega}) \sin(\omega t) \tag{5.12}$$

identical to the standard dipole term to within a choice of gauge [60]. The quadrapole term similarly becomes:

$$W_{QE} = -\frac{qE_0}{2} k_\parallel \langle \psi_f | r_\parallel \cdot r_\perp | \psi_i \rangle (i \frac{\omega_{fi}}{\omega}) \cos(\omega t) \tag{5.13}$$

Within the single band model both final and initial states are given by an envelope function with a z dependence only, multiplied by the same Bloch state (S>). We thus see that the only non-zero terms for radiation propagating at an angle σ with the growth direction will be:

$$W_{DE} \propto \langle \psi_f(z) | z | \psi_i(z) \rangle \cdot \sin(\sigma) \tag{5.14}$$

for the dipole interaction, and:

$$W_{QE} \propto \langle \psi_f(z) | z^2 | \psi_i(z) \rangle \cdot \sin(2\sigma) \tag{5.15}$$

for the quadrapole interaction. The ratio of the quadrapole to the dipole interaction strengths is hence:

$$\left| \frac{W_{QE}}{W_{DE}} \right| = \frac{\pi}{\lambda} \frac{\langle \psi_f(z) | z^2 | \psi_i(z) \rangle}{\langle \psi_f(z) | z | \psi_i(z) \rangle} \cdot \cos(\sigma) \tag{5.16}$$

The contribution of the quadrapole term relative to that of the dipole term is thus roughly proportional to the dipole matrix element to wavelength ratio; a ratio that was shown by Khurgin [14] not to be inherently greater for intersubband transitions than for interband ones. Therefore the quadrapole contribution to intersubband transition is not inherently large. It may nevertheless be of some interest because of the resonant enhancement and the selection rules. The dipole element between even parity states is identically zero, forbidding the ground to second state transition (0→2) in symmetric structures. The quadrapole term on the other hand, is maximized between even parity states, allowing for second-harmonic generation [48] despite the symmetry. For the one-dimensional envelope functions of subbands in direct gap quantum wells the quadrapole interaction term also has a different geometrical selection rule. The requirement for components of both the propagation and of the polarization vector along the quantization direction (Equation 5.13) maximizes the interaction for propagation at an angle of 45° with respect to the quantum well planes. For such a propagation scheme (Figure 3.1a) the quadrapole interaction may lead to second-harmonic generation via intersubband transitions in symmetric quantum wells.

Quadrapole induced second-harmonic generation in centrosymmetric materials has indeed been observed [61] as early as 1962, and analyzed more recently for intersubband transitions [47]. It is of limited importance for intersubband transitions because the quadrapole contribution is not particularly large and because the quantum wells may be designed to be asymmetric, making all dipole transitions allowed. Actually, growth asymmetry [62] in quantum wells is difficult to avoid. In reference [16] the second-harmonic generation coefficient in nominally symmetric structures was found to have a minimum for an applied ‘dc’-bias of 3V - indicating a large built-in asymmetry. As a footnote it is worth noting that since the wavefunctions in quantum wells are quite accurately known, the full interaction Hamiltonian (Equation 5.9) may be evaluated in a straightforward fashion and there is no real need for either the dipole or the quadrapole approximation.

5.7 The Slowly Varying Envelope Approximation

Due to the resonant-enhancement and high density of states the extinction length induced by intersubband transitions in quantum wells often becomes comparable to the optical wavelength. This calls into question both the slowly varying envelope approximation (SVA), and the standard relations between the susceptibility and the absorption and dispersion coefficients (Equations 3.2a and 3.2b). The simplest means of examining these approximations is by considering the propagation of an infinite plane wave in a linear and homogenous media. Although both approximations may be trivially avoided for this case, it clarifies the limitations upon their use for situations involving nonlinear processes as well. The latter, however, would require more complex solutions.

Beginning with Maxwell's equations for an infinite plane wave in a linear and homogenous media, the second-order wave equation is derived without approximation as:

$$\nabla^2 E(z) = \mu_0 \frac{\partial^2}{\partial t^2} D(z) \tag{5.17}$$

with the displacement vector given by:

$$D = \varepsilon_0 E \cdot [n^2 + \chi' + i\chi''] \tag{5.18}$$

Defining the solution in the form of:

$$E(z) = \tilde{E}(z) \cdot e^{ikz} \tag{5.19}$$

and inserting it into Equation 5.17 we obtain:

$$\tilde{E}''(z) + 2ik\tilde{E}'(z) - k^2\tilde{E}(z) = -\frac{\omega^2}{c^2}\{n^2 + \chi' + i\chi''\}\tilde{E}(z) \tag{5.20}$$

Since we have assumed a linear and homogeneous media, a simple solution can be found by assuming: $\tilde{E}(z) = \tilde{E}(0)$ which directly leads to the expression:

$$E(z) = E(0) \cdot e^{-i(\frac{\omega}{c}\sqrt{n^2+\chi'+i\chi''})z} = E(0) \cdot e^{-i(\frac{2\pi}{\lambda}\sqrt{n^2+\chi'+i\chi''})z} \tag{5.21}$$

derived without any approximation. If, on the other hand, we define k as the bulk value of the propagation vector (k=ωn/c) we obtain:

$$\tilde{E}'(z) + \frac{c}{2i\omega n}\tilde{E}''(z) = -\frac{\omega}{2nc}\{i\chi' - \chi''\}\tilde{E}(z) \tag{5.22}$$

Making the slowly varying envelope approximation:

$$\frac{\partial^2 \tilde{E}}{\partial z^2} << k\frac{\partial \tilde{E}}{\partial z} \tag{5.23}$$

then leads to:

$$E(z) = E(0)\cdot e^{-\frac{2\pi}{n\lambda}(\frac{\chi''}{2})z} \cdot e^{i\frac{2\pi}{\lambda}(n+\frac{\chi'}{2n})z} \equiv E(0)\cdot e^{-\alpha z}\cdot e^{i\frac{2\pi}{\lambda}(n+\Delta n)z} \tag{5.24}$$

Although the SVA could have easily been avoided in this case, the difference between the solution obtained with (Equation 5.24) and without (Equation 5.21) the approximation allows us to estimate the magnitude of the correction required in situations where it is more difficult to avoid. Treating the intersubband contribution to the induced polarization (χ'+iχ'') as a perturbation upon the bulk's response (n), the square root in the exponential of the accurate solution (Equation 5.21) may be expanded as the power series:

$$E(z) = E(0)\cdot e^{-\frac{2\pi}{n\lambda}(\frac{\chi''}{2})z} \cdot e^{i\frac{2\pi}{\lambda}(n+\frac{\chi'}{2n})z} \cdot e^{-i\frac{\pi}{4n^3\lambda}[(\chi')^2-(\chi'')^2+2i\chi'\chi'']z} \cdot\ldots \tag{5.25}$$

The first two exponential terms of this series are:

$$\alpha\equiv\pi\chi''/n\lambda \tag{5.26a}$$

and:

$$n'\equiv n+\chi'/2n\equiv n+\Delta n \tag{5.26b}$$

the familiar (approximate) definitions [63] for the absorption and the refractive index induced by the transitions respectively. Keeping only these first two terms in the expansion, Equation 5.25 corresponds exactly to Equation 5.24. Solving the wave equation with the SVA thus amounts to an equivalent approximation to those made in the definitions of the linear coefficients in Equation 5.26, i.e., keeping only first-order terms in the expansion in powers of χ/n^2.

The next-order terms in Equation 5.25 give us the magnitude of the correction to the SVA. Treating a line center frequency for simplicity (χ'=0), the power of the third term in the exponential reduces to:

$$-i\frac{\pi z}{4n^3\lambda}[(\chi')^2-(\chi'')^2+2i\chi'\chi'']\cong\frac{-i}{4\pi n}(\alpha\lambda)(\alpha z) \tag{5.27}$$

Since the interaction length in nonlinear devices is on the order of the extinction-length ($z\cong 1/\alpha$), and since absorption coefficients as high as one over the wavelength ($\alpha\lambda\cong 1$) are easily obtained in quantum well intersubband transitions, the correction can be quite significant - on the order of a few percent. Although not negligible, this correction is difficult to observe in linear interactions due to the finite accuracy with which the transition parameters are known. On the other hand if the theoretically predicted [64] intersubband absorption coefficients are approached, the SVA will become completely invalid ($\alpha\lambda \approx \pi n \Rightarrow \chi'' \approx n^2$). An accurate treatment of intersubband transitions in highly doped quantum wells thus falls neither in the dielectric ($\alpha\lambda \ll \pi n$) nor in the metallic [65] ($\alpha\lambda \gg \pi n$) regimes.

Avoiding the SVA and obtaining accurate expressions for the absorption and dispersion in terms of the susceptibility is trivial for linear interactions - the square root in the exponential of Equation 5.21 may be directly divided into its real and complex components, corresponding to the phase delay and absorption, respectively. The problem is not straightforward however for nonlinear interactions and a coupled-mode analysis may be in order. The large index change on a wavelength scale distance may cause the generation of a back-propagating beam. An alternative way of viewing this phenomena is that when significant frequency conversion takes place on a wavelength-scale distance, the phase-matching conditions are sufficiently relaxed so they may be met by the backward propagating wave as well. Although the shortcomings of the slowly-varying envelope approximation and the standard expressions for the absorption and refractive index corrections (Equation 5.26) have not played significant roles in our experimental results to date, they may do so as volumetric densities of the doping are further raised to increase the interaction strength.

References:

---

[1] L. C. West, and S. J. Eglash, "1st observation of an extremely large-dipole transition within the conduction band of a GaAs quantum well," *Appl. Phys. Lett.*, **46**, 1156, 1985.

[2] G. Bastard, *Wave Mechanics Applied to Semiconductor Heterostructures*, ch. III, Paris, France: Les Editions de Physique, Les Ulis Cedex, 1988.

[3] D. L. Smith, and C. Mailhiot, "Theory of semiconductor superlattice electronic structure," *Rev. Mod. Phys.*, **62**, 173, 1990.

[4] Bloembergen N., *Nonlinear Optics*, Addison-Wesley Publishing, Co., Inc., 1992.

[5] A. Yariv, *Quantum Electronics*, New-York: John Wiley & Sons, 1988.

[6] Boyd. R. W, *Nonlinear Optics*, San-Diego, California: Academic Press Inc., 1992.

[7] R. Dingle, W. Wiegmann, and C. H. Henry, "Quantum states in confined carriers in very thin $Al_xGa_{1-x}As/GaAs/Al_xGa_{1-x}As$ heterostructures," *Phys. Rev. Lett.*, **33**, 827, 1974.

[8] J. Faist, F. Capasso, D. L. Sivco, C. Sirtori, A. L. Hutchinson and, A. Y. Cho, "Quantum cascade laser - An intersubband semiconductor-laser operating above liquid-nitrogen temperature," *Electron. Lett.*, **30**, 1360, 1994.

[9] C. M. Kellington, "Resonant harmonic Generation in Ruby," *Phys. Rev. Lett.*, **9**, 57 1962.

[10] G. Almogy, and A. Yariv, "Resonantly-enhanced nonlinear optics of intersubband transitions," *J. of Nonlinear Opt. Phys. Mat.*, in press.

[11] D. S. Chemla, D. A. B. Miller, and P. W. Smith, *Semiconductors and Semimetals*, R. Dingle, Ed., New-York: Academic Press Inc., 1987, **24**, ch. 5.

[12] S. Scandolo, A. Baldereschi, and F. Capasso, "Interband near-infrared second-harmonic generation with very large $|\chi^{(2)}(2\omega)|$ in AlSb/GaSb-InAsSb/AlSb asymmetric quantum wells," *Appl. Phys. Lett.*, **62,** 3138, 1993.

[13] J. Faist, C. Sirtori, F. Capasso, L. Pfeiffer, and K. W. West, "Phonon limited intersubband lifetimes and linewidths in a two-dimensional electron gas," *Appl. Phys. Lett.* **64**, 872, 1994.

[14] J. Khurgin "Comparative analysis of the intersubband versus band-to-band transitions in quantum wells," *Appl. Phys. Lett.*, **62**, 1390, 1993.

[15] M. K. Gurnick, and T. A. DeTemple, "Synthetic nonlinear semiconductors," *IEEE J. Quantum Electron.*, **QE-19**, 791, 1983.

---

[16] M. M. Fejer, S. J. B. Yoo, R. L. Byer, A. Harwit, and J. S. Harris, Jr., "Observation of extremely large quadratic susceptibility at 9.6-10.8 mm in electric-field -biased AlGaAs quantum wells," *Phys. Rev. Lett.*, **62**, 1041, 1989.

[17] E. Rosencher, P. Bois, J. Nagle, E. Costard, and S. Delaitre, “Observation of nonlinear optical rectification at 10.6μm in compositionally asymmetrical AlGaAs multiquantum wells,” *Appl. Phys. Lett.*, **55,** 1597, 1989.

[18] E. Rosencher, P. Bois, J. Nagle, and S. Delaitre, “Second-harmonic generation by intersubband transitions in compositionally asymmetrical MQWs,” *Electron. Lett.*, **25**, 1063, 1989.

[19] P. Boucaud, F. H. Julien, D. D. Yang, J-M. Lourtoiz, E. Rosencher, P. Bois, and J. Nagle, "Detailed analysis of second-harmonic generation near 10.6μm in GaAs/AlGaAs asymmetric quantum wells," *Appl. Phys. Lett.*, **57,** 215, 1990.

[20] Z. Chen, D. Cui, M. Li, C. Jiang, J. Zhou, and G. Yang, "High conversion efficiency of second-harmonic generation in step quantum wells," *Appl. Phys. Lett.*, **61,** 2401, 1992.

[21] C. Sirtori, F. Capasso, D. L. Sivco, S. N. G. Chu, and A. Y. Cho, "Observation of large second-order susceptibility via intersubband transitions at λ≅10μm in asymmetric coupled AlInAs/GaInAs quantum wells," *Appl. Phys. Lett.*, **59,** 2302, 1991.

[22] C. Sirtori, F. Capasso, D. L. Sivco, A. L. Hutchinson, and A. Y. Cho, "Resonant Stark tuning of second-order susceptibility in coupled quantum wells," *Appl. Phys. Lett.*, **60**, 151, 1992.

[23] C. Sirtori, F. Capasso, J. Faist, L. N. Pfeiffer, and K. W. West, "Far-infrared generation by doubly-resonant difference frequency mixing in a coupled well two-dimensional electron gas system," *Appl. Phys. Lett.*, **65,** 445, 1994.

[24] E. L. Martinet, G. L. Woods, H. C. Chui, J. S. Harris, Jr., M. M. Fejer, C. A. Bella, and B. A. Richman, "Free-electron laser nonlinear spectroscopy of doubly resonant (5.5-3.0 μm and 4.1-2.1 μm) InGaAs/AlGaAs asymmetric quantum wells," 1994 SPIE OE/LASE proc., *Quantum well and superlattice physics*, vol. 2139.

[25] H. C. Chui, S. M. Lord, E. Martinet, M. M. Fejer, and J. S. Harris, Jr., "Intersubband transitions in high indium content InGaAs/AlGaAs quantum wells," *Appl. Phys. Lett.*, **63**, 364, 1993.

[26] S. M. Lord, B. Pezeshki, J. S. Harris, Jr., "Investigation of high In content InGaAs quantum wells grown on GaAs by molecular beam epitaxy," *Electron. Lett.*, **28**, 1193, 1992.

[27] L. H. Peng, J. H. Smet, T. P. E. Broekaert, and C. G. Fonstad, "Transverse electric and transverse magnetic polarization active intersubband transitions in narrow InGaAs quantum wells," *Appl. Phys. Lett.*, **61**, 2078, 1992.

[28] L. Tsang, and S. L. Chuang, "Second-harmonic generation and optical rectification using intersubband transitions in biased p-type semiconductor quantum wells," *Appl. Phys. Lett.*, **60,** 2543, 1992.

[29] S. Li, and J. Khurgin, "Second order optical susceptibility in p-doped asymmetric quantum wells," *Appl. Phys. Lett.*, **62,** 1390, 1993.

[30] X. H. Qu, and H. Rudda, “Second-harmonic generation using heavy-hole/light-hole intersubband transitions in asymmetric quantum wells,” *Appl. Phys. Lett.*, **62,** 1946, 1993.

[31] D. Vakhshoori, M. C. Wu, and S. Wang, “Surface-emitting second-harmonic generator for waveguide study,” *Appl. Phys. Lett.*, **60**, 1277, 1992.

[32] D. Walrod, S. Y. Auyang, P. A. Wolf, and M. Sugimoto, “Observation of third-order optical nonlinearity due to intersubband transitions in AlGaAs/GaAs superlattices,” *Appl. Phys. Lett.*, **59**, 2392, 1991.

[33] C. Sirtori, F. Capasso, D. L. Sivco, and A. Y. Cho, "Giant, triply resonant, third-order nonlinear susceptibility $\chi^{(3)}_{3\omega}$ in coupled quantum wells," *Phys. Rev. Lett.*, **68,** 1010, 1992.

[34] F. Capasso, C. Sirtori ,and A. Y. Cho, "Coupled quantum well semiconductors with giant electric field tunable nonlinear optical properties in the infrared," *IEEE J. Quantum Electron.*, **QE-30,** 1313, 1994.

[35] C. Sirtori, F. Capasso, D. L. Sivco, and A. Y. Cho, "Resonant multiphoton electron emission from a quantum well," *Appl. Phys. Lett.*, **60,** 2678, 1992.

[36] J. N. Schulman, and Y-C. Chang, “Reduced Hamiltonian method for solving tight-binding model of interfaces,” *Phys. Rev. B*, **27,** 2346, 1983.

[37] M. F. H. Schuurmans, and G. W. ‘t Hooft, “Simple calculations of confinement states in a quantum well,” *Phys. rev. B*, **31**, 8041, 1985.

[38] M. Jaros, “Microscopic phenomena in ordered superlattices,” in *Strained-Layer Superlattices: Physics*, T. P. Pearsall, Ed., *Semiconductors and Semimetals*, San-Diego, California: Academic Press Inc., 1992, **32**, ch. 5, and references therein.

[39] U. Ekenberg, "Nonparobolicity effects in a quantum well: Sublevel shift, parallel mass, and Landau levels," *Phys. Rev. B*, **40,** 7714, 1989.

[40] W. Chen, and T. G. Andersson, “Effect of the nonparabolic mass on the electron confinement in arbitrarily shaped quantum wells,” *Phys. rev. B*, **44**, 9068, 1991.

[41] U. Rossler, “Nonparobolicity and warping in the conduction band of GaAs,” *Solid. St. Com.,* **49,** 943, 1984.

[42] C. Sirtori, F. Capasso, J. Faist, and S. Scandolo, “Nonparabolicity and a sum rule associated with bound-to-bound and bound-to-continuum intersubband transitions in quantum wells,” *Phys. Rev. B*, **50**, 8663, 1994.

[43] E. P. O’Reillly, “Valence band structure and optical gain of GaAs-AlGaAs quantum wells,” *Semicond. Sci. Technol.*, **4**, 904, 1989.

[44] T. Ando, A. B. Fowler, and F. Stern, “Electronic properties of two-dimensional systems,” *Rev. Mod. Phys.*, **54**, 437, 1982.

[45] L. Pfeiffer, E. F. Schubert, K. W. West, and C. W. Magee, “SI dopant migration and the AlGaAs/GaAs inverted interface,” *Appl. Phys. Lett.*, **58,** 2258, 1991.

[46] H. C. Liu, Z. R. Wasilewski, M. Buchanan, and H. Chu, “Segregation of Si δ doping in GaAs-AlGaAs quantum wells and the cause of the asymmetry in the current-voltage characteristics of intersubband infrared detectors,” *Appl. Phys. Lett.*, **63,** 761, 1993.

[47] A. Sa'ar, "On the question of intersubband electric quadrapole transitions in quantum well structures, " *J. Appl. Phys.*, **74**, 5263, 1993.

[48] See page 142 of reference 4.

[49] A. Pinczuk, S. Schmitt-Rink, G. Danan, J. P. Valladares, L. N. Pfeiffer, and K. W. West, “Large exchange interaction in the electron gas of GaAs quantum well,” *Phys. Rev. Lett.,* **63**, 1633, 1989.

[50] S. L. Chuang, M. S. C. Luo, S. Schmitt-Rink, and A. Pinczuk, “Many-body effects on intersubband transitions in semiconductor quantum-well structures,” *Phys. Rev. B*, **46,** 1897, 1992.

[51] K. M. S. Bandara, D. D. Coon, O. Byungsung, Y. F. Lin, and H. Francombe, “Exchange interactions in quantum well subbands,” *Appl. Phys. Lett.*, **53**, 1931, 1988.

[52] W. L. Bloss, “Effects of Hartree, exchange, and correlation energy on intersubband transitions,” *J. Appl. Phys.*, **66**, 3639, 1989.

[53] P. Von Allmen, “Electron-electron interaction and intersubband absorption coefficient in a GaAs/$Al_xGa_{1-x}As$ quantum well,” *Phys. Rev. B,* **46**, 13351, 1992.

[54] J. Khurgin, “Coulombic enhancement of ultrafast nonlinearities in quantum-well structures,” *J. Opt. Soc. B*, **9,** 157, 1992.

[55] M. Zaluzny, “Coulomb enhancement of the 3rd-order optical nonlinearities in quantum wells,” *Appl. Phys. Lett.*, **61,** 2509, 1992.

[56] A. Tong, G. Almogy, and A. Yariv, “Self-consistent calculation of quantum wells with voltage boundary conditions,” unpublished.

[57] D. J. Newson, and A. Karobe, “Possibility of optical bistability due to resonant intersubband excitation in stepped modulation-doped quantum wells,” *Appl. Phys. Lett.* **51**, 1670, 1987.

[58] F. H. Julien, J-M. Lourtoiz, N. Herschkorn, D. Delacourt, J. P. Pocholle, M. Papuchon, R. Planel, and G. Le Roux, "Optical saturation of intersubband absorption in GaAs-$Al_xGa_{1-x}As$ quantum wells," *Appl. Phys. Lett.*, **53,** 116, 1988.

[59] D. Cui, Z. Chen, S. Pan, H. Lu, and G. Yang, "Absorption saturation of optical transitions in GaAs/$Al_xGa_{1-x}As$ multiple quantum wells," *Phys. Rev. B,* **47,** 6755, 1993.

[60] C. Cohen-Tannoudji, B. Diu, F. Laloe, *Quantum Mechanics*, Paris, France: Hermann, 1977, vol. 2, ch. A_{XIII}.

[61] R. W. Terhune, P. Maker, and C. M. Savange, “Optical harmonic generation in calcite,” *Phys. Rev. Lett.*, **8**, 404, 1962.

[62] P. M. Young, and E. Ehrenreich, “Evidence for quantum well asymmetry in optical absorption,” *Appl. Phys. Lett.,* **61,** 1069, 1992.

[63] A. Yariv, *Quantum Electronics,* New-York: John Wiley & Sons, 1988, ch. 8.

[64] K. J. Khun, G. U. Iyengar, and S. Yee, "Free carrier induced changes in the absorption and refractive index for intersubband optical transitions in $Al_xGa_{1-x}As$/GaAs/$Al_xGa_{1-x}As$ quantum wells," *J. Appl. Phys.*, **70**, 5010, 1991.

[65] M. Born and E. Wolf, *Principles of Optics*, 6th ed., New-York: Pergamon Press, 1989, ch. XIII.

Chapter 6

Resonantly - Enhanced Optical Interaction

6.1 Introduction

In this chapter we develop a formalism for the nonlinear response of resonantly-enhanced optical interactions. After presenting the general density matrix formalism in section 6.1, we limit it to a single optical frequency and its multiples in section 6.2. This results in a treatment which is valid for optical self-modulation and all orders of harmonic generation. Attempts to write a more general formalism which includes all other nonlinear processes as well, equivalent to the perturbative one, lead to extremely cumbersome results which are best avoided with a rederivation of the formalism for each specific case of interest. In sections 6.3 and 6.4, respectively, we examine the limitations of the rotating-wave approximation and use it to reduce the optical Bloch equations to their algebraic form. This formalism is then used in Chapter 7 to study all-optical modulation and in Chapter 9 to study second-harmonic generation.

6.2 Density Matrix Formulation

Within the single band model (Chapter 5.4) and the dipole approximation (Chapter 5.6), the semi-classical Hamiltonian for a single electron in a quantum well interacting with a monochromatic electric field is reduced to:

$$H = H_0(z) + H_{DE}(z,t) + H_r \tag{6.1}$$

where:

$$H_0(z) = \frac{p^2}{2m^*(z)} + V(z) \tag{6.2}$$

is the unperturbed quantum well's effective mass Hamiltonian, and $H_{DE}=-qzE$ is the dipole interaction Hamiltonian. At this stage we consider many body effects (Chapter 5.5) only through their average contribution to the relaxation, which we denote by the phenomenological relaxation Hamiltonian $\mathrm{H_r}$. The Heisenberg equation of motion:

$$\dot{\rho} = [\mathrm{H}, \rho]/i\hbar \tag{6.3}$$

is used to find the temporal behavior of the density matrix, which in turn will be used to derive the induced polarization:

$$\vec{P} = qNTr(\rho\mu). \tag{6.4}$$

where N is the total subband population. The expectation values of the density matrix elements are defined over the base of the unperturbed quantum well's wavefunctions (ψ_i) as:

$$\rho_{ij} \equiv \langle \psi_i | \rho | \psi_j \rangle \tag{6.5}$$

and the optical dipole matrix elements as:

$$\mu_{ij} \equiv \langle \psi_i | \mu | \psi_j \rangle . \tag{6.6}$$

Writing Equation 6.3 for the complete set of eigenstates, we obtain an infinite set of coupled first-order differential equations for the density matrix elements as:

$$\dot{\rho}_{jk} = \frac{-i}{\hbar} \{ (E_j - E_k) \rho_{jk} - qE(\mu_{jl}\rho_{lk} - \rho_{jl}\mu_{lk}) - i\hbar \frac{(\rho_{jk} - \rho^e_{jk})}{T_{jk}} \} \tag{6.7}$$

where E_j is the eigenenergy of the j'th state, ρ_{ij}^e the equilibrium value of ρ_{ij} (identically zero for the off-diagonal elements), and T_{ii} and T_{ij} are taken as the phenomenological lifetimes and dephasing times, respectively. The interaction term contains an implicit summation of over all states (*l*).

The infinite set of equations given above (Equation 6.7) may be solved by considering only the finite number of states contributing to the optical interaction and than reducing them to algebraic form via the rotating-wave approximation [1]. Although such a derivation may be followed in general, it is difficult to achieve a compact formulation valid for all optical nonlinearities (similar to the general perturbative expansions). We thus limit our derivation to multi-harmonic generation when all of the optical frequencies present are multiples of a fundamental frequency ω. All-optical modulation (Chapter 7) is also included in this formalism as the trivial case. The same approach may be followed for nondegenerate processes such as sum- or difference-frequency generation and any other resonantly-enhanced nonlinear phenomena. Although the details will vary, basic limitations on the use of the nonlinear coefficients and on the magnitudes of the obtainable nonlinear effects remain similar.

6.3 Multi-Harmonic Generation Formalism

The local electric field in the presence of multiple harmonics of a fundamental frequency (ω) is expressed as:

$$E(t) = \frac{1}{2}\sum_{m=0}^{m_f}(E_m e^{im\omega t} + E_m^* e^{-im\omega t}) \tag{6.8}$$

The density matrix components are accordingly defined to filter out the dominant temporal variation as:

$$\rho_{jk} = \tilde{\rho}_{jk} e^{i(k-j)\omega t} \tag{6.9}$$

and the Rabi frequencies are defined as:

$$\Omega_{jk} \equiv \frac{q\mu_{jk}E}{\hbar} = \sum_{m=-m_f}^{m_f} \frac{q\mu_{jk}E_m}{2\hbar} e^{im\omega t} \equiv \sum_{m=-m_f}^{m_f} \Omega_{jkm} e^{im\omega t} \tag{6.10}$$

where Ω_{jkm} is the Rabi frequency of the m'th field component's interaction with the j'th and k'th states ($E_{-m} \equiv E_m^*$). This leads to a set of equations for the off-diagonal terms given as:

$$\dot{\tilde{\rho}}_{jk} = -i\{\Delta\omega_{jk} \cdot \tilde{\rho}_{jk} + \sum_{m=-m_f}^{m_f}(\Omega_{lkm}\tilde{\rho}_{jl}e^{i(l-k+m)\omega t} - \Omega_{jlm}\tilde{\rho}_{lk}e^{i(j-l+m)\omega t})\} \tag{6.11}$$

with an implicit summation on *l* and where the complex detuning is defined as:

$$\Delta\omega_{jk} \equiv (E_j - E_k)/\hbar - (j-k)\omega - i/T_{jk} \tag{6.12}$$

and a similar set of equations for the diagonal terms given as:

$$\dot{\rho}_{kk} = -i\{-i(\rho_{kk} - \rho_{kk}^{e}) / T_{kk} + \sum_{m=-m_f}^{m_f} (\Omega_{lkm}\tilde{\rho}_{kl} e^{i(l-k+m)\omega t} - \Omega_{klm}\tilde{\rho}_{lk} e^{i(k-l+m)\omega t})\} \tag{6.13}$$

Using the hermiticity of the density matrix these equations may be converted to a set of d^2 coupled real differential equations for a process involving d states.

6.4 Beyond the Rotating-Wave Approximation

The first approximation required to solve the infinite set of coupled density matrix equations (Equations 6.11-6.13) involves reducing them to a finite set. In a quantum well with an infinite binding potential, 96% of the ground state's transition strength (proportional to the dipole matrix element squared) is with the following subband [2]. Even when finite barriers or more complex structures are taken into account, only a few subbands have significant dipole matrix elements with the ground state. The dominance of a given transition is further enhanced when it is nearly resonant with the optical frequency. It should be noticed however, that at high intensities, resonantly-enhanced transitions may become saturated to the point where other transitions or even the non-synchronous terms may no longer be neglected. In the presence of a single optical frequency, the contribution of a given transition is inversely proportional to the square of its generalized Rabi frequency [1], defined as:

$$\Omega' \equiv \sqrt{\Omega^2 + (\Delta\omega)(\Delta\omega)^*} \tag{6.14}$$

where Ω is the transition's Rabi frequency (Equation 6.10) and $\Delta\omega = (\omega_2 - \omega_1) - \omega - i/T_{21}$ is its (complex) detuning. The definition of the generalized Rabi frequency thus emphasizes the similar reduction in the interaction strength brought on by saturation and detuning. The same general principal but with somewhat more complicated expressions is valid when more optical frequencies and more energy levels are involved.

Making no other approximations, beyond the consideration of only a finite number of states, the resultant set of coupled differential equations requires a numerical solution and a Fourier transform to the frequency domain. The full solution displays not only the obvious saturation effects, but also a host of other phenomena at high intensities such as frequency shifts, higher-order frequency generation, and even probe-gain for pump-probe interactions [1,3,4]. In the following sections we briefly review the possibility of even-harmonic generation in symmetric quantum wells and mention some novel pump-probe phenomena.

6.4.1 Symmetry Breaking by Intense Laser Fields

Coupling of two symmetric wells may lead to an isolated two-level system if the coupling energy is small with respect to the intersubband spacing. Such a structure was considered by Bavli et al. [5] in studying the effects of intense optical fields. Besides a numerical treatment, an analytic solution was obtained in the high field limit by using an inverted perturbative expansion. In this limit the potential of the quantum well is considered a perturbation on the potential induced by the optical field. They found that either an intense radiation field interacting with a system prepared in certain non-equilibrium states or pulses with specific rise profiles interacting with a system in initial thermal equilibrium, will lead to localization and even-harmonic generation. We added relaxation to their treatment and showed that the even-harmonics may be generated by pulses with quite general profiles even for systems in initial thermal equilibrium, but that the effects will decay within the system's dephasing time [6]. Essentially, the initial field direction of an optical field which is sufficiently strong to coherently drive the system removes the symmetry until it is regained through relaxation. From the point of view of standard nonlinear optics [7] these phenomena are not allowed in centrosymmetric systems, and are hence termed symmetry-breaking. They become significant roughly when the Rabi frequency becomes comparable to the transition frequency, i.e. when the influence of the binding potential and the 'ac'-fields become comparable. The Rabi frequency of a transition's saturation amplitude is equal to its half line width times the square root of the lifetime over the dephasing time. Since the frequency to half line width ratio in typical mid-infrared intersubband transitions is between 10 and 100 [13] and the ratio of the lifetime to the dephasing time roughly 10, these novel phenomena are expected to become significant only for intensities at least 3 to 5 orders of magnitude larger than the saturation intensity. Hence they are of limited experimental accessibility due to the short dephasing times, the limited surface breakdown intensity [8], the many body effects and the limited available band offsets (limiting the coupled well scheme to long wavelengths - $\lambda \sim 100\mu m$).

6.4.2 Pump-Probe Interactions

An interaction with both a strong pump beam and a variable probe beam leads to a modification of the transition's absorption lineshape. The arising phenomena for a two-level system include the 'ac'-stark shift, the Raleigh resonance and the three-photon resonance, where the two latter ones may lead to probe gain. A thorough review of the resonant nonlinear response of a two-level atomic system in presence of more than one optical wave was recently presented by Boyd and Sargent [9]. Figure 6.1, following their treatment, shows the absorption spectra of a probe wave as a function of its detuning from resonance in the presence of a strong pump wave. The probe absorption is plotted for a given dephasing time with three different lifetimes (T_1/T_2=0.5, 4, 40). The spectrum for all three displays the absorption peak shifted by the 'ac'-Stark effect, the Raleigh resonance, and the three-photon resonance which leads to gain for a probe at a detuning of $\Delta\omega T_2=-\Omega'$. Larger lifetimes are seen to lead to greater saturation but at the same feature separation - making it much harder to effectively utilize the gain features. This treatment was later used by Zhao et al. [10] to analyze pump-probe phenomena induced by quantum well intersubband transitions. The short relaxation times characterizing semiconductors require strong pump intensities for observation of significant pump-probe effects in intersubband transitions. As a result they have not been demonstrated to date.

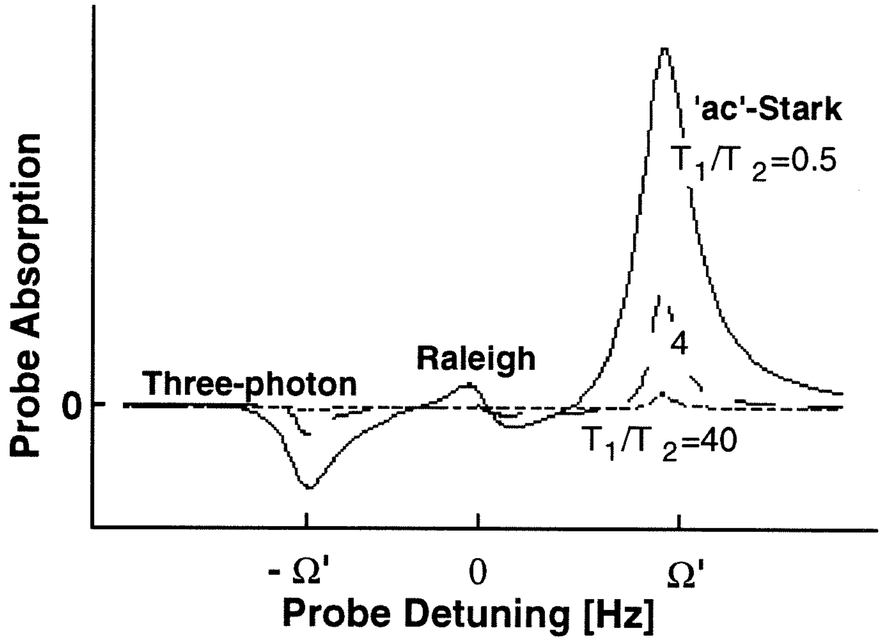

Figure 6.1 Absorption spectrum of a probe wave as a function of its detuning in presence of a pump wave detuned by $\Delta\omega \times T2 = -3$ *with an amplitude of* $\Omega \times T2 = 8$*, and three different values of the life over dephasing time ratio:* $T_1/T_2 = 0.5, 4, 40$*. The spectrum displays the absorption peak shifted by the 'ac'-Stark effect, the Raleigh resonance, and the three-photon resonance which leads to gain for a probe at a detuning of* $\Delta\omega' = -\Omega$*. Larger lifetimes are seen to lead to much greater saturation but with the same feature separation.*

6.5 The Rotating-Wave Approximation (RWA)

In the remainder of our treatment we shall be concerned with the intensity regime where the perturbative power series expansion of the susceptibilities breaks down but the optical interaction is still weaker than the confining potential. Within this limit we can assume that the system reacts only at sums and differences of the driving frequencies. Hence, assuming a steady-state response ($\dot{\tilde{\rho}}_{jk} = 0$), the set of coupled differential equations (Equation 6.13) is reduced to:

$$\Delta\omega_{jk} \cdot \tilde{\rho}_{jk} = \sum_{m=-m_f}^{m_f} (\Omega_{jlm}\tilde{\rho}_{lk} e^{i(j-l+m)\omega t} - \Omega_{lkm}\tilde{\rho}_{jl} e^{i(l-k+m)\omega t}) \tag{6.15a}$$

for the off-diagonal terms, and:

$$(\rho_{kk} - \rho_{kk}^{e}) / T_{kk} = \sum_{m=-m_f}^{m_f} (\Omega_{lkm}\tilde{\rho}_{kl} e^{i(l-k+m)\omega t} - \Omega_{klm}\tilde{\rho}_{lk} e^{-i(l-k-m)\omega t}) / i = 2\,\mathrm{Im}[\sum_{m=-m_f}^{m_f} \Omega_{jkm}\tilde{\rho}_{kl} e^{i(l-k+m)\omega t}] \tag{6.15b}$$

for the diagonal ones. Transient phenomena, such as the Rabi flopping [11], are neglected as they will decay within the system's relaxation time which is extremely short for intersubband transitions (0.1~1ps). Making the Rotating-Wave Approximation (RWA), we thus only keep terms close to resonance with one of the optical frequencies to obtain:

$$\Delta\omega_{jk} \cdot \tilde{\rho}_{jk} = \sum_{m=-m_f}^{m_f} [\Omega_{jlm}\tilde{\rho}_{lk}\delta(j-l+m) - \Omega_{lkm}\tilde{\rho}_{jl}\delta(l-k+m)] \tag{6.16a}$$

and:

$$(\rho_{kk} - \rho_{kk}^{e}) / T_{kk} = 2\,\mathrm{Im}[\sum_{m=-m_f}^{m_f} \Omega_{lkm}\tilde{\rho}_{kl}\delta(l-k+m)] \tag{6.16b}$$

Where δ is the Kronecker delta function - ensuring that only contributions due to the resonantly-enhanced terms in the summations over energy levels (*l*) and field harmonics (*m*) are kept. This set of coupled linear algebraic equations is general for all orders of resonantly-enhanced harmonic generation processes. In the following chapters we will show that the usefulness of such a formalism is not limited to novel high intensity phenomena, but that it must be used for proper design and analysis of intersubband-transition-based nonlinear devices.

References:

[1] R. W. Boyd, *Nonlinear Optics*, San-Diego, California: Academic Press Inc., 1992, Ch. 5.3.

[2] E. Rosencher, and P. Bois, “Model system for optical nonlinearities: asymmetric quantum wells,” *Phys. Rev. B.*, **44**, 11315, 1991.

[3] C. Cohen-Tannoudji, *Frontiers in Laser Spectroscopy*, Amsterdam, Holland: North-Holland, 1977.

[4] B. W. Shore, *The Theory of Coherent Atomic Excitation*, New-York: John Wiley & Sons, 1989, **1,** ch. 4.

[5] R. Bavli, and H. Metius, “Laser-induced localization of an electron in a double-well quantum structure,” *Phys. Rev. Lett.*, **69,** 1986, 1992.

[6] A. Levinson, M. Segev, G. Almogy, and A. Yariv, "Symmetry breaking effects induced by intense laser fields," *Phys. Rev. A*, **49**, R661, 1994.

[7] A. Yariv, *Quantum Electronics*, New-York: John Wiley & Sons, 1988, Ch. 16.

[8] P. Boucaud, F. H. Julien, D. D. Yang, J. M. Lourtoiz, E. Rosencher, and P. Bois, "Saturation of Second-harmonic generation in GaAs-AlGaAs asymmetric quantum wells," *Optics Lett.*, **16**, 199, 1991.

[9] R. W. Boyd, and M. Sargent III, “Population pulsations and the dynamic Stark effect,” *J. Opt. Soc. Am. B*, **5**, 99, 1988.

[10] Y. Zhao, D. Huang, and C. Wu, "Electromagnetically induced transparency and lasing without population inversion in semiconductor quantum wells," LEOS'94, (Boston, MA, October 31 - November 3, 1994).

[11] A. Yariv, *Quantum Electronics*, New-York: John Wiley & Sons, 1988, ch. 15.

Chapter 7

The Intensity-Dependent Refractive Index

7.1 Introduction

The large optical nonlinearities of intersubband transitions have naturally drawn attention to the possibility of their application for all-optical modulation in a wavelength region (3-20μm) where there are currently no viable alternatives. The large 'ac'-Kerr term led to the assumption that efficient all optical phase-modulation may be achieved despite the resonantly-enhanced absorption accompanying the resonantly-enhanced nonlinearities. In this chapter we use a private case of the nonlinear formalism derived in the previous chapter to rigorously analyze this issue. Our conclusions show that the propagation length and optical intensity demands for all-optical phase modulation using intersubband transitions are beyond current technological capabilities. In almost all situations, resonantly-enhanced phase-modulation is shown to be an extremely problematic approach which is inherently inferior to absorption modulation. It also becomes clear that the standard perturbative nonlinear formalism [1], particularly the 'ac'-Kerr effect, is not applicable to device applications of intersubband transitions.

7.2 Optical Interaction with a Two-Level System

The formalism derived in Chapter 6.3 allows for a calculation of the resonantly-enhanced interaction of a multi-level system with a field composed of arbitrary orders of a fundamental frequency. In this chapter we shall be concerned with the trivial case of that formalism - that of a single harmonic interacting with a two-level system. Essentially, we rederive the well-known results for the saturation of a two-level system, and relate them to the perturbative nonlinear formalism, particularly to the 'ac'-Kerr effect. The nonperturbative treatment is shown not only to be more generally valid but also to be necessary for the analysis of nonlinear applications of quantum well intersubband transitions, in particular of all optical switching.

For a monochromatic field interacting with a two-level system the general formalism of Equation 6.16 is reduced to:

$$\Delta\omega_{12} \cdot \tilde{\rho}_{12} = \Omega_{121}(\tilde{\rho}_{22} - \tilde{\rho}_{11}) \tag{7.1a}$$

for the off-diagonal term, and:

$$(\rho_{11} - \rho_{22}) / T_1 = (\rho_{11}^e - \rho_{22}^e) / T_1 + 4\,\mathrm{Im}[\Omega_{121}\tilde{\rho}_{12}] \tag{7.1b}$$

for the diagonal one. Solving for the former we find:

$$\tilde{\rho}_{12} = \frac{(\rho_{11}^e - \rho_{22}^e)\Omega_{121}\Delta\omega_{12}^*}{\Delta\omega_{12}\Delta\omega_{12}^* + 4T_1\Omega_{121}\,\mathrm{Im}[\Delta\omega_{12}]} \tag{7.2}$$

Defining the polarization to factor out the dominant temporal variation:

$$P(t)=\frac{1}{2}\sum_{m=0}^{m_f}(P_m e^{im\omega t}+P_m^* e^{-im\omega t}) \tag{7.3}$$

and recalling the definition of the susceptibility:

$$\frac{P_\omega}{\varepsilon_0 E_\omega}=\frac{Nq\tilde{\rho}_{12}\mu_{12}}{\varepsilon_0 E_\omega}\equiv\chi_{(\omega,\omega)}\equiv\chi'_{(\omega,\omega)}+i\cdot\chi''_{(\omega,\omega)} \tag{7.4}$$

we obtain the well known saturation equation [2]:

$$\chi_{(\omega,\omega)}=\frac{N(\rho_{11}^e-\rho_{22}^e)q^2\mu_{12}^2T_2}{\varepsilon_0\hbar}\frac{\Delta\omega T_2+i}{1+(\Delta\omega T_2)^2+4\Omega_\omega^2T_1T_2} \tag{7.5a}$$

where in the last equation we have returned to the standard (non-complex) definition of the detuning ($\Delta\omega\equiv\omega_2-\omega_1$), the standard definition of the Rabi frequency in a two-level system ($\Omega_\omega\equiv q\mu_{12}E/\hbar$), and where $T_1\equiv T_{11}$ and $T_2\equiv T_{22}$ are defined as the life- and dephasing-times respectively. Defining I_{sat}^{res} as the line center saturation intensity, this may be re-written as:

$$\chi_{(\omega,\omega)}=\frac{N(\rho_{11}^e-\rho_{22}^e)q^2\mu_{12}^2T_2}{\varepsilon_0\hbar}\frac{\Delta\omega T_2+i}{1+(\Delta\omega T_2)^2+I/I_{sat}^{res}} \tag{7.5b}$$

Although we have used the general formalism of Chapter 6, the nonperturbative solution of the optical Bloch equations for the case of a single frequency interaction with a two-level system could be derived directly. Within the assumptions of a dipole interaction and the rotating wave approximation this is the full expression of the susceptibility.

To relate the nonperturbative expression of Equation 7.5b to the standard nonlinear perturbative susceptibilities we may express it as a series in powers of the field defined by:

$$\chi_{(\omega,\omega)} \equiv \chi^{(1)}_{(\omega,\omega)} + 3\cdot\chi^{(3)}_{(\omega,\omega,\omega,\omega)}E^2_\omega + 5\cdot\chi^{(5)}_{(\omega,\omega,\omega,\omega,\omega,\omega)}E^4_\omega + \dots\dots\dots \tag{7.6}$$

The first term of this series is given as:

$$\chi^{(1)}_{(\omega,\omega)} = \frac{N(\rho^e_{11}-\rho^e_{22})q^2\mu^2_{12}T_2}{\varepsilon_0\hbar}\frac{\Delta\omega T_2 + i}{1+(\Delta\omega T_2)^2} \tag{7.7a}$$

and is merely the standard linear susceptibility. The next term is given as:

$$\chi^{(3)}_{(\omega,\omega,\omega,\omega)} = -\frac{4}{3}\cdot\frac{N(\rho^e_{11}-\rho^e_{22})q^4\mu^4_{12}T^2_2T_1}{\varepsilon_0\hbar^3}\frac{1}{[(\Delta\omega T_2)-i]^2\cdot[(\Delta\omega T_2)+i]} \tag{7.7b}$$

and is the 'ac'-Kerr term, identical to the one obtained by keeping only the resonant terms in the standard nonlinear formalism (e.g. one out of the general 24 third-order susceptibility components [1] for $\chi^{(3)}$). Figure 7.1 compares the perturbative predictions (Equation 7.7) to the accurate ones (Equation 7.5) for the imaginary (a) and real (b) components of the susceptibility. It is apparent that the 'ac'-Kerr term becomes inadequate long before the onset of saturation ($I = I^{res}_{sat}$), and its use at higher intensities leads to clearly unphysical predictions.

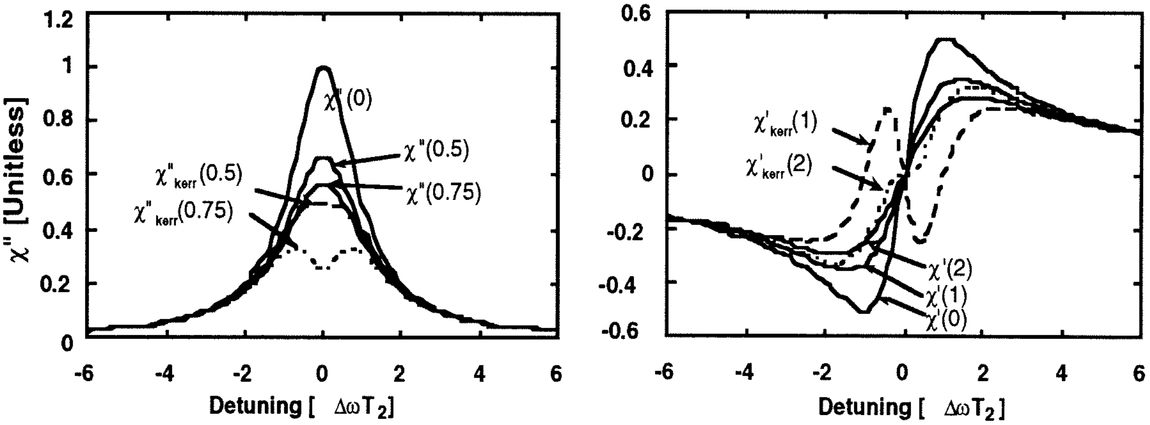

Figure 7.1: The imaginary (χ'') and real (χ') components of the susceptibility versus normalized detuning for several values of the optical intensity (in units of the line center saturation intensity). The solid curves are the full solution (Equation 7.5) and the dashed curves are the result of considering only the first two perturbative terms - the linear term (Equation 7.7a) and the 'ac'-Kerr term (Equation 7.7b).

For most materials it is difficult to accurately derive the wavefunctions and energies of the states causing the optical nonlinearities. The perturbative nonlinear coefficients are thus experimentally found and used to give a fit which is typically quite satisfactory. The situation, however, is quite different for resonant nonlinearities, particularly of quantum well intersubband transitions, where the basic parameters are highly controlled by the structure design. For these, the nonperturbative expressions can be analytically derived, often at no greater effort than the perturbative coefficients. Furthermore, the magnitude of resonantly enhanced nonlinearities leads to the divergence of the perturbative expansion at even moderate intensities. We go on to show that these saturating intensities are not only experimentally accessible, but are required for most practical device applications of resonantly-enhanced nonlinearities.

7.2.1 Limits on the Perturbative Regime

Examination of Equation 7.5 shows that the susceptibility may only be expressed as a power series in increasing orders of the field for:

$$4\Omega_\omega^2 T_1 T_2 < 1 + (\Delta\omega T_2)^2 \tag{7.8}$$

The upper limit to a perturbative approach is thus simply the saturation amplitude:

$$E_{sat} = \frac{\hbar}{2q\mu_{12}}\sqrt{[1+(\Delta\omega T_2)^2]/T_1T_2} \tag{7.9a}$$

or the saturation intensity:

$$I_{sat} = \frac{n\varepsilon_0 c\hbar^2}{2q^2\mu_{12}^2}\frac{1+(\Delta\omega T_2)^2}{T_1T_2} \tag{7.9b}$$

This intensity was measured for quantum well intersubband transitions by Julien et al. [3] who found I_s=340kW/cm^2 in 85A° GaAs quantum wells with 290A° $Ga_{0.7}Al_{0.3}As$ barriers, n-doped in the center 240A° to 5.5×10^{17} cm^{-3}. This saturation intensity corresponds to an excited state's lifetime of over 10ps. Similar results were deduced in two other experiments [4,5]. As suggested by the results of Plodereder et al. [6] and by our self-consistent calculations [7], the observed relaxation times may be influenced by the coupling of electrons from the excited states to the triangular potential outside the wells which will be created by charge migration from the barriers to the wells. Another contribution which is indistinguishable from the saturation in a pump-only experiment is the many-body induced transition energy shift [8,9] leading to reduced absorption at the original line center [10,11]. Experiments in which these effects were eliminated [12] observe an excited state's lifetime of under 10^{-12}ps, smaller by roughly an order of magnitude than previous estimates. This result suggests, assuming that the relaxation mechanisms are independent of the optical intensity, that the saturation intensities may also be higher by an order of magnitude from what was originally believed. In all cases it is important to remember that the measured saturation intensity in a given system sets an upper limit on the perturbative approach - even if that intensity is not simply given by Equation 7.9b.

7.3 All-Optical Switching

Self-phase modulation [13,14] in typical non-resonant optical media is described by the 'ac'-Kerr term ($\chi^{(3)}_{(\omega,\omega,-\omega,\omega)}$) - quadratically proportional to the field amplitude. Since subsaturation intensities are typically used, the nonlinearity may be treated perturbatively. For resonantly-enhanced interactions on the other hand, the nonperturbative treatment must be used at the field amplitudes required for all optical modulation. Furthermore, the phase contribution near resonance [15] is unavoidably accompanied by absorption. Before returning to these points we briefly recall the perturbative treatment of phase-modulation.

7.3.1 Perturbative Phase-Modulation

The nonlinear phase shift ($\Delta\phi$) accumulated in a propagation length *l* is given as [16] :

$$\Delta\phi_{NL} = \frac{2\pi}{\lambda}\Delta n_{NL} l \tag{7.10}$$

where a phase shift of π is required for all optical switching. Within the standard perturbative approach the nonlinear index change (Δn_{NL}) due to the third-order (Kerr) term is given by:

$$\Delta n_{NL} \cong \Delta n_2 = \frac{3\mathrm{Re}[\chi^{(3)}_{(\omega,-\omega,\omega)}]}{2n} E_\omega^2 \tag{7.11}$$

where n is the material's unperturbed refractive index. The necessary optical intensity and propagation length are determined by setting $\Delta\phi_{NL}=\pi$. The naive conclusion from these equations (Equations 7.10-7.11) would be that all optical modulation should be possible for any propagation distance (*l*) for sufficiently high intensities, but this, it turns out, is not the case. As we have shown above (Equation 7.8) the power series expansion of the susceptibility is limited to subsaturation optical intensities. Use of the first term only: the quadratic nonlinear phase delay proportional to $\chi^{(3)}$ (Figure 7.1), is even more limited. Furthermore, since the nonlinear terms are merely a power series expression of the linear term's saturation (Equation 7.5), the total induced refractive index is limited to the transition's linear refractive index contribution [15].

7.3.2 Phase Modulation in Absorptive Media

Optical phase modulation near-resonance will differ from that in nearly-transparent materials in several aspects: 1) the transmission efficiency will be directly reduced by the absorption loss; 2) due to the absorption loss the π-phase delay will be accompanied by a less than 90° polarization rotation - further reducing the transmission efficiency as shown in the inset of Figure 7.3a; 3) the decaying optical field will lead to a decaying refractive index change along the propagation path; 4) a nonperturbative approach is required for the calculation of the refractive index change. We thus begin the treatment by re-examining the solution of the wave equation for an infinite plane wave propagating in an homogeneous media with a discrete transition and a nondipersive bulk refractive index n:

$$E(z) = E(0) \cdot e^{-i\left(\frac{\omega}{c}\sqrt{n^2+\chi'+i\chi''}\right)z} \qquad (7.12)$$

where χ' and χ'', respectively, are the real and imaginary components of the transition's susceptibility. Directly from Equation 7.5, the intensity absorption coefficient is given by: [17]

$$\alpha(\Delta\omega, I) \cong \frac{2\pi}{n\lambda} \cdot \chi''(\Delta\omega, I) = \frac{2\pi}{n\lambda} \cdot \frac{\chi_{res}}{(1 + \Delta\tilde{\omega}^2 + I/I_{sat}^{res})} \tag{7.13a}$$

where we have defined the detuning in units of half the line width as: $\Delta\tilde{\omega} \equiv \Delta\omega \cdot T_2$, and χ_{res} as the line center, nonsaturated value of the susceptibility ($\Delta\omega=I=0$). The induced change per unit length in the optical phase will similarly be:

$$\frac{\partial(\Delta\phi)_{NL}}{\partial l} \cong \frac{\pi}{n\lambda} \cdot \Delta\chi'_{(\omega,\omega)}(\Delta\omega, I) \tag{7.13b}$$

where $\Delta\chi'_{(\omega,\omega)}(\Delta\omega,I)$ is defined as the change in the real component of the susceptibility as a function of intensity and detuning, given by:

$$\Delta\chi'_{(\omega,\omega)}(\Delta\omega, I) \equiv \chi'_{(\omega,\omega)}(\Delta\omega, 0) - \chi'_{(\omega,\omega)}(\Delta\omega, I) = \frac{\Delta\tilde{\omega} \cdot \chi_{res} \cdot (I/I_{sat}^{res})}{(1 + \Delta\tilde{\omega}^2) \cdot (1 + \Delta\tilde{\omega}^2 + I/I_{sat}^{res})} \tag{7.14}$$

For practical modulation purposes it is important that the phase shift be generated with the minimal absorption loss, with 3dB transmission being an accepted figure of merit [18]. It thus becomes favorable to have the high-intensity state, leading to a saturated absorption, as the on-state. Demanding zero transmission in the off-state, and using simple geometrical considerations (inset of Figure 7.3a) the cross-polarizer transmission efficiency in the on-state is:

$$T(\Delta\omega, I) = \frac{(t_{on} + t_{off})^2}{2(1 + t_{off}^2)} \tag{7.15}$$

where t_{on} and t_{off} are respectively defined as the amplitude transmission efficiencies of the interacting polarization in the on- and off-states before the output cross-polarizer ($t_{on} \equiv E_{on}/E_{in}$, $t_{off} \equiv E_{off}/E_{in}$). Considering only the direct absorption loss without saturation we find from Equations 7.12 through 7.14 that a minimal detuning from resonance of $\Delta\omega T_2 > 2\pi * 10\log_{10}(e)/3 \cong 9.1$ is required. As shown in the next section, saturation of the absorption somewhat relaxes this condition.

7.4 Nonperturbative Analysis of All-Optical Switching

Using the nonperturbative expression for the intensity-dependent change in the real component of the susceptibility (Equation 7.14), the demand for a π-phase delay becomes:

$$(\Delta\phi)_{NL} = \frac{\pi}{n\lambda}\int_0^{L_\pi} dz \cdot \Delta\chi'_{(\omega,\omega)}(\Delta\omega, I(z)) = \pi \tag{7.16a}$$

where the intensity will be given by the solution of the differential equation:

$$\frac{dI(z)}{dz} = -\left(\frac{2\pi}{n\lambda}\chi_{res}\right)\frac{I(z)}{1+\Delta\tilde{\omega}^2 + I(z)/I_{sat}^{res}} \tag{7.16b}$$

For high initial intensities the absorption is almost completely saturated so that the intensity, and hence the refractive index, are almost constant along the propagation path. In this case the required propagation distance (L_π) is given in units of the line center nonsaturated extinction length [$1/\alpha(0,0)$] as:

$$\alpha(0,0)L_\pi \cong \frac{2\pi(1+\Delta\tilde{\omega}^2)(1+\Delta\tilde{\omega}^2 + I(0)/I_{sat}^{res})}{\Delta\tilde{\omega}\cdot(I(0)/I_{sat}^{res})} \tag{7.17}$$

And the amplitude transmission before the cross-polarizer becomes (Equation 7.13):

$$t_{on} \cong Exp[-\alpha(\Delta\omega, I(0)) \cdot L_\pi / 2] = Exp[-\frac{\pi}{\Delta\tilde{\omega}} \cdot \frac{(1+\Delta\tilde{\omega}^2)}{(I(0)/I_{sat}^{res})}] \tag{7.18a}$$

in the on-state, and:

$$t_{off} \cong Exp[-\alpha(\Delta\omega, 0) \cdot L_\pi / 2] = Exp[-\frac{\pi}{\Delta\tilde{\omega}} \cdot \frac{(1+\Delta\tilde{\omega}^2 + I(0)/I_{sat}^{res})}{(I(0)/I_{sat}^{res})}] \tag{7.18b}$$

in the off-state. Figure 7.2 shows the cross-polarizer transmission efficiency as a function of both detuning and intensity using this constant intensity approximation (Equation 7.18). Figure 7.3a, on the other hand, plots the transmission efficiency versus intensity for several values of the detuning obtained by numerically solving Equations 7.16a and b. It can be seen that for a given detuning there is a critical intensity below which a 50% transmission efficiency will not be obtained at any propagation length because of the decay of the intensity and hence the decay of the refractive index-correction along the propagation path. Larger values of the detuning lead to a lower transmission efficiency at low to moderate optical intensities, but cross over to a higher transmission efficiency at larger intensities, asymptotically approaching the transparent result in the large detuning limit. Since the saturation intensity is quadratically proportional to the detuning, phase modulation may be obtained at intensities that are lower than the saturation intensity of a detuned frequency. Still, these intensities must be many times the line center saturation intensity of the transition inducing the nonlinearity. The propagation distance required to obtain π-phase modulation is plotted versus intensity in Figure 7.3b for several values of the detuning. For the minimal intensity leading to a 50% transmission efficiency: $I/I_{sat}^{res} \cong 51$ at $\Delta\tilde{\omega} \cong 3$, a propagation length of roughly 26 times the line center nonsaturated extinction length is required. For a detuning of half the width ($\Delta\tilde{\omega} \cong 1$) the high intensity limit of the required propagation length asymptotically approaches 4π times the line center extinction length. Again, phase-modulation may be obtained far-off resonance at distances which are shorter than the extinction length for that frequency, but not shorter than the line center extinction length.

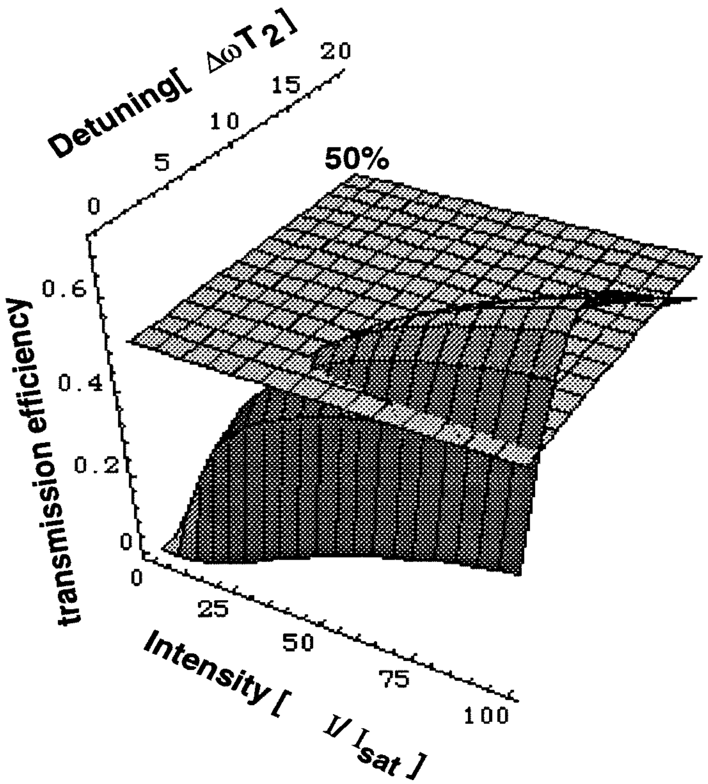

Figure 7.2 The transmission efficiency in a cross-polarizer experiment as a function of the optical intensity and of the normalized detuning assuming a constant optical intensity throughout the propagation path . The plane denotes 50% transmission efficiency.

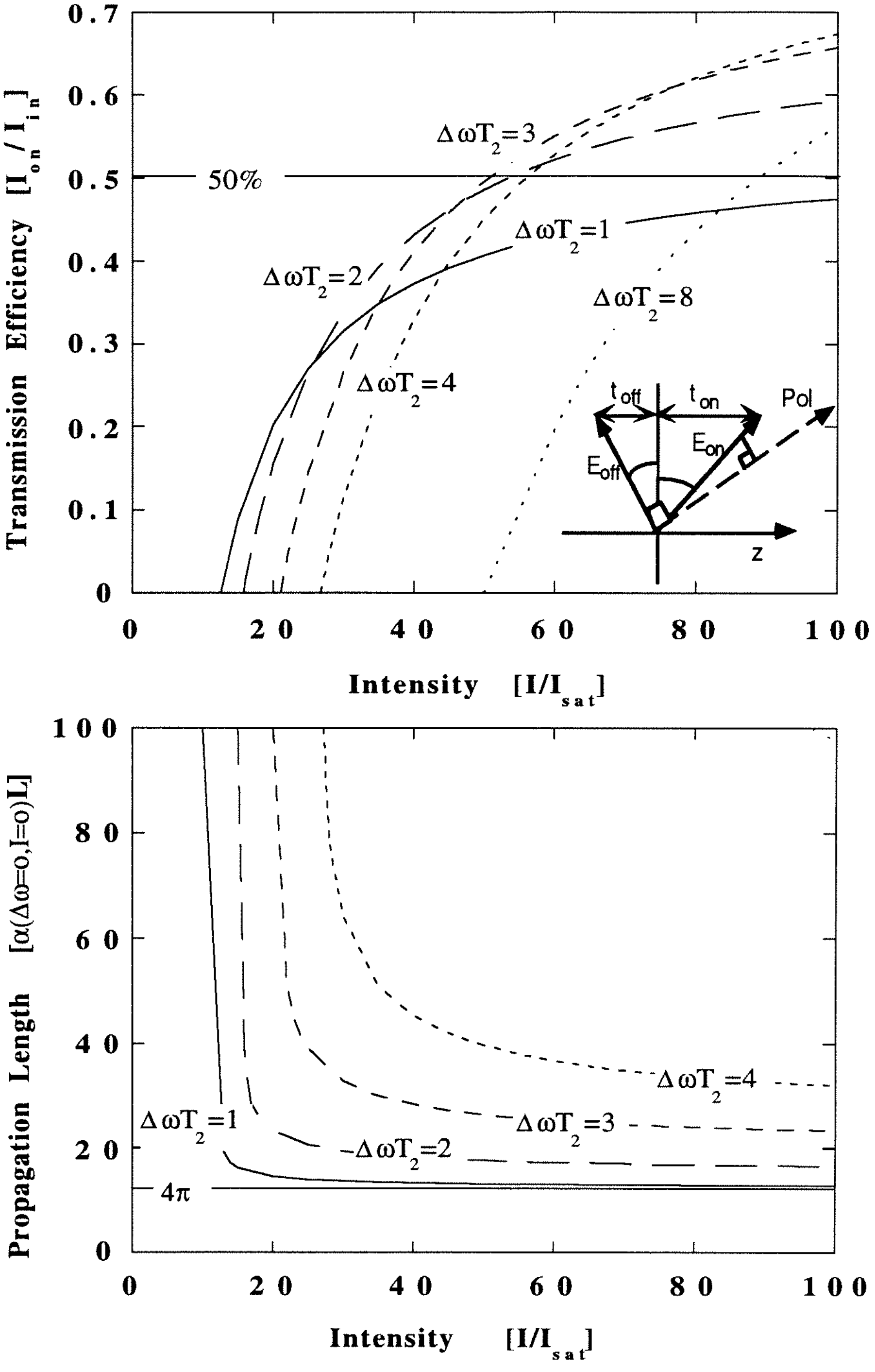

Figure 7.3: The numerically derived (Equations 7.13-17) transmission efficiency (a) and propagation length (in units of the line center nonsaturated extinction length) required to obtain a π-phase modulation (b) plotted versus the optical intensity (in units of the line center saturation intensity) for several values of the normalized detuning. The inset (a) depicts the polarization rotation induced by a π-phase delayed when accompanied by absorption.

For typical quantum well intersubband transitions the required intensity ($I/I_{sat}^{res} \cong 51$) is somewhere between 25-250MW/cm^2 (of internal intensity with polarization parallel to the growth direction). The required interaction length ($\alpha(0,0)L_\pi=4\pi$) may be translated to a demand for a propagation through a total subband surface charge density. For typical parameters of intersubband transitions (λ=10μm, μ=2nm, T_2=125fs, 45° coupling) this density becomes 6.8×10^{14}cm^{-2}, i.e. close to 700 individual quantum wells each doped to 10^{12}cm^{-2}. Such an interaction length is beyond current growth capabilities for single-pass configurations (Figures 3.1a-c) and requires waveguiding (Figures 3.1d). The latter is incompatible with the two-dimensional arrays required for many applications. We therefore conclude that previous observations of extremely large nonlinear coefficients bear little relevance on the feasibility of all-optical phase-modulation using intersubband transitions in particular, and resonantly-enhanced transitions in general. The nonperturbative analysis, on the other hand, provides a straightforward and accurate tool for analyzing both phase and amplitude modulation processes, clearly suggesting the superiority of amplitude modulation.

References:

---

[1] R. W. Boyd, *Nonlinear Optics*, San-Diego, California: Academic Press Inc., 1992, ch. 3.2.

[2] A. Yariv, *Quantum Electronics*, New-York: John Wiley & Sons, 1988, ch. 8.

[3] F. H. Julien, J-M. Lourtoiz, N. Herschkorn, D. Delacourt, J. P. Pocholle, M. Papuchon, R. Planel, and G. Le Roux, "Optical saturation of intersubband absorption in GaAs-$Al_xGa_{1-x}As$ quantum wells," *Appl. Phys. Lett.*, **53,** 116, 1988.

[4] D. Cui, Z. Chen, S. Pan, H. Lu, and G. yang, "Absorption saturation of optical transitions in GaAs/$Al_xGa_{1-x}As$ multiple quantum wells," *Phys. Rev. B*, **47,** 6755, 1993.

[5] A. Seilmeier, H. J. Hubner, G. Abstreiter, G. Weimann, and W. Schlapp, "Intersubband relaxation in GaAs-$Al_xGa_{1-x}As$ quantum well structures observed directly by an infrared bleaching technique," *Phys. Rev. Lett.*, **59,** 1345, 1987.

[6] U. Plodereder, T. Dahinten, A. Seilmeier, and G. Weimann, "Influence of doping concentration on intersubband relaxation in modulation-doped quantum well structure," *Physica. Status. Solidi. B*, **173**, 373, 1992.

[7] A. Tong, G. Almogy, and A. Yariv, "Self-consistent calculation of quantum wells with voltage boundary conditions," unpublished.

[8] M. Ramsteiner, J. D. Ralston, P. Koidl, B. Dischler, H. Bebl, J. Wagner, and H. Ennen, "Doping density dependence of intersubband transitions in GaAs/$Al_xGa_{1-x}As$ quantum well structures," *J. Appl. Phys.*, **67,** 3900, 1990.

[9] G. Almogy, Y. Xu, A. Tong, A. Shakouri, and A. Yariv, "Direct observation of population-induced broadening in quantum well intersubband transitions," QELS'95 - QWJ2, Baltimore, MD, May 95.

[10] J. Khurgin, "Coulombic enhancement of ultrafast nonlinearities in quantum-well structures," *J. Opt. Soc. B*, **9,** 157, 1992.

[11] M. Zaluzny, "Coulomb enhancement of the 3rd-order optical nonlinearities in quantum wells," *Appl. Phys. Lett.*, **61,** 2509 1992.

[12] J. Faist, F. Capasso, C. Sirtori, D. L. Sivco, A. L. Hutchinson, S. N. G. Chu, and A. Y. Cho, "Measurement of intersubband scattering rate in semiconductor quantum wells by excited state differential absorption spectroscopy," *Appl. Phys. Lett.*, **63**, 1354, 1993.

[13] Boyd. R. W, *Nonlinear Optics*, San Diego, California: Academic Press Inc., 1992, Ch. 4.2, p.199.

[14] S. Noda, T. Uemura, T. Yamashita, and A. Sasaki, "All-optical modulation using an n-doped quantum well structure," *J. Appl. Phys.*, **68**, 6529, 1990.

[15] G. Almogy, A. Shakouri, and A. Yariv, "Observation of intersubband-transition-induced birefringence," *Appl. Phys. Lett.*, **63,** 2720, 1993.

[16] A. Yariv, *Quantum Electronics*, New-York: John Wiley & Sons, 1988, Ch. 14.

[17] Within the slowly-varying envelope approximation as discussed in section 5.7.

[18] S. T. Ho, C. T. Soccolich, M. N. Islam, W. S. Hobson, A. F. J. Levi, and R. E. Slusher, "Large nonlinear phase shifts in low loss $Al_xGa_{1-x}As$ waveguides near half gap," *Appl. Phys. Lett.*, **59**, 2558, 1991.

Chapter 8

Interaction of Quantum Wells with 'dc'-Electric Fields

8.1 Electrooptic Phase Modulation

The original goal of our work on quantum well intersubband transitions was to use the extremely large electrooptic coefficients of asymmetric quantum wells to obtain ultrafast electrooptic modulation in the mid-infrared range ($\lambda \cong 10\mu m$). The first step towards achieving that goal, the observation of the refractive index contribution of the intersubband transitions, was described in Chapter 3. The shortcoming of the standard perturbative formalism, became apparent however, when the use of the standard electrooptic coefficient [1] led to predictions of unrealistically large refractive index changes (as high as $\Delta n \cong 5$). Such predictions are clearly beyond the applicability regime of several approximations: the perturbative derivation of nonlinear coefficients, the slowly varying envelope approximation, and the neglect of local field corrections. We therefore derived an adiabatic nonperturbative formalism for the nonlinear optical response of intersubband transitions induced by 'dc'-electric fields. Interactions with 'dc'- electric fields may be treated within the standard approach based on time-dependent perturbation theory [2,3], i.e., with the electrooptic and the 'dc'-Kerr coefficients. Static fields, however, do not lead to transitions and are hence more naturally described with the time-independent approach derived in this chapter. We show that the expansion of the susceptibility using the standard nonlinear coefficients diverges at moderate 'dc' fields and therefore cannot be used to analyze electrooptic modulation in systems with resonantly-enhanced transitions. The conclusion of the analysis using the adiabatic approach contradicts our initial intuitive assumptions. It shows that using intersubband transitions absorption modulation rather than phase modulation is much more easily obtained. This was later applied in our demonstration of a mid-infrared modulator described in Chapter 10 [4].

8.2 Adiabatic Approach

We begin our treatment by examining the dipole interaction Hamiltonian of a quantum well with a 'dc'-electric field (E_{dc}) and an 'ac' near-resonant optical field (E_ω) given as:

$$H_{DE}(z,t) = -qzE(z,t) = \frac{-qz}{2}\{(E_{dc}e^{i\omega_{dc}t} + E_{dc}^{*}e^{-i\omega_{dc}t}) + (E_\omega e^{i\omega t} + E_\omega^{*}e^{-i\omega t})\} \qquad (8.1)$$

where ω_{dc} is the modulation frequency and ω is the 'ac' frequency which is close to the intersubband transition frequency. As long as the modulation frequency is much smaller than the system's relaxation times ($\omega_{dc} \ll 1/T_1, 1/T_2$) the material response adiabatically follows the modulation field, which may hence be considered 'dc'. Since the relaxation times are extremely short for intersubband transitions in quantum wells ($T_1 \cong 10^{-12}$ps and $T_2 \cong 10^{-13}$ps) all practical modulation frequencies fall into the adiabatic regime inducing no transitions. Rather than treat all of the electric field in Equation 8.1 as a perturbation to the quantum well Hamiltonian (H_o), we may divide it into its fast (optical) and slow (modulation) components: H_ω and H_{dc} respectively. The slowly varying component may be added to the unperturbed quantum well to give the biased quantum well's Hamiltonian as:

$$H_o'(z,t) = \frac{p^2}{2m^*(z)} + V(z) - qzE_{dc}\cos(\omega_{dc}t) \tag{8.2}$$

As this Hamiltonian changes adiabatically on a much longer time scale than the optical interaction, the problem of a quantum well (H_o) interacting with two field components (E_{dc} , E_ω) is now reduced [5] to that of a biased quantum well $H_o'(z,t')$ interacting with a single (optical) field component (E_ω).

The solution of the Schrödinger equation for a biased quantum well is similar to that of an unbiased well, but with the wavefunctions given as combinations of Airy functions rather than sinusoids [6]. Since subbands in a finite depth well under bias are only quasi-confined, infinite potential barriers have to be artificially defined to obtain eigenstates (Chapter 2). This problem, however, is easily overcome and we find that the application of 'dc'-electric fields leads not only the variation of the transition energy, but to a change in the dipole element size, a change in the population distribution at a finite temperature

(Fermi statistics), and a change in the transition width. In principle, the quantum well problem should thus be solved for all the relevant values of the 'dc' field, and the resultant field-dependent parameters considered for the interaction with an 'ac' field component only. This nonperturbative adiabatic approach allows treatment of larger 'dc' fields but sacrifices the simplicity of the standard perturbative one.

To regain the simplicity of the perturbative approach but with relaxed limitations on the magnitudes of the 'dc'-fields, we may treat the slow component of the interaction [$H'_d(z,t')$] with a time-independent perturbative approach. As we go on to show, this extends the regime in which the perturbative regime may be applied by the ratio of the transition frequency to its detuning from the optical field (on-resonance this simply becomes the ratio of the transition's frequency to its half-line width). This extension is equivalent to the one made in replacing the perturbative treatment by the full algebraic solution within the rotating-wave approximation for 'ac' nonlinearities described in Chapter 7.

8.3 Time-Independent Perturbative Expansion

From first-order time-independent perturbation theory the intersubband transition frequency in the presence of a 'dc' electric-field becomes:

$$\omega_{12}'(E_{dc}) = \omega_{12}(0) + q\delta_{12}E_{dc}/\hbar \tag{8.3}$$

where:

$$\delta_{12} \equiv \mu_{11} - \mu_{22} \equiv \langle \psi_1 | z | \psi_1 \rangle - \langle \psi_2 | z | \psi_2 \rangle \tag{8.4}$$

is the spatial separation between the subbands. The first-order correction to the wavefunctions also results in a correction of the off-diagonal dipole matrix element (μ_{12}), which becomes:

$$\mu_{12}' = \mu_{12}\{1 + \frac{q\delta_{12}E}{\hbar\omega_{12}} - (\frac{q\mu_{12}E}{\hbar\omega_{12}})^2\} \tag{8.5}$$

Another effect of the electric field is an increase in the transition width caused by the field induced tunneling and scattering [7]. It also modifies the intersubband population difference by changing the subband spacing and hence the Fermi distribution at finite temperatures. Taking all these effects into account, the modified optical susceptibility (Equation 7.5) becomes:

$$\chi^{eff}_{(\omega,\omega)}(E_{dc}) = \frac{N(\rho_{11}^{e'} - \rho_{22}^{e'})q^2 \mu_{12}'^{\,2} T_2'}{\varepsilon_0 \hbar} \frac{(\Delta\omega T_2 + \delta_{12}E_{dc}T_2' / \hbar) + i}{1 + (\Delta\omega T_2' + \delta_{12}E_{dc}T_2' / \hbar)^2 + 4\Omega_\omega'^{\,2} T_1' T_2'} \tag{8.6}$$

where the primes (T_1', T_2', Ω_ω', μ_{12}', ρ') denote the modified values of the parameters under the influence of the 'dc'-electric field. For practical quantum well designs and applicable 'dc' fields the correction to the susceptibility is dominated by the 'dc'-Stark-shift. Therefore only the shift in the transition frequency was written explicitly in Equation 8.6. For symmetric media, where the linear stark shift is identically zero, this shift becomes second-order in the applied field. The latter case is not treated here because the obtainable 'dc'-modulation (the 'dc'-Kerr effect) is inherently smaller and its applications limited.

For simplicity we consider the case of a weak (and hence linear) optical interaction but the treatment may be easily extended to include strong 'dc' and 'ac' fields simultaneously. Expanding Equation 8.6 as a series in powers of the 'dc' field we obtain the first-order (linear) term of the susceptibility:

$$\chi^{(2)}_{(\omega,0,\omega)} = -\frac{N(\rho^{e}_{11} - \rho^{e}_{22})q^{2}\mu_{12}^{\;2}T_{2}^{\;2}}{\varepsilon_{0}\hbar^{2}}\delta_{12} \tag{8.7}$$

which is identical to the standard electrooptic coefficient [1] for a two-level system. Further expansion would generate the higher-order perturbative terms. This power series expansion has a region of convergence limited by:

$$\Omega_{dc} < \sqrt{(1/T_{2})^{2} + (\Delta\omega)^{2}}\,. \tag{8.8}$$

where Ω_{dc} is the 'dc' equivalent of the Rabi frequency defined as:

$$\Omega_{dc} \equiv q\delta_{12}E_{dc}/\hbar \tag{8.9}$$

The time-independent perturbation theory, used to derive Equation 8.6, is valid on the other hand for:

$$q\delta_{12}E_{dc} < \hbar\omega_{12}, \tag{8.10a}$$

or:

$$\Omega_{dc} < \omega_{12} \tag{8.10b}$$

Hence the upper limit on the amplitude for which the adiabatic approach may be used (Equation 8.10b) is larger than the limit on the standard perturbative approach (Equation 8.8) by the ratio of the transition energy to its half-width (25-100 for intersubband transitions). Furthermore, a few important limitations become obvious from the adiabatic approach. Figure 8.1 shows the change in the real component of the susceptibility at line center calculated via the electrooptic coefficient from standard time-dependent perturbation theory (Equation 8.7), by the time-independent perturbation theory (Equation 8.6 with the primed parameters taken to be constants), and by the nonperturbative adiabatic solution (Equation 8.6 - explicitly calculating the primed parameters). It is clear that the use of the electrooptic coefficient is only valid over a very limited amplitude range. A summation of all orders of the time-dependent perturbative expressions will converge to the first-order term of the time-independent perturbative expansion [5], but only when the dc-Rabi frequency is smaller than half a line width ($\Omega_{dc}<1/T_2$). Beyond this point the time-dependent perturbative expansion diverges - i.e. the contribution of the perturbative terms increases with their order. An important conclusion is that the induced index change will not only saturate (as expected from higher order terms in the perturbative expansion), but actually diminish for fields beyond the divergence point (Equation 8.8). This is the point where the 'dc'-Stark effect has swept the transition's half width point across the optical frequency.

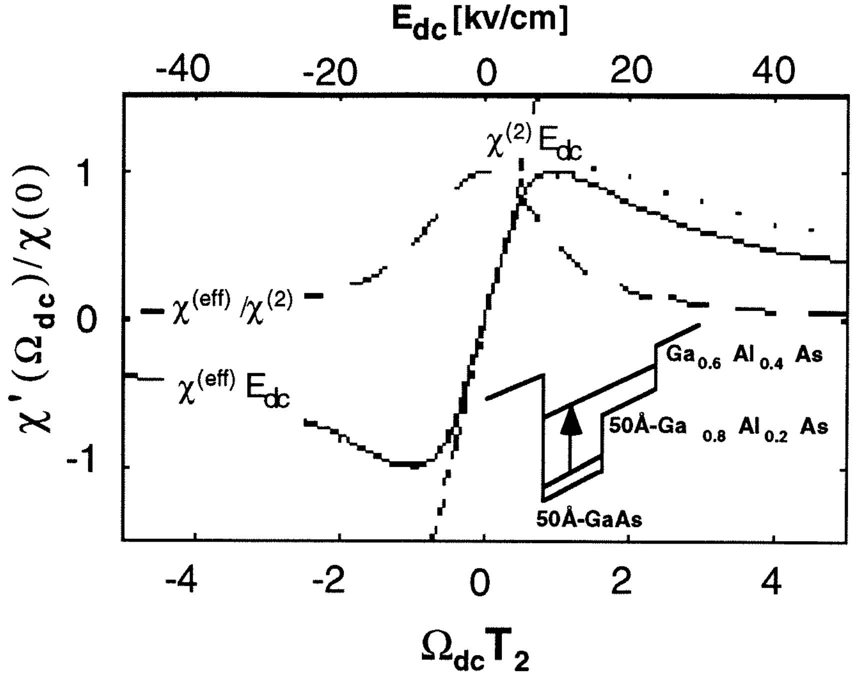

Figure 8.1 The change in the real component of the susceptibility versus the 'dc' Rabi frequency in units of the half line width ($\Omega_{dc}T_2$) at line center. The upper axis gives the corresponding 'dc'-field for a typical step well shown in the inset (with a transition half width of 4 meV). The narrow-dashed line is based on the electrooptic coefficient (Equation 8.7); the solid curve is the result of first-order time-independent perturbation theory (Equation 8.6 - with all parameters but the transition frequency taken to be constants); and the dots are derived from the full adiabatic calculation (Equation 8.6 - explicitly calculating all parameters using the self-consistent solution of Chapter 2). The wide dashed curve is the ratio of the effective susceptibility derived from the time-independent perturbative expansion to that predicted from the use of the electrooptic coefficient - the inaccuracy of the latter even at moderate amplitudes is apparent.

The amplitudes at which the perturbative expression diverges for near resonance frequencies are moderate in comparison with those commonly applied to multiquantum well stacks [8]. Whereas, as described in Chapter 7, the 'ac' perturbative coefficients ('ac'-Kerr,...) amount to a series expansion of the saturation, the 'dc' perturbative coefficients (electrooptic, 'dc'-Kerr,...) amount to a series expansion of the transition frequency shift, i.e. the 'dc'-Stark effect. This is shown in Figure 8.2. As in the 'ac' case analyzed in section 7.4, the linear susceptibility's maximum is the upper limit on the total contribution of all the nonlinear terms (with a potential factor of two obtained by a transition shift of one line width - moving the optical frequency from the lower to higher half line width point). In both cases the time-dependent perturbative approach breaks down at the amplitudes required for effective phase-modulation.

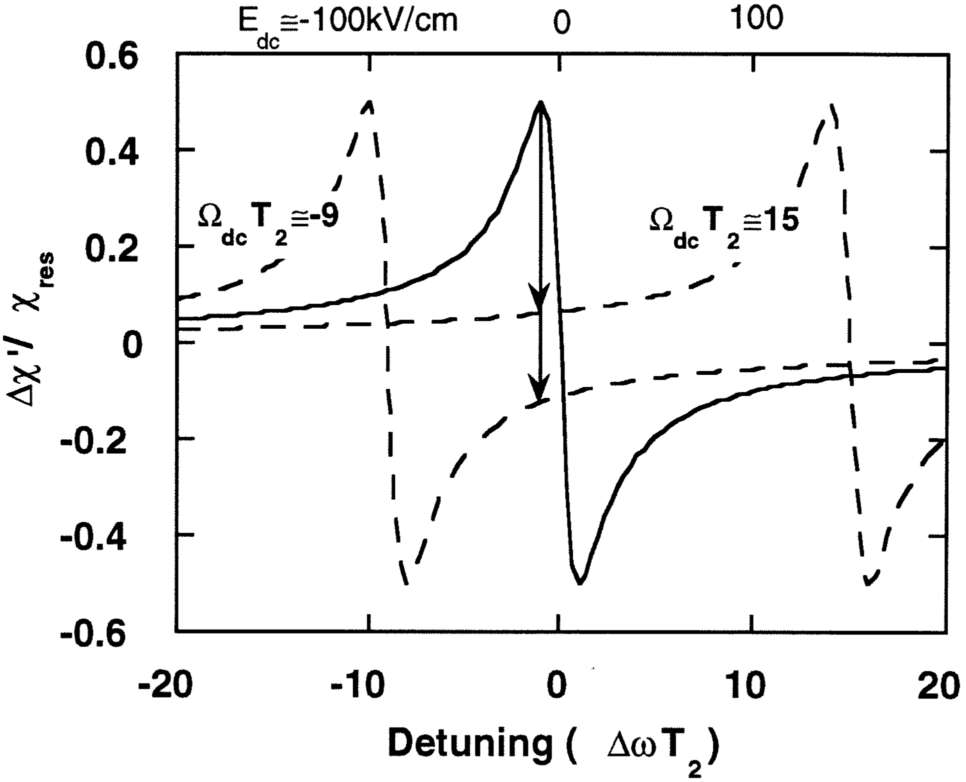

Figure 8.2 The real component of the susceptibility versus normalized detuning from line center. The solid curve is for no applied bias whereas the dashed curves are for positive ($\Omega_{dc}T_2\cong 15$) and negative biases ($\Omega_{dc}T_2\cong -9$). These are the minimal required biases for electrooptic modulation with under 3dB loss for a frequency detuned by a half width from the unbiased line center. The electric field (top horizontal axis) is given for the quantum well shown in the inset of Figure 8.1.

8.4 Electrooptic Modulation

The change in the real part of the susceptibility obtained by shifting the transition frequency and hence changing the optical detuning from: $\Delta\omega_o$ to: $\Delta\omega(E_{dc})=\Delta\omega_o+\Omega_{dc}$ is given by:

$$\Delta\chi'_{(\omega,\omega)}(\Omega_{dc}) \equiv \chi'_{(\omega,\omega)}(0)-\chi'_{(\omega,\omega)}(\Omega_{dc}) = \chi_{res}\cdot\frac{\Delta\omega_0\Omega_{dc}T_2^{\,3}(\Delta\omega_0+\Omega_{dc})-\Omega_{dc}T_2}{[1+(\Delta\omega_0+\Omega_{dc})^2T_2^{\,2}]\cdot[1+(\Delta\omega_0T_2)^2]} \tag{8.11}$$

where, as defined before, χ_{res} is the line center nonsaturated value of the susceptibility. The modified absorption is given as a function of bias as:

$$\alpha(\Delta\omega,\Omega_{dc})=\frac{2\pi}{n\lambda}\cdot\chi''(\Delta\omega,\Omega_{dc})=\frac{2\pi}{n\lambda}\cdot\frac{\chi_{res}}{1+(\Delta\omega_0+\Omega_{dc})^2T_2^2} \tag{8.12}$$

and the extinction (αl) accompanying the π-phase delay becomes:

$$\alpha(\Delta\omega,\Omega_{dc})\cdot l=\left|\frac{2\pi[1+(\Delta\omega_0T_2)^2]}{\Delta\omega_0\Omega_{dc}T_2^{\,3}(\Delta\omega_0+\Omega_{dc})-\Omega_{dc}T_2}\right| \tag{8.13a}$$

in the on-state, and;

$$\alpha(\Delta\omega,0)\cdot l=\left|\frac{2\pi[1+(\Delta\omega_0+\Omega_{dc})^2T_2^{\,2}]}{\Delta\omega_0\Omega_{dc}T_2^{\,3}(\Delta\omega_0+\Omega_{dc})-\Omega_{dc}T_2}\right| \tag{8.13b}$$

in the off-state. The propagation distance required to obtain a π-phase delay is given as a function of the 'dc' amplitude in units of the on-resonant, nonsaturated extinction length as:

$$\alpha(0,0)L_\pi=\left|\frac{2\pi[1+\Delta\omega_0^{\,2}T_2^{\,2}][1+(\Delta\omega_0+\Omega_{dc})^2T_2^{\,2}]}{\Delta\omega_0\Omega_{dc}T_2^{\,3}(\Delta\omega_0+\Omega_{dc})-\Omega_{dc}T_2}\right| \tag{8.14}$$

By inserting Equations 8.13a and b into Equation 7.15 we find the transmission efficiency. It depends on the normalized detuning of the optical frequency from the line center of the unbiased well, and on the shift of that line center induced by the applied 'dc' field. We see from Figure 8.3 that the detuning requiring the smallest 'dc'-field to obtain a π-phase shift with over 50% transmission efficiency in the on-state is roughly 10 times the transition's half-width. For this detuning the 'dc'-field must shift the transition frequency by at least 5.33 times its half-width (Ω_{dc}>5.33/T_2). This is slightly more than the largest intersubband transition 'dc'-Stark shift obtained to date [9].

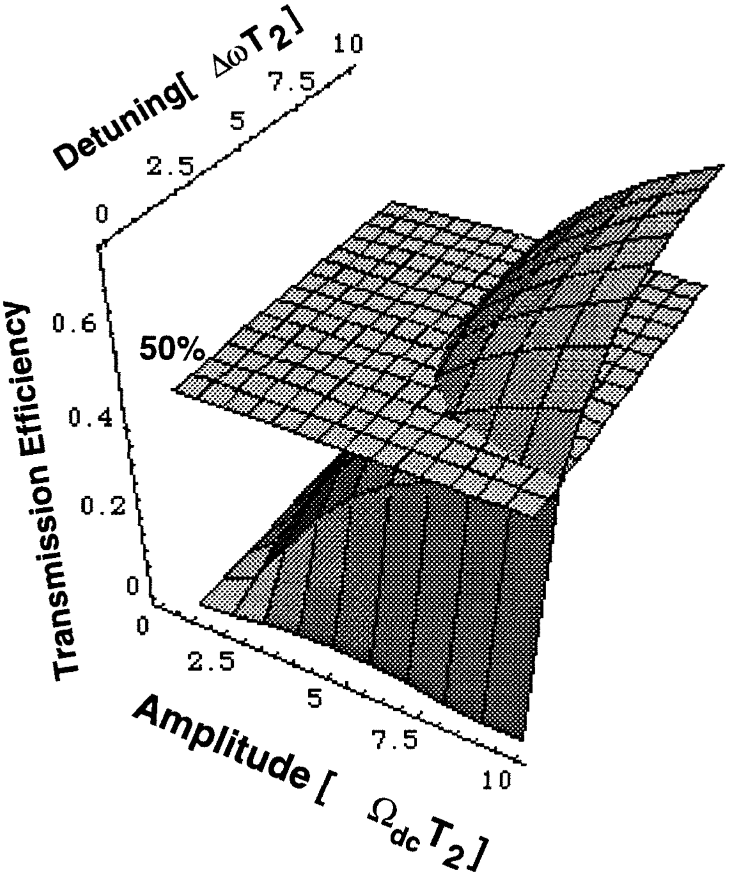

Figure 8.3 The cross-polarizer transmission efficiency in the on-state as a function of the applied 'dc' field and of the normalized detuning. The plane denotes 50% transmission efficiency.

Figure 8.4a plots the transmission efficiency and the required interaction length versus the applied field for an optical frequency detuned by a half-width from the unbiased well's line center. This detuning leads to the possibility of a π-phase shift in the smallest possible distance ($\alpha l=2\pi$), but with a very low ($T\cong3\%$) transition efficiency due to the large absorption in both the on- and off-states. The 50% transmission efficiency requirement leads to a demand for a minimal 'dc'-stark shift of $\Omega_{dc}T_2\cong15.1$ when the resonance is shifted towards the optical frequency, and $\Omega_{dc}T_2\cong-8.8$ when the resonance is shifted away from it. A smaller propagation length, roughly 10 times the line center nonsaturated extinction length, is required in the latter case. This is still beyond current experimental capabilities. It also suggests that amplitude modulation, rather than phase modulation, would be preferable for near-resonant transitions. One of the main advantages of the latter in non-resonant medium, the possibility of zero transmission in the off-state, becomes irrelevant when the required propagation length ($\alpha l\cong10$) allows for absorption-modulation with a negligible line center transmission in the off- (nonsaturated) state: $T_{off}\cong5\times10^{-5}$.

The feasibility of absorption modulation using the Stark effect is examined in Figure 8.4b. The optimal case is for the optical frequency to be at line center of the transition frequency in the off-state. The propagation length requirement is hence set directly by the maximal transmission allowed in the off-state. The three curves in Figure 8.4b correspond to three such demands: 10%, 1%, and 0.1% transmission in the off-state, which correspond to a propagation length of 2.3, 4.6, and 6.9 times the extinction length, respectively. From the data presented in Chapter 10 we can deduce that the minimal requirement of 10% off-state transmission may be met in a single pass through a quantum well stack roughly 10μm thick. We can also see that the applied fields required to obtain transmission in the on-state are within experimental capabilities. Even with a demand for under 1% transmission in the off-state, the 3dB on-state transmission requirement may be met by as little as 20kV/cm, and 90% on-state transmission should be achievable with an applied field of approximately 60kV/cm.

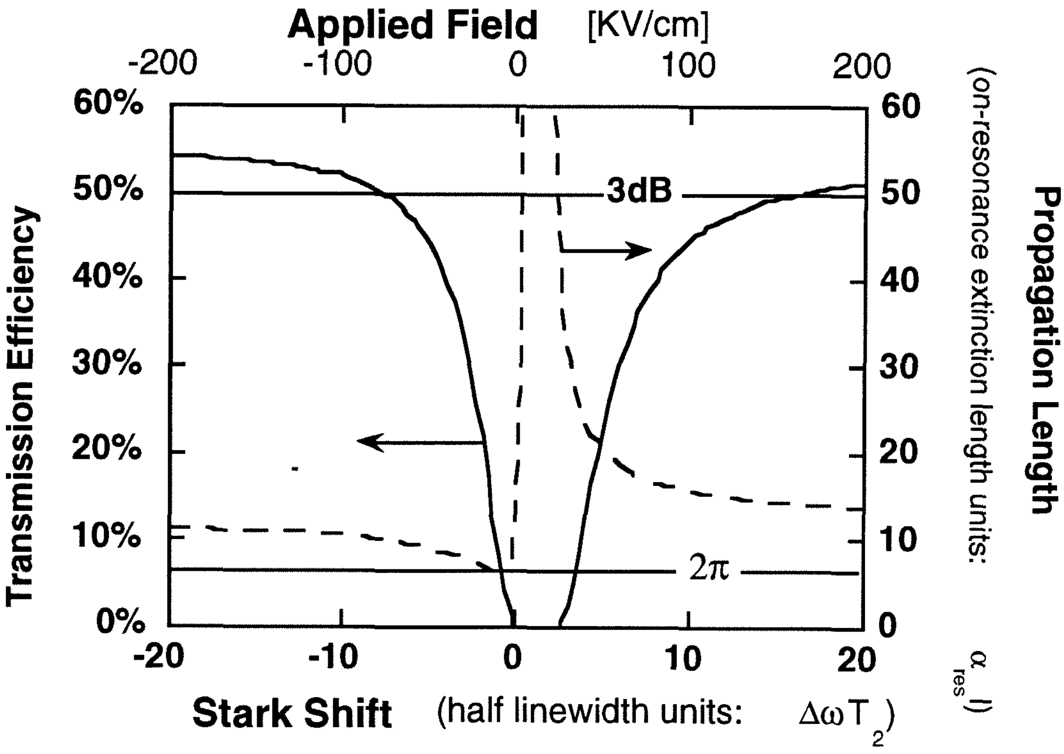

Figure 8.4a: The transmission efficiency and the required interaction length for a π–phase delay versus the applied 'dc' field for an optical frequency a half-width away from the unbiased line center. The 'dc' field amplitudes on the top axis are for the step well shown in the inset of Figure 8.1.

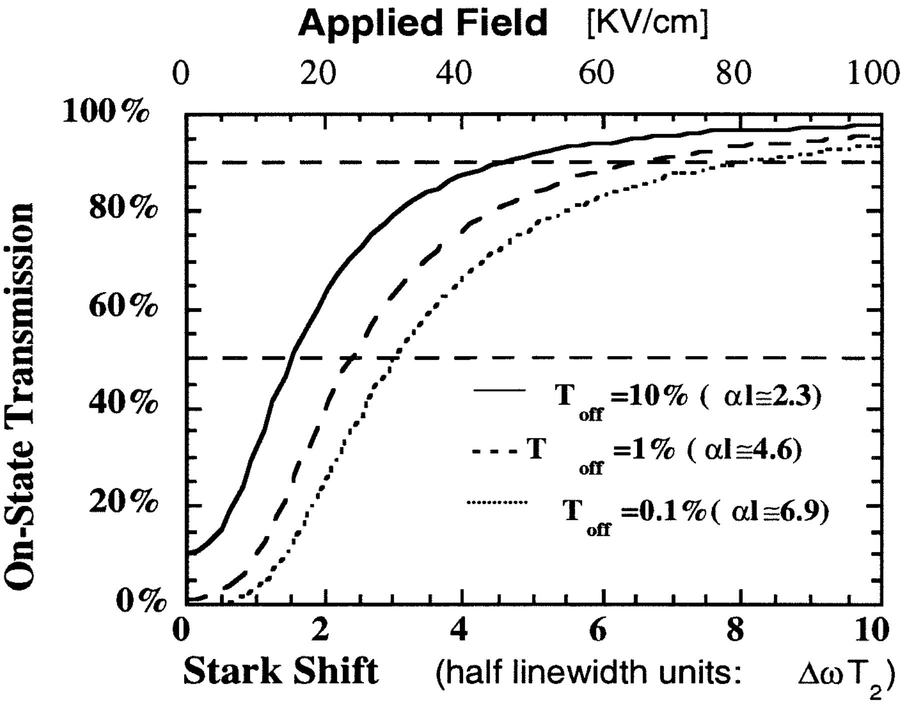

Figure 8.4b: The transmission efficiency in the on-state as a function of the applied 'dc' field for an optical frequency on the unbiased line center. The three curves are for different values of the allowed off-state transmission (T_{off}) with the corresponding propagation length demand (in units of the extinction length) given in parentheses. The 'dc' field amplitudes on the top axis are for the step well shown in the inset of Figure 8.1

We have therefore shown, just as for the case of all optical phase modulation, that the observation of an extremely large electrooptic coefficient [1] bears little relevance on the feasibility of electrooptic phase modulation using intersubband transitions. The nonperturbative analysis, on the other hand, provides a straightforward and accurate tool for analyzing both phase and amplitude modulation processes. The conclusion of the analysis using the adiabatic approach, contradicting our initial intuitive assumptions, is that absorption rather than phase modulation is preferable for intersubband transitions. This was later applied in our demonstration of a mid-infrared intersubband transition based modulator described in Chapter 10.

8.5 Alternative Modulation Schemes

Besides the 'dc'-Stark shift, the control over quantum well parameters makes other options for amplitude or phase modulation via intersubband transitions feasible. These include inducing a change in either the populations of the different subbands or in the intersubband optical dipole matrix elements between them. The former may be achieved by transfer of electrons between quantum wells with different transition wavelengths as demonstrated by Vodjdani et al. [10] or by transfer of electrons from a Schottky gate as demonstrated by Kane et al. [11] Suggestions have also been made [12] for electron transfer between the L and Γ-valley states in material systems where they are relatively close and can be made to cross by an applied electric field. Recently, we demonstrated a bias induced shift of 40% of the total population ($\sigma \cong 10^{12}\text{cm}^{-2}$) between adjacent and lightly coupled quantum wells, leading to absorption of 40% of the optical field in a single pass ($\alpha l \cong 0.5$) [4]. Another method for modulation of the intersubband transmission is by interband excitation. This scheme was used by Julien et al. [13] to obtain a 20dB on/off ratio in propagation through quantum wells grown between waveguiding layers. The second modulation scheme, which is control of the dipole matrix element by coherent interference of the wavefunction components in two coupled wells, was recently demonstrated by Faist et al. [14]. The dipole interaction between energy levels separated by even integers becomes forbidden when the coupled structure becomes symmetric. The total absorption of that transition, quadratically proportional to the dipole matrix element, may be modified by a 'dc' field controlling the symmetry of the structure. This scheme relies on the existence of a coherent state across both coupled wells and is hence limited to narrow barriers and high quality material. A similar concept was used earlier by Dupont et al. [15] to obtain both amplitude and phase modulation in asymmetric coupled quantum wells. The total phase-delay obtained, however, was limited to 60mrad.

An accurate comparison of the relative advantages of the alternative modulation schemes: the 'dc'-stark shift, population transfer, and the modification of the dipole elements, requires a better understanding of the broadening mechanisms of intersubband transitions than is presently available. In general the requirement for both a large absorption and the ability to modulate it impose contradictory demands on the volume doping density [9]. In all cases, the maximal linear transition strength is the upper limit on the total obtainable nonlinearities.

References:

---

[1] E. Rosencher, P. Bois, B. Vinter, J. Nagle, and D. Kaplan, "Giant nonlinear optical rectification at 8-12μm in asymmetric coupled quantum-wells," *Appl. Phys. Lett.*, **56**, 1822, 1990.

[2] E. Rosencher, and P. Bois, "Model system for optical nonlinearities: asymmetric quantum wells," *Phys. Rev. B*, **44,** 11315, 1991.

[3] J. Khurgin, “Second-order nonlinear effects in asymmetric quantum-well structures,” *Appl. Phys. Lett.*, **38,** 4056, 1988.

[4] G. Almogy, Y. Xu, A. Tong, A. Shakouri, and A. Yariv, “Monolithic integration of quantum well infrared photodetector and modulator,” submitted to *Appl. Phys. Lett.*

[5] G. Almogy, M. Segev, and A. Yariv, “Adiabatic nonperturbative derivation of electric-field-induced nonlinearities in quantum wells,” *Phys. Rev. B*, **48,** 10950, 1993.

[6] E. J. Austin, and M. Jaros, “Electronic structure of an isolated GaAs-AlGaAs quantum wells in a strong electric field,” *Phys. Rev. B*, **31,** 5569, 1987.

[7] G. Weber, “The effect of electric field on intrasubband and intersubband transitions via interface phonons in GaAs-AlAs quantum wells,’ *J. Phys. Cond.*, **4**, 9831, 1992.

[8] A. Harwit, and J. S. Harris, Jr., “Observation of Stark shifts in quantum well intersubband transitions,” *Appl. Phys. Lett.*, **50**, 685, 1987.

[9] E. Martinet, F. Luc, E. Rosencher, P. Bois, and S. Delaitre, “Electrical tunability of infrared detectors using compositionally asymmetric GaAs/AlGaAs multiquantum wells,” *Appl. Phys. Lett.*, **60**, 895, 1992.

[10] N. Vodjdani, B. Vinter, V. Berger, E. Bockenhoff, and E. Costard, “Tunneling assisted modulation of the intersubband absorption in double quantum wells,” *Appl. Phys. Lett.*, **59**, 555, 1991.

[11] M. J. Kane, M.T. Emeny, N. Apsley, and C. R. Whitehouse, “Novel electrooptic modulation effect at 10μm wavelength in GaAs/AlGaAs quantum wells,” *Electron. Lett.*, **25**, 220, 1989.

---

[12] H. Xie, W. I. Wang, J. R. Meyer, C. A. Hoffman, and F. J. Bartoli, "Enhancement of intersubband stark effects in l-valley step quantum-wells for infrared modulation and voltage tunable detection," *J. Appl. Phys.*, **74**, 1195, 1993.

[13] F. H. Julien, P. Vagos, J.M. Lourtioz, D. D. Yang, and R. Planel, "Novel all-optical 10μm waveguide modulator based on intersubband absorption in GaAs/AlGaAs quantum wells," *Appl. Phys. Lett.*, **59**, 2645, 1991.

[14] J. Faist, F. Capasso, A. L. Hutchinson, L. Pfeiffer, and K. W. West, "Suppression of optical absorption by electric-field-Induced quantum interference in coupled potential wells," *Phys. Rev. Lett.*, 71, 3573, 1993.

[15] E. Dupont, D. Delacourt, and M. Papuchon, 'Midinfrared amplitude and phase modulation by intersubband transitions in biased double quantum wells," *Appl. Phys. Lett.*, **63**, 2514, 1993.

Chapter 9

Resonantly-Enhanced Second-Harmonic Generation in Quantum Wells

9.1 Introduction

Most of the research into the nonlinear optical properties of intersubband transitions in quantum wells has focused on resonantly-enhanced frequency conversion. Control over both the quantum well dimensions and composition has led to multi-resonant systems with optimized dipole matrix elements, which in turn have led to the extremely large nonlinear coefficients observed (references 17-33 of Chapter 5). Despite these observations, expectations for high conversion efficiencies have, as yet, failed to materialize. This, at least in part, is due to the fundamental differences between resonantly-enhanced second-harmonic generation and second-harmonic generation in transparent materials. First, as resonance is approached, there is the obvious trade-off between increased generation of the second-harmonic and increased absorption of both harmonics. This trade-off led most studies of second-harmonic generation in quantum wells to assume that some detuning is preferable. Our rigorous derivation showed the contrary [1], i.e., that full resonance is the optimal conversion condition within the second-order perturbative approach.

The issue of resonantly-enhanced second-harmonic generation is greatly complicated, however, by the breakdown of the perturbative approach even at moderate pump intensities. We approached it by examining the Bloch equations for a two-frequency-three-level system interaction within the rotating-wave-approximation both analytically and numerically [2]. Our derivation begins by showing that for high conversion efficiencies to be obtained using resonantly-enhanced transitions, pump intensities which lead to saturation are required (section 9.2). The analysis of this problem thus has to take into account the coupled issues of absorption, saturation, phase-matching, and many body effects (sections 9.4-9.5). Due to the host of parameters involved in the two-frequency-three-level system interaction, no simple or intuitive scheme for optimizing the quantum well structure can be given and individual optimization must be carried out for each specific propagation length and pump intensity. The results we obtained differ on several principal issues from those previously obtained by De-Temple et al., [3], who in 1981 presented the first general treatment of the subject, and from those of Boucaud and Julien [4] who specifically examined second-harmonic generation in quantum wells. We also derive a general limit on the second-harmonic intensity that may be generated in a given propagation length. Although of little practical importance except for resonantly-enhanced transitions, this limit applies to all materials. Along with the rest of the derivation, this limit goes beyond our direct goal of optimizing the design of quantum wells for resonantly-enhanced second-harmonic generation, and sheds some light on the basic nature of the second-harmonic generation process.

9.2 The Perturbative Regime

Our treatment of resonantly-enhanced second-harmonic generation begins with the standard perturbative approach. The conclusions derived using second-order perturbation theory will serve as a starting point from which the modifications brought about by saturation at higher intensities will be examined. The induced second-harmonic polarization in a three-level system interacting with a first (E_ω) and second-harmonic ($E_{2\omega}$) optical fields is thus given as [5]:

$$P_{2\omega} = \varepsilon_0 \{ (n_{2\omega}^2 + \chi^{(1)}_{(2\omega,2\omega)}) E_{2\omega} + \chi^{(2)}_{(2\omega,\omega,\omega)} E_\omega^2 \} \tag{9.1a}$$

where the right-hand side includes the bulk's linear (and real) susceptibility $n_{2\omega}$, the resonantly-enhanced linear susceptibility $\chi^{(1)}_{(2\omega,2\omega)}$, and the resonantly-enhanced second-harmonic susceptibility $\chi^{(2)}_{(2\omega,\omega,\omega)}$. Similarly the induced first-harmonic polarization is given as:

$$P_\omega = \varepsilon_0 \{ (n_\omega^2 + \chi^{(1)}_{(\omega,\omega)}) E_\omega + \chi^{(2)}_{(\omega,2\omega,-\omega)} E_{2\omega} E_\omega^* \} \tag{9.1b}$$

Where the right hand side includes the bulk's linear susceptibility n_ω, the resonantly-enhanced linear susceptibility $\chi^{(1)}_{(\omega,\omega)}$, and the depletion coefficient $\chi^{(2)}_{(\omega,2\omega,-\omega)}$. The relevant nonlinear coefficients for a nearly-resonant three-level system are given from second-order time dependent perturbation theory as [5]:

$$\chi^{(1)}_{(\omega,\omega)} = \frac{\mathrm{N}q^2\mu_{10}{}^2\mathrm{T}_{10}}{\hbar\varepsilon_0}\frac{1}{(\Delta\tilde{\omega}_{10} - i)} \tag{9.2a}$$

$$\chi^{(1)}_{(2\omega,2\omega)} = \frac{\mathrm{N}q^2\mu_{20}{}^2\mathrm{T}_{20}}{\hbar\varepsilon_0}\frac{1}{(\Delta\tilde{\omega}_{20} - i)} \tag{9.2b}$$

$$\chi^{(2)}_{(2\omega,\omega,\omega)} = \frac{\mathrm{N}q^3\mu_{10}\mu_{21}\mu_{20}\mathrm{T}_{10}\mathrm{T}_{20}}{2\hbar^2\varepsilon_0}\frac{1}{(\Delta\tilde{\omega}_{10} - i)(\Delta\tilde{\omega}_{20} - i)} \tag{9.2c}$$

where ε_0 is the vacuum permmitivity, N the equilibrium population assumed in the ground state, μ_{ij} the optical dipole matrix element between the i'th and j'th state, T_{ij} the corresponding dephasing time, and $\Delta\tilde{\omega}_{ij}$ is the corresponding normalized detuning defined as: $\Delta\tilde{\omega}_{ij} = (\omega_{ij} - (i-j)\omega)\mathrm{T}_{ij}$. The second-harmonic susceptibility is proportional to $\chi^{(2)}_{(2\omega,\omega,\omega)}$ which is the coefficient of the second-harmonic frequency component in the perturbative expansion of the susceptibility. The depletion coefficient $\chi^{(2)}_{(\omega,2\omega,-\omega)}$ is merely twice the complex conjugate of the second-harmonic generation coefficient $\chi^{(2)}_{(2\omega,\omega,\omega)}$. In deriving these coefficients we have considered only the near-resonant interaction of the first-harmonic with the ground to first (0→1) and first to second state (1→2) transitions, and the second-harmonic with the ground to second state transition (0→2). Although, in general, each of these terms could represent a summation of several paths, the resonantly-enhanced terms completely dominate.

To solve the wave equations we define the propagating optical field as:

$$E(z,t) = \frac{1}{2}\{E_{\omega}(z)e^{i\omega t}e^{-ikz} + E_{2\omega}(z)e^{2i\omega t}e^{-2ikz} + c.c\} \tag{9.3}$$

In the latter definition, unlike standard convention [6] we arbitrarily assign the second-harmonic a propagation vector of 2k, where k is the first-harmonic's propagation vector defined by:

$$k \equiv \frac{\omega}{c}\sqrt{n_{\omega}^{2} + \mathrm{Re}[\chi^{(1)}_{(\omega,\omega)}]} \equiv \frac{\omega n}{c} \tag{9.4}$$

This definition includes the phase-mismatch from both the host material and the transition induced dispersion in the complex nature of $E_{2\omega}(z)$. As long as the treatment is limited to only an incident pump wave, there is no need to take the phase contribution of the nonlinear term into account. The amplitude absorption coefficients are defined as:

$$\alpha_{\omega}(\Delta\omega_{01}) \equiv -\frac{\omega}{2nc}\mathrm{Im}[\chi^{(1)}_{(\omega,\omega)}] \tag{9.5a}$$

and:

$$\alpha_{2\omega}(\Delta\omega_{02}) \equiv -\frac{\omega}{nc}\mathrm{Im}[\chi^{(1)}_{(2\omega,2\omega)}] \tag{9.5b}$$

for the first and second-harmonics, respectively, and a phase mismatch coefficient is defined as:

$$\beta_{2\omega}(\Delta\omega_{01},\Delta\omega_{02}) \equiv \frac{\omega}{nc}\{n_{2\omega}^{2} - n_{\omega}^{2} + \mathrm{Re}[\chi^{(1)}_{(2\omega,2\omega)}] - \mathrm{Re}[\chi^{(1)}_{(\omega,\omega)}]\} \tag{9.5c}$$

The wave equations are thus reduced with the slowly varying amplitude approximation (section 5.7) to:

$$\frac{dE_\omega}{dz} = -\alpha_\omega E_\omega - i\frac{\omega}{2nc}\chi^{(2)}_{(\omega,2\omega,-\omega)}E_{2\omega}E^*_\omega \tag{9.6a}$$

and:

$$\frac{dE_{2\omega}}{dz} = -(\alpha_{2\omega} + i\beta_{2\omega})E_{2\omega} - i\frac{\omega}{nc}\chi^{(2)}_{(2\omega,\omega,\omega)}E^2_\omega \tag{9.6b}$$

for the fundamental (E_ω) and the doubled harmonic ($E_{2\omega}$), respectively. An analytic solution requires the neglect of either the absorption or the depletion for the equations to be decoupled.

9.2.1 Transparent Approximation

When the absorption is neglected the total optical intensity is conserved and we may substitute:

$$E_\omega(z)E^*_\omega(z) = E_\omega(0)E^*_\omega(0) - E_{2\omega}(z)E^*_{2\omega}(z) \tag{9.7}$$

into Equation 9.6b. Assuming phase-matching, ($\beta_{2\omega}$=0) we obtain:

$$\frac{dE_{2\omega}}{dz} \equiv i\frac{\omega}{nc}\chi^{(2)}_{(2\omega,\omega,\omega)}(E^2_\omega(0) - E^2_{2\omega}(z)) \tag{9.8}$$

and hence an amplitude conversion efficiency of [6]:

$$\left|\frac{E_{2\omega}(z)}{E_\omega(0)}\right| = \mathrm{Tanh}[(\omega/nc)\chi^{(2)}_{(2\omega,\omega,\omega)}E_\omega(0)z] \tag{9.9}$$

9.2.2 Nondepleted Approximation

On the other hand, considering the absorption while neglecting the depletion (second term on the R.H.S of equation 9.6a) leads to the solution given as:

$$\left|\frac{E_{2\omega}(z)}{E_{\omega}(0)}\right| = -i\frac{\omega}{nc}\frac{\chi^{(2)}_{(2\omega,\omega,\omega)}}{(\alpha_{2\omega}-2\alpha_{\omega})}\{e^{-2\alpha_{\omega}z}-e^{-\alpha_{2\omega}z}\}E_{\omega}(0) \tag{9.10}$$

which is obtained by solving Equation 9.6a and substituting into Equation 9.6b. The conversion is thus maximized at an optimal propagation length ($z_{\max}$) of:

$$z_{\max} = \frac{1}{\alpha_{2\omega}-2\alpha_{\omega}}\ln(\frac{\alpha_{2\omega}}{2\alpha_{\omega}}) \tag{9.11}$$

leading to a conversion efficiency maximum of:

$$\left|\frac{E_{2\omega}(z_{\max})}{E_{\omega}(0)}\right| = \frac{\omega}{nc}E_{\omega}(0)\left|\chi^{(2)}_{(2\omega,\omega,\omega)}\right|\{\frac{1}{\alpha_{2\omega}}(\frac{2\alpha_{\omega}}{\alpha_{2\omega}})^{\frac{2\alpha_{\omega}}{\alpha_{2\omega}-2\alpha_{\omega}}}\} \tag{9.12}$$

Substituting equations 9.2 and 9.5 in equation 9.12, we find that the conversion efficiency is maximized when the absorption of the second-harmonic is twice that of the first's ($\alpha_{2\omega}=2\alpha_{\omega}$). This occurs when the imaginary components of the linear susceptibilities for the two frequencies are equal ($\mathrm{Im}[\chi^{(1)}_{(\omega,\omega)}] = \mathrm{Im}[\chi^{(1)}_{(2\omega,2\omega)}]$), in which case the conversion efficiency is maximized at the propagation distance of:

$$z_{\max} = 1/\alpha_{2\omega} \tag{9.13}$$

This result may be derived by taking the limit of Equation 9.11 as $\alpha_{2\omega} \rightarrow 2\alpha_{\omega}$, or more simply by re-solving Equation 9.9 for $\alpha_{2\omega}=2\alpha_{\omega}$. The conversion efficiency at $z_{\max}$ reaches a value of:

$$\left|\frac{E_{2\omega}(z_{\max})}{E_{\omega}(0)}\right| = \frac{\omega}{nc}\frac{\left|\chi^{(2)}_{(2\omega,\omega,\omega)}\right|E_{\omega}(0)}{e\cdot\alpha_{2\omega}} = \frac{1}{e}\cdot\frac{\left|\chi^{(2)}_{(2\omega,\omega,\omega)}\right|E_{\omega}(0)}{\mathrm{Im}[\chi^{(1)}_{(2\omega,2\omega)}]} \tag{9.14}$$

which is proportional to the ratio of the nonlinear to linear susceptibilities. For equal optical dipole elements ($\mu_{02}=\mu_{01}$), equal detuning from the one and two-photon resonance

($\Delta\omega_{02}=\Delta\omega_{01}$), and equal dephasing times ($T_{02}=T_{01}\equiv T_2$), the conversion efficiency simply becomes:

$$\left|\frac{E_{2\omega}(z_{\max})}{E_{\omega}(0)}\right| = \frac{1}{e}\cdot\frac{\mu_{21}E_{\omega}(0)}{2\hbar}T_2 \equiv \frac{1}{e}\cdot\Omega_{21}T_2 \tag{9.15}$$

where Ω_{21} is the Rabi frequency of the initial pump (first-harmonic) field interacting with the first to second excited state transition. From this private solution emerges the importance of the generalized Rabi frequencies which we define for later use as:

$$\begin{aligned}
\Omega_{10}(z)T_{10} &\equiv \frac{\mu_{10}E_{\omega}(z)}{2\hbar}T_{10} \equiv \Omega_{\omega}\\
\Omega_{20}(z)T_{20} &\equiv \frac{\mu_{20}E_{2\omega}(z)}{2\hbar}T_{20} \equiv \Omega_{2\omega}\\
\Omega_{21}(z)T_{21} &\equiv \frac{\mu_{21}E_{\omega}(z)}{2\hbar}T_{21} = \Omega_{\omega}(\frac{\mu_{21}T_{21}}{\mu_{10}T_{10}})
\end{aligned} \tag{9.16:a-c}$$

i.e. the Rabi frequencies in units of the relevant transition's linewidth. Thus, for the above conditions the maximal conversion efficiency is proportional (Equation 9.15) only to the optical dipole matrix element between the first and second excited states (μ_{12}), to the pump amplitude ($E_{\omega}(0)$) and to the dephasing time (T_2). The peak efficiency is maximized when the dipole matrix elements between the ground state and both excited states are equal ($\mu_{01}=\mu_{02}$) but surprisingly independent of their absolute value. Only the propagation length at which this maximal conversion is obtained (Equation 9.13) is inversely proportional to the square of the ground state's dipole matrix elements ($\mu_{01}=\mu_{02}$), quadratically proportional to the detuning ($\Delta\omega_{02}=\Delta\omega_{01}$), and inversely proportional to the total population (N). Since for equal strength transitions (dipole elements and dephasing times) equal detuning is the optimal condition, and since equal detuning quadratically increases the propagation length, full resonance is the optimal conversion condition despite the enhanced absorption losses.

9.2.3 Numerical Propagation Equations

At first glance neither the non-depleted (section 9.2.2) nor the transparent (section 9.2.1) perturbative derivations presented above are justified. The validity of the non-depleted approximation simply depends on the conversion efficiency; as long as the amplitude of the second-harmonic is much smaller than that of the first it is justified (see rigorous justification in section 4.2.3). The commonly used transparent approximation [6], however, warrants justification not just for resonantly-enhanced interactions. Whereas all optical transitions contribute to the absorption, only the ones originating from asymmetric systems contribute to second-harmonic generation. Furthermore, in a three-level system the second-harmonic generation coefficient is inversely proportional to the product of the first and second-harmonics' detuning, whereas the absorption of each harmonic is inversely proportional to the respective detuning squared (Equations 9.2 and 9.5). Hence the ratio of the second-harmonic generation to the dominating absorption process is, at best, unchanged with detuning from resonance. Since any nonlinear-optical material may be viewed as a summation of discrete level systems, the transparency assumption is *a priori* unjustified for any material.

The above argument leads us to expect that a numerical solution of Equation 9.6, taking both absorption and depletion into account [7], is always needed. In practice, however, it is seldom of any use in the perturbative regime. We generally expect that saturation in a three-level system will occur at roughly the saturation intensity of a similar two-level system (the rigorous derivation of section 9.4 will verify this to within a factor of two). The Rabi frequencies for which the perturbative treatment is meaningful are hence:

$$\Omega_{21} < \frac{1}{2}\sqrt{\frac{T_2}{T_1}}\sqrt{1+\Delta\tilde{\omega}^2} \tag{9.17}$$

where T_1 is the excited state's lifetime. The perturbative treatment near resonance is thus limited to small amplitudes (Ω_{21}<<1), and, using Equation 9.15, to small conversion efficiencies for which we are justified in neglecting the depletion of the first-harmonic. Therefore, when limited to nearly-resonant sub-saturation intensities, the non-depleted approximation is valid and a numerical solution using perturbative nonlinear coefficients [7] barely extends this range of validity. In Figure 9.1 we compare the predictions for the maximal amplitude conversion efficiency obtained by: neglecting the absorption (Equation 9.9), neglecting the depletion (Equation 9.15), using a numerical solution of the propagation equation with the perturbative coefficients (Equation 9.6), and using the nonperturbative solution of section 9.5 (Equation 9.35). Neglect of the depletion is shown to be a good approximation for resonantly-enhanced transitions in the intensity regime where a perturbative treatment is reasonable, i.e., $\Omega_{\omega} \overset{\sim}{<} 0.3$ (Figure 9.2a). This is essentially due to the fact that only small conversion efficiencies may be obtained near-resonance at subsaturation intensities. In the regime of high intensities and large values of the detuning, on the other hand (Figure 9.2b), the depletion must be included but neglect of the absorption is a reasonable approximation. Off-resonance, large values of the Rabi frequency (Ω_ω) do not lead to saturation and significant conversion is obtained at distances much shorter than the absorption length ($1/\alpha_{2\omega}$). Therefore, for optical frequencies detuned by more than the Rabi frequency (Ω_ω) the neglect of the absorption, which like the second-harmonic coefficient is second order in the detuning, may be *a postriori* justified. This regime is typical of second-harmonic generation in non-dispersive nonlinear crystals, but it is not relevant to intersubband transitions, where the transition frequency to line width ratio is limited.

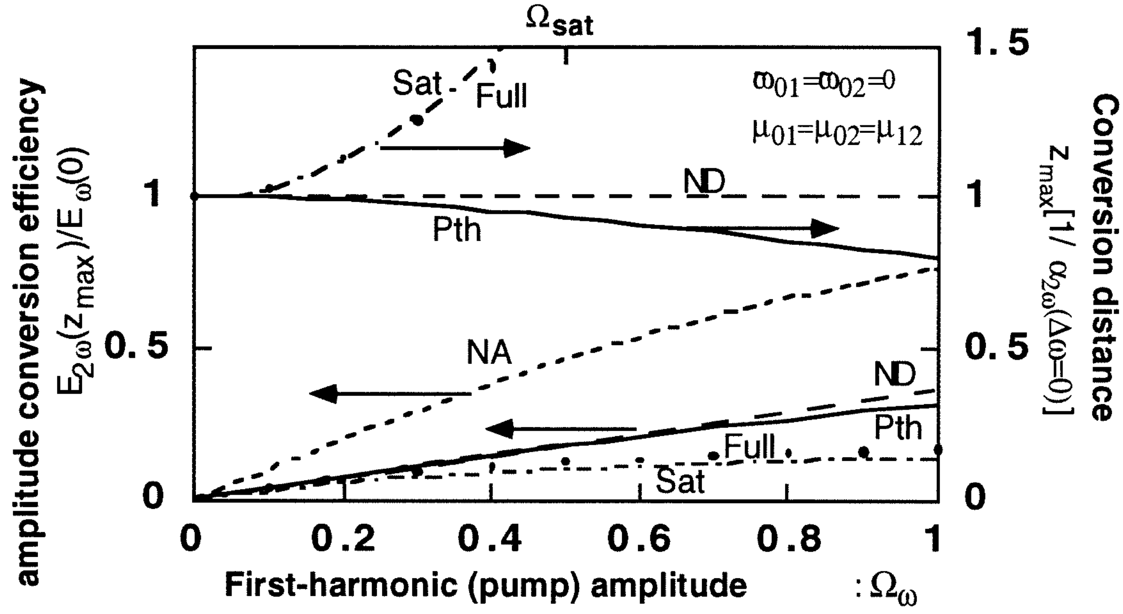

Figure 9.1a The second-harmonic amplitude conversion efficiency: $E_{2\omega}(z_{max})/E_\omega(0)$ and conversion length (z_{max}) versus normalized amplitudes at moderate pump intensities. The solid curve (Pth) is the results of the perturbative numerical solutions (Equation 9.6), the narrow-dashed curve (NA) is the "transparent" approximation (Equation 9.9), the wider dashed curve (ND) is the perturbative non-depleted approximation (Equation 9.15), the dashed-dotted line is the non-depleted and constant saturation approximation (Equation 9.34), and solid dots (Full) is the results of the nonperturbative treatment (Equation 9.35) for the double-resonant case ($\Delta\bar{\omega}=0$). Ω_{sat} stands for the saturation amplitude of an equivalent two-level system.

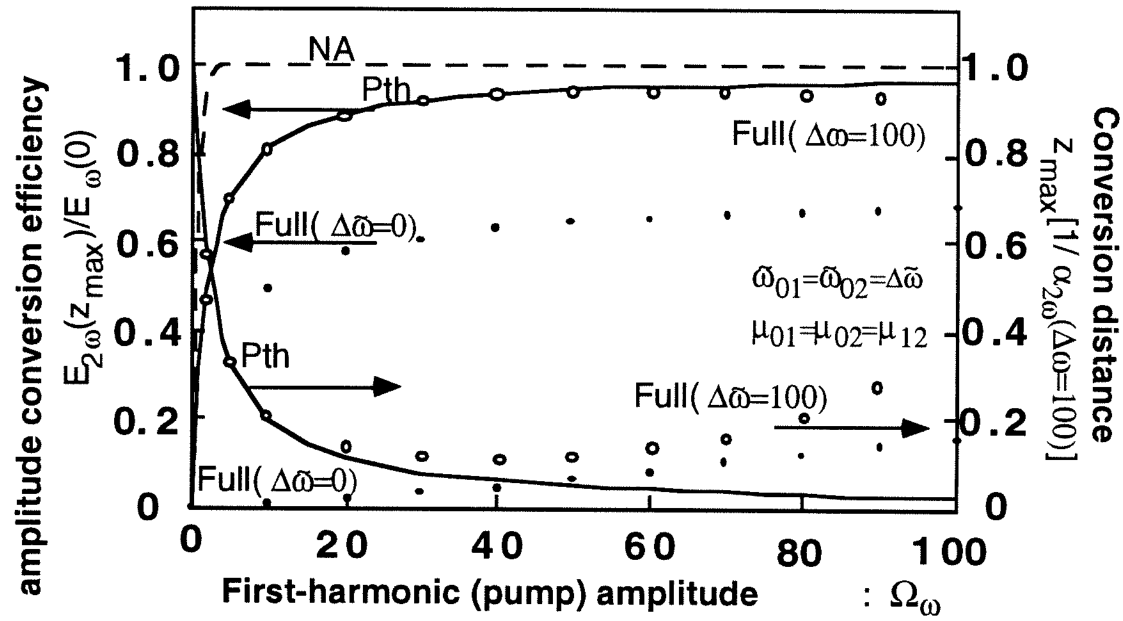

Figure 9.1b The second-harmonic amplitude conversion efficiency: $E_{2\omega}(z_{max})/E_{\omega}(0)$ *and conversion length* (z_{max}) *versus normalized amplitudes for strong pump intensities. The solid curve (Pth) is the results of the perturbative numerical solutions (Equation 9.6), the dashed curve (NA) is the "transparent" approximation (Equation 9.9), the solid dots (Full) are the results of the nonperturbative treatment (Equation 9.35) for the double-resonant case* ($\Delta\tilde{\omega}=0$)*, and the empty dots are the results of the nonperturbative treatment for a highly detuned case* ($\Delta\tilde{\omega}=100$)*.*

9.3 Transition Induced Phase-Mismatch

Before proceeding with a nonperturbative treatment of second-harmonic generation it is worthwhile to analyze the influence of the dispersion generated by the intersubband transitions [8]. It is common practice to assume that the strong interactions of intersubband transitions, and hence conversion lengths which are much shorter than the bulk's coherence length, allow for phase-matching issues to be neglected. In practice, saturation may greatly increase the interaction distances required for second-harmonic generation and the bulk's phase-mismatch may need to be considered. Furthermore, phase-matching may not be taken for granted even for subsaturation intensities and short propagation distances because of the large dispersion accompanying the intersubband transitions in accordance with the Kramers-Kronig relations [6]. These large index contributions could, as discussed in Chapter 4, compensate for the bulk phase-mismatch if correctly designed [9], but could, on the other hand, significantly limit conversion efficiencies even at short propagation lengths.

For the case of a non-dispersive host medium ($n_{2\omega}=n_{\omega}$) the phase-matching condition $\beta_{2\omega}=0$ (Equation 9.5c) becomes $\mathrm{Re}[\chi^{(1)}_{(\omega,\omega)}]=\mathrm{Re}[\chi^{(1)}_{(2\omega,2\omega)}]$. Thus, while equal imaginary components of the susceptibility satisfy the optimal ratio between the first and second-harmonic's absorption, equal real components satisfy the phase-matching condition. For equal strength transitions these conditions are simultaneously met by equal normalized detuning of the two harmonics ($\Delta\tilde{\omega}_{20}=\Delta\tilde{\omega}_{10}$). Full-resonance is the trivial case of equal detuning that has the advantage of no transition induced dispersions even when the interaction strengths are initially unequal or altered by saturation. When the real components of the linear susceptibilities are not equal, however, they constitute a transition induced phase mismatch which limits the coherence length to:

$$l_c \equiv \frac{\pi}{\beta_{2\omega}} = \frac{n\lambda/2}{\mathrm{Re}[\chi^{(1)}_{(2\omega,2\omega)}] - \mathrm{Re}[\chi^{(1)}_{(\omega,\omega)}]} \tag{9.18}$$

where λ is the first-harmonic's free space wavelength. For case of opposite normalized detuning ($\Delta\tilde{\omega}_{20}$=$-\Delta\tilde{\omega}_{10}$) the transition induced coherence length has a minimum of:

$$l_c = \frac{1}{2\alpha_{2\omega}(\Delta\tilde{\omega})}\left(\frac{\pi}{|\Delta\tilde{\omega}|}\right) = z_{\max}\frac{\pi}{2|\Delta\tilde{\omega}|} = \frac{\pi(1+\Delta\tilde{\omega}^2)}{2|\Delta\tilde{\omega}|\cdot\alpha_{2\omega}(0)} \tag{9.19}$$

where we have used the ratio between the real and imaginary components of the linear susceptibilities, and $1/\alpha_{2\omega}(0)$ and $1/\alpha_{2\omega}(\Delta\tilde{\omega})$ denote the amplitude extinction length for a line center and a detuned second-harmonic respectively. The transition-induced coherence length increases linearly with detuning, but its ratio to the length required for maximal conversion ($z_{\max}=1/\alpha_{2\omega}(\Delta\tilde{\omega})$) is inversely decreased. We thus see that for normalized values of the detuning larger than π/2, the transition-induced dispersion, rather than absorption, becomes the factor limiting second-harmonic generation conversion efficiencies. Thus for intersubband transitions in quantum wells, where the interaction length is typically significantly shorter than the bulk coherence length but on the order of the absorption length, phase-matching considerations may not be neglected. The effect of the intersubband transitions induced dispersion on the second-harmonic generation process is shown in Figure 9.2 for a pump amplitude where the perturbative treatment is still valid (Ω_ω=0.01). Phase-matched detuning ($\Delta\tilde{\omega}_{01}$=$\Delta\tilde{\omega}_{02}$) quadratically increases the conversion length but does not affect the absolute conversion; the anti-phase matched detuning ($\Delta\tilde{\omega}_{01}$=$-\Delta\tilde{\omega}_{02}$) on the other hand, leads to a phase mismatch with a coherence length given by Equation 9.19, or roughly: $l_c \cong \pi|\Delta\tilde{\omega}|/[2\alpha_{2\omega}(0)]$.

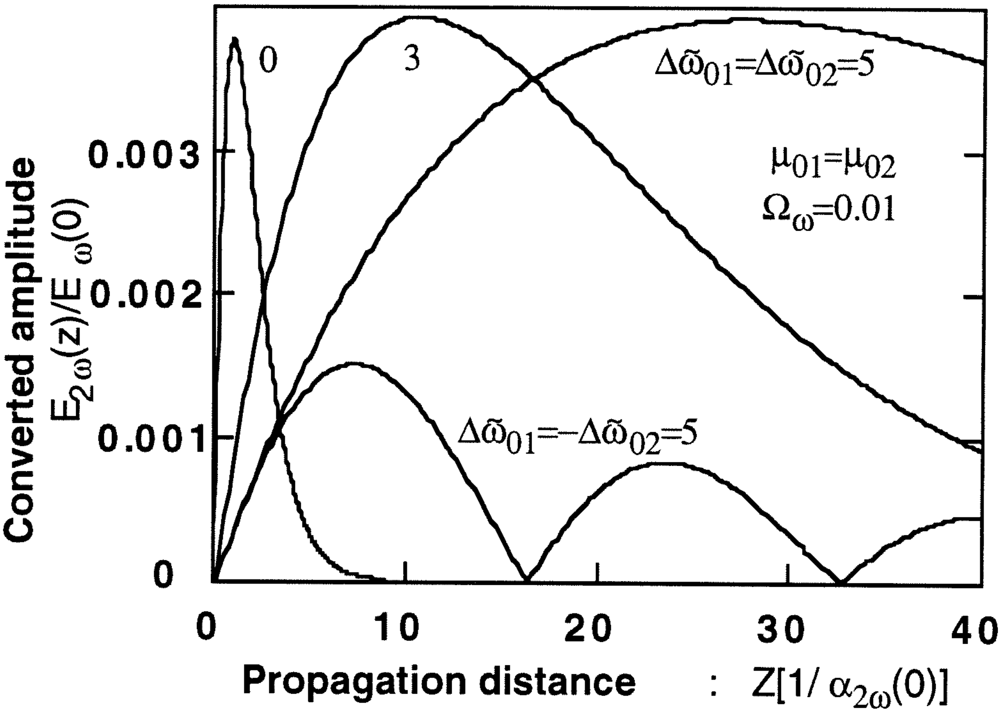

Figure 9.2: The generated second-harmonic amplitude ($E_{2\omega}(z)/E_{\omega}(0)$) in the perturbative regime (Ω_{ω}= 0.01) versus the propagation length (in units of the line center non-saturated extinction length) for several values of the detuning. It can be seen that phase-matched detuning ($\Delta\tilde{\omega}_{01} = \Delta\tilde{\omega}_{02}$) leads to equal conversion efficiencies but at increasing propagation lengths, whereas anti-phase matched detuning ($\Delta\tilde{\omega}_{01} = -\Delta\tilde{\omega}_{02}$) leads to a much smaller conversion efficiency (Equation 9.19).

9.4 Non-Perturbative Analysis

Nonperturbative models have been previously presented by DeTemple et al., for resonantly-enhanced second- [3] and third-harmonic generation [10] using the rotating-wave approximation. They show that, besides the obvious increase in the propagation length, saturation leads to a lower maximal conversion efficiency than would be expected from the perturbative treatment. Further conclusions show a nontrivial dependence of the conversion efficiency on the ratios between the optical dipole matrix elements. Boucaud et al. [11] experimentally demonstrated the saturation of second-harmonic generation in GaAs/AlGaAs asymmetric quantum wells. A maximal conversion efficiency of 3.4×10^{-4} was obtained for a 2.2μm propagation length at Brewster angle incidence. This conversion efficiency was obtained for an external pump intensity of $16\mathrm{MW/cm}^2$, equivalent to an effective intensity (internal and polarized along the growth direction) of $450\mathrm{kW/cm}^2$. A further increase in the pump intensity led to a decrease in the conversion efficiency demonstrating the saturation of the SHG coefficient.

We base our nonperturbative analysis of second-harmonic generation on the general formalism of section 6.1 which reduces all orders of harmonic generation to a coupled set of algebraic equations within the rotating wave approximation (Equations 6.11 and 6.13). For an n-level system the problem becomes that of n^2 real equations with $(n+4)(n-1)$ free parameters. For any given nonlinear process the equations are analytically soluble and effective nonperturbative nonlinear coefficients may be derived to replace the standard perturbative ones. Because these coefficients are intensity dependent, however, they vary along the propagation path rendering the propagation equations without an analytic solution. The multitude of parameters also leads to extremely complex expressions for the coefficients making any attempt at deriving simple optimization criteria difficult. These difficulties have caused the conclusions of the various treatments of resonantly-enhanced second-harmonic generation to differ. DeTemple [3] concluded that full-resonance maximized the conversion and that large efficiencies (>50%) are possible on-resonance at high intensities due to the "ac" -stark effect. Boucaud and Julien [4] later arrived at the opposite conclusion: i.e. that some detuning is necessary to obtain high conversion efficiencies. Ikonic et al. [12] considered the possibility of both tuning the transitions and quasi-phase matching via applied 'dc'-fields, assuming that larger efficiencies may be obtained at double-resonance. More recently, Meyer et al. [13] found, that some detuning may be advantageous, but of a rather limited contribution. Rosencher [7] used a numerical solution of the propagation equations but with perturbative coefficients and concluded that conversion efficiencies larger than 20% may be obtained on-resonance before the onset of saturation - questioning the practical necessity of the non-perturbative solutions. The inconsistencies between these various treatments [3,4,7,12,13] are due in part to the different approaches used, the multitude of free parameters involved and the different numerical values assumed.

As a starting point of the nonperturbative analysis we use the analytic solution of second-harmonic generation in the perturbative limit (section 9.2) which we modify to treat the high-intensity corrections [1,2]. Effective intensity dependent coefficients are defined for both the second-harmonic generation and the absorption enabling a qualitative analysis of the effects of saturation. We attempt to qualitatively clarify the behavior of resonantly-enhanced second-harmonic generation in the various regimes and obtain quantitative results from a full numerical solution. As we have shown above for nonparametric processes (Chapters 7 and 8), the perturbative expansion diverges at saturating intensities. Furthermore, upper limits can also be derived for the n$^{\underline{th}}$-Harmonic generation as a function of both the linear behavior and the saturation intensity. These limits are explicitly derived below for second-harmonic generation, a derivation that may be repeated for higher order harmonic generation or for sum/difference frequency generation.

The equations derived in chapter 6 for general orders of harmonic generation (Equation 6.15) are reduced in the case of second-harmonic generation to:

(9.20a-c)

$$(\Delta\tilde{\omega}_{01}\tilde{\rho}_{01} - i) = \tilde{\rho}_{12}^{*}\Omega_{2\omega}(\frac{T_{01}}{T_{02}}) - \tilde{\rho}_{02}\Omega_{\omega}^{*}(\frac{\mu_{12}}{\mu_{01}}) - (\rho_{00} - \rho_{11})\Omega_{\omega}$$

$$(\Delta\tilde{\omega}_{12}\tilde{\rho}_{12} - i) = \tilde{\rho}_{02}\Omega_{\omega}^{*}(\frac{T_{12}}{T_{01}}) - \tilde{\rho}_{01}^{*}\Omega_{2\omega}(\frac{T_{12}}{T_{02}}) - (\rho_{11} - \rho_{22})\Omega_{\omega}(\frac{\mu_{12}T_{12}}{\mu_{01}T_{01}})$$

$$(\Delta\tilde{\omega}_{02}\tilde{\rho}_{02} - i) = \tilde{\rho}_{12}\Omega_{\omega}(\frac{T_{02}}{T_{01}}) - \tilde{\rho}_{01}\Omega_{\omega}(\frac{\mu_{12}T_{02}}{\mu_{01}T_{01}}) - (\rho_{00} - \rho_{22})\Omega_{2\omega}$$

plus their complex conjugates for the off-diagonal susceptibility terms, and:

(9.20:g-i)

$$\frac{\rho_{00} - \rho_{00}^{e}}{2}(\frac{T_{01}}{T_{00}}) = \mathrm{Im}[\tilde{\rho}_{01}\Omega_{\omega}^{*} + \tilde{\rho}_{02}\Omega_{2\omega}^{*}(\frac{T_{01}}{T_{02}})]$$

$$\frac{\rho_{11} - \rho_{11}^{e}}{2}(\frac{T_{01}}{T_{11}}) = \mathrm{Im}[\tilde{\rho}_{12}\Omega_{\omega}^{*}(\frac{\mu_{12}}{\mu_{01}}) - \tilde{\rho}_{01}\Omega_{\omega}^{*}]$$

$$\frac{\rho_{22} - \rho_{22}^{e}}{2}(\frac{T_{02}}{T_{22}}) = -\mathrm{Im}[\tilde{\rho}_{02}\Omega_{2\omega}^{*} + \tilde{\rho}_{12}\Omega_{\omega}^{*}(\frac{\mu_{12}T_{02}}{\mu_{01}T_{01}})]$$

for the diagonal terms, where we have defined normalized first- and second-harmonic Rabi frequencies as: $\Omega_\omega \equiv \Omega_{101} T_{10}$ and $\Omega_{2\omega} \equiv \Omega_{202} T_{20}$, respectively ($\Omega_{ijk}$ is defined in Equation 9.16). To examine the modification of the perturbative conclusions we define effective linear and nonlinear coefficients ($\chi^{(eff)}_{(2\omega,\omega,\omega)}$) according to:

$$Nq\mu_{02}\tilde{\rho}_{02} \equiv \varepsilon_0 \chi^{(eff)}_{(2\omega,2\omega)} \cdot E_{2\omega} + \varepsilon_0 \chi^{(eff)}_{(2\omega,\omega,\omega)} E_\omega^{\ 2} \tag{9.21a}$$

and:

$$Nq(\mu_{01}\tilde{\rho}_{01} + \mu_{12}\tilde{\rho}_{12}) \equiv \varepsilon_0 \chi^{(eff)}_{(\omega,\omega)} \cdot E_\omega + \varepsilon_0 \chi^{(eff)}_{(\omega,2\omega,-\omega)} \cdot E_{2\omega} E_\omega^* \tag{9.21b}$$

These effective coefficients, defined analogously with the standard linear and second-order coefficients, are no longer constants and must be found for each specific set of field components. They are only uniquely defined when one field component is negligible, or as derivatives in a small-signal approach.

The general algebraic solution for the set of nine susceptibility equations with 14 free parameters (Equation 9.20) is extremely cumbersome. Since the generated second-harmonic is still quite small at the divergence of perturbative treatment (Figure 9.1a), we begin by considering an arbitrary first-harmonic but a weak second-harmonic. By presenting solutions for several selected cases we obtain a qualitative understanding of the high-intensity phenomena, isolate the influence of the various system parameters, and in particular study the saturation of the effective linear and non-linear coefficients.

The simplest solution for equation 9.20 is found in the case of double-resonance, all equal dipole matrix elements, and all equal relaxation times. The effective second-harmonic generation coefficient becomes:

$$\chi^{(eff)}_{(2\omega,\omega,\omega)} \equiv \frac{Nq\mu_{02}\tilde{\rho}_{02}}{\varepsilon_0 E_\omega^2} = \frac{[\chi^{(2)}_{(2\omega,\omega,\omega)}]_{res}}{1+8\Omega_\omega{}^2} \tag{9.22a}$$

In a case which is more realistic for intersubband transitions, the lifetimes ($T_{ii}\equiv T_1$) are different (larger) than the dephasing times ($T_{ij}\equiv T_2$), in which case the effective susceptibility becomes:

$$\chi^{(eff)}_{(2\omega,\omega,\omega)} = \frac{\chi^{(2)}_{(2\omega,\omega,\omega)}}{[1+2\Omega_\omega^2(1+3T_1/T_2)]} \tag{9.22b}$$

This equation resembles the expression for the absorption in a two-level system (Equation 7.5), but with a faster rate of saturation. The self-saturation in a three-level system is obtained as:

$$\chi^{(eff)}_{(\omega,\omega)} = \frac{\chi^{(1)}_{(\omega,\omega)}}{(1+2\Omega_\omega^2 T_1/T_2)}, \tag{9.23a}$$

for the linear susceptibility of the first (pump) harmonic, and:

$$\chi^{(eff)}_{(2\omega,2\omega)} \equiv \frac{Nq\mu_{02}}{\varepsilon_0}\frac{\partial\tilde{\rho}_{02}}{\partial E_{2\omega}} = [\chi^{(1)}_{(2\omega,2\omega)}]_{res}\frac{(1+5\Omega_\omega{}^2)}{(1+8\Omega_\omega{}^2)(1+2\Omega_\omega{}^2)} \tag{9.24}$$

for the linear susceptibility of the second-harmonic (where the case of equal relaxation times is given for simplicity). The higher coefficient in the denominator of Equation 9.22a shows a faster rate of saturation for the second-harmonic generation process versus the saturation of either harmonic's absorption. We can conclude from this (without resorting to the numerical solution used to obtain Figure 9.1) that the perturbative treatment of second-harmonic generation is limited to intensities lower than the saturation intensity of a two-level system with the same dipole matrix elements and relaxation times. Another conclusion is that since the second-harmonic generation coefficient saturates more readily than the absorption in a three-level system, and since the second-harmonic conversion efficiency is generally proportional to the ratio of the second-harmonic generation to the absorption coefficients (Equation 9.14), the conversion efficiencies at saturating intensities will be smaller than those predicted from the perturbative treatment. This also suggests that at high intensities intentional detuning from resonance will lead to higher conversion efficiencies by reducing saturation. The influence of detuning on the conversion efficiency, however, turns out to be quite involved [2] as is discussed in more detail in section 9.5.2.

9.4.1 Optical Dipole Matrix Elements

Before proceeding with the full numerical solution in section 9.5, we analyze the influence of the optical dipole matrix elements and of the relaxation times in this and the next section, respectively. The perturbative solution (Equation 9.15) showed that, since up to second-order perturbation theory the transition between the excited states (1→2) contributes to the second-harmonic generation but not to either harmonic's linear absorption, the maximal (amplitude) conversion efficiency is linearly proportional to the optical dipole matrix element between them (μ_{12}). For saturating intensities, however, where a non-negligible part of the population is transferred to the excited states, the dependence on the excited states dipole element (μ_{12}) becomes more complex. To isolate this dependence we assume double-resonance and equal ground state dipole elements ($\mu_{01}=\mu_{02}$), and solve the density matrix equations (Equation 9.20) to obtain:

$$\chi^{(eff)}_{(2\omega,\omega,\omega)} \equiv \frac{N\mu_{02}\tilde{\rho}_{02}}{\varepsilon_0 E_\omega^{\ 2}} = [\chi^{(2)}_{(2\omega,\omega,\omega)}]_{res}\frac{(\mu_{12}/\mu_{01})[1+2\Omega_\omega^2(2(\mu_{12}/\mu_{01})^2-1)]}{[1+4\Omega_\omega^2((\mu_{12}/\mu_{01})^2+1)][1+\Omega_\omega^2((\mu_{12}/\mu_{01})^2+1)]} \tag{9.25}$$

We find by differentiation that in the high-intensity limit the absolute value of $\chi^{(2)}_{(2\omega,\omega,\omega)}$ has maximums at $\mu_{12}/\mu_{01}=\sqrt{9\pm\sqrt{73}}/2\cong 2.09$ or 0.338. We also see that for:

$$\Omega_\omega = \sqrt{\frac{1}{2[1-2(\mu_{12}/\mu_{01})^2]}} \tag{9.26}$$

the second-harmonic generation coefficient becomes identically zero ($\chi^{(eff)}_{(2\omega,\omega,\omega)}=0$) due to destructive interference. Thus for all dipole element ratios obeying: $(\mu_{12}/\mu_{01})<1/\sqrt{2}$ there exists an amplitude of the first-harmonic where the second-harmonic generation disappears. In the high amplitude limit that dipole element ratio becomes $(\mu_{12}/\mu_{01})=1/\sqrt{2}$. This zero crossing of the second-harmonic generation coefficient has no analog in the perturbative treatment as it does not occur for $\Omega_\omega<1/\sqrt{2}$. It is also not shared by the first-harmonic's linear absorption coefficient given by:

$$\chi^{(eff)}_{(\omega,\omega)} \equiv \frac{N\mu_{12}(\tilde{\rho}_{01}+\tilde{\rho}_{12})}{\varepsilon_0 E_\omega} = [\chi^{(1)}_{(\omega,\omega)}]_{res}\frac{[1+\Omega_\omega^2+3\Omega_\omega^2(\mu_{12}/\mu_{01})+4\Omega_\omega^2(\mu_{12}/\mu_{01})^2]}{[1+4\Omega_\omega^2((\mu_{12}/\mu_{01})^2+1)][1+\Omega_\omega^2((\mu_{12}/\mu_{01})^2+1)]} \tag{9.27}$$

The first harmonic's absorption ($\chi^{(1)}_{(\omega,\omega)}$) thus has a maximum for a ratio of ($\mu_{12}/\mu_{01}=\sqrt{2}$) and then monotonicly decreases for increasing ratios. Figure 9.3 shows the second-harmonic generation coefficient (a) and the first-harmonic absorption (b) versus the dipole element ratio at several intensities. We see that at low intensities the effective second-harmonic generation coefficient is maximized for: μ_{12}/μ_{01}->$1/\Omega_\omega$ and does not monotonicly increase with μ_{12}/μ_0 as expected from the perturbative treatment. Increasing dipole ratios do, however, lead to a higher conversion efficiency, as the absorption decreases more steeply with them.

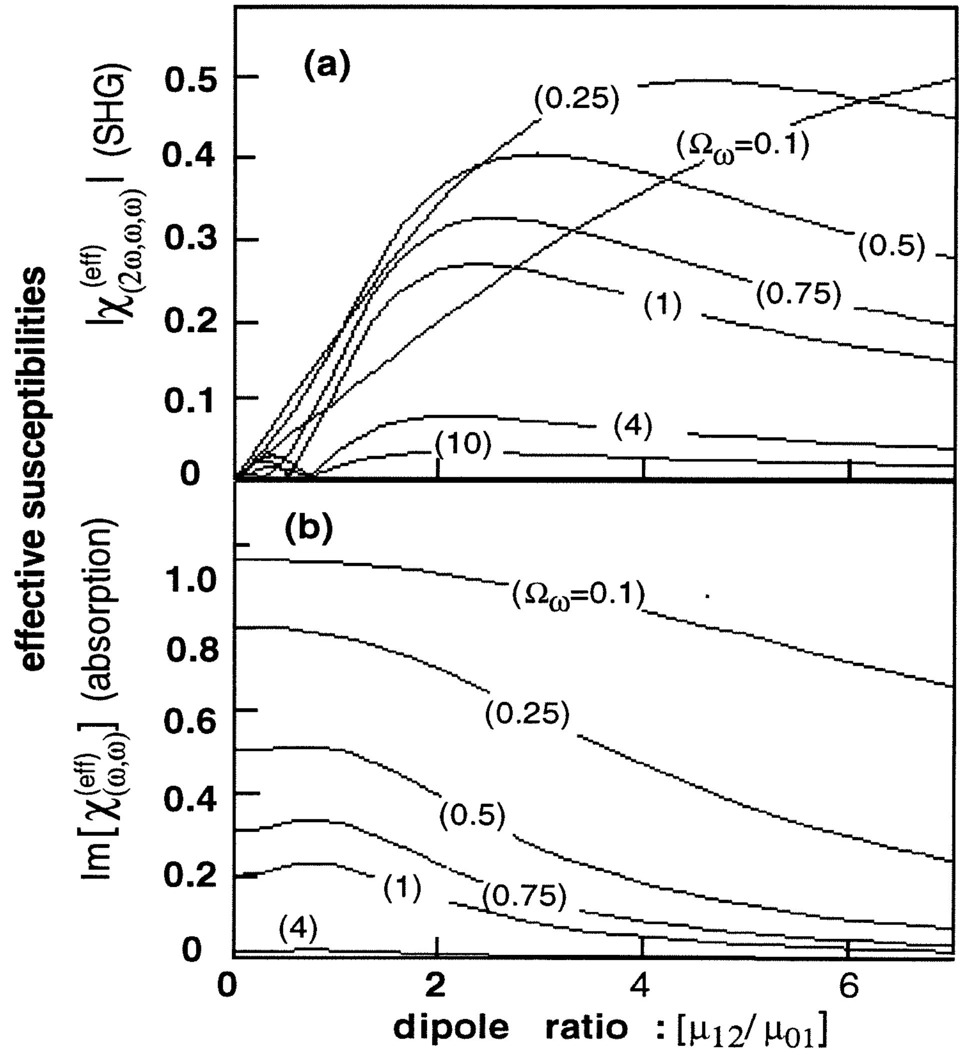

Figure 9.3: The effective second-harmonic generation coefficient (Equation 9.25) and first-harmonic absorption coefficient (Equation 9.27) versus the ratio of the optical dipole matrix elements (μ_{12}/μ_{01}) for several values of the first-harmonic amplitude (Ω_ω).

9.4.2 Relaxation Rates

Although the relaxation times in quantum wells are more difficult to modify than the transition energies or the optical dipole matrix elements, it is still worthwhile to examine their influence upon second-harmonic generation. Because for intersubband transitions the life time may be up to an order of magnitude greater than the dephasing time, we examine the situation of a uniform lifetime ($T_{00}=T_{11}=T_{22}\equiv T_1$), and a uniform but different dephasing time ($T_{12}=T_{23}=T_{13}\equiv T_2$). By solving the density matrix equations (Equation 9.20) for the double-resonance and equal dipole matrix elements case we find the effective second-harmonic generation coefficient as:

$$\chi^{(eff)}_{(2\omega,\omega,\omega)} = \frac{\chi^{(2)}_{(2\omega,\omega,\omega)}}{[1+2\Omega_\omega^2(1+3T_1/T_2)]} \tag{9.28}$$

and the effective first-harmonic linear coefficient as:

$$\chi^{(eff)}_{(\omega,\omega)} = \frac{\chi^{(1)}_{(\omega,\omega)}}{(1+2\Omega_\omega^2 T_1/T_2)} \tag{9.29}$$

Hence, as expected, a larger ratio between lifetimes and dephasing times (T_1/T_2) increases the saturation rates. This will limit the perturbative solution to smaller normalized amplitudes (Ω_ω) and hence smaller conversion efficiencies before the onset of saturation.

9.4.3 Pump Saturation of Second-Harmonic Absorption

Following the notation of this chapter, the effective linear susceptibility of a two-level system (Equation 7.5) is given as:

$$[\chi^{(eff)}_{(\omega,\omega)}]_{2-level} \equiv -\frac{N\mu_{01}\tilde{\rho}_{01}}{\varepsilon_0 E_\omega} = i[\chi^{(1)}_{(\omega,\omega)}]_{res}\frac{(\Delta\omega - i)}{(1+\Delta\omega^2+4\Omega_\omega^{\ 2}T_1/T_2)} \tag{9.30}$$

Comparing this to the absorption in a three-level system derived in Equation 9.23a, we see that the addition of a third equidistant level halves the saturation rate. In a three-level system, however, the pump will not only saturate its own absorption but that of the second-harmonic as well. To examine this a finite second-harmonic term is kept in the solution of the density matrix equations. Solving for the simplest case: on-resonance and all equal relaxation times and dipole elements, we obtain:

$$\tilde{\rho}_{02} = \frac{-\Omega_\omega^{\ 2}(1+2\Omega_\omega^{\ 2})+\Omega_{2\omega}(1+5\Omega_\omega^{\ 2}+2\Omega_{2\omega}\Omega_\omega^{\ 2}+\Omega_{2\omega}^{\ 2})}{(1+10\Omega_\omega^{\ 2}+16\Omega_\omega^{\ 4}+5\Omega_{2\omega}^{\ 2}+16\Omega_\omega^{\ 2}\Omega_{2\omega}^{\ 2}+4\Omega_{2\omega}^{\ 4})} \tag{9.31}$$

By keeping only first order terms of the second-harmonic this simplifies to:

$$\tilde{\rho}_{02} = \frac{-\Omega_\omega^{\ 2}}{(1+8\Omega_\omega^{\ 2})}+\Omega_{2\omega}\frac{(1+5\Omega_\omega^{\ 2})}{(1+8\Omega_\omega^{\ 2})(1+2\Omega_\omega^{\ 2})} \tag{9.32}$$

The first term on the R.H.S is the second-harmonic generation term (Equation 9.22a) and the second is the second-harmonic's linear (absorption) term. The effective second-harmonic linear susceptibility is thus:

$$\chi^{(eff)}_{(2\omega,2\omega)} \equiv \frac{N\mu_{02}}{\varepsilon_0}\frac{\partial\tilde{\rho}_{02}}{\partial E_{2\omega}} = [\chi^{(1)}_{(2\omega,2\omega)}]_{res}\frac{(1+5\Omega_\omega^{\ 2})}{(1+8\Omega_\omega^{\ 2})(1+2\Omega_\omega^{\ 2})} \tag{9.33a}$$

where:

$$[\chi^{(1)}_{(2\omega,2\omega)}]_{res} = -i\frac{N\mu_{02}^2 T_2}{\hbar\varepsilon_0} \tag{9.33b}$$

is the second-harmonic's line center non-saturated linear susceptibility.

From Equation 9.33 we see that the real component of the susceptibility for the second-harmonic saturates at a different rate than that of the first-harmonic given by Equation 9.23. This may introduce a phase-mismatch at high intensities even when the susceptibility at the two frequencies is equal in the perturbative regime. Only in the double-resonance case, when the linear susceptibility terms are pure imaginary, the transitions cannot induce a phase-mismatch. Figure 9.4, generated with the numerical solution of section 9.5, shows the dispersion induced by uneven saturation for values of the detuning that would not lead to a phase-mismatch in the perturbative regime (wide-dashed curve). It is interesting that, for this specific case, opposite detuning actually leads to a greater conversion efficiency than equal detuning. There is however, as shown in section 9.5.2, no simple guideline for optimizing the tradeoff between the reduced saturation and the increased dispersion accompanying detuning.

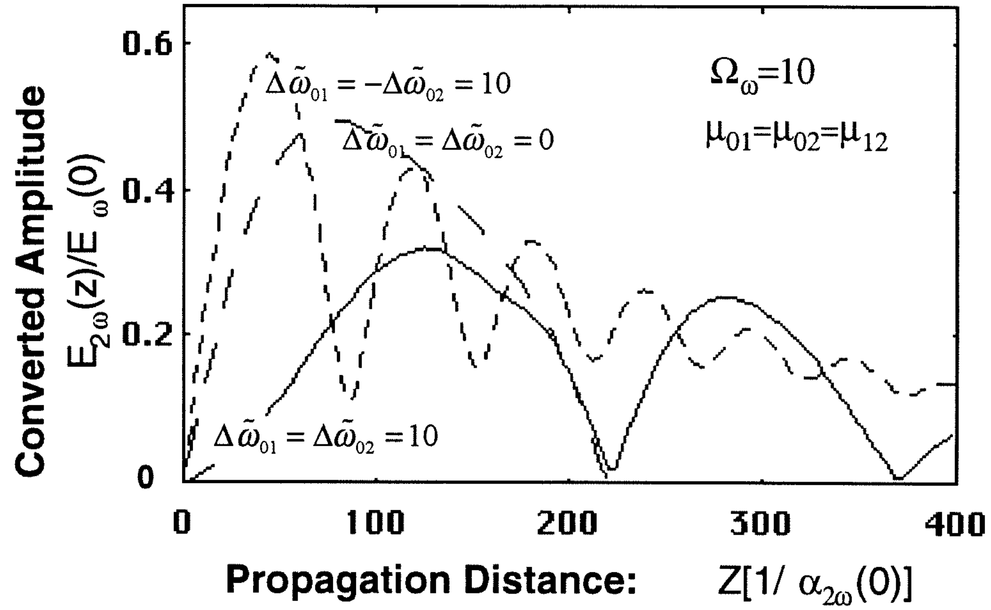

Figure 9.4: The generated second-harmonic amplitude versus propagation length demonstrating saturation induced phase-mismatch. Whereas the doubly-resonant case (wide dashed curve) remains phase-matched, the equally detuned case (the solid curve) looses its phase-matching because of the unequal saturation of the ground to first and ground to second state transitions. The narrow-dashed curve shows the case of opposite detuning which is not phase-matched even at perturbative pump intensities.

9.4.4 Saturated Propagation Equations

The effective susceptibilities derived above (Equations 9.21 through 9.33) may be used to crudely include the effects of saturation in an analytic solution of the propagation equations (Equation 9.6). By considering no depletion of the first-harmonic, only linear dependence on the second-harmonic, and a uniform level of saturation along the propagation path, the perturbative coefficients in the solution (Equation 9.14) may be replaced with the saturated ones. On resonance and for equal dipole elements and relaxation times we obtain:

$$\Omega_{2\omega}(\tilde{z}) = i\frac{(1+2\Omega_{\omega}^{2})}{3\Omega_{\omega}}\{e^{-2\tilde{z}/(1+2\Omega_{\omega}^{2})} - e^{-2\tilde{z}(1+5\Omega_{\omega}^{2})/[(1+8\Omega_{\omega}^{2})(1+2\Omega_{\omega}^{2})]}\} \qquad (9.34)$$

This non-depleted and constant saturation approximation is plotted as the dashed-dotted curve (Sat) in Figure 9.1a, along with the perturbative results presented above (section 9.2) and the full numerical solution of the next section (9.5). It can be seen that this crude approximation is a significant improvement over the perturbative approach for moderate pump intensities.

9.5 Propagation Equations

9.5.1 Upper Limits on Second-Harmonic Generation

Since the induced second-harmonic polarization is no longer a simple quadratic function of the first-harmonic amplitude, the wave-equations (Equation 5.17) can no longer be analytically solved. They are hence rewritten as:

$$\frac{\partial\Omega_{2\omega}}{\partial\tilde{z}}=\frac{i(n_{\omega}^{2}-n_{2\omega}^{2})}{[\chi^{(1)}_{(\omega,\omega)}]_{res}}\Omega_{2\omega}-i\tilde{\rho}_{02}(\frac{\mu_{02}}{\mu_{01}})^{2} \tag{9.35a}$$

and:

$$\frac{\partial\Omega_{\omega}}{\partial\tilde{z}}=\frac{-i}{2}(\tilde{\rho}_{01}+\tilde{\rho}_{12}\frac{\mu_{12}}{\mu_{01}}) \tag{9.35b}$$

where the normalized distance $\tilde{z}$ is defined in units of half the line center's non-saturated absorption extinction length (i.e. the intensity extinction length) as:

$$\tilde{z}\equiv(2\alpha_{\omega})\cdot z=\frac{\omega}{nc}[\chi^{(1)}_{(\omega,\omega)}]_{res}\cdot z=\frac{\omega}{nc}\frac{N\mu_{01}^{2}T_{01}}{\varepsilon_{0}\hbar}\cdot z \tag{9.36}$$

The second-harmonic generation rate (Equation 9.35a) is proportional to $\tilde{\rho}_{02}$ which saturates (Equation 9.28) to a value of $1/[2\times(1+3T_1/T_2)]$, or simply 1/8 for equal diagonal and off-diagonal relaxation rates. Since the second-harmonic only induces transitions between the ground and second subbands, its saturation amplitude is identical to that of a two-level system (Equation 7.5 - $\Omega_{2\omega}^{sat} = 1/2\sqrt{T_2/T_1}$). The upper limit on the second-harmonic amplitude that may be generated in a given interaction distance is thus:

$$\frac{\Omega_{2\omega}(\tilde{z})}{\Omega_{2\omega}^{sat}} \leq \frac{\tilde{z}}{\sqrt{T_2/T_1} + 3\sqrt{T_1/T_2}} \tag{9.37a}$$

In terms of intensity this limit becomes:

$$I_{2\omega}(\tilde{z}) < I_{2\omega}^{sat} \cdot (\tilde{z}/4)^2 \qquad \forall \;\; T_2 = T_1 \tag{9.37b}$$

and:

$$I_{2\omega}(\tilde{z}) < I_{2\omega}^{sat} \cdot \frac{T_2}{T_1} \cdot (\tilde{z}/3)^2 \quad \forall \;\; T_1 >> T_2 \tag{9.37c}$$

These are absolute upper limits on the generated second-harmonic and not on the conversion efficiency. They will only be reached when the transitions are completely saturated all through the propagation length, i.e., increasingly larger pump intensities will be necessary to approach this limit for increasing propagation lengths. It is easy to show that $\eta \leq \tilde{z}^2/[8(1+3T_1/T_2)]$ is a crude upper bound for the (intensity) conversion efficiency, but a more accurate estimate requires a numerical solution of the propagation equations.

To demonstrate the fundamental limit derived in Equation 9.37 we consider the case of propagation through the nonsaturated extinction length of the first-harmonic: $\tilde{z}=1$, i.e., $z \cong 10\mu m$ for typical intersubband transitions. Assuming: $T_1/T_2=10$, and a saturation intensity of 500kW/cm^2, the upper limit on the generated second-harmonic intensity is roughly 5kW/cm^2. Figure 9.5 shows the conversion efficiency (for $T_1/T_2=1$) as a function of the incident first-harmonic (pump) amplitude for several values of the detuning and for three given propagation lengths. For a propagation distance of one extinction length the conversion efficiency is limited to about 1%. This value is even further reduced for unequal relaxation rates ($T_1>T_2$). Similarly to the case of phase-modulation discussed in Chapters 7 and 8, a demand for a given generated second-harmonic intensity leads to a demand for a minimal propagation length.

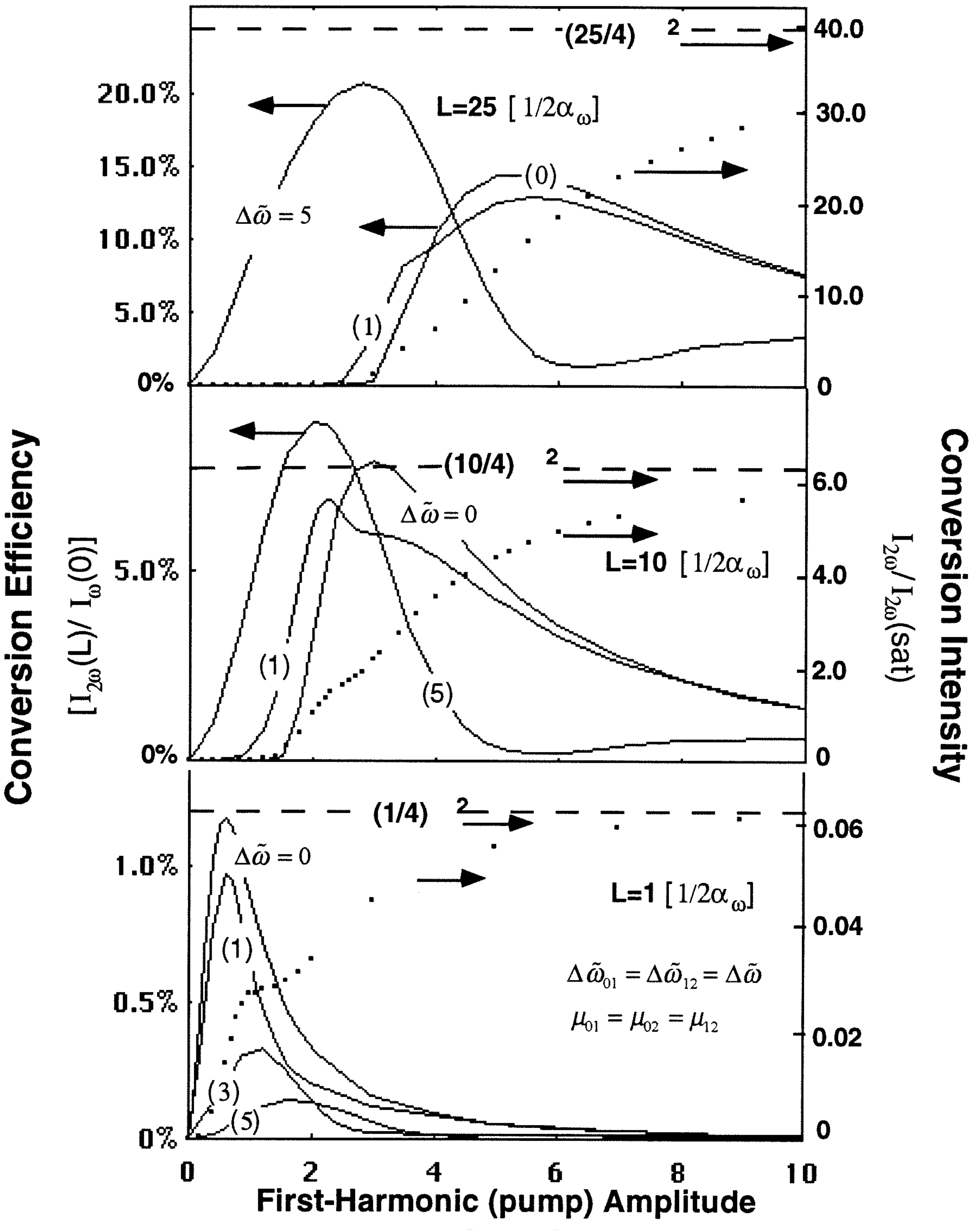

Figure 9.5: The second-harmonic intensity conversion efficiency at the end of a finite thickness propagation layer versus the initial pump amplitude for several values of the detuning for a propagation layer thickness (L) of $L=25/\alpha_{2\omega}$ (a), of $L=10/\alpha_{2\omega}$ (b) and of $L=1/\alpha_{2\omega}$ (c). The absolute converted second-harmonic intensities are shown (the dots) for the resonant cases only.

Figure 9.6, shows the conversion efficiency and length as a function of pump intensity for various ratios of the dipole matrix elements (μ_{01}/μ_{02}). For the case of all equal lifetimes and dipole matrix elements, a propagation length of roughly 100 times the unsaturated extinction length and a pump intensity of over 100 times the saturation intensity will be needed to reach 25% intensity conversion efficiency. The limited second-harmonic generation conversion efficiencies presently obtained using intersubband transitions can be understood in this view. It seems some more optimistic predictions [7] will probably not be realized unless propagation lengths are significantly extended. Although a larger ratio of the excited state dipole matrix element (μ_{12}) to that of the ground state (μ_{01}) leads to a better conversion efficiency, it should be remembered that there are practical limits on the magnitudes of the obtainable dipole matrix elements. A high value of the ratio would therefore come at the expense of a small μ_{01} and hence lead to a quadratic increase in the required propagation length.

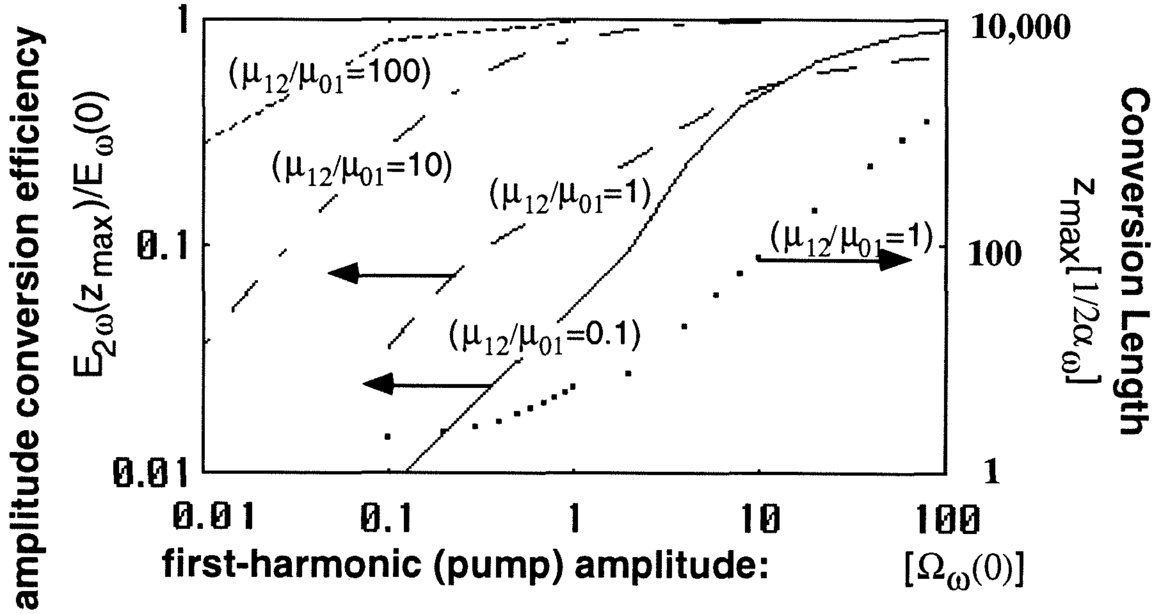

Figure 9.6: The numerically derived on-resonance conversion efficiency versus normalized amplitude (Ω_ω) for several values of the dipole matrix element ratio: μ_{12}/μ_{01}. The conversion distance (the dots) is only shown for $\mu_{12}/\mu_{01}=1$, but this curve is typical of the other ratios.

9.5.2 Detuning Considerations

In sections 9.2 and 9.3 we showed that within the perturbative treatment, and with the nondepleted first-harmonic approximation, full resonance is the optimal conversion condition. However, when saturation of the nonlinear coefficients is taken into account the conclusions become considerably more complex. The multitude of parameters involved in a three-level system make it impossible to reach a general conclusion on the preferred detuning, but it is apparent from the unequal saturation rates of the second-harmonic generation (Equation 9.28) and absorption (Equation 9.29) coefficients that the perturbative conclusions will be modified. An example of the influence of detuning on second-harmonic generation at high-intensities ($\Omega_\omega=10$) is shown in Figure 9.7. It can be seen that unlike in the perturbative regime (Figure 9.2), saturation makes some detuning advantageous despite the created phase-mismatch - although at the expense of longer propagation lengths. As the dashed curves in Figure 9.7 show, the advantage becomes even more significant when phase-matching is externally imposed (PM).

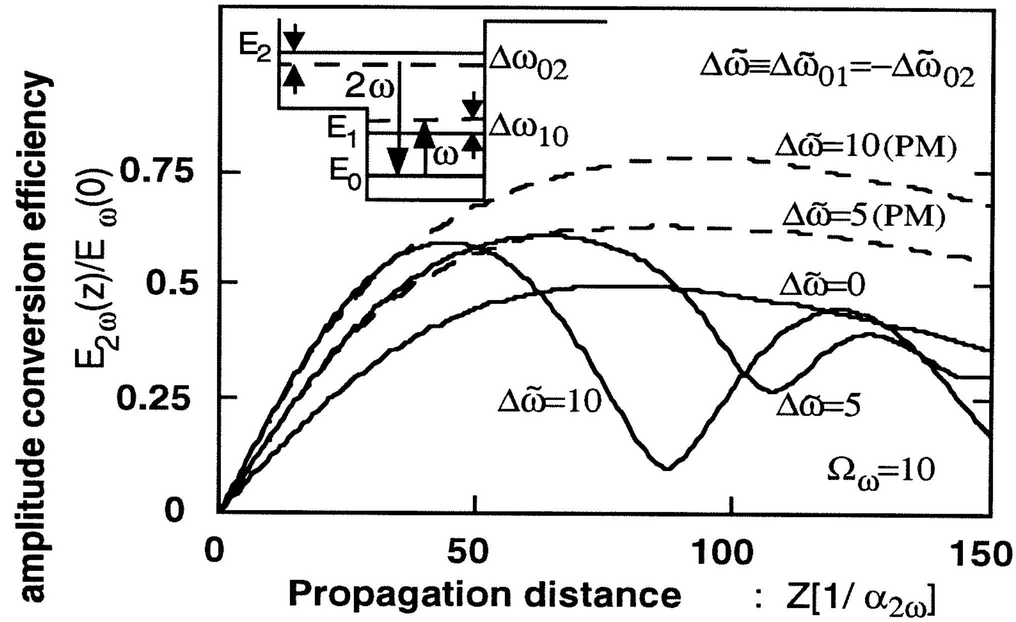

Figure 9.7 The numerically derived second-harmonic amplitude: $E_{2\omega}(z)/E_\omega(0)$*, versus propagation length for several values of opposite detuning (*$\Delta\tilde{\omega}_{01} = -\Delta\tilde{\omega}_{02}$*) at a saturating (*$\Omega_\omega=10$*) optical intensity. It can be seen that in this case larger anti-phase matched detuning (*$\Delta\tilde{\omega}_{01} = -\Delta\tilde{\omega}_{02}$*) leads to a higher conversion efficiency despite the induced phase-mismatch. The dashed curves show that the contribution of detuning is much greater when phase-matching is externally enforced (PM). The inset depicts the energy levels in a corresponding step quantum well.*

Since the conclusions of Figure 9.7 may not be simply generalized, a more systematic study of the effects of detuning is needed. The numerically derived conversion efficiency and conversion length, for a low ($\Omega_\omega=0.1$), a moderate ($\Omega_\omega=1$), and a highly saturating ($\Omega_\omega=10$) initial first-harmonic amplitude are plotted versus detuning in Figure 9.8. This is repeated for equal detuning of both harmonics (Figure 9.8a-b), and for opposite detuning of the two harmonics (Figure 9.8c-d). We see that, even for moderate amplitudes, increasing (equal) detuning leads to some improvement in the maximal conversion efficiency. This is in contrast with the perturbative results which showed that the conversion efficiency is independent of detuning (Figure 9.5). At moderate amplitudes, however, the minor improvements that may be obtained with increased detuning come with the penalty of a quadratic increase in the conversion length (Figure 9.8b). Only at high amplitudes (Ω_ω=10), where the conversion distance hardly increases with detuning, does it actually become favorable to detune from resonance. The crossing behavior between the high and low amplitude curves, seen in Figure 9.8b, is due to the transition from the saturated to the perturbative regime with increased detuning.

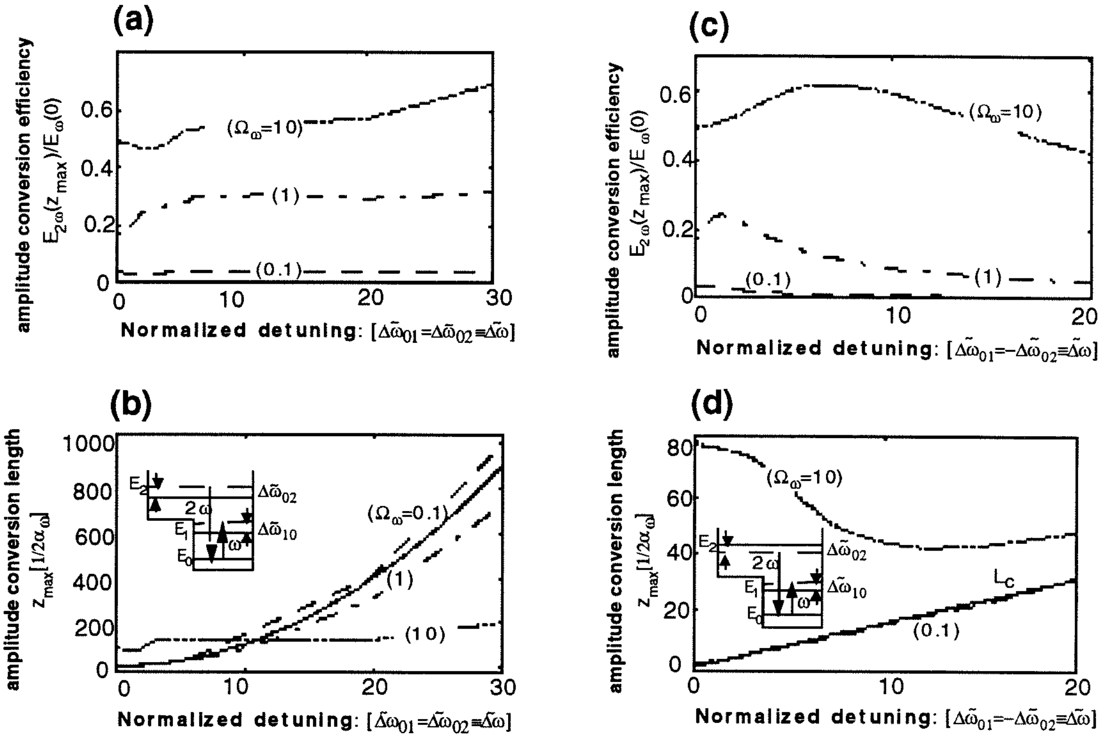

Figure 9.8: The numerically derived conversion efficiency and the distance at which it is obtained versus detuning for a low ($\Omega_\omega=0.1$), a moderate ($\Omega_\omega=1$), and a highly saturating ($\Omega_\omega=10$) initial first-harmonic amplitudes for equal (a and b) and opposite (c and d) detuning of the two harmonics. The solid curve in d is the transition-induced coherence length (Equation 9.19).

From the perturbative treatment (Equation 9.19) we expect a larger induced phase-mismatch for unequal detuning, where the extreme phase-mismatch occurs for the case of opposite detuning ($\Delta\tilde{\omega}_{01}=-\Delta\tilde{\omega}_{02}$) which is shown in Figure 9.8c and d. The trade-off between the reduced saturation and increased phase-mismatch as a result of detuning leads to the maximums in the conversion efficiency curves shown in Figure 9.8c. Figure 9.7 thus represents only a specific case of anti-phase-matched detuning that is actually favorable. The conversion distances in Figure 9.8d eventually approach the perturbative coherence length linear limit of $L_C=|\Delta\tilde{\omega}|*\pi/2$ for all amplitudes (Equation 9.19). This dependence is quite distinct from the quadratic one, approaching the extinction length, seen for the phase-matched case in Figure 9.8b.

In some recent studies of intersubband second-harmonic generation it has been suggested that detuning of the second-harmonic may improve the conversion efficiency by reducing the absorption of the generated harmonic. Figure 9.9a and Figure 9.9b plot the conversion efficiency and length for a resonant first-harmonic versus detuning of the second-harmonic. It can be seen that the optimal detuning is roughly $\sqrt{2}$ times the first-harmonic's Rabi frequency when the propagation length is not otherwise limited. Thus, unlike the perturbative regime, where we've shown detuning of the second-harmonic to be detrimental, some detuning ($\Delta\tilde{\omega}_{21}=\sqrt{2}*\Omega_{\omega}$) helps reduce saturation at higher intensities. Figure 9.9c and Figure 9.9d plot the conversion efficiency and length for a resonant second-harmonic versus detuning of the first-harmonic. Both the low and high amplitude limits display a monotonic decrease in the conversion efficiency with the first-harmonic's detuning, while in the moderate regime there is a local maximum for finite detuning.

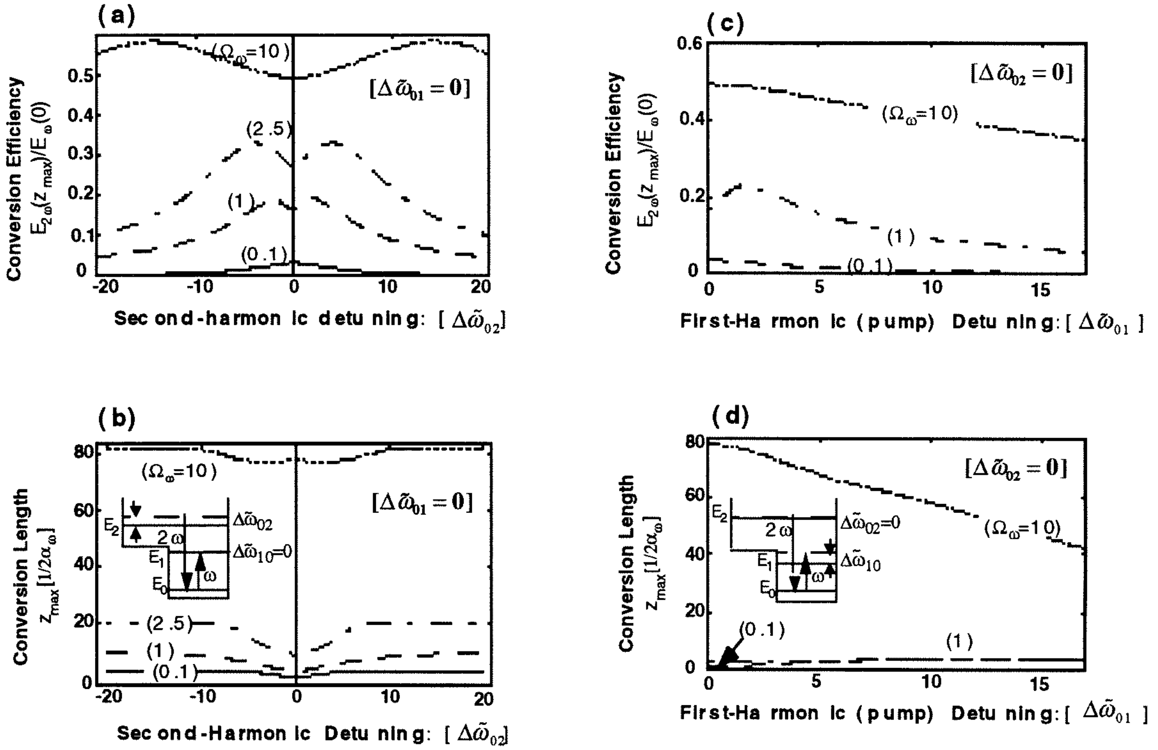

Figure 9.9: The numerically derived conversion efficiency a (c) and the distance at which it is obtained b (d) versus detuning for a low (Ω_{ω}= 0.1), a moderate (Ω_{ω}= 1), and a highly saturating (Ω_{ω}= 10) initial first-harmonic amplitude shown for a resonant first(second)-harmonic versus detuning of the second(first)-harmonic.

9.6 Summary

The generalized form in which we have presented our results should enable the treatment of resonantly-enhanced SHG without recourse to unjustified approximations or to numerics. We have shown that double-resonance is the optimal conversion condition in the weak intensity limit but not necessarily at saturating intensities, that full conversion is theoretically approachable on-resonance, and that the phase-mismatch is an inherent consequence of second-harmonic generation via off-resonant transitions. The effects of detuning, dipole matrix elements, and relaxation times on the conversion efficiency and conversion length at high intensities were examined. The fundamental limits derived on second-harmonic generation in a finite propagation layer clarify the limitations upon intersubband transition-induced second-harmonic generation despite the resonantly-enhanced nonlinearities. Whereas resonantly-enhanced transitions display impressive nonlinear coefficients and moderate conversion efficiencies have been demonstrated at relatively low intensities, we have shown here that the generation of a strong second-harmonic requires thick propagation layers. The large nonlinear coefficients of quantum well intersubband transitions do not therefore lead to an inherent advantage at high powers. Rather, it is the possibility of achieving moderate conversion efficiencies at low pump intensities and for sub-wavelength propagation lengths that seems to be the most promising feature of these designable transitions.

It should be noticed that the limits on the second-harmonic intensity that may be generated in a given propagation length (Equation 9.38), similarly to the limits derived in Chapters 7 and 8 for resonantly enhanced phase-modulation, may be extended to arbitrarily detuned transitions. Hence, at least in principle, they are valid for any nonlinear optical media. In practice, for most materials it is difficult to isolate the exact parameters of the transitions inducing the nonlinearities (which are typically not discrete). Because the saturation intensity is proportional to the detuning over the homogeneous broadening squared, it is typically extremely large for “transparent” media. Hence the perturbative treatment of the second-harmonic generation remains sufficient.

References:

[1] G. Almogy and A. Yariv, "Second-harmonic generation in absorptive media," *Optics Lett.*, **19,** 1828, 1994.

[2] G. Almogy and A. Yariv, "Fundamental limits on resonantly-enhanced second-harmonic generation," *J. Opt. Soc. Am. B*, in press.

[3] T. A. DeTemple, L. A. Bahler, and J. Osmundsen, "Semiclassical theory of resonant three-wave parametric interactions: second-harmonic generation," *Phys. Rev. A*, **24**, 1950, 1981.

[4] P. Boucaud and F. H. Julien, "Generation de second-harmonique dans les puits quantiques asymetriques GaAs-AlGaAs," *J. Phys. III*, **1**, 13, 1991.

[5] R. W. Boyd, *Nonlinear Optics*, San-Diego, California: Academic Press Inc., 1992.

[6] A. Yariv, *Quantum Electronics*, New-York: John Wiley & Sons, 1988.

[7] E. Rosencher, "Two-photon optical nonlinearities in a resonant quantum well system," *J. Appl. Phys.*, **73**, 1909, 1993.

[8] G. Almogy, A. Shakouri, and A. Yariv, "Observation of intersubband-transition-induced birefringence,” *Appl. Phys. Lett.*, **63**, 2720, 1993.

[9] G. Almogy, M. Segev, and A. Yariv, "Intersubband-transition-induced phase-matching," *Optics. Lett.*, **19**, 1192, 1994.

[10] T. A. DeTemple, M. K. Gurnick, and F. H. Julien, “Resonant four-wave parametric interactions: Adiabatic formulation,” *Phys. rev. A*, **37**, 3358, 1988.

[11] P. Boucaud, F. H. Julien, D. D. Yang, J. M. Lourtoiz, E. Rosencher, and P. Bois, “Saturation of second-harmonic generation in GaAs-AlGaAs asymmetric quantum wells,” *Optics Lett.*, **16**, 199, 1991.

[12] Z. Ikonic, V. Milanovic, and D. Tjapkin, “Resonant-second harmonic generation by a semiconductor quantum well in electric field,” *IEEE J. of Quant. Electron.*, **25**, 54, 1989.

[13] J. R. Meyer, C. A. Hoffman, F. J. Bartoli, E. R. Youngdale, and L. R. Ram-Mohan, “Momentum-space reservoir enhancement of intersubband second-harmonic generation,” *IEEE J. Quant. Electron.*, **31**, 706, 1995.

Part IV

Monolithic Integration of Quantum Well Infrared Photodetector and Modulator

Chapter 10

Monolithic Integration of Quantum Well Infrared Photodetector and Modulator

10.1 Introduction

With the on going transition from infrared (IR) imaging systems based on single detector elements, or lines of detectors, to two-dimensional focal-plane arrays (FPAs) there is an emerging need for temporal modulation (chopping) of the IR scene in order to achieve full TV rate integration and to reduce 1/f noise problems [1]. The rapid improvements in the performance of GaAs/AlGaAs quantum well infrared photodetectors [2,3] (QWIPs) together with the well developed technology of III-V materials has made them natural candidates for such IR FPAs [4]. Bandgap engineering techniques have also led to recent demonstrations of IR modulation using the short extinction length and ultrafast response characteristic of intersubband transitions [5,6,7]. In this chapter we report on the monolithic vertical integration of an optimized quantum well infrared modulator with a QWIP. The results, demonstrated for a single detector element, show the potential for efficient focal-plane IR modulation. Such modulation is particularly important for QWIPs, as their inherently large [8] and spatially nonuniform [9] dark-current leads to saturation of the readout circuits, thereby limiting integration times. Beyond monolithic integration with quantum well intersubband photodetectors (QWIPs), the multiquantum well modulator (MQWM) may also find other applications as it may be hybridized to FPAs of alternative materials. Indeed, some higher operating temperature IR-FPAs in development [1] require a mechanical chopper, introducing a moving component and thus negating one of the inherent advantages of FPAs over scanning systems. The monolithic integration of the multiquantum well modulator with the detector also turned out to be a uniquely simple and accurate scheme for studying the optical properties of electrons in quantum wells under bias.

The idea of the monolithic integration of the modulator and detector is a direct result of our analysis of the nonlinear optical response of intersubband transitions (Part II), and of considerations arising from the design of an infrared FPA monolithically integrating GaAs QWIPs and GaAs readout electronics. That design was carried out last summer in the Submicron center at the Weizmann Institute of Science in collaboration with Prof. Israel Bar-Joseph and Prof. Udi Meirav. The work on the modulator was carried out in collaboration with Yuanjian Xu who processed the samples and carried out the QWIP measurements, Ali Shakouri who grew the sample, Andrew Tong who wrote the self-consistent program (Chapter 2) that led to the uniquely accurate design capability, and with John O'Brien who consulted on the growth and other matters.

10.2 Motivation

Scanning IR imaging systems typically have a small number of detectors that may be individually addressed by external electronics. For staring FPAs, with between 10^4 to a few times 10^5 elements, individual connections becomes impractical, and the array is typically hybridized via indium bumps to a Silicon readout array [4]. The charge integration capacity of the individual capacitors in these readout circuits is currently limited by their pitch to roughly 10^7 electrons for a $10^{-5}cm^2$ pixel. Even with predicted improvements, charge-handling capacity is expected to be insufficient for T.V rate integration (40ms) of the total QWIP current ($\sim 10^{-4}A/cm^2$) at LiN_2 temperatures [10]. The shortened integration period thus negates the fundamental advantage of staring over scanning arrays: that of increased integration times (reduced bandwidths), and hence reduced noise-equivalent temperature differences (NETDs). As a result the NETD will be linearly proportional to the dark current rather than to its square root, as it is in the single detector case without charge integration limitations. Furthermore, a large integrated voltage on the readout capacitor places high demands on the injection transistor [11] and induces a nonlinear detector response. Off-chip integration, such as external sampling and averaging of the video signal, is impractical as a full alternative as it requires prohibitively fast electronics (and hence also cooling requirements) for full scale (640×480) arrays.

By modulating (chopping) the incident radiation it is possible to separate the 'ac' photo-response from the 'dc' dark current. If the detector's dark-current (modulator in off-state) is subtracted from the detector's joint signal and dark-current (modulator in on-state), only the net current (and noise) will accumulate on the capacitor. Thus the combination of an IR-modulator and a minimal on-pixel electronics circuit [12] allows collection of the detector's signal current only, leading to increased integration times. A schematic of this idea is shown in Figure *10.1*. An increase in the integration time by a factor of N (from T_{fill} to T_{frame}) will improve the signal to noise ratio by a factor of $\sqrt{N/2}$. Furthermore, even if charge integration limitations are somehow removed (or dark currents are reduced), temporal modulation reduces 1/f noise by shifting the central bandwidth from near 'dc' to the modulator's frequency. The benefits of the modulator may be compared to replacing cw operation by a chopper + lock-in amplifier mode of operation. Thus, on-pixel, super-T.V. - frame-rate integration, for enhanced viewing of slowly varying scenes also becomes possible. Non-temporal schemes for T.V. rate integration, such as constant current or dark cell subtraction do not lead to reduced 1/f noise. Spatial subtraction schemes are in fact susceptible to the large dark current nonuniformity (10-20%) of QWIPs [9].

Mechanical choppers, although used in some currently developed IR-FPAs [1], constitute a fast-moving component with the associated power requirements, reliability issues, and operating noise which compromise the inherent advantages of FPAs over scanning detectors. Development of a fast reliable electrooptic modulator in the IR would therefore be an important step towards realizing the full potential of staring IR-FPAs.

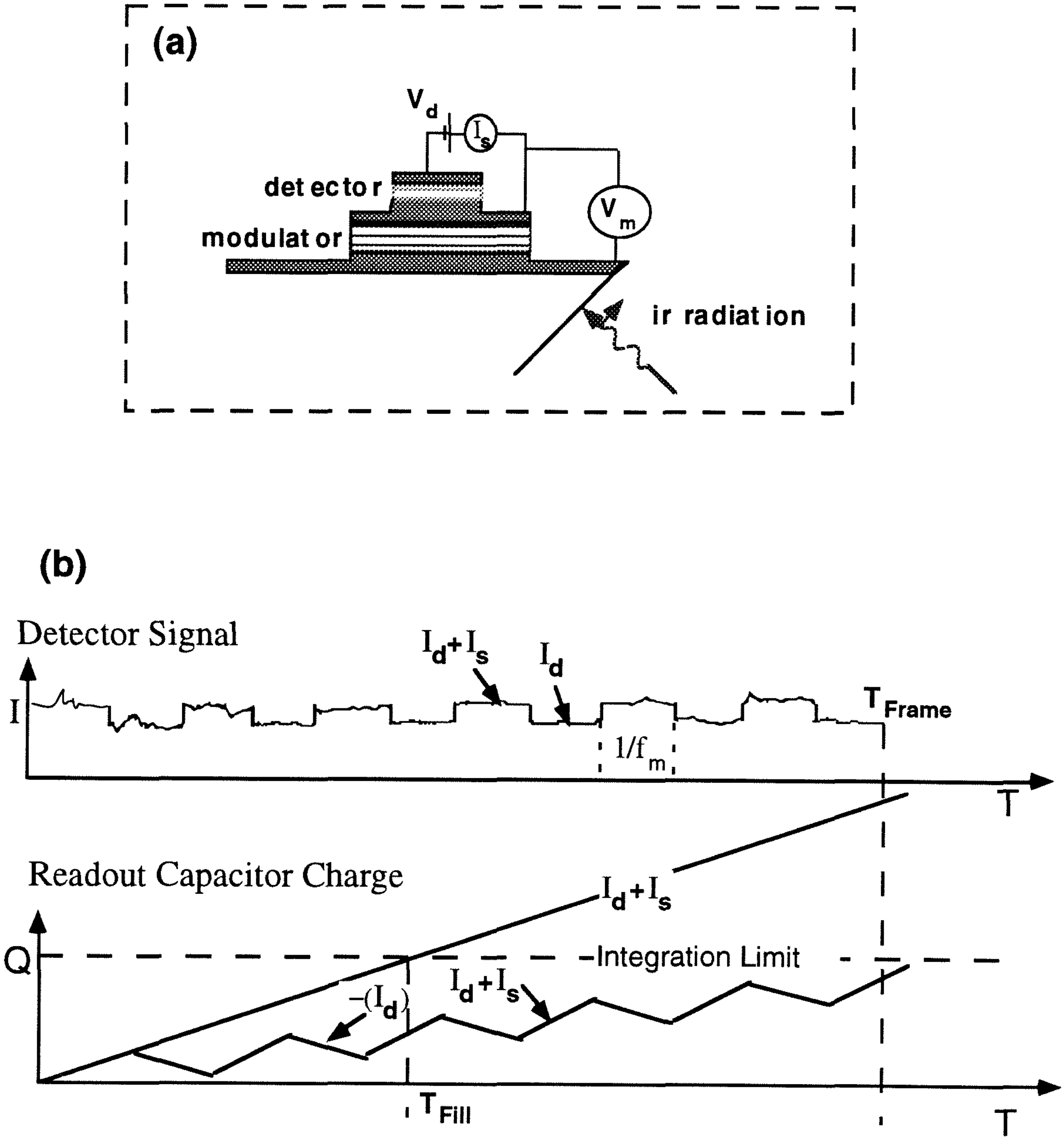

Figure 10.1: The monolithically integrated intersubband modulator and QWIP are shown in a and the separation of the 'ac'-signal from the 'dc' dark current are schematically shown in b. The top half of b shows the detector output signal versus time and the bottom part shows the integrated charge with (alternating slope) and without (constant slope) chopping. The former increases the integration time from T_{fill} *to* T_{Frame}.

10.3 Proposed Solution

The application which this project was designed for is schematically drawn in Figure 10.2. A 'dc'-electric-field will be used to enhance the absorption of a multi-quantum well modulator (MQWM) in the spectral response range of a vertically integrated IR-detector array - hence chopping the radiation flux impinging upon it. The modulator may be implemented as a single large element, the size of the FPA array, or as an array of individually addressable pixels overlapping the detector elements. The latter design is more processing intensive, but also more forgiving to material imperfections. It also offers a potential for novel image processing applications, essentially a mid-IR spatial light modulator, and is more compatible with the use of microlenses [13].

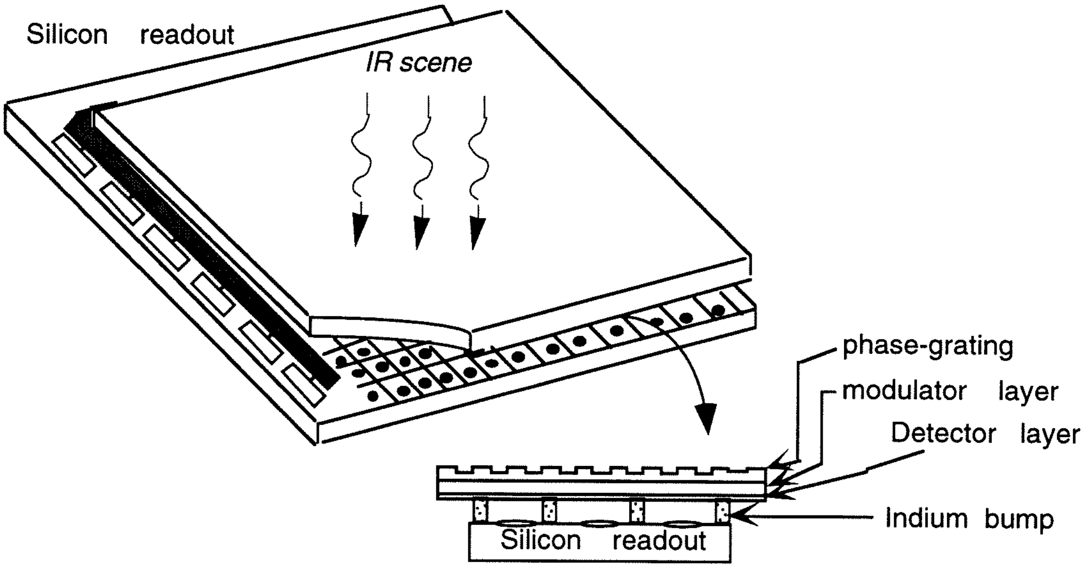

Figure 10.2: schematic illustration of an infrared-FPA with a monolithically integrated modulator.

10.3.1 Modulation Schemes

Quantum wells designed for modulation differ from those designed for photo-detection in their barrier height: both photocurrents and dark currents are undesirable so the excited states should be as confined as possible. Furthermore, the variation of the absorption spectra with applied bias, minimized in quantum well detectors for a constant gain spectrum, needs to be maximized for efficient modulation. Realization of quantum well modulators thus sets two basic requirements: that sufficient absorption can be created in the MQWM layers and that the absorption can be sufficiently controlled. Each of these requirements has been individually met: QWIPs with a near-unity quantum efficiency [14] and several methods of effectively controlling the intersubband transition-induced absorption [5-7] have been demonstrated. By combining these achievements we obtained a high-contrast modulator.

Electric field modulation of intersubband absorption may be obtained either by a shift of the resonance energy using the ‘dc’-Stark effect in asymmetric wells [5], control of overall structure symmetry in coherently coupled asymmetric quantum wells [6], or by modulation of the quantum well population [7]. The compatibility of the quantum coherence effect with the high doping levels and relatively narrow barriers required for an efficient modulator is still undetermined. Which of the two other techniques is preferable depends on the electric fields that may be applied without excessive current and on the transition broadening. Whereas population transfer leads to absorption amplitude control with a minor wavelength shift, the ‘dc’-stark effect modifies the absorption spectra and has a smaller effect on the total integrated absorption amplitude. Since the goal of our modulator was chopping of infrared radiation rather than tuning we chose the scheme of lightly coupled quantum wells. This scheme insures minimal modification of the detector's line shape and robustness at the high doping densities required. Applied bias was used to move electrons from a narrow well, with a resonance frequency designed to be at the maximum of the detector's photoresponse, to a wide (reservoir) quantum well with a transition energy at the tail of the detector's photoresponse spectrum.

Since the intersubband dephasing time is on the order of 0.1ps and inter-well electron transport times are on the order of 1ps, there are only electronic capacitance limits to the modulation frequency. Fundamentally, the combination of the fast relaxation rates and the extremely short propagation length required for full modulation (order of one wavelength) make these modulators promising candidates for ultra-high speed modulation. With the on going development of large band offset materials [15] and the initial observation of intersubband transitions at fiber-optic wavelengths [16] (1.55μm) the basic modulation principles developed in this project may find numerous other applications.

10.4 Charge Transfer Between Coupled Quantum Wells

The dynamic range of the modulator is determined by the voltage control over the electron surface density in the ground state of the narrow quantum well (Figure 10.3). The most accurate way of calculating this dependence is by using the self-consistent program described in Chapter 2. A simple analytic model taking into account the density of states, Coloumbic repulsion and flat-band boundary conditions can, however, reproduce the numeric solution with extremely high accuracy. This model for charge transfer between two wells is valid as long as each well by itself is symmetric and they are only lightly coupled. In this case the wavefunctions remain unmodified to the first order by the electric field (to the second order they shift by the same amount) so their separation remains constant. The separation of the coupled quantum wells and the length of the structure period are shown below to be the only parameters controlling charge transfer as a function of applied voltage.

10.4.1 Coulombic Repulsion

Assuming that the Fermi level is above both ground subbands, that there is no thermal distribution of charges, and that the wavefunctions remain unmodified by the electric field, we can solve for the charge transfer as a function of applied bias. As a starting point for the self-consistent derivation we do not include Coloumbic repulsion. This leads to a surface charge transfer (σ) between quantum wells as a result of voltage applied between the centroids of the subbands (V) given as:

$$\frac{d\sigma}{dV} = \frac{d(\sigma q)}{d(Vq)} = \frac{1}{2} \cdot \frac{m^* q}{\pi \hbar^2} \tag{10.1}$$

where m* is the electron effective mass, q the electronic charge, $m^*/\pi\hbar^2$ is the 2-d density of states per subband, and the factor of 1/2 comes from lowering of the Fermi level (equal surface density of states in both wells).

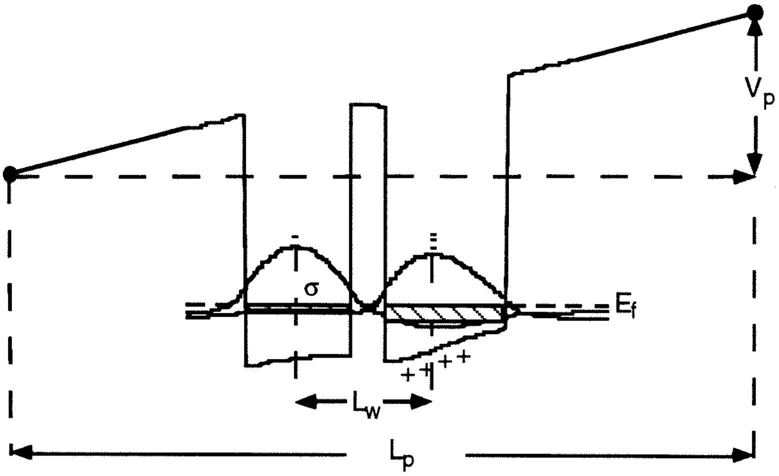

Figure 10.3: A schematic defining the parameters used in the calculation of the charge transfer between coupled quantum wells.

The charge transfer will lead, however, to a screening electric field (E_σ), which will offset some of the external field (E_{ext}) which originally induced it. The internal field (E_{in}) will hence become:

$$E_{\text{int}} = E_{ext} - E_\sigma = E_{ext} - \frac{\sigma q}{\varepsilon_o \varepsilon} \tag{10.2}$$

where ε_0 is the vacuum susceptibility and ε is the susceptibility in the quantum wells, given by $\varepsilon \cong 13.1-3.0x$, where x is the aluminum concentration in $Al_xGa_{1-x}As$. As a result of the reduced field (E_{int}) the corrected charge transfer will be given by :

$$\sigma = L_w \cdot E_{\text{int}} \cdot \frac{m^* q}{2\pi\hbar^2} = L_w (E_{ext} - \frac{\sigma q}{\varepsilon_o \varepsilon}) \cdot \frac{m^* q}{2\pi\hbar^2} \tag{10.3}$$

where the charge shift distance is defined as:

$$L_w \equiv \left| \langle \psi_{n0} | z | \psi^*_{n0} \rangle - \langle \psi_{w0} | z | \psi^*_{w0} \rangle \right| \tag{10.4}$$

i.e., the separation between the ground states of the narrow and wide quantum wells: Ψ_{n0} and Ψ_{w0} , respectively. Since the field is linear with charge there is no approximation involved in considering charge transfer between two district points rather than between wavefunctions. Solving Equation 10.3 for σ we thus obtain:

$$\sigma = \frac{\frac{m^* q L_w}{2\pi\hbar^2} \cdot E_{ext}}{1 + \frac{m^* q^2 L_w}{2\varepsilon_o \varepsilon \pi \hbar^2}} = \frac{\varepsilon_o \varepsilon / q}{y+1} E_{ext} \tag{10.5}$$

where we have defined the screening term as:

$$y \equiv \frac{2\varepsilon_o \varepsilon \pi \hbar^2}{m^* q^2 L_w} \tag{10.6}$$

10.4.2 Voltage Boundary Conditions

Since the voltage drop across the structure is held constant, the electric field must maintain the condition:

$$V_p = E_{ext}(L_p - L_w) + (E_{ext} - E_\sigma)L_w = E_{ext}L_p - (\frac{\sigma q}{\varepsilon_o \varepsilon})L_w \tag{10.7}$$

where L_p is the total length of one period (well + barrier) and V_p is defined as the voltage applied across a period. Hence, using Equation 10.5 the field between periods will be given by:

$$E_{ext} = V_p / (L_p - \frac{L_w}{y+1}) \tag{10.8}$$

The correction in the applied field will come as a result of interperiod charge transfer as discussed in section 2.8. The charge transfer density will hence become:

$$\sigma = \frac{\varepsilon_o \varepsilon}{q} \frac{V_p}{L_p - L_w + L_p y} \tag{10.9}$$

Equation 10.9 shows that the highest charge transfer for a given voltage will be achieved for the largest intra- to inter-period separation (L_w/L_p). This added dynamic range will however come at the expense of a slower response. The conclusion remains valid as long as the barrier is much smaller within each period than between periods. Although a rigorous analysis requires inclusion of transport issues, they may be neglected (at low temperatures) as long as the barrier area above the Fermi level is much smaller within each period than between periods.

10.4.3 Absorption Induced by Population Transfer

Neglecting the contribution of carriers in the reservoir (wider) well, the absorption within the detector's response spectrum is given for a single pass through a multiquantum well stack as:

$$A(\Delta E) \equiv -\log_{10}(I_{out}/I_{in}) = \log_{10}(e) \cdot \frac{2\pi q^2}{n\lambda\varepsilon_0} \cdot \frac{\sigma\mu^2}{\Gamma[1+(\Delta E/\Gamma)^2]} \cdot \frac{\sin^2(\theta)}{\cos(\theta)} \tag{10.10}$$

where λ is the optical wavelength, n the refractive index, and θ the angle between the polarization vector and the plane of the quantum wells (accounting for both the reduction in the interaction strength and the decrease in the propagation length as the propagation direction approaches the normal to the quantum well planes). The dipole matrix element, the transition's half-width at half-maximum (HWHM) energy, the total surface charge density in the narrow wells, and the detuning energy are defined as: μ, Γ, σ, and ΔE, respectively. For an estimate of the obtainable performance we consider a stack of 100 quantum wells, each doped to $\sigma=1\times10^{12}\text{cm}^{-2}$, optical matrix elements (μ) of 20A°, a wavelength (λ) of 10μm, and a half-width at half broadening energy (Γ) of 3.3meV (a dephasing time of $T_2\cong200\text{fs}$). This leads to an absorption ($e^{-\alpha l}$) of greater than 98% for normal polarization; at an angle of 45° the absorption is reduced to 95% due to selection rules. The variation of the surface density with applied bias is given in Equation 10.9, which when inserted into equation 10.10 gives the variation of the absorption with the applied bias.

10.5 Monolithic Detector and Modulator: Results

10.5.1 Design and Structure

To meet the rather severe design criteria both the bound-to-quasicontinuum detector and the multiquantum well modulator were designed with a self-consistent program (Chapter 2) using feedback from a single previous iteration. The program includes nonparabolicity, both direct and indirect Coulombic interactions with their explicit temperature dependence, and a self-consistent electric field correction to match voltage boundary conditions. The integrated device was grown on a semi-insulating GaAs substrate by molecular beam epitaxy (MBE). The multiquantum well modulator, consisting of 50 periods of weakly coupled asymmetric quantum wells, was grown following a 0.6μm

n^+-GaAs contact layer and a 0.2μm GaAs buffer layer. The growth sequence of each modulator period consisted of a 9nm undoped GaAs well, a 3nm undoped $Al_{0.4}Ga_{0.6}As$ separation barrier, and a 10.8nm storage well. The latter was Si-doped to a nominal volume density of $2\times10^{18}cm^{-3}$ in a 4nm thick region beginning 0.5nm away from the barrier (Figure 10.4). The modulator periods were separated by 42.2nm $Al_{0.4}Ga_{0.6}As$ barriers. To maximize the modulator's dynamic range this structure was designed so that about 20% of the charge would be contained in the narrow well at low temperatures. In fact, while it contained roughly 28% of the population at room temperature, this reduced to roughly 11% at 80K and 8% at 10K. Using the self-consistent solution (Chapter 2) and attempting to take into account possible inaccuracy of the growth parameters we find that donor segregation of around 3nm is the most likely candidate accounting for the observed population distribution. Such segregation is expected [17] and will have a minor influence on the separation energy or on the voltage dependence of the charge transfer.

The QWIP was grown on top of the modulator following a 0.2μm GaAs buffer layer and a 0.6μm n^+-GaAs contact layer. It consisted of fifteen 6.5nm-thick Si-doped GaAs QWs with a nominal doping density of $1.1\times10^{12}cm^{-2}$ and sixteen 44nm-thick $Al_{0.18}Ga_{0.82}As$ barriers. Single element mesas where fabricated in a two-step etching process and an edge of the sample was polished to 45° to couple IR radiation in accordance with the intersubband selection rules. The room temperature absorption of the sample is shown in Figure 10.5. After a standard intersubband FTIR measurement, the top detector layer was chemically etched, and the absorption of the modulator stack alone was measured. The curve fit to the difference between these measurements allows us to deduce the detector's absorption spectrum at room temperature. It should be remembered, however, that the absorption spectrums of both the modulator and detector will be shifted at lower temperatures. There is also some nonuniformity across the wafer. Furthermore, there is some offset between the detector's absorption and photocurrent spectrums because the latter also depends on the escape probability from the quantum well.

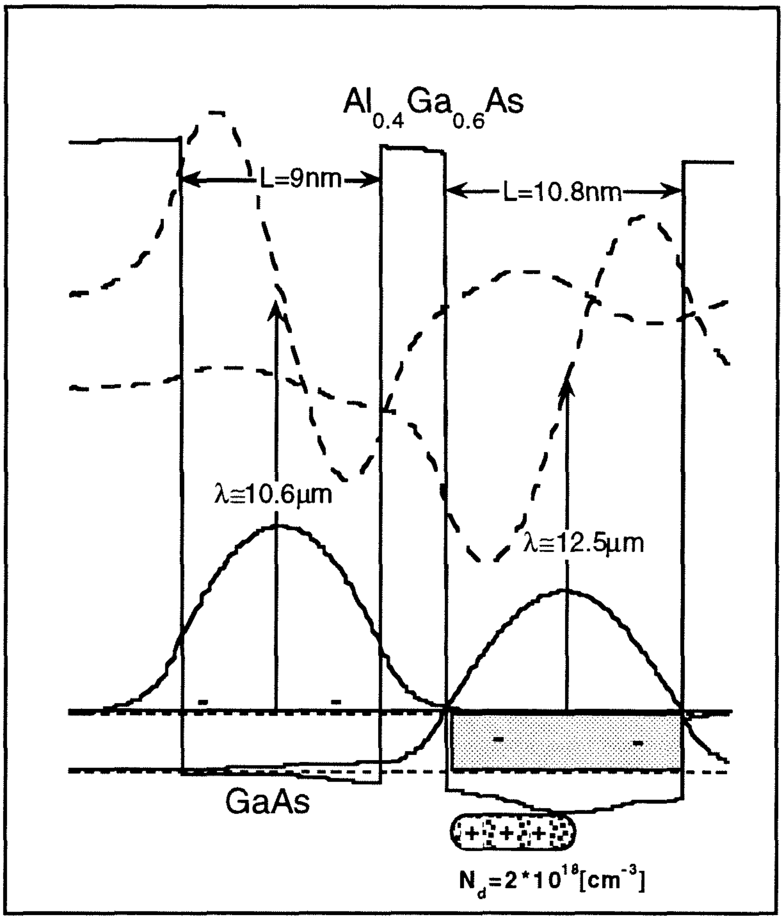

Figure 10.4: The self-consistent solution of the coupled quantum wells at 30K. The left (narrow) well, with an absorption peak at 10.6μm, is designed to contain 20% of the population. The right (wide) well, with an absorption peak at 12.5μm, is designed to contain 80% of the population. The nominal charge location and density in the wide well are also shown. The ground states are the solid lines and the excited states the dashed lines.

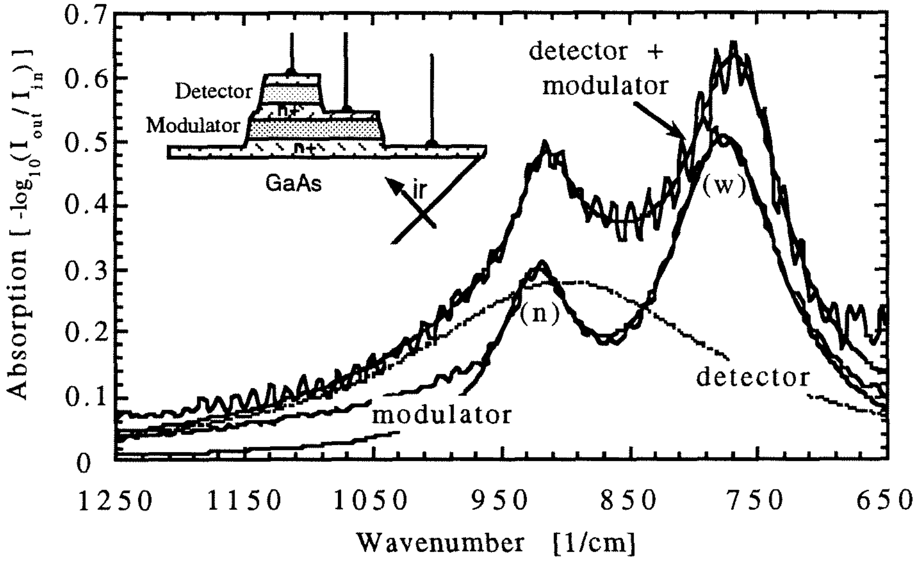

Figure 10.5: The room temperature absorption spectra of the asymmetric double quantum wells and the detector jointly and separately (obtained by chemically etching the detector). A schematic of the fabricated modulator and detector structure is shown in the inset.

10.5.2 Modulation

Modulation was measured in a Mattson FTIR at 10K with the (monolithic) QWIP replacing the original MCT detector. The operating temperature was not limited by the modulator, but, as expected, by the detector. Since the latter was unoptimized, the experiment was limited to sub-LN$_2$ temperatures. As derived in the previous section, the modulator's dynamic range will depend on the charge transfer and hence on the applied voltage. The maximal applied voltage was limited by the leakage current produced in the modulator which varied between samples, where we limited the current to 100μA for a 300×400mm mesa to prevent heating damage. This leakage current nonuniformity, together with the high concentration of oval defects in our samples and the fact that the current is orders of magnitude above the expected thermal current at 10K and does not display an exponential dependence on the activation energy, show that it is limited by material quality issues and not by fundamental transport mechanisms as in QWIPs. Improved quality should hopefully allow application of higher electric fields and hence increase the modulation depth.

The detector's photoresponse is plotted in Figure 10.6 for a negative bias (-13V, E≅−36kVcm) at which the narrow well is almost completely depleted, and for a positive bias (14V, E≅38kVcm) at which nearly half the population has been transferred to the narrow well. The transmission at line center of the narrow well is seen to vary from almost 100% to 60%. It can also be seen that the modulator's peak response is, as designed, within a fraction of the broadening (≅1mev) of the detector's photoresponse maximum. In another sample processed from the same wafer a slightly higher modulation depth of 45% was obtained (for a voltage of 20V), but with a slightly larger separation between the peaks of the detector's response and the modulator's absorption.

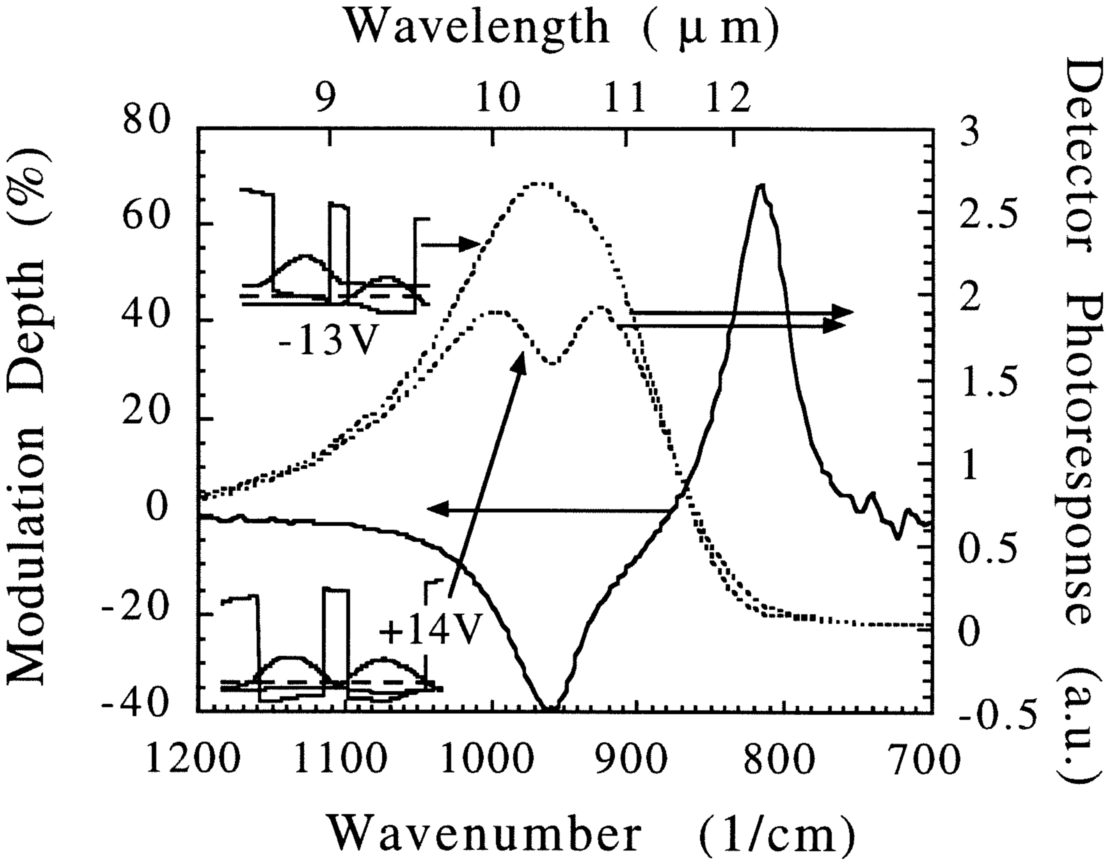

Figure 10.6: The detector's photoresponse for a negative (-13V) and positive (+14V) modulator bias leading to the depletion and the filling of the narrow well respectively. Their ratio gives the modulation depth. The self-consistent solutions of the quantum well under the positive and negative bias are also schematically shown.

Figure 10.7 displays the self-consistent solutions of the coupled quantum wells under the negative bias depleting the narrow well (-36kV/cm) and under the maximal positive bias applied to this sample (38kV/cm). From the former we can deduce that the only charge remaining in the narrow well at E_{ext}=-36kV/cm is due to nonuniformity. This remaining charge, no more than one percent of the total doping, leads to the barely discernible kink in the detector's absorption spectrum at 10.7μm (Figure 10.6). From the solution for a field of E_{ext}=38kV/cm we can deduce that the voltage applied on this sample (+14V) is below that necessary for the crossing of the ground subbands.

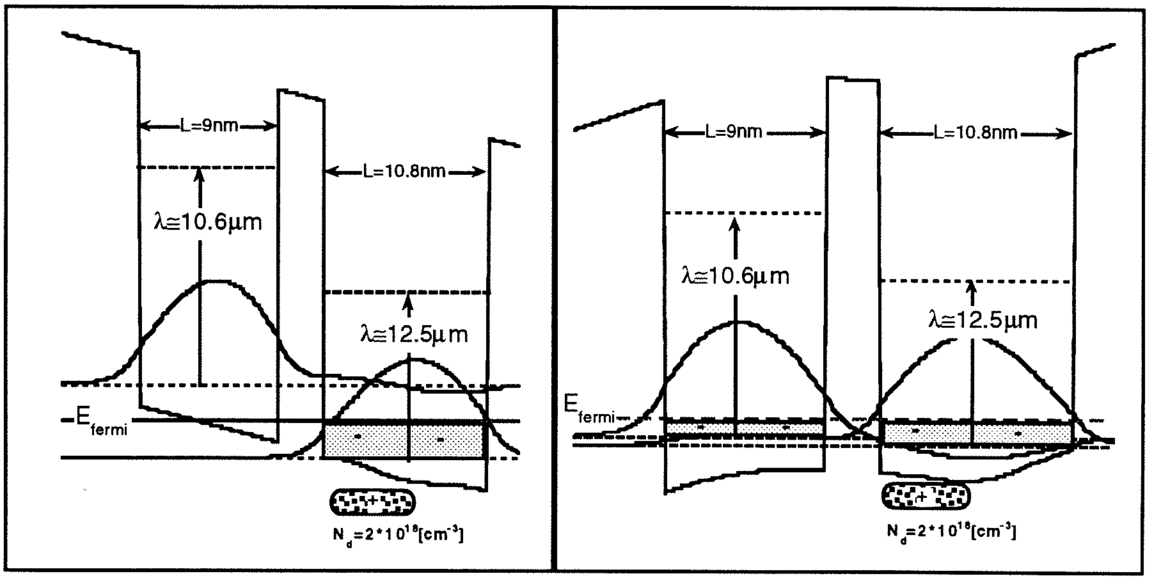

Figure 10.7: The self-consistent solution of the coupled quantum well modulator at the negative (-36kV/cm) and positive (38kV/cm) applied fields for which the detector's response spectrum is shown in Figure 10.6.

10.6 Voltage and Population Dependence

By subtracting the detector's response when it is blocked by the modulator from its full response we may deduce the absorption in the modulator. This is done by subtracting the detector's response for a given bias, applied to the modulator from the detector's response when the maximal negative voltage applied to the modulator (-13V). The results of this for voltages between -12V and +14V are shown in Figure 10.8. Whereas the absorption of the narrow well is accurately derived this way, the spectrum obtained for the wide well is not. Since we cannot apply sufficient bias to completely empty the wide well we have to curve fit the detector's unperturbed response at those wavelengths.

Furthermore, because the detector has a very low efficiency at the wavelength of the wide well's absorption (≅12.5μm), the measured signal will be close to the noise level.

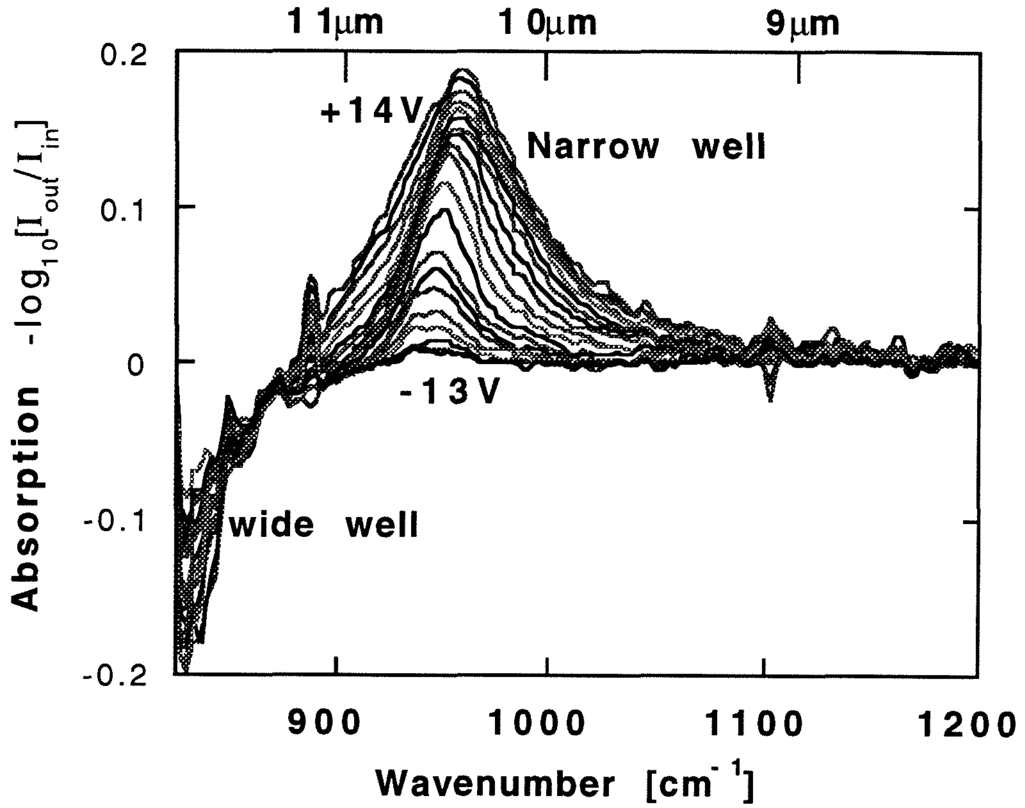

Figure 10.8: The modulator's absorption change given by the ratio of the detector's response at -13V to its response at voltages between that and +14V.

By curve fitting the absorption spectrum of the narrow quantum well with a Lorentzian line shape we obtain the dependence of the transition parameters on the applied bias. These parameters (given here for a different sample on the same wafer for which a higher bias could be applied) are shown in Figure 10.9.

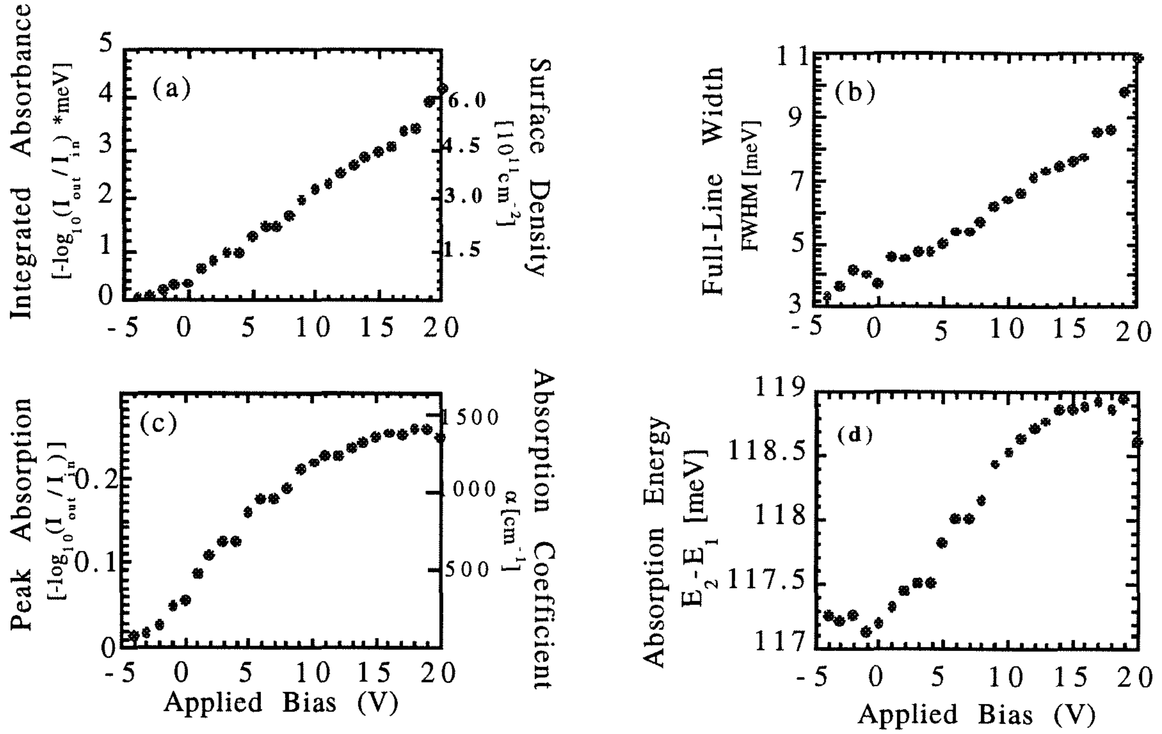

Figure 10.9: The voltage dependence of the (narrow-well) intersubband transition parameters.

Figure 10.9a shows the integrated absorption as a function of applied bias, with an almost perfectly linear slope in the 0V to 17V range. Equation 10.10 is used to correlate the integrated absorption change to the population transferred (the left to right hand axes of Figure 10.9a). The population transfer per applied voltage is about 15% larger than expected from Equation 10.9 or from the self-consistent solution of Chapter 2. Inclusion of exchange interaction within the Hartree-Fock model [18], however, accounts for this correction. As population is moved into the narrow well its exchange energy (negative) increases while that of the wide well decreases as its population is reduced. As expected, the exchange interaction partially offsets the Coloumbic interaction.

Figure 10.9b shows the full width at half-maximum transition broadening energy (FWHM) versus applied bias. From application of the opposite (depleting) bias, from the bias-induced broadening of wells with constant populations, and from theoretical models [19], we deduce that the bias induced broadening contribution accounts for only a fraction of the observed broadening. The rest of the broadening is consistent with the filling of the ground subband of the narrow well. This will lead to increased broadening both through the contribution of single-particle nonparabolicity [20] and through the effective nonparabolicity created by the momentum dependence of the exchange interaction [21]. The contribution of the electron-electron scattering is also expected to be minor [22] at these densities.

The direct consequence of the increased broadening with increased population is shown in Figure 10.9c - although the integrated absorption area of the narrow well (Figure 10.9b) monotonicly increases with applied bias, the peak amplitude saturates at roughly 15V and eventually declines. Examining Equation 10.10 we see that the added broadening cancels out the contribution of the added population to the peak absorption. This means that application of larger biases and hence a greater charge transfer no longer contribute to the peak modulation depth beyond the saturation point. An increase of the modulation depth beyond the maximal value obtained (45%) thus requires more coupled quantum well periods in the modulator. Increased bias, on the other hand, will lead to increased broadening which is also useful if it is important to cover a larger spectral range (as can be seen in Figure 10.6 the absorption spectrum of the bound-to-bound modulator is much narrower that that of the bound-to-continuum QWIP).

The observed broadening may have important consequences for many intersubband transition based devices. One apparent conclusion is that previous estimates of the separation required between the donors and the electrons to reduce the donor induced broadening were greatly exaggerated [23] as they did not consider the population induced broadening. Obtaining the population induced broadening limit on the maximal value for the absorption in optimized quantum well structures is also of fundamental importance for nonlinear processes. As discussed in Part II of the thesis the maximal linear interaction strength sets upper limits on the obtainable nonlinear phenomena in a given propagation thickness. The issue of population induced broadening, which we have briefly touched upon here, definitely merits a more comprehensive treatment.

Figure 10.9d shows the increase in the intersubband transition energy as function of applied bias. The self-consistent solution shows that this shift is due to the increased population and hence increased exchange interaction. This has been measured before by comparing growths of nominally identical structure with increasing doping concentration [24], but has never been directly observed.

10.7 Future Directions

The immediate improvement required of the multiquantum well modulator is a significantly higher modulation depth. The signal transmitted through the modulator in its off-state will add to the 'dc' rather than 'ac' component and hence translate to a reduced detector efficiency. From equation 10.10 and from the results of Figure 10.9 we can deduce that 200 coupled quantum well periods, requiring a growth of an epitaxial layer about 8μm thick, with a voltage swing of 30V, will lead to an absorption of roughly 95% - a result which should be quite sufficient for most applications. Once this goal is obtained, several other improvements could greatly increase the potential applications of this concept.

10.7.1 Normal Incidence

One of the main difficulties encountered in attempts to utilize intersubband transitions is the selection rule dictating interaction only with polarization perpendicular to their planes. This selection rule may be overcome by a two-dimensional phase grating [25] or by transitions between states with relaxed selection rules: either in p-doped wells or quantum wells in indirect bandgap materials [26]. Achievement of normal incidence modulators via the use of intersubband transitions violating the selection rules of the diagonal effective mass model (section 1.4) would allow for natural integration with alternate IR-detectors. The reduced mobility of the latter limits their potential as detectors, but may lead to reduced currents and hence be an advantage for modulators.

10.7.2 Operating Temperature

Since the proposed modulator is monolithically integrated with a QWIP which operates at 77K or below, and since the quantum wells in the modulators are designed with higher barriers than those in the detectors - the former will not impose a cooling requirement. Indeed, unlike in detectors where the dark current is fundamentally related to the absorption wavelength [8], the final state in modulator intersubband transitions may be well confined. Thus the use of MQWMs in conjunction with elevated operating temperature detectors [27], or even room temperature ones [1], should be possible as conduction band offsets of over 1V have been obtained on GaAs substrates [15].

10.7.3 Spectroscopy

The 'dc'-stark effect may be used to shift the absorption spectrum of an asymmetric modulator and hence control the detector's gain spectrum. This method is preferred over the direct tuning of an asymmetric quantum well detector because the bias change will unavoidably change its gain and dark current along with its spectrum. Furthermore, the modulator, which is based on a bound-to-bound transition, can be designed to have a significantly narrower absorption line width than the detector. Thus, it is feasible to monolithicly build a fast imaging infrared spectrometer which may find applications in remote sensing and environmental monitoring.

References:

---

[1] C. M. Hanson "Uncooled thermal imaging at Texas Instruments," *SPIE Infrared Technology XIX*, **2020**, 330, 1993.

[2] L. C. Chiu, J. S. Smith, S. Margalit, A. Yariv, and A. Y. Cho, "Application of internal photoemission from quantum-well and heterojunction super-lattices to infrared photodetectors," *Infrared Physics*. **23**, 93 1983.

[3] B. F. Levine, "Quantum-well infrared photodetectors," *J. Appl. Phys.*, **74**, R1-R80, 1993.

[4] C. G. Bethea, B. F. Levine, et al., "Long wavelength infrared 128×128 $Al_xGa_{1-x}As$/GaAs quantum well infrared camera and imaging system," *IEEE Electron. Dev.*, **40**, 1957, 1993.

or: L. J. Kozlowski, G. M. Williams, G. J. Sullivan, C. W. Farley, and R. J. Anderson, "LWIR 128×128 GaAs/AlGaAs multiple quantum well hybrid focal plane array," *IEEE Electron. Dev.*, **38**, 1124, 1991.

or: T. S Fasaka, W. A. Beck, J. W. Little, A. C. Goldberg, B. Rosner, and M. Stegall, "Staring LWIR MBT quantum-well sensor performance using the commercial infrared ImagIR camera system," *Proc. of SPIE Infrared Imaging Systems: Design, Analysis, Modeling and Testing IV*, vol.1969-25, 1993.

[5] E. Martinet, F. Luc, E. Rosencher, P. Bois, and S. Delaitre, "Electrical tunability of infrared detectors using compositionally asymmetric GaAs/AlGaAs multiquantum wells," *Appl. Phys. Lett.*, **60**, 895, 1992.

[6] J. Faist, F. Capasso, A. L. Hutchinson, L. Pfeiffer, and K. C. West, "Suppression of optical absorption by electric-field-induced quantum interference in coupled potential wells," *Phys. Rev. Lett.*, **71**, 3573, 1993.

[7] N. Vodjdani, B. Vinter, V. Berger, E. Bockenhoff, and E. Costard, “Tunneling assisted modulation of the intersubband absorption in double quantum wells,” *Appl. Phys. Lett.*, **59**, 555, 1991.

[8] M. A. Kinch and A. Yariv, “Performance limitations of GaAs/AlGaAs infrared superlattices,” *Appl. Phys. Lett.*, **55**, 2093, 1989.

[9] V. Swaminathan, “Producibility of GaAs/AlGaAs quantum well infrared photodetector arrays - material and processing issues," in *NATO Advanced Research Workshop on Quantum Well Intersubband Transition Physics and Devices,* Canada: Whistler, September 1993.

[10] R. E. DeWames, J. M. Aria, L. J. Kozlowski, and G. M. Williams, "An assessment of HgCdTe and GaAs/AlGaAs technologies for LWIR infrared imagers," *SPIE- infrared Detectors: state-of-the-art*, **1735**, 2, 1992.

[11] N. Bluzer, and A. S. Jensen, "Current readout of infrared detectors," *Optical Eng.*, **26**, 241, 1987.

[12] B. Pain, S. K. Mendis, R. C. Schober, R. H. Nixon, E. R. Fossum, "Low-power low-noise analog circuits for on-focal-plane signal processing of infrared sensors," *Proc SPIE Infrared Detectors and Instrumentation*, **1946**, 365, 1993.

[13] N. T. Gordon, C. L. Jones, and D. J. Purdy, "Application of microlenses to infrared detector arrays," *Infrared Phys.*, **3196**, 599, 1991.

[14] J. Y. Andersson, and L. Lundqvist, "Near-unity quantum efficiency of AlGaAs/GaAs quantum well infrared detectors using a waveguide with a doubly periodic grating coupler," *Appl. Phys. Lett.*, **59**, 857, 1991.

[15] E. L. Martinet, G. L. Woods, H. C. Chui, J. S. Harris, Jr., M. M. Fejer. C. A. Bella and B. A. Richman, "Free-electron laser nonlinear spectroscopy of doubly resonant (5.5-3.0 mm and 4.1-2.1 mm) InGaAs/AlGaAs asymmetric quantum wells," *SPIE OE/LASE proceedings, Quantum well and superlattice physics*, **2139**, 1994.

[16] J. H. Smet, L. H. Peng, Y. Hirayama, C. G. Fonstad, "Electron intersubband transitions to 0.8eV (1.55mm) in InGaAs/AlAs single quantum-wells," *Appl. Phys. Lett*, **64**, 986, 1994.

[17] L. Pfeiffer, E. F. Schubert, K. W. West, and C. W. Magee, "Si dopant migration and the AlGaAs/GaAs inverted interface," *Appl. Phys. Lett.*, **58,** 2258, 1991.

[18] K. M. S. V. Bandara, D. D. Koon, Byungsung O, Y. F. Lin, and M. H. Francombe, "Exchange interactions in quantum well subbands," *Appl. Phys. Lett.*, **53**, 1931, 1988.

[19] R. Ferreira and G. Bastard, "Evaluation of some scattering times for electrons in unbiased and biased single- and multiple-quantum-well structures," *Phys. Rev. B*, **40**, 1074, 1989.

[20] M. Zaluzny, "On the intersubband absorption line width in semiconductor quantum wells," *Solid State Comm.*, **82**, 565, 1992.

[21] J. W. Choe, O. Byungsung, K. M. S. V. Bandara, and D. D. Coon, "Spectral line widths of quantum well intersubband transitions," *Superlattices and Microstructures*, **10**, 1, 1991.

[22] P. Sotirelis, P. Von Allmen, and K. Hess, "Electron intersubband relaxation in doped quantum wells," *Phys Rev. B*, **47**, 12744, 1993.

[23] E. B. Dupont, D. Delacourt, D. Papillon, J. P. Schnell, and M. Papuchon, "Influence of ionized impurities on the linewidth of intersubband transitions in GaAs/GaAlAs quantum wells," *Appl. Phys. Lett.*, **60**, 2121, 1992.

[24] M. O. Manasreh, F. Smulowicz, T. Vaughan, K. R. Evans, C. E. Stutz, and D. W. Fischer, "Intersubband infrared absorption in a GaAs/$Al_{0.3}Ga_{0.7}As$ multiple quantum well," in "*Intersubband Transitions in Quantum Wells*," E. Rosencher, B. Vinter, and B. F. Levine, Eds., NATO ASI Series, Series B, Physics, **287**, New York: Plenum, 1992.

[25] L. S. Yu, S. L. Sheng, Y. H. Wang, and Y. C. Kao, "A study of the coupling efficiency versus grating period in a normal incident GaAs/AlGaAs multiquantum well infrared detector," *J. Appl. Phys.*, **72**, 2105, 1992.

[26] J. Katz, Y. Zhang, and W. I. Wang, "Normal incidence infrared absorption in AlAs/AlGaAs x-valley multiquantum wells," *Appl. Phys. Lett*, **61**, 1697, 1992.

[27] L. J. Kozlowski, W. V. McLevige, S. A. Cabelli, A. H. B. Vanderwyck, D. E. Cooper, E. R. Blazejewski, K. Vural, and W. E. Tennant, "Attainment of high sensitivity at elevated operating temperatures with staring hybrid HgCdTe-on-sapphire focal plane arrays," *Optical Engineering*, **33**, 704, 1994.